Study of the fundamental properties of III-V based diluted magnetic semiconductor GaMnAs and its related heterostructures

III-V 族希薄磁性半導体 GaMnAs および GaMnAs ベース・ヘテロ構造の基本物性研究

Toshiaki Hayshi

林　稔晶

Study of the fundamental properties of III-V based diluted magnetic semiconductor GaMnAs and its related heterostructures

Toshiaki Hayashi

Professor M. Tanaka's laboratory

Department of Electronic Engineering

The University of Tokyo

Preface

This manuscript was drawn up for a doctor thesis of the graduate school Electronic Engineering, The University of Tokyo, 1999. The fundamental properties of a new class of III-V based diluted magnetic semiconductor (DMS), GaMnAs, and its related heterostructures are described here. The author, Toshiaki Hayashi, has studied the electric, magnetic, and optical properties of GaMnAs as well as the growth of its films since 1994. The subject has extended to one of the challenges for the application of GaMnAs, tunneling magnetoresistance (TMR) effects.

Current electronics industry is on the basis of semiconductor technologies. For this quarter century, the semiconductor electronics has ignored the magnetic properties of semiconductors which are hard to handle for device applications. In this sense the researches described here are a very unique and challenging project to combine electronics and magnetism both of which lie at the heart of solid state physics.

Magnetism has developed for a long time its independent culture which is completely distinguished from that of semiconductor physics. Therefore, sometimes, readers might be perplexed with the difference of point of views between electronics and magnetism. I wish that many of those problems would be made clear after reading to an end.

I begin the thesis with the brief introduction of semiconductor spin electronics in chapter 1. A new degree of the interplay between electronic spin and local magnetic moments are introduced to semiconductor electronics. And the meaning of the study of GaMnAs is ascertained there. The fundamental properties of GaMnAs are discussed from various aspects in chapter 2. Some possible models to explain each experimental result of GaMnAs have been proposed but none of them has been generally accepted so far. Therefore I gave my own thought of some problems based on many discussions with my coworkers. Especially, the metal-insulator (nonmetal) transition, the ferromagnetism and the *p-d* exchange interaction of GaMnAs are related to one another and deduced from one picture. In chapter 3 the topic of GaMnAs / AlAs superlattices is discussed as one of the

bandengineering approaches to magnetic semiconductor heterostructures. Chapter 4 is devoted to spin-dependent tunneling spectroscopy of GaMnAs. The metal-insulator transition is discussed again. In chapter 5 tunneling magnetoresistance effects (TMR) of GaMnAs based heterostructure are discussed. A new type of TMR effect will be proposed which makes use of quantum interference phenomenon of electrons. The interference phenomenon in magnetic multilayer systems is characteristic of magnetic semiconductor heterostructures with abrupt interfaces. Finally the conclusion of study of GaMnAs and general remarks will be given in the end chapter.

This work has been done with many coworkers. I acknowledge many labo. friends of mine here. Especially, K. Seto, K. Takahashi, M. Takenaka, T. Nanmu, and H. Shimizu. I have been fortunate in receiving many help and support from them.

I am grateful to Dr. K. Ando at Electrotechnical Laboratory. He has guided me in my magneto-optical studies. I would like to express my thanks to Dr. H. Shimada. I have received generous direction from him in terms of low temperature transport measurements. I also acknowledge Prof. A. Asamitsu. He has given me a lot of enlightening explanations of magnetism. Their suggestions and comments have influenced my notion of this study.

I have worked under the powerful support of Prof. T. Nishinaga and Dr. S. Naritsuka. Their frank comments have always inspired me. And I would like to express my special thanks to Prof. M. Tanaka. He has listened to my interpretations of the experiments eagerly and encouraged me.

Tokyo
January 2000 *Toshiaki Hayashi*

Contents

1. *Introduction ~ semiconductor spin electronics ~*

Materials are generally classified into three parts (metals, semiconductors, and insulators) in terms of conductivity. Metals are good conductors (10^6 ~ 10^4 $(\Omega cm)^{-1}$) while nonmetals (insulators) are poor conductors (less than 10^{-10} $(\Omega cm)^{-1}$). Semiconductors are defined as substances with conductivities between 10^4 ~ 10^{-10} $(\Omega cm)^{-1}$ which extensively vary with temperature. The electron theory of solids has successfully discriminated between the three materials from the viewpoint of energy band diagrams. Electrons partially fill the conduction band of metals, which leads to good electron conduction. On the other hand, the valence bands of insulators and semiconductors are completely filled by electrons and the conduction bands are empty. There is an energy gap between the valence bands and the conduction bands of insulators and semiconductors. The transition between semiconductors and insulators is gradual and depends on the ratio of the energy gap to the temperature under investigation. At absolute zero Kelvin, pure perfect crystals of most semiconductors, which are called as intrinsic semiconductors, will be insulators. Some exceptions of this explanation based on energy band diagram have been discovered so far. For example, Anderson localization of metals due to the quantum interference of carrier wavefunctions in random potential and Mott insulators of half filled metals with the strong electron correlation.

Semiconductors enjoy some striking features unlike metals and insulators for device applications. Current electronics industry is mainly based on semiconductor technologies. In this sense, it is not too much to say that the subject of semiconductor electronics has the widest practical applications in solid state physics. The development of crystal growth technology and processing technology of semiconductors allows us to produce a lot of kinds of practical semiconductor devices which include transistors, switches, diodes, photovoltaic cells, detectors, and thermistors. On the other hand, study of semiconductor materials has not been limited to the device application but included a variety of fundamental physics. Therefore many intriguing discoveries such as quantum Hall effect (QHE), fractional QHE and electron configuration in artificial atoms (quantum dots) have been achieved so far in semiconductor devices.

Semiconductor electronics have developed rapidly up to now and will expand furthermore from now on, deducing the size and the energy consumption of the devices. The device size arrived at an order of nano meter already. In this device range, quantum effects will be negligible any more. Especially, spin effects of electrons would play an important role in semiconductor devices. Unfortunately, however, magnetism of semiconductors has not been taken into account in the semiconductor industry. On the contrary, current semiconductor electronics has completely ignored spin effects of electrons in semiconductors for this quarter century. It is simply because the spin relaxation time of electrons in semiconductors is so short that spin polarized state can be hardly maintained in semiconductors. Spin is one of the natures of an electron, as well as electronic charge. Obviously one would be able to obtain much more diversity in semiconductor electronics by introducing the spin information of electrons. We call this new class of electronics as semiconductor spin electronics.

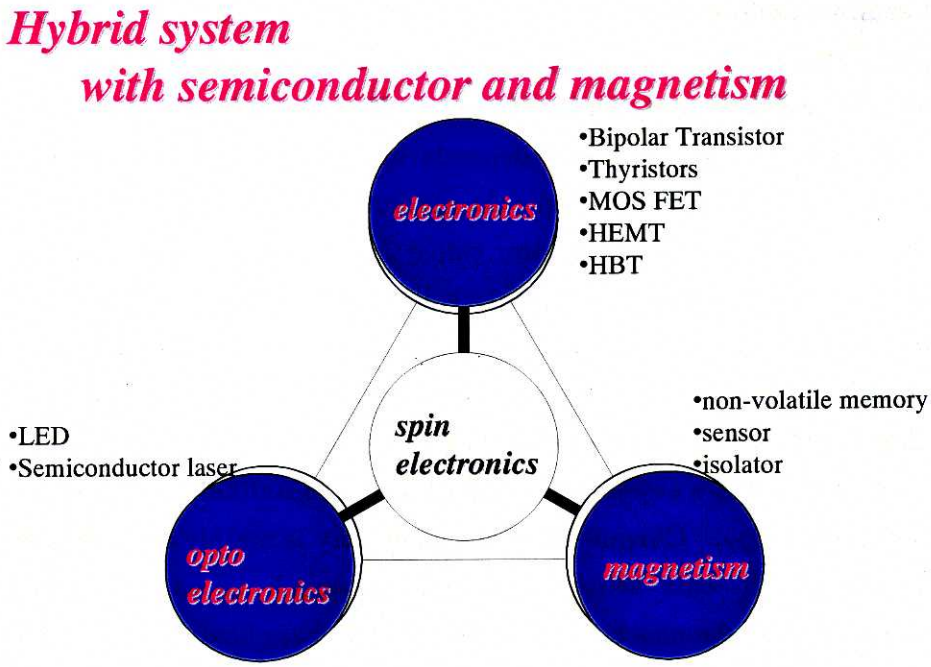

Fig. 1.1 General idea of semiconductor spin electronics.

Although spin dependent variables are not directly implied in the formula of the Coulomb interaction, electron correlation caused by the Coulomb interaction happens spin-dependently due to the Pauli exclusion principal. Therefore the magnetism of substances originates essentially from the electron correlation due to Coulomb repulsion. The central problems of the contemporary research into

magnetism lie in the study of the electron correlation. Consequently strong electron correlation is essential to realize definite magnetic effects in semiconductors. A lot of attempts to combine electronics with magnetism have been done in various ways so far. We categorize them as follows.

1. Low dimensional quantum devices of nonmagnetic semiconductors [1.1-4].
2. Epitaxial heterostructures of magnetic metals and semiconductors: MnGa / GaAs (001) [1.5], MnAs / GaAs [1.6-9], MnAs / Si (001) [1.10-11], Fe / FeSi (or amorphous Si) multilayers [1.12-15] and MnGa / (Mn, Ga, As) / MnGa trilayers [1.16-17].
3. Magnetic semiconductors: EuO [1.18], EuS [1.19]and EuTe[1.20-21].
4. Magnetic metal clusters embedded in semiconductors: MnAs clusters in GaAs [1.22].

Diluted magnetic semiconductors (DMSs) are one of the best candidates to combine electronics and magnetism. II-VI based DMSs have been studied for a long time [1.23]. The reason is that it is easy to grow II-VI based DMSs so that magnetic ions (Mn2+) could be easily incorporated into II-VI by substituting cations in the host II-VI semiconductors. II-VI based DMSs show giant Faraday effects caused by the strong interaction of electrons of the host semiconductors with the local magnetic moments. Indeed the giant Faraday effects of II-VI based DMSs have been already employed in low loss optical isolators [1.24]. However doping control of II-VI based DMSs is difficult, which is a common problem in II-VI semiconductors. The difficulty of doping control of II-VI based DMSs restricts their application range. In addition, most of the II-VI based DMSs do not show ferromagnetic ordering of the local magnetic moments even at low temperature but show paramagnetic or spin-glass properties, although they have a large amount of magnetic ions.

On the other hand, although Mn concentration in III-V semiconductors grown by normal growth methods is quite low (at most $10^{18} \sim 10^{19}cm^{-3}$), IBM group has successfully grown III-V based DMS, InMnAs, by using low temperature molecular beam epitaxy (LT-MBE) in 1989 [1.25-27]. InMnAs shows *p*-type conduction and is ferromagnetic at low temperature induced by carriers, unlike II-VI based DMSs. Koshihara et al. reported the inducement of a ferromagnetic order by photo-generated carriers in *p*-InMnAs / GaSb [1.28]. Carrier induced ferromagnetism of InMnAs is a big advantage over II-VI based DMSs. However,

InMnAs has some disadvantages. The bandgap of InMnAs is small ($\leqq$ 0.4 eV) because its host semiconductor InAs is one of narrow gap semiconductors. Also, the lattice mismatch of InMnAs to GaAs substrate is very large (~7%).

We have studied GaMnAs which is based on the most widely used III-V semiconductor GaAs [1.29-30]. GaMnAs is a ferromagnetic semiconductor which has good compatibility with the existing III-V semiconductors. In addition, GaMnAs has a lot of interesting fundamental features. This thesis presents comprehensive studies on the fundamental properties of GaMnAs and its quantum heterostructures. Also, the necessity of building a theory for GaMnAs beyond the simple energy band diagram is emphasized in designing devices of GaMnAs.

References

[1.1] G. Fasol and H. Sakaki, Solid State Commun., 84 (1992) 77.

[1.2] G. Fasol and H. Sakaki, Phys. Rev. Lett. 70 (1993) 3643.

[1.3] S. Tarucha, D. G. Austing, and T. Honda, R. J. van der Hage and L. P. Kouwenhoven, Phys. Rev. Lett. 77 (1996) 3613.

[1.4] R. J. Radtke, P. I. Tamborenea and S. Das Sarma, Phys. Rev. B54 (1996) 13832.

[1.5] M. Tanaka, J. P. Harbison, T. Sands, B. Philips, T. L. Cheeks, J. De Boeck, L. T. Florez, V. G. Keramidas, Appl. Phys. Lett. 63 (1993) 696.

[1.6] M. Tanaka, J. P. Harbison, T. Sands, T. L. Cheeks, V. G. Keramidas, G. M. Rothberg, Presented at the 13th North American Molecular Beam Epitaxy Conference, Stanford, USA, September 1993.

[1.7] M. Tanaka, J. P. Harbison, T. Sands, T. L. Cheeks, V. G. Keramidas, G. M. Rothberg, J. Vac. Sci. Technol. B12 (1994) 1091.

[1.8] M. Tanaka, J. P. Harbison, M. C. Park, Y. S. Park, T. shin, G. M. Rothberg, Appl. Phys. Lett. 65 (1994) 1964.

[1.9] M. Tanaka, J. J. P. Harbison and G. M. Rothberg, J. Cryst. Growth, 150 (1995) 1132.

[1.10] K. Akeura, M. Tanaka, M. Ueki, T. Nishinaga, Appl. Phys. Lett., 67 (1995) 3349.

[1.11] K. Akeura, M. Tanaka, T. Nishinaga, J. De. Boeck, J. Appl. Phys., 79 (1996) 4957.

[1.12] B. Briner, M. Landolt, Phys. Rev. Lett. 73 (1994) 340.

[1.13] J. E. Mattson, S. Kumar, E. E. Fullerton, S. R. Lee, C. H. Sowers, M. Grimsdich, S. D. Bader, F. T. Parker, Phys. Rev. Lett. 71 (1993) 185.

[1.14] K. Inomata, K. Yasu, Y. Saito, Jpn. Appl. Phys. 33 (1994) L1670.

[1.15] K. Inomata, K. Yasu, Y. Saito, Phys. Rev. Lett. 74 (1995) 1863.

[1.16] W. Van Roy, H. Akinaga, S. Miyanishi, K. Tanaka, Appl. Phys. Lett. 69 (1996) 711.

[1.17] W. Van Roy, H. Akinaga, S. Miyanishi, K. Tanaka, L. H. Kuo, J. Magn. Magn. Mater. 165 (1997) 149.

[1.18] B. T. Mattias et al., Phys. Rev. Lett. 7 (1961) 160.

[1.19] J. Callaway and D. C. McCollum, Phys. Rev. 130 (1963) 1741.

[1.20] T. R. McGuire et al., J. Appl. Phys. 34 (1963) 1345; 35 (1964) 984.

[1.21] N. F. Oliveria et al., J. Appl. Phys. 42 (1971) 1783.

[1.22] J. De Boeck, R. Oesterholt, A. Van Esch, H. Bender, C. Bruynseraed, C. Van

Hoof and G. Borghs, Appl. Phys. Lett. 68 (1996) 2744.

[1.23] Semiconductors and Semimetals, vol. 25, "*Diluted Magnetic Semiconductors*" ed. J. K. Furdyna and J. Kossut, Academic Press (1988).

[1.24] K. Onodera, T. Masimoto and M. Kimura, Electron Lett., 30 (1994) 1954.

[1.25] H. Munekata, H. Ohno, S. von Molnar, Armin Segmuller, L. L. Chang and L. Esaki, Phys. Rev. Lett., 63 (1989) 1849.

[1.26] H. Ohno, H. Munekata, S. von Molnar and L. L. Chang, J. Appl. Phys., 69 (1991) 6103.

[1.27] H. Ohno, H. Munekata, T. Penney, S. von Molnar and L. L. Chang, Phys. Rev. Lett., 68 (1992) 2664.

[1.28] S. Koshihara, A. Oiwa, M. Hirasawa, S. Katsumoto, Y. Iye, C. Urano, H. Takagi, H. Munekata, Phys. Rev. Lett. 78 (1997) 4617.

[1.29] T. Hayashi, M. Tanaka, T. Nishinaga, H. Shimada, H. Tsuchiya and Y. ootuka, J. Cryst. Growth 175/176 (1997) 1063.

[1.30] H. Ohno, A. Shen, F. Matsukura, A. Oiwa, A. Endo, S. Katsumoto and H. Iye, Appl. Phys. Lett. 69 (1996) 363.

2. *Fundamental properties of GaMnAs*

GaMnAs is a very new material. We succeeded in growing GaMnAs thin films on GaAs (001) substrates in 1995. Since then, we have studied the properties of GaMnAs in order to apply the ferromagnetic semiconductor, GaMnAs, to semiconductor spin electronics. In this chapter, we will show various experimental results and a lot of unique characters of GaMnAs. And we will introduce two models to describe the properties of GaMnAs. They are definitely different mechanisms, although they are very similar each other. The whole picture of GaMnAs has not been clear yet. However, it is important to grasp the proper model of GaMnAs in order to design some devices of GaMnAs.

2.1. Epitaxial growth and crystal structures of GaMnAs [2.1-5]

The first step of this study is to grow GaMnAs epitaxial films. The solubility of Mn atoms in GaAs is quite low, limited to the order of doping levels about $10^{19}cm^{-3}$. In order to obtain epitaxial GaMnAs ternary alloy films, we keep the substrate temperature low (< 300°C) during the MBE growth. This low temperature MBE (LT-MBE) realizes strong non-equilibrium growth conditions, allowing a large amount of Mn atoms to be incorporated into the host GaAs lattice far above its solubility.

The growth process is the following: At first, a GaAs buffer layer was grown at about 580°C on a semi-insulating GaAs(001) substrate. Then, the substrate temperature was decreased to 200 – 300°C in As_4 atmosphere. When the temperature was stable, the growth of $Ga_{1-x}Mn_xAs$ films was started. The Ga flux was the same as that of the buffer layer, and the Mn flux was determined so that the ratio of Mn flux to Ga flux was $x : 1 - x$ and calibrated by electron probe micro analyzer (EPMA) measurements after the growth. The growth process of GaMnAs is depicted in Fig 2.1. With this process, $Ga_{1-x}Mn_xAs$ films were grown under various conditions of the Mn concentration x and substrate temperature. The surface reconstruction was monitored by RHEED (reflection high energy electron diffraction) observation during the growth. Table 2.1 shows the various growth

conditions and the RHEED patterns of obtained samples.

2.1.1 Homogeneous GaMnAs films grown on GaAs (001) substrates

Fig. 2.2(a) shows a typical RHEED pattern during the growth of homogeneous GaMnAs with Mn concentration x = 0.005 at a substrate temperature of 250°C with [110] azimuth. The observed streaky RHEED pattern indicates that a homogenous GaMnAs film was obtained under these growth conditions. Similar streaky RHEED patterns of GaMnAs with (1x1) or (1x2) reconstruction (twofold steaks were weak) were observed when the Mn concentration x and the growth temperature were relatively low. In this case, clear RHEED oscillations were observed at the initial stage of the growth, indicating that epitaxial growth proceeds layer by layer.

In order to characterize the structure of the homogeneous GaMnAs films, we have measured X-ray diffraction spectra. Fig.2.3 shows $\theta - 2\theta$ spectra of the various homogeneous GaMnAs films grown at 250°C: (x, thickness) = (0.037, 1.4 μm), (0.064, 0.44 μm), (0.074, 1.4 μm). The peaks of GaMnAs were observed very close to the peak of GaAs (400) reflection. The splittings are due to Cu-kα1 and Cu-kα2. One can see that the lattice constants of the GaMnAs films are slightly larger than that (a_0 = 5.6533 Å) of GaAs. The linewidth of GaMnAs peaks was about 150sec, only a little broader than that of GaAs substrates, indicating high epitaxial quality. No indication of MnAs formation was seen in these samples. We estimated the values of lattice constants of GaMnAs from double-crystal X-ray diffraction measurements. Since the GaMnAs films grown on GaAs are under compressive strain, their lattice spacings are expanded in the vertical direction. We calculated intrinsic lattice constants of cubic GaMnAs assuming that the elastic constants of GaMnAs are equal to that of GaAs, and plotted in Fig. 2.4 as a function of Mn content x. The values of lattice constants of GaMnAs are on a nearly straight line, following the Vegard's law, which is a common feature in alloy systems. The maximum lattice mismatch to GaAs $\Delta a/a_0$ is only 0.37% at x of 0.078, indicating good structural compatibility with well-established GaAs/AlAs systems. Local structures around Mn in the GaMnAs films were investigated using Mn K-edge extended X-ray fine structure (EXAFS) technique [2.6]. It was found that Mn atoms are substituted for the Ga sites in zincblende GaAs lattice. The Mn-As bonds cause local disorder in the GaAs lattice, the degree of which increases with the Mn concentration.

2.1.2 Inhomogeneous GaMnAs films grown on GaAs (001) substrates

In contrast, when the nominal Mn concentration and growth temperature are relatively high, clustering of hexagonal MnAs in the GaMnAs layer became significant. Fig. 2.2(b) shows a RHEED pattern during the growth of GaMnAs at x = 0.10 grown at 300°C. Diffractions from hexagonal MnAs were observed as well as those of zincblende GaAs (or GaMnAs). Analyzing the RHEED patterns with various azimuths, the most frequently observed epitaxial orientations were (-1101) MnAs // (001) GaAs, [-1-120] MnAs // [110] GaAs, similar to the "type-B" MnAs / GaAs heterostructures [2.7]. MnAs formation was also observed in X-ray spectra, as shown in Fig. 2.5 which was taken from the sample with nominal x of 0.08 grown at 300°C. This shows the limitation of the Mn solubility in GaAs by LT-MBE. One can see an intense peak of MnAs (-1101) as well as that of GaAs (200). A small peak of MnAs (-1100) was also seen. This indicates that the crystal orientation of the MnAs clusters in GaAs (or possibly GaMnAs) is mainly the (-1101) of the hexagonal structure, in agreement with the results of RHEED. In Fig. 2.6, we summarized our results of homogeneous and inhomogeneous film properties in relation to the two important growth parameters (Mn concentration and growth temperature).

In general, technological advantage of LT-MBE is to decrease dopant diffusion and to suppress surface segregation. However, it is known that the electronic and optical properties of low temperature grown GaAs (LT-GaAs) are very sensitive to the growth conditions such as the substrate temperature and the As overpressure. This is because LT-GaAs contains excess As atoms such as As antisites and interstitial defects with their typical concentration in the range of $10^{20} \sim 10^{21}$ cm^{-3} [2.8]. To make the most use of the high-resistivity, LT-GaAs films have been used as the buffer layer [2.9] and as the gate insulator [2.10,11] for metal-insulator-semiconductor FET's (MIS FET's) to eliminate backgating and improve break down voltage.

The properties of GaMnAs grown at LT-MBE are also expected to be sensitive to the growth parameters [2.5,12]. In particular, the ferromagnetism of GaMnAs is strongly affected by its crystal quality because it is considered to be induced by itinerant holes, as will be discussed later. Therefore it is important to optimize the growth parameters and reduce the defect density in GaMnAs. We will come back to this point later.

The feasibility of growing the host semiconductors by LT-MBE is essential to

III-V based DMSs. It is possible to grow a GaAs epitaxial layer on GaAs (001) substrates by using LT-MBE. On the other hand, it is difficult to grow it on GaAs (111)A and (111)B substrates by using LT-MBE. In these cases, it is presumably more difficult to obtain a expitaxial GaMnAs film in the growth direction of (111) on these substrates. Indeed we have tried to grow GaMnAs films on GaAs (111)A and (111)B substrates at low temperature. However a lot of twin structures were formed from the beginning of the growth and we could not obtain homogeneous GaMnAs films.

GaMnAs epitaxial films grown on GaAs (001) substrates are metastable crystals. MnAs ferromagnetic particles are formed in a high quality GaAs matrix by annealing GaMnAs at 625 °C [2.2]. It makes a granular system of MnAs particles embedded in a GaAs matrix.

2.2. *Magnetic properties of GaMnAs thin films* [2.1-5]

2.2.1 Magnetism in semiconductors

In general, non-magnetic semiconductors show diamagnetism. According to Lenz's law, an electric current is induced in a superconductor or in an electron orbit within an atom by an applied magnetic field. And it persists as long as the field is present. The magnetic field of the induced current is opposite to the applied field, and the magnetic moment associated with the current is a diamagnetic contribution from the conduction electrons, and this diamagnetism is not destroyed by collisions of the electrons [2.13].

The magnetization of II-VI based DMSs has been investigated [2.14]. Although they have a large amount of magnetic ions, they do not show ferromagnetic ordering of local moments, but show paramagnetic or spin-glass properties. For example, the $Cd_{1-x}Mn_xTe$ is a typical DMS system. It can be considered as a mixed crystal between CdTe and MnTe. CdTe is a non-magnetic semiconductor. And the local moments of zincblende phase MnTe have antiferromagnetic interaction. In contrast with II-VI based DMSs, InMnAs, which is the first discovered III-V based DMS, shows ferromagnetic behavior (maximum T_c ~ 7.5 K) [2.15]. It is quite marvelous that the ferromagnetic transition occurs in InMnAs although the distance between Mn-Mn is not so short that they couple directly. Likewise GaMnAs is expected to have a ferromagnetic phase. In this chapter, we will discuss about the magnetic properties of GaMnAs.

2.2.2 Field dependence of magnetization of GaMnAs

Magnetization measurements were performed on the homogeneous GaMnAs films using a superconducting quantum interference device (SQUID). Fig 2.7(a) shows a magnetization (*M-H*) curve of a 1.4 μm-thick $(Ga_{1-x}Mn_x)As$ film with x = 0.074 measured at 1.9K, when the magnetic field H was applied in plane along the <110> axis. Here, diamagnetic contribution of the GaAs was subtracted from the raw data of the *M-H* curves, and *M-H* curves of the GaMnAs epilayer was plotted in Fig.2.7. Possibly, this process gives rise to an error in estimating the saturation magnetization M_s of GaMnAs. The hole concentration and mobility of this sample at room temperature were 2.6 x 10^{20} cm^{-3} and 7.24 cm^2/Vs, respectively.

At low field, a square-like hysteresis in the *M-H* characteristics directly indicates the presence of ferromagnetic ordering. The values of coercive field H_c and saturation magnetization M_s (at 5 T) were estimated to be 56 Oe and 34.9 emu/cm^3, respectively. The effective magnetic moment per Mn ion of this sample is estimated to be about 2.30 μ_B, where μ_B is the Bohr magneton, from the value of M_s, which is smaller than the expected value (S = 5/2). The clear hysteresis behavior remained when the temperature was increased up to 55 K, above which the hysteresis behavior disappeared. Fig. 2.8 shows the temperature dependence of residual magnetization M_r, indicating that the Curie temperature of this sample is 55 ~ 60 K, much higher than that (7.5 K) of *p*-type InMnAs [2.15]. The highest T_c so far obtained is 110 K, Matsukura et al. reported [2.16].

Ferromagnetic ordering between the Mn ions in InMnAs is induced by holes through *p-d* exchange interaction. Koshihara et al. showed that photogenerated holes induce ferromagnetic ordering between the local magnetic moments in *p*-InMnAs / GaSb heterostrctures [2.17]. Because of the unique band profile of the heterostructure, holes of the photoexcited carriers in a GaSb layer accumulate in the InMnAs layer. Electrons will drift towards the opposite direction, so that holes do not recombine immediately with electrons when the light is switched off. Holes thus transferred to the InMnAs layer enhance the ferromagnetic spin exchange among Mn ions. They concluded that it was a clear experimental demonstration of ferromagnetism induced by holes in InMnAs.

The ferromagnetism of GaMnAs is expected to be generated by the same mechanism. Matsukura et al. investigated the strong correlation between the Curie temperature T_c and the hole concentration p of GaMnAs, as shown in Fig. 2.9

[2.16]. GaMnAs has reentrant metal-insulator transition, depending on Mn concentration [2.18]. Samples in metallic region have the higher T_c and the higher hole concentration p in Fig. 2.9. Yoshino et al. showed n-type GaMnAs which is compensated by doping Sn does not have a ferromagnetic phase even at low temperature [2.19]. Shimizu et al. found the metal-insulator transition of GaMnAs films with the same amount of Mn ions (x = 0.043) by controlling the substrate temperature and the As overpressure during the growth, as will be introduced later [2.5]. The hole concentration of GaMnAs certainly changes in terms of the compensation of Mn acceptors by the point defects of excess As. They clearly observed correlation of the Curie temperatures with the conducting hole concentration. Considering all described above, the conducting holes play an essential role in the ferromagnetism of GaMnAs. The possibility of the contribution of ferromagnetic or super-paramagnetic MnAs precipitates is excluded from the structural analysis and the magneto-optic measurements which will be described in the following section.

Itinerate holes are considered to carry minus entropy, together with their electric charges, leading to ferromagnetic interaction between the Mn spins in GaMnAs. In other words, they drag magnetic clouds of Mn spins along with them. Although local magnetic moments of most Mn ions abruptly change in the direction of the applied magnetic field at the coercive force, the magnetization of GaMnAs is gradually saturated at higher field (Fig. 2.7). Oiwa et al. pointed out that the magnetization curve in the paramagnetic regime follows a modified Brillouin function which is a Brillouin function with temperature T substituted by $T + T_{AF}$, where T_{AF} stands for the Neel temperature of antiferromagnetism between the Mn moments [2.18].

In general, ferromagnets are composed of small regions called domains, within each of which the local magnetization is saturated [2.13]. Landau and Lifshitz showed that domain structure is a natural consequence of the various contribution to the energy – exchange, anisotropy, and magnetic – of a ferromagnetic body. Magnetic domains are formed to prevent the energy loss of the static magnetic field. In a weak applied field, the volume of domains favorably oriented with respect to the field increases at the expense of unfavorably oriented domains. At the critical field H_c, most of the magnetic domains suddenly rotate towards the direction of the applied magnetic field. In case of GaMnAs, the domain structure and the coercivity will be determined by the random distribution of Mn ions or a lot of point defects which obstruct the motion of magnetic domains. And the local Mn moments in a

magnetic domain slightly cant side by side due to the randomness. The coercivity of GaMnAs is not large (the typical coercive force H_c of GaMnAs is 50 ~ 100 Oe, that is, it is a soft material) because it is epitaxial. However there are some obscure points in what determines the coercive force of GaMnAs films. A strong magnetic field forces the canted states of magnetic domains to align in the field direction. This process will account for the paramagnetic behavior of GaMnAs superimposed on its ferromagnetism. However, the detail of magnetization process of GaMnAs in a magnetic field is still not clear.

2.2.3 The mechanism of the ferromagnetism of GaMnAs

The mechanism of *p-d* interaction in GaMnAs is still controversial. Matsukura et al. has extensively analyzed the magnetotransport properties of GaMnAs and showed that the RKKY formula can explain their data very well [2.16]. There are a lot of excellent textbooks to explain the RKKY interaction mechanism. Here we are following the interpretation of the RKKY interaction by Yoshida, who is one of the contributors of this theory [2.20]. When a spin S exists on the magnetic impurity atom which is introduced into nonmagnetic metals, an interaction between this localized spin and the spins of the conduction electrons can be written in the form

$$H_{exch} = -2Jv\sum_i \delta(r_i)(s_i \cdot S) = -\frac{2J}{N}\sum_{qi} e^{-iqr_i}(s_i \cdot S), \tag{2.1}$$

where s_i and r_i represent the spin and the position vector of the conduction electron, respectively. J is the exchange integral between conduction electrons and the electron localized at the impurity, and v is the volume per lattice point. We consider the case in which there exist two localized spins at lattice points R_n and R_m. By the interaction between spin S_{mz} localized at R_m and the spin density of conduction electrons polarized by spin S_{nz} localized at R_n, the following interaction between S_n and S_m is expressed as

$$\begin{aligned} &-2J\frac{V}{N}\int \delta(r-R_m)\frac{1}{g\mu_B}\sigma(r-R_n)S_{mz}dr \\ &= -9\pi\frac{J^2}{\varepsilon_F}\left(\frac{N_e}{N}\right)^2 F(2k_F|R_n-R_m|)S_{mz}S_{nz}. \end{aligned} \tag{2.2}$$

$$\sigma(r) = \frac{1}{V}\sum_q \chi_q H_q e^{-iq\cdot r} = \frac{12\pi}{V}\frac{N_e}{N}\frac{J}{g\mu_B}S_z\chi_{\text{Pauli}}F(2k_F\cdot r), \tag{2.3}$$

$$F(x)=\frac{-x\cos x+\sin x}{x^4}, \tag{2.4}$$

where $\sigma(r)$ represents the magnetic-moment density of conduction electrons induced by the internal magnetic field. When we include the transverse components of spins, $S_{nz}S_{mz}$ in (2.2) is replaced by S_nS_m. This interaction was derived directly by Runderman and Kittel [2.21] for the nuclear spins I_n in metals as the second-order term in the perturbation expansion with respect to (2.1). In this case, J is replaced by the hyperfine coupling between the conduction electrons and the nuclear spins, and S_n is replaced by the nuclear spin I_n. Using this interaction, Kasuya [2.22] also discussed the ferromagnetism of the rare-earth metals. On the other hand, Yoshida [2.23] discussed, on the basis of the *s-d* interaction, the magnetism and the electrical resistivity of dilute CuMn alloys, and studied the spin polarization of conduction electrons around the localized spin. The interaction (2.2) between the localized spins in metals, which is mediated by the conduction electrons, is now called the RKKY interaction.

In contrast with Matsukura et al., Akai has theoretically proved that the ferromagnetic ordering of Mn spins in InMnAs and GaMnAs is induced by the double exchange interaction [2.24]. The double exchange interaction accounts for the magnetism of manganese oxides (manganites) with perovskite or related structures like $La_{1-x}Sr_xMnO_3$ [2.25], where Mn^{3+} ions and Mn^{4+} ions coexist. The double exchange interaction is introduced by Zener [2.26] to explain the ferromagnetism of mangnites and elaborated by Anderson and Hasegawa [2.27].

The electric states of a free atom, which has spherical symmetry centered at the nucleus, are the eigenstates of orbital angular momenta due to accidental degeneracy. In a crystal with a peculiar symmetry, the $2L + 1$ sublevels which are degenerate in the free ion may now be split by the crystal field produced by neighboring ions [2.28]. Fig. 2.10 shows the energy splitting of $3d$ orbits of transition metals to e_g and T_{2g} levels in a crystal with O symmetry [2.29]. In case of T symmetry, which is the symmetry of the crystal structure of GaAs, e_g and T_{2g} are replaced each other.

Now we consider the case of two splitting bands (A and B) for simplicity. In general, the intra-atomic exchange interaction J tends to align the spin direction of electrons in the orbits with the same angular momentum, which is called as Hund's rule. Assuming $J\rightarrow\infty$, the conducting electrons in A orbit feel random potential through the Hund's coupling when the spin configuration of electrons in B orbit is antiferromagnetic. In contrast, in case of the ferromagnetic configuration, the

motion of the conducting electrons is not obstructed. In other words, the ferromagnetic configuration is more stable than the antiferromagnetic one by the kinetic energy of the conducting electrons. This is at the heart of the double exchange interaction [2.29].

Basically the RKKY interaction and the double exchange interaction are derived from the same mechanism of Coulomb interaction between conduction electrons and unfilled shell electrons of transition metals or of rare earth metals. In the picture of the RKKY interaction, however, the term which includes the transition between the conduction electrons and the unfilled shell electrons is omitted because it is of a higher order than the term which does not contain the transition [2.22]. The RKKY interaction plays an important role in dilute magnetic alloys like CuMn, and rare-earth metals and their intermetallic compounds. As described above, the RKKY interaction is incorporated into the Hamiltonian of electron systems as perturbation. In the framework of the RKKY interaction, it is impossible to treat the strong interaction which leads to the phase transition of ferromagnetic ordering. And ferromagnetism caused by the RKKY interactions has never been observed in any real systems, irrespective of the carrier density. In dilute alloys of CuMn, the RKKY interaction acts among Mn impurity spins [2.20,23]. Since Mn spins occupy randomly the points of the Cu lattice, the internal magnetic field acting on the spin of one Mn atom differs from that acting on other spins because of the different distribution of surrounding Mn atoms. This internal magnetic field differs from others not only in its magnitude but also in its direction. At sufficiently low temperatures, the Mn spins are frozen in the direction of the randomly oriented internal field. This state of spins is called a *spin glass*. However no spin glass phase in GaMnAs have been reported so far.

Akai explained ferromagnetism of InMnAs and GaMnAs on the basis of the results of KKR-CPA-LDA calculations [2.24]. According to it, the ground state is ferromagnetic. Moreover, the larger part of the carriers consists of the spin-polarized Mn *d* states in which they are induced automatically. The RKKY interaction mediated by unpolarized nearly free electrons might not be the good picture of ferromagnetism of III-V DMSs. And then he concluded that the mechanism of the ferromagnetism of InMnAs and GaMnAs comes from the double exchange interaction. That is, introducing the holes to the valence bands lowers the band energy more in ferromagnetic state than the local-moment disordered state although the kinetic energy of holes increases. His point is very clear, but more investigation might be necessary because KKR-CPA-LDA calculation includes a lot

of approximation.

2.2.4 Magnetic anisotropy of GaMnAs films

To characterize the magnetic anisotropy, we have done magnetization measurements on the same sample with the magnetic field H applied perpendicular to the film plane [2.1]. Fig 2.7(b) shows the result of M-H characteristics measured at 1.9K, exhibiting much higher saturation field (1500 ~ 2000 Oe). Though a little hysteresis behavior was observed, its shape is far from square. The results of Fig. 2.7 indicate that the easy magnetization axis of the present GaMnAs film is not perpendicular but aligned in the film plane. The magnetic anisotropy comes from compressive strain in GaMnAs films because the lattice constants of GaMnAs is slightly larger than that of GaAs (see Fig. 2.4). Shen et al. showed experimentally that GaMnAs films grown on InGaAs buffer layer which has larger lattice constant has perpendicular magnetic anisotropy [2.30].

2.3. Magneto-transport properties of GaMnAs thin films [2.31]

2.3.1 Electric conduction in a magnetic field

The most common effect of a magnetic field on electric current and thermal flow is the generation of electric field and temperature graduation under the equilibrium condition, caused by Lorentz force on electrons which carry charge and thermal energy. They are called as galvanomagnetic effect for electric current and thermomagnetic effect for thermal flow, respectively. In particular, the magnetotransport effect of ferromagnetic materials in a magnetic field is quite intriguing because they already have quite a large internal magnetic field generated by the spontaneous magnetization.

Magnetoresistance effect (MR) is one of galvanomagnetic effects. It is called longitudinal effect when the electric current is parallel to an applied magnetic field, and transverse effect when the electric current is perpendicular to an applied magnetic field, respectively. The measurement geometry is depicted in Fig. 2.11. In non-magnetic materials, the resistance always increases with a magnetic field larger. In other words, the MR effect is positive: $\Delta\rho/\rho \propto B^2$. On the other hand, anomalous magnetoresistance effect (AMR) caused by asymmetrical scattering through spin-orbital interaction is dominant in magnetic materials.

2.3.2. Extraordinary Hall effect (EHE) of GaMnAs

Hall effect is one of the most important techniques to investigate the carrier type and the carrier concentration of semiconductors. In magnetic materials, the Hall voltage depends on the magnetization rather than on the external field due to electron scattering. It is called as extraordinary Hall effect (EHE). EHE has two mechanisms: skew scattering and side jump [2.32]. The Hall resistance R_{xy} of ferromagnetic materials generally satisfies the following equation.

$$R_{xy} = \frac{R_0}{d}B + \frac{R_s}{d}M, \tag{2.5}$$

where R_0 is the ordinary Hall constant, R_s the extraordinary Hall constant, and d the sample thickness. In the simplest case, R_s is considered to be proportional to the resistivity ρ: $R_s = c\rho$, where c is constant. Here the second term is the extraordinary Hall effect. Since the carrier (hole) concentration is quite high in GaMnAs, the first term is negligible compared with the second term. Therefore the Hall resistance R_{xy} is approximately proportional to the perpendicular component of magnetization of a sample. At high temperature, because the susceptibility of magnetization of GaMnAs follows the Curie-Weiss law, Hall coefficient R_{Hall} is considered as following way.

$$R_{Hall} = \frac{R_{xy}d}{B} = R_0 + \frac{c\rho}{\mu_0}\cdot\frac{C}{T-\theta} \tag{2.6}$$

, where C is the Curie constant.

All the GaMnAs (x = 0.005 ~ 0.078) samples we have grown showed p-type conduction with the hole concentration of 3.8 x 10^{17} cm^{-3} ~ 2.58 x 10^{20} cm^{-3}, and no ferromagnetic behavior was observed at room temperature. We measured the Hall effect of 1.4 μm-thick $(Ga_{1-x}Mn_x)As$ film with x = 0.074 (B672) at low temperature (Fig. 2.12). Transport measurements were performed on photolithograthically patterned Hall bars with a width and a length of 200 μm and 1.3 mm. The shape of field dependence of the Hall resistance is similar to the *M-H* characteristics from SQUID measurements (Fig. 2.7(b)). This fact indicates that one can investigate the magnetic properties of GaMnAs through the magneto-transport measurements. Fig. 2.12 also shows that this sample has magnetic anisotropy in plane.

We measured temperature dependence of the Hall effect of GaMnAs extensively. Fig. 2.13 shows magnetic field dependence of the Hall resistance of GaMnAs (B801: 5000 Å, Mn concentration x = 3.7%) at various temperatures. No

hysteresis loop was observed in the measured temperature range because of the strong in-plane magnetic anisotropy. Therefore, it is difficult to estimate the spontaneous magnetization and the Curie temperature of GaMnAs.

In general, the Arrott plot is one of the powerful ways to determine the spontaneous magnetization M_s and the Curie temperature T_c of ferromagnets. In the mean field approximation, the magnetization of ferromagnets near the Curie temperature follows this equation:

$$M^2 = a(T_c - T) + b\frac{H}{M}, \tag{2.7}$$

where a and b are constants. That is, M^2 is proportional to H/M at enough high field that the magnetization is not influenced by the magnetic anisotropy. The spontaneous magnetization M_s is estimated by extrapolating Eq. (2.7) linearly from the high field to $H/M \rightarrow 0$. And then the Curie temperature T_c is estimated from the crossing point of the M_s^2-T curve and the T axis.

In case of GaMnAs, the Curie temperature was calculated by performing Arrott Plot of R_{xy} / ρ according to the relation of Hall resistance to magnetization: $R_{xy} / \rho \sim cM$. Fig. 2.14 shows $(R_{xy} / \rho)^2$ of B801 in the neighborhood of the Curie temperature. Clear linearity is seen in this graph. The Curie temperature was determined from these data as $T_c = 50.6$K.

Curie temperature can be also determined from the Curie-Weiss law more directly in the following way,

$$\frac{1}{\chi} = \frac{T - T_c}{C}, \tag{2.8}$$

That is, the inverse of the susceptibility of ferromagnets is linearly dependent on $T - T_c$ above the Curie temperature. Experimentally, the susceptibility for $T \gg T_c$ is given quite accurately by $C / (T - \theta)$, where θ is appreciably greater than the actual transition temperature T_c [2.13]. We plotted $dH/d(R_{xy} / \rho) \sim 1 / \chi$ versus temperature (Fig. 2.15) and estimated the Curie temperature T_c = 53.3K, which shows good agreement with the Curie temperature determined by using the Arrott plot (T_c = 50.6K).

It is worth while noting that $1 / \chi$ is proportional to temperature even at room temperature. In other words, the EHE term is dominant in the Hall effect of GaMnAs at room temperature, which makes it difficult to determine the carrier concentration of GaMnAs. We performed direct fitting of the Hall resistance R_{Hall} in Eq. (2.6) by using fitting parameters as R_0 and T_c (Fig. 2.16). According to it, the hole concentration and the Curie temperature of sample B801 is $p = 1.51 \times 10^{20}$ cm^{-3}

and T_c = 56.5K. From its Hall effect at room temperature, the hole concentration of B801 is estimated to be 1.06 x 10^{20} cm^{-3}, which is slightly smaller than that determined by the fitting because this estimation does not take the extraordinary Hall effect into account. The expected Mn concentration (x = 3.7%) of B801 is 8.15 x 10^{20} cm^{-3}. The carrier activation ratio of Mn ions is quite low (18.5%). Apparently, there is some experimental errors in the estimation of the carrier concentration of GaMnAs. Table 2.2 shows the summary of the Curie temperatures and the hole concentrations calculated from EHE.

Ohno et al. pointed out that the more accurate carrier concentration of GaMnAs could be estimated from Eq. (2.6) by measuring the Hall effect at quite low temperature and at quite high magnetic field, where the magnetization of the GaMnAs film is almost completely saturated [2.33]. Omiya et al. performed Hall measurements of a GaMnAs (200nm, x = 0.053) film at 50mK up to 27T and calculated the carrier concentration at 3.5 x 10^{20} cm^{-3} from the Hall coefficient above 20T [2.34]. The activation ratio of holes is about 30%. This value is also low, that is, the discrepancy between the carrier concentration and the Mn concentration of GaMnAs is large. One possible reason is that it is difficult to ionize Mn atoms because the ionization energies for Mn impurities in GaAs is relatively large (~110meV [2.35,36] or ~95meV [2.37]). Another possible reason is that the holes which originally come from Mn acceptors are compensated by a number of As anti-site point defects, as will be discussed later. Other reason is that, even in the sufficiently high magnetic field, it is difficult to estimate the hole concentration of GaMnAs from the Hall effect in which the Drude model is assumed because GaMnAs is a heavily doped semiconductor.

2.3.3 Magnetoresistance (MR) effect of GaMnAs

Fig. 2.17 shows magnetoresistance R_{xx} of GaMnAs (Mn concentration x = 0.074, B672) at 4.2K., where the magnetic field is applied in-plane parallel to the current. Large negative MR was observed. Clear hysteresis loop was seen at low field. Small hysteresis loops were observed at around +/-2000 Oe where the magnetization of this sample is almost saturated. The mechanism of magnetoresistance of GaMnAs is unclear at present. In general, two-current model generally works well for an analysis of magnetotransport of ferromagnets. Electric currents of up spin holes and down spin holes are considered separately because they sense different potentials respectively. This model is applied to the magnetotransport of GaMnAs.

The ferromagnetic ordering between Mn spins in GaMnAs is induced by itinerant holes through *p-d* exchange interaction, as described above. That is to say, itinerant holes drag magnetic clouds of Mn spins along with them. The kinetic energy of transmitting holes back and forth between Mn ions could be increased by the magnetic ordering of Mn spins forced by an applied magnetic field: $t = t_0\cos(\delta\theta/2)$, where t is the effective transfer integral and $\delta\theta$ is the relative angle between adjacent Mn spins [2.27]. And, at the same time, a magnetic field smoothes the potential and breaks time-reversal symmetry. Both effects prevent Anderson localization of the conducting holes, thus contributing to the electric conduction of GaMnAs. In summary, a magnetic field tends to increase the effective carrier concentration of GaMnAs.

At zero field, magnetization of GaMnAs is not saturated sufficiently. Mn spins do not line up completely. Majority spin holes feel random potential as well as minority spin holes. With a magnetic field larger at around zero field, the random potential becomes rougher, and the resistance increases. At the coercive field (in this sample, ~50 Oe), most of magnetic domains suddenly turn around towards the field direction and the resistance suddenly decreases because majority spin holes feel relatively flat potential. The magnetoresistance continues to decrease gradually as a magnetic field increases and magnetic domains become larger.

2.3.4. Temperature dependence of the resistivity of GaMnAs (the metal-nonmetal transition of GaMnAs)

We also have studied temperature dependence of the resistivity of GaMnAs. Fig. 2.18 shows the temperature dependence of DC resistance of various GaMnAs films. At low temperature ($T_c > T$), the resistance increases with decreasing temperature for some samples, showing a nonmetallic behavior, while for other samples the resistance decreases with decreasing temperature at $T > T_c$ which is a metallic behavior. Oiwa et al. have systematically studied temperature dependence of resistivity of GaMnAs films with x ranging from 0.015 to 0.071, as shown in Fig. 2.19 [2.18]. It indicates a nonmetal-metal-nonmetal transition as a function of the Mn concentration x. The relation of the magnetic properties and transport properties are depicted in Fig. 2.9 [2.16].

i) Metal-nonmetal transition

Metal-nonmetal (M-NM) transition can be commonly observed in heavily doped semiconductors [2.38]. The general interpretation of the M-NM transition of doped semiconductors will be introduced here. Depending on the temperature and the impurity concentration N, electron transport in doped semiconductor is governed by different conduction processes. In the following, the concentration regions will be classified into major categories. For simplicity, we consider here n-type semiconductors. Fig. 2.20 shows a hypothetical sketch of the density of states corresponding to the various concentration regimes for a doped semiconductor, where compensation of carriers is very little. The shaded regions represent localized states. The dashed line depicts the density-of-states of the conduction band, $D(E) \propto E^{1/2}$. Since N increases by a factor of about 50 from Fig. 2.20(a) to (d), the scale of $D(E)$ increases in proportion so that the height of the impurity bands can be kept constant. As a consequence the steepness of $D(E)$ of the conduction band decreases from (a) to (d).

Mott [2.39] thought that the M-NM transition might abruptly occur when the wavefunction of an impurity state overlaps with the wavefunction of another impurity state in the neighborhood and introduced the notion of a critical concentration n_c. By solving a Schrodinger equation of an impurity state in semiconductors, the Mott criterion is derived as follows,

$$n_c^{1/3} a_H^* = 0.026, \tag{2.11}$$

where a_H^* is the effective Bohr radius of the impurity center. The general applicability of the Mott criterion, Eq. (2.11), has been elegantly demonstrated by Edwards and Sienko [2.40] who assembled the experimental data.

In Fig. 2.20(a), where the impurity concentration is much lower than n_c, the neutral donor states D^0 lie E_D below the conduction band edge. The singlet D^- states are centered at the band edge because they barely bound. Here the electron correlation plays an essential role in the D^- states. They form a broader band because the extent of their wavefunctions is about 3 ~ 4 times larger than that of the D^0 states. E_C is the mobility edge of the D^- band so that the activation energy into this band is $\varepsilon_2 = E_C - E_F$. The conductivity in this regime is expressed as the following.

$$\sigma = \sigma^{(1)} \exp\left(-\frac{\varepsilon_1}{k_B T}\right) + \sigma^{(3)} \exp\left(-\frac{\varepsilon_3}{k_B T}\right), \tag{2.9}$$

Conduction at higher temperatures takes place in the conduction band with an activation energy. The first term of Eq. (2.9) represents the conduction of the electrons thermally excited from the impurity band to the conduction band. ε_1 means the activation energy of donors. At low temperature, conduction takes place by phonon-assisted hopping between neutral and ionized impurity centers. Some compensation is necessary to provide the unoccupied centers [2.41]. The second term of Eq. (2.9) represents the conduction hopping from one impurity site to another site with the activation energy ε_3, which is caused by the random fields of the compensating impurities [2.38].

At higher N (Fig. 5.20(b)), the D^0 and D^- bands begin to merge because of disorder and stronger wavefunction overlap. Since each donor atom has one electron, the lower D^0-band is completely filled and therefore the conduction occurs by exciting electrons to a higher D^--band. In this concentration region, the electrons excited to the mobility edge E_C which is introduced by considering Anderson localization [2.42] yield an activated-type conduction of the form

$$\sigma = \sigma^{(2)} \exp\left(-\frac{\varepsilon_2}{k_B T}\right), \tag{2.10}$$

where $\sigma^{(2)} = \sigma_0$ is the minimum metallic conductivity. Thus both electron correlation and disorder are involved in the M-NM transition in doped semiconductor. Aoki and Kamimura calculated the density-of-states of the impurity band for a half-filled case on the base of the Mott-Hubbard model [2.43]. The two bands are separate at the sufficiently low concentration, as described above. In case of a perfect crystal, the M-NM transition occurs at the concentration at which the band split becomes extinct for one electron per atom. This is the Mott-Hubbard transition [2.44]. In random systems, however, a system can be an insulator with a finite density of states at E_F. ε_2 is decreased with increasing N. The M-NM transition corresponds to the concentration ($\varepsilon_2 = 0$) at which the states at E_F are no longer Anderson localization and become the extended states. In this sense, n_c will be different from the Mott criterion. If there is compensation of carriers, the M-NM transition occurs at higher N, that is, compensation delays the M-NM transition, because of the vertical disorder which produces Anderson localization. $D(E_F)$ is sufficiently high to yield variable range hopping (VRH) at very low temperature.

In the first metallic regime, $n_c < N < n_{cb}$, Fig.2.20(c), E_F presumably lies below the conduction band. The conduction band shifts downwards with increasing

N because of the average positive potential of the donor ions and the rapid increase of the dielectric constant as N approaches n_c. One generally believes that E_F lies below the conduction band in this range.

In the metallic range, $N > n_{cb}$, the Fermi level has entered the conduction band and a truly metallic conduction is observed similar to that of an impure metal. The states have the character of the conduction band of the host matrix. However the transition to the second metallic regime at n_{cb} is difficult to pin down. The position of E_F is obtained from a simple degenerate model in which the conduction band is remarkably undisturbed by the impurities except near the band edge as shown in Fig. 2.20(d).

ii) Metal-nonmetal transition of GaMnAs

Let us go back to the discussion of the M-NM transition of GaMnAs which is doped in the host semiconductor GaAs by a large amount of Mn impurities. One would like to know which category GaMnAs belongs to in above pictures and what is the mechanism of the reentrant M-NM transition of GaMnAs. Woodbury and Blakemore reported that the critical density n_c in GaAs:Mn systems is $(2.1\pm0.4) \times 10^{19}$ cm^{-3} and the effective Bohr radius a_B^* estimated from the experimental ionization energy is 10.1Å [2.45], which are in good agreement with the Mott criterion. In spite of it, the M-NM transition in GaMnAs systems occurs at Mn concentration $x \sim 0.03$, that is, $n_c \sim 7 \times 10^{20}$ cm^{-3}, as Oiwa et al. reported [2.18]. There is a fatal discrepancy of the critical concentration of the M-NM transition between the GaAs:Mn systems and the GaMnAs systems. No one can explain it very well at present. Surprisingly, ferromagnetic GaMnAs with low Mn concentration ($x < 0.03$) in the non-metallic region involves much more Mn impurities than the Mott criterion. It means that the wavefunctions of Mn impurity levels should be overlapped to one another in GaMnAs systems. One possible reason of this discrepancy is the delay due to the strong Anderson localization of a super large amount of Mn impurities together with large compensation by excess As point defects. The correlation between the jiggling (diffusive) carriers and the local magnetic moments should be taken into account in the theory of the M-NM transition of GaMnAs, because the strong ferromagnetism of GaMnAs ($0.03 < x < 0.05$) makes the conduction be metallic. $3d$ bands as well as the impurity states of Mn ions are considered to be strongly hybridized with the valence band of the host semiconductor. In this situation, some correlation might

well work between the 3*d* local states and the channel of the hole conduction. Or one of the 3*d* bands itself might be the conduction channel. The local magnetic moments align to reduce the total energy because their randomness makes the Anderson localization stronger. The ferromagnetism which derives from the above mechanism is similar to the Nagaoka ferromagnetism [2.46] and this kind of M-NM transition is called the Mott-Hubbard transition. Note that it is apparently different from the Mott-Hubbard transition in the impurity band as described above. In this case it is not suitable to simply call it Anderson localization, because the idea of Anderson localization, which describes the interference of the wavefunction of a jiggling carrier in a random potential back and forth, is basically in one electron approximation. The reentrant M-NM transition is probably assisted by the anisotropic strain between [110] and [1-10], as pointed out by Katsumoto et al [2.47]. With the increase of Mn concentration, the increase of the spin-dependent scattering rate overcomes that of the Fermi energy in the sense of Anderson localization, and the system reenters the insulating phase, in which the conduction is sensitive to the tail of the wave function.

The compensation degree of heavily doped semiconductors is one of the essential factors in terms of the M-NM transition. It has to be strictly taken into account in the study. However it is difficult to estimate the compensation degree exactly. In case of GaMnAs, excess As atoms such as As antisites and interstitial defects compensate Mn atoms and the compensation degree affects the properties of GaMnAs, as described above [2.5,12]. Therefore it is considered important to carefully control the growth condition of GaMnAs. Further work should be required to clarify the precise mechanism of the M-NM transition of GaMnAs. The M-NM transition is one of the key issues with respect to the magnetic properties of GaMnAs as well as its transport properties.

2.4. *Magneto-optic properties of GaMnAs thin films* [2.48]

2.4.1 Magneto-optics: basics and general formula [2.49]

Magneto-optic effects, Faraday effect, Cotton-Muton effect, magnetic Kerr effect, and magnetic circular dichroism, are caused by optical anisotropy in magnetic materials. Magneto-optical phenomena can be classified into two types in terms of the relative orientation of the wave vector $\boldsymbol{k}$ and the applied magnetic field $\boldsymbol{H}$.

(1) Faraday geometry: the light travels along the field direction ($\boldsymbol{k} // \boldsymbol{H}$),

(2) Voigt geometry: the light travels perpendicularly to the field direction ($k \perp H$).

Here I describe the phenomenological explanation of magneto-optic effect. When the incident light into a substance has a frequency ω and a wave number k, the electric and magnetic vectors are expressed in the following way:

$$\mathbf{E} = \mathbf{E}_0 \exp i(\omega t - \mathbf{k}\cdot\mathbf{r}) = \mathbf{E}_0 \exp[i\omega\left(t - \frac{\tilde{N}}{c}\mathbf{s}\cdot\mathbf{r}\right)]$$
$$\mathbf{H} = \mathbf{H}_0 \exp i(\omega t - \mathbf{k}\cdot\mathbf{r}) = \mathbf{H}_0 \exp\left[i\omega\left(t - \frac{\tilde{N}}{c}\mathbf{s}\cdot\mathbf{r}\right)\right], \tag{2.12}$$

where s is an unit vector perpendicular to the wave front, and

$$\tilde{N} \equiv \tilde{N}(\omega) = n(\omega) - i\kappa(\omega) \tag{2.13}$$

is the complex refractive index. The following relation is derived by substituting these equations for the Maxwell equations,

$$\tilde{N}^2\left(E - s(s\cdot E)\right) = \tilde{\varepsilon}(\omega)E\,. \tag{2.14}$$

The dielectric tensor of a material with one-direction anisotropy is expressed in the following way.

$$\tilde{\varepsilon} = \begin{pmatrix} \varepsilon_\perp & \varepsilon' & 0 \\ -\varepsilon' & \varepsilon_\perp & 0 \\ 0 & 0 & \varepsilon_{//} \end{pmatrix}. \tag{2.15}$$

In case of Faraday configuration, a linearly polarized light propagating to the z-direction can be separated into two circular polarized lights which can be analyzed separately. They have the different wave velocities of c / n_+ and c / n_-, respectively. Therefore, when the light proceeds at a distance l in the material, the polarization plane rotates (the Faraday rotation) by

$$\theta(\omega) = \frac{\omega l}{2c}(n_- - n_+)\,. \tag{2.16}$$

On the other hand, the difference of $\kappa_\pm$ of the left / right circular lights gives rise to the difference of absorption, which is called as magnetic circular dichroism (MCD). The incident linear polarized light has ellipticity Δ due to MCD,

$$\Delta = -\tanh\frac{\omega l}{2c}(\kappa_+ - \kappa_-) \approx \frac{\omega l}{cn}\mathrm{Re}\,\varepsilon'\,. \tag{2.17}$$

Faraday angle is correlated with ellipticity by the Kramers-Kronig relation.

2.4.2 Magnetic circular dicroism (MCD)

In order to investigate magneto-optic properties and bandstructure of GaMnAs, we have performed MCD measurements on our samples. MCD measures the optical reflectance difference between σ_+ and σ_- circular polarizations [2.48]. Alternating polarized light (50 kHz) was produced by a quartz stress-modulator. The direction of input and reflected lights deviate from the film normal by 10 degree. One degree of MCD corresponds to 7% difference of reflectivity. The magnetic field was applied perpendicular to the sample plane from the surface to the substrate direction.

MCD of zincblende-type semiconductors was explained in the following way [2.50]. When a magnetic field is not applied, the transmitted light intensity can be expressed as

$$I = I_0 \exp[-k(E)l], \tag{2.18}$$

where $k(E)$ is the optical-absorption coefficient at energy E without applied magnetic field, L is the thickness of the sample, and I_0 is the input light intensity.

The top of valence bands of zincblende-type semiconductors has Γ_8 symmetry and the bottom of conduction bands Γ_6 symmetry, as shown in Fig.2.21. The Γ_8 (J_z = -3/2) $\rightarrow\Gamma_6$ (J_z = -1/2) transition and the Γ_8 (J_z = -1/2) $\rightarrow\Gamma_6$ (J_z = 1/2) transition occur for the σ_+ polarized light. Similarly, The Γ_8 (J_z = 3/2) $\rightarrow\Gamma_6$ (J_z = 1/2) transition and the Γ_8 (J_z = 1/2) $\rightarrow\Gamma_6$ (J_z = -1/2) transition occur for the σ_- polarized light. In a magnetic field, each band splits and the difference of each absorption arises, which causes the MCD effect. We will hereafter neglect the transition from the light hole band Γ_8 ($J_z = \pm 1/2$) because its transition probability is much smaller than that from the heavy hole band Γ_8 ($J_z = \pm 3/2$) [2.51,52]. Therefore, the absorption coefficients k_+ and k_- for the σ_+ and σ_- circularly polarized light in a magnetic field can be expressed by

$$k_+(E) = k\left[E + \frac{\Delta E}{2}\right]$$

and (2.19)

$$k_-(E) = k\left[E - \frac{\Delta E}{2}\right],$$

respectively, where ΔE is the Zeeman-splitting energy. In general, the Zeeman-spliting energy of magnetic semiconductors is expressed as [2.53]

$$\Delta E = -\langle S^z \rangle N_0(\alpha - \beta) \tag{2.20}$$

in the first-order perturbation treatment of the *sp-d* interaction. $\langle S^z \rangle$ is the average spin per magnetic ion, N_0 is the number of cation per unit volume. α and β are the integrals of the *sp-d* exchange interaction for the Γ_6 conduction and Γ_8 valence bands, respectively.

MCD θ per unit light propagation distance expressed in degree units is given by

$$\theta = \frac{180}{4\pi}(k_- - k_+). \tag{2.21}$$

By substituting Eq.(2.19) and Eq.(2.20) for Eq.(2.21), a following expression is derived:

$$\theta(E) = -\frac{180}{4\pi}\Delta E \frac{dk(E)}{dE}. \tag{2.22}$$

In case of the reflection MCD, it can be transformed as

$$\theta(E) = -\frac{1}{4}N_0(\alpha - \beta) \times \langle S^z \rangle \frac{1}{R}\frac{dR}{dE}. \tag{2.23}$$

2.4.3 MCD of GaMnAs

At first, we measured the MCD spectrum of GaAs. The band structure of GaAs has been extensively studied to date. Fig. 2.22(a) shows the band structure of GaAs. The various direct transitions at critical points are marked by arrows. And Table 2.3 shows the comparison of theoretical and experimental critical point energies (in eV) for GaAs [2.54].

Fig. 2.22(b) shows the MCD spectrum of a GaAs substrate at 5K under the perpendicular magnetic field of 5T. Although the MCD signal of GaAs was very weak, sharp peaks corresponding to the optical transitions at Γ and Λ critical points are clearly observed. They are denoted as E_0 and E_1, respectively.

According to Eq.(2.23), the MCD of zincblende-type semiconductors is proportional to the reflectivity derivative $1/R \cdot (dR/dE)$ because the zeeman-splitting energy is not zero (~1 meV at 10 T) even in non-magnetic semiconductors. Fig. 2.23 shows the $1/R \cdot (dR/dE)$ spectrum of GaAs [2.55]. The MCD spectrum of GaAs is very similar to its reflectivity derivative spectrum.

Fig. 2.24 (a) and (b) shows MCD spectra of two GaMnAs films at 5K under the magnetic field of 1T: (a) for B595 ($x = 0.005$) and (b) for B672 ($x = 0.074$) [2.48]. For GaMnAs, MCD intensity is greatly enhanced with increasing the Mn content x, particularly at the critical point energies of E_0 and E_1. This indicates that *sp-d*

hybridization is very strong, and the bandstructure of GaMnAs is similar to that of zincblende type semiconductors. Oscillating structures around the energy of E_0 shown in Fig. 2.24 arise from the optical interference effect within the epitaxial films. The oscillating periods agree with the expected periods calculated from the film thickness and the refractive index of GaAs. We noted that near the band-gap energy of GaAs, 1.52 eV, a sharp negative MCD peak is superimposed on the interference pattern. This indicates that the MCD is negative at E_0 in GaMnAs. From the negative polarity of MCD at E_0, we can estimate the character of the *p-d* exchange. The polarity of MCD is a good indicator of the polarity of the *p-d* exchange constant $N_0\beta$. For example, at E_0 critical point, the antiferromagnetic (AF) *p-d* exchange ($N_0\beta$ <0) in CdMnTe showed a negative MCD peak, and the ferromagnetic (F) *p-d* exchange ($N_0\beta$ >0) in ZnCrSe showed a positive MCD peak [2.56]. Mn ions in DMS occupy the tetrahedrally (Td) coordinated sites, and their *d* orbits mix with the *p* valence band, not with the *s* conduction band [2.57]. Since the absolute value of $N_0\beta$ should be larger than that of $N_0\alpha$, the polarity of MCD is determined by the polarity $N_0\beta$. The negative MCD at E_0 critical point of GaMnAs corresponds to the AF *p-d* exchange, $N_0\beta$ <0.

As shown in Fig. 2.25, the magnetic field dependence of the MCD intensity of GaMnAs at E_1 shows ferromagnetic hysteresis which corresponds to the SQUID data (see Fig. 2.7(b)). The MCD spectrum of MnAs, which was measured for comparison, has no common feature with that of GaMnAs. Therefore, we can exclude the possibility that the observed ferromagnetism comes from possible small clusters of MnAs precipitations. The observed ferromagnetic is the intrinsic property of GaMnAs.

2.4.4 Discussion

i) Other experimental results with respect to the polarity of the *p-d* exchange of GaMnAs

Our tentative conclusion of the *p-d* exchange is $N_0\beta < 0$, as discussed above. It is still controversial although it has been supported by some papers [2.58-60]. Because it is probably difficult to determine the polarity of the MCD signal at around the band gap energy E_0 due to the interference oscillation of the light in the sample film, and the polarity at around E_1 due to broadening. Here the *p-d* exchange interaction of GaMnAs is discussed again on the basis of other

experimental results.

Okabayashi et al. claimed that the polarity of the exchange depends on whether the Mn impurity is 2+ or 3+ [2.58]. In case of the Mn^{2+} state, the spin-up states are fully occupied and only the valence electrons which have spins antiparallel to the Mn *d* spins can be transferred to the empty Mn 3*d* states, so that the *p-d* exchange interaction becomes antiferromagnetic. On the other hand, in case of Mn^{3+} state, valence electron with parallel spin can also be transferred to the Mn 3*d* orbitals, making ferromagnetic *p-d* exchange interaction possible. Photoemission spectroscopy is one of the powerful techniques to investigate the electric states of solids, especially of correlated-electron systems such as 3*d* transition-metal compounds. They performed X-ray photoemission spectroscopy (XPS) experiments and analyzed them on the basis of the cluster-model. Unfortunately, however, their results are consistent with both the Mn^{2+} and Mn^{3+} ground states and they could not determine the sign of $N_0\beta$.

One of the interesting experiments is the Faraday effect measurement of GaMnAs [2.61]. Faraday effect comes from the same mechanism as MCD. In other words, they are the different views of one physical phenomenon. Therefore one can determine the polarity of the *p-d* exchange of GaMnAs from the polarity of the Faraday rotation angle. Kuroiwa et al. measured the Faraday rotation of GaMnAs (2μm, x = 0.043, T_c = 59 K). The measurements were performed in the fundamental absorption edge region (1.24 – 1.8 eV) at 10 K and at room temperature. The oscillatory behavior was seen in the low energy at 10 K due to interference by the internal multiple reflection of light in the sample film. The absorption edge is not as sharp as that of LT-GaAs which was measured for comparison. It is probably because GaMnAs has the large carrier concentration due to the existence of a large amount of Mn acceptors. The field dependence of Faraday rotation was found to be proportional to the magnetization of the sample. And then they concluded that the polarity of the *p-d* exchange interaction of GaMnAs is ferromagnetic $N_0\beta > 0$ by comparing the polarity of Faraday angle of II-VI DMSs measured at the same time. The polarity of the *p-d* exchange interaction of II-VI DMSs has been already established.

Another example is the transmission MCD of GaMnAs. Beschoten et al. performed the transmission-type MCD measurements of GaMnAs (x = 0.053, T_c = 101 K), which measured the difference of absorption $\Delta = (k_- - k_+) / (k_- + k_+)$ [2.59]. The measurements were done at a filed of B = 1 T for temperature from 5 to 130 K, as shown in Fig. 2.26(a). In the MCD spectra of all measured GaMnAs

samples, the broad peak structures centered at approximately 1.9 eV were observed in both the ferromagnetic and paramagnetic phases and the MCD signal was positive over most of the energy range. This is also opposite to our results. Their experimental results [2.59] are very clear, but their analysis and explanation is a little doubtful. Their main point is, if the MCD signal is due to an effective field proportional to the magnetization of the population of Mn moments, the MCD data at a given energy is expected to be proportional to the thermodynamic magnetization multiplied by a temperature independent matrix element. They normalized it by the thermodynamic magnetization, namely, the value of the MCD at a fixed energy (they used the value at 1.85 eV). As shown in Fig. 2.26(b), all data above T_c collapsed to a single curve at all energies. However, at $T < T_c$, significant deviations were observed at 1.8 eV, where the magnitude of the relative MCD decreases. They thought that it would be clear if the high-temperature normalized data were subtracted from each of the curves. And then they obtained the negative peak that grows with decreasing temperature below T_c and does not saturate at low temperature. According to it, they concluded that the extracted negative peak was due to the spin splitting of the hole density of states and that the *p-d* exchange interaction was antiferromagnetic. They suggested that the broad positive MCD at higher energies came from *d-d* intra-transition of Mn ions in the range 2 ~ 3 eV or from the Burstein-Moss shift, which is unique in heavy doped semiconductors. However these procedures of their analysis might not have any physical meaning because the host valence bands and the *d* bands of Mn ions are expected to be strongly mixed and one can not distinguish electrons in the host valence bands from electrons in the *d* bands due to quantum indistinguishability of electrons. In addition, the *d-d* intra-transition of Mn ions is prohibited below T_c.

In general, when the photon energy is increased from below to above the bandgap, the semiconductor absorption coefficient increases rapidly. As a result, the sample becomes opaque for photon energies higher than the bandgap even if its thickness is very small. Therefore, it is difficult to measure transmission MCD spectrum around Λ point of GaAs and GaMnAs (~ 3eV). However, the polarity of the *p-d* exchange at Λ point will be an important clue because it is hardly affected by the Burstein-Moss shift, assuming the band shape of GaMnAs is not drastically modified from the band structure of GaAs by introducing a large amount of Mn ions. We will discuss about the magento-optic effect at Λ point later. One will see that it does not support their results of the negative polarity.

The observed Faraday effect and MCD are supposed to come from the same

origin, that is, the different optical transition profile of right / left circularly polarized light. One can easily see it in the absorption spectra (note that MCD simply means the difference of absorption coefficient, see Eq. (2.22)). Szczytko et al. measured the absorption spectra of GaMnAs films (x = 0.032 and 0.042) at 2 K under a magnetic field of 5 T [2.60], as shown in Fig. 2.27, where the absorption edge of GaMnAs is plotted. They found the absorption edge increasing monotonously above 1.5 eV and a rather weak structure below 1.5 eV. They though that those spectra split under a magnetic field due to the band splitting. The absorption spectra for σ- polarized light shifts to lower energy and for σ+ polarized light to higher energy, respectively. Note that the shapes of absorption spectra for σ- polarized light is slightly different from that for σ+ polarized light. Apparently, the shift of the absorption spectra leads to positive Faraday effect and positive MCD. The field dependence of this edge splitting has good agreement with the magnetization curve. The splitting is in the opposite way to that of CdMnTe. Therefore the *p-d* exchange interaction of GaMnAs may be interpreted as ferromagnetic type ($N_0\beta > 0$) according to the observed spin-dependent absorption spectra. But they did not conclude in such a way, in Ref. [2.60].

They thought that the edge splitting did not exactly reflect the band splitting of the valence band of GaMnAs because of the Burstein-Moss shift. According to them, optical transition does not occur at the top of the valence band in case of GaMnAs. They claim that the optical transition occurs from the electrons with minority spin at the Fermi energy E_F, which have the large wave number corresponding to E_F. For ferromagnetic *s-d* exchange $N_0\alpha > 0$ and antiferromagnetic *p-d* exchange $N_0\beta < 0$, σ+ transitions occur at higher energy than σ- ones, that is, the edge splitting is of ferromagnetic type. Had one assumed $N_0\beta > 0$ (ferromagnetic *p-d* exchange), the antiferromagnetic-type splitting [$E(\sigma+) > E(\sigma-)$] would be observed. Eventually they concluded that *p-d* exchange of GaMnAs is of antiferromagnetic type ($N_0\beta < 0$). Apparently, their conclusion does not have the same meaning with the conclusion according to the reflective MCD measurements because their experimental results were $k_-(E) > k_+(E)$ in observed energy range. But their explanation of the experimental results is not satisfactory because they completely forget the *d* bands which are supposed to be strongly mixed with the host *p* band.

ii) Model of the *p-d* exchange coupling of GaMnAs

Here one possible interpretation is proposed for the magneto-optical effects of GaMnAs. It is on the side of the interpretation of the ferromagnetism of GaMnAs caused by the double exchange interaction, which is applied to GaMnAs by Akai for the first time [2.24], rather than the RKKY interaction. This model will satisfy the experimental results discussed above. Here the optical transition is assumed to happen from the top of the valence band to the bottom of the conduction band of the host GaAs. According to the double exchange model, electrons transport back and forth between *d* levels of Mn^{2+} and Mn^{3+} through the host valence band, keeping their spin direction unchanged. It is not the case of II-VI DMSs because their *d* electrons are strictly localized. Note again that in GaMnAs the host *p* bands and Mn *d* bands are strongly hybridized and one can not distinguish electrons in the host valence bands from electrons in the *d* bands due to quantum indistinguishability of electrons. The spin direction of electrons is parallel to that of the local *d* electrons due to the strong Coulomb interaction in the 3*d* shell of the Mn ions. In fact, it is easy to consider that holes, which are opposite to electrons in terms of spin direction, contribute to the electric transport. That is, the holes in the 3*d* bands expand through the valence band of the host GaAs. Therefore the polarity of *p-d* exchange of GaMnAs is of ferromagnetic type, which is supported by the experimental results. Although the existence of the impurity band should be taken into account, it is assumed to merge with the valence band for simplicity.

The ferromagnetic *p-d* exchange might not be the main reason of positive MCD. In case of II-VI DMSs, the absorption edge splitting only comes from the band splitting. Therefore the absorption edges are very similar in shape to one another. However, it is not exactly the case for GaMnAs . The shape of the absorption spectra for σ- polarized light is not completely same as that for σ+ polarized light, leading to the observed positive MCD of GaMnAs (Fig. 2.26). The difference of the σ+ and σ- absorption spectra in shape are due to the difference of density-of-states at Fermi energy. The difference of density-of-states of the conducting hole band is expected to have something to do with the ferromagnetism of GaMnAs.

Hirakawa et al. measured optical conductivity $\sigma(\omega)$ of GaMnAs in far infrared region [2.62]. They found that the $\sigma(\omega)$ in the low-frequency range is almost frequency independent. The fact suggests the conduction of holes in GaMnAs is not Drude-like but diffusive even in the samples which show metallic behavior. They also found that the soaring of the $\sigma(\omega)$ of GaMnAs below the Curie temperature. They pointed out that it is very similar to the characteristic of the optical conductivity observed in Mn perovskite systems, in which their ferromagnetism can

be explained by the picture of the double exchange interaction. In fact, optical conductivity of $La_{1-x}Sr_xMnO_3$ (x = 0.175 and 0.3) increases below T_c [2.63]. In addition, the intensity of the UPS (ultraviolet photoemission spectroscpy) spectrum of $La_{1-x}Sr_xMnO_3$ (x = 0.4) around the Fermi energy increases with decreasing the temperature [2.64]. By analogy with $La_{1-x}Sr_xMnO_3$, Hirakawa et al. deduce that the increase of the $\sigma(\omega)$ of GaMnAs is due to the change in the density-of-states of the spin bands, that is, the density-of-states of holes with the majority spin increases below T_c and that such a rearrangement in the density-of-states due to ferromagnetic transition comes from the double exchange mechanism [2.62]. However they do not assign the optical excitation of carriers from which band to which band, that is, they do not describe about the electronic states of the spin band at all. It is the most likely interpretation that electrons are excited by far infrared light from the Fermi level to the mobility edge. The soaring of density-of-states might occur mainly in the majority spin band (note that we are discussing about the hole system). It accounts for the absorption edge splitting. They also found a broad peak in the conductivity spectra over the energy range of 200 meV [2.62], which is near the peak energy (1.85 eV) of the MCD spectra (Fig. 2.26). According to them, the peak is due to the formation of small polarons. However the interpretation of the peak has not been established yet.

To sum up, the increase of density-of-states of the mixed *p-d* band at Fermi surface in the majority spin band leads to the difference of the shapes of the absorption spectra (Fig. 2.27). Therefore, the spin polarization of conducting holes of GaMnAs at zero field, where Mn ions are ordered partially, is not expected to be large. Fig. 2.28 shows the hypothetical band diagram of GaMnAs summing the above discussion.

iii) Interpretation of the MCD at Λ point

In this section we show some experimental data which support the positive *p-d* exchange. It is already shown that MCD is proportional to reflectivity derivative $1/R \cdot (dR/dE)$. We have measured the real and imaginary parts of the dielectric function of a GaAs substrate and GaMnAs films by ellipsometry measurements at room temperature. The complex dielectric function $\varepsilon(\omega) = \varepsilon_r(\omega) + i\varepsilon_i(\omega)$, complex index of refraction $N(\omega) = n(\omega) + ik\ (\omega)$, and reflectivity $R(\omega)$ are the most commonly used optical functions. They are related to one another as follows:

$$
\begin{aligned}
N^2 &= \varepsilon_r + i\varepsilon_i, \\
\varepsilon_r &= n^2 - k^2, \\
\varepsilon_i &= 2nk, \\
R &= \left|\frac{N-1}{N+1}\right|^2 = \frac{(n-1)^2 + k^2}{(n+1)^2 + k^2}.
\end{aligned} \tag{2.24}
$$

Fig. 2.29, 30, 31 shows the $\varepsilon(\omega)$, $N(\omega)$ and $R(\omega)$ of GaAs and GaMnAs (B595 x = 0.005, B672 x = 0.074). In this case, multiple reflection in sample films is not a big problem, because the incident light is not perpendicular to the sample surface. The band edge of GaMnAs was not sharp, while the band edge of GaAs is very clear. It is because electrons near the band edges of GaMnAs tend to be very diffusive. Reflectivity derivative $1/R \cdot (dR/dE)$ is easily derived from them, as shown in Fig. 2.32. The reflectivity derivative (Fig. 2.32) of GaAs from the ellipsometry measurements at room temperature seems to have the same feature of that of GaAs (Fig. 2.23). The observed reflective MCD spectrum of GaAs (Fig. 2.22) certainly reflects the reflectivity derivative of GaAs (Fig. 2.23). However, there is no peak around 2.85 eV in the MCD spectrum of GaAs, although a sharp peak around 2.85 eV is seen in the reflectivity derivative function of GaAs. In the reflectivity derivative function of GaMnAs (Fig. 2.32), the corresponding peaks are broad, which is very similar to the MCD spectrum of GaMnAs (Fig. 2.24), except the polarity. Remind that the g-factor of GaAs valence band is negative. Therefore, the p-d exchange of GaMnAs at Λ point is positive. We can conclude that the p-d exchange of GaMnAs at Γ point is also positive, assuming that the band shape of host GaAs is not modified drastically by introducing a large amount of Mn ions. This fact is consistent with the above explanation of the absorption spectra. It might be able to confirmed by reflective MCD of very diluted doped GaAs:Mn. We can not exclude the possibility of the existence of a phase transition between GaAs:Mn systems and GaMnAs systems depending on Mn concentration.

2.5 Summary

- Homogeneous GaMnAs films (Mn concentration $x < 0.08$) are grown on GaAs (001) substrate at 200 ~ 300 °C by using low-temperature molecular beam epitaxy.
- GaMnAs is a ternary alloy with zincblende type crystal structure. The lattice constant is slightly larger than that of GaAs.

- GaMnAs shows *p*-type conduction with hole concentration ranging from low 10^{18} to low 10^{20} cm^{-3}.
- Conductive GaMnAs samples show ferromagnetic behavior at low temperature, while insulating GaMnAs samples do not have a ferromagnetic phase even at low temperature.
- Ferromagnetic GaMnAs shows extraordinary Hall effects, which allows us to investigate the magnetic properties through magnetotransport measurements.
- Applying a magnetic field reduces the resistivity of ferromagnetic GaMnAs by breaking up the Anderson localization of hole carriers.
- Ferromagnetic GaMnAs shows large magneto-optic effects caused by the strong interaction of electrons in the host valence band with the local magnetic moments.

References

[2.1] T. Hayashi, M. Tanaka, T. Nishinaga, H. Shimada, H. Tsuchiya, and Y. Ootuka, J. Cryst. Growth **175/176** (1997) 1063.

[2.2] H. Ohno, A. Shen, F. Matsukura, A. Oiwa, A. Endo, S. Katsumoto and H. Iye, Appl. Phys. Lett. **69** (1996) 363.

[2.3] J. De Boeck, R. Oesterholt, A. Van Esch, H. Bender, C. Bruynseraede, C. Van Hoof and G. Borghs, Appl. Phys. Lett. **68** (1996) 2744.

[2.4] M. Tanaka, J. Vac. Sci. Technol. **B16** (1998) 2267.

[2.5] M. Tanaka, J. Cryst. Growth **201/202** (1999) 660.
H. Shimizu, T. Hayashi, T. Nishinaga, and M. Tanaka, Appl. Phys. Lett. **74** (1999) 398.

[2.6] R. Shioda and K. Ando, T. Hayashi, M. Tanaka, Phys. Rev. **B58** (1998) 1100.

[2.7] M. Tanaka, J. P. Harbison, M. C. Park, Y. S. Park, T. Shin and G. M. Rothberg, Appl. Phys. Lett. **65** (1994) 1964.

[2.8] S. O'Hagan, M. Missous, J. Appl. Phys. **75** (1994) 7835.

[2.9] F. W. Smith, A. R. Calawa, C. L. Chen, M. J. Manfra, and L. J. Mahoney, IEEE Electron Device Lett., **9** (1988) 77.

[2.10] L. –W. Yin, Y. Hwang. J. H. Lee, R. M. Kolbas, R. J. Trew, and U. K. Mishra, IEEE Electron Device Lett., **11** (1990) 561.

[2.11] C. L. Chen, F. W. Smith, B. J. Clifton, L. J. Mahoney, M. J. Manfra, and A. R. Calawa, IEEE Electron Device Lett., **12** (1991) 306.

[2.12] A. Shen, F. Matsukura, S. P. Guo, Y. Sugawara, H. Ohno, M. Tani, H. Abe, and H. C. Liu, J. Crst. Growth **201/202** (1999) 679.

[2.13] C. Kittel, "*Introduction to Solid State Physics*" (Jon Wiley, 1996).

[2.14] "*Semiconductors and Semimetals*", edited by J. K. Furdyna and J. Kossut (Academic, Boston, 1988), Vol. 25.

[2.15] H. Munekata, H. Ohno, S. von Molnar, Armin Segmuller, L. L. Chang, and L. Esaki, Phys. Rev. Lett., **63** (1989) 1849.
H. Ohno, H. Munekata, S. von Molnar and L. L. Chang, J. Appl. Phys. **69** (1991) 6103.
H. Ohno, H. Munekata, T. Penny, S. von Molnar and L. L. Chang, Phys. Rev. Lett. **68** (1992) 2664.

[2.16] F. Matsukura, H. Ohno, A. Shen, and Y. Sugawara, Phys. Rev. **B57** (1998) R2037.

[2.17] S. Koshihara, A. Oiwa, M. Hirasawa, S. Katsumoto, Y. Iye, C. Urano, H. Takagi, and H. Munekata, Phys. Rev. Lett. **78** (1997) 4617.

S. Koshihara, H. Munekata, A. Oiwa, M. Hirasawa, S. Katsumoto, Y. Iye, C. Urano, and H. Takagi, Physica E2 (1998) 417.

[2.18] A. Oiwa, S. Katsumoto, A. Endo, M. Hirasawa, Y. Iye, H. Ohno, F. Matsukura, A. shen, and Y. sugawara, Solid State Commum. 103 (1997) 209.

[2.19] J. Yoshino, Y. Satoh, M. Odahara, D. Okazawa, proceeding of the PRESTO project of JDC, Grant-in-Aids for Scientific Research from the Ministry of Education, Science, Sports and Culture, Japan, May 27-28 (1999) p2.

[2.20] K. Yoshida, "*Theory of magnetism*" (Springer-Verlag, 1998).

[2.21] M. A. Runderman and C. Kittel, Phys. Rev. **96** (1954) 99.

[2.22] T. Kasuya, Prog. Theor. Phys. **16** (1956) 45.

[2.23] K. Yoshida, Phys. Rev. **106** (1957) 893; ibid. **107** (1957) 396.

[2.24] For InMnAs, H. Akai, Phys. Rev. Lett. **81**, (1998) 3002. For GaMnAs, S. Watanabe and H. Akai, proceeding of the 5th symposium on "the Physics and Application of Spin-Related Phenomena in Semiconductors", Japan, Dec. 16-17 (1999) p.162.

[2.25] M. Imada, A. Fujimori, and Y. Tokura, Rev. Mod. Phys. **70**, (1998) 1039.

[2.26] C. Zener, Phys. Rev. **81** (1951) 440; ibid. **82** (1951) 403.

[2.27] P. W. Anderson and H. Hasegawa, Phys. Rev. **100** (1955) 675.

[2.28] Y. Onodera, "*Introduction to group theory in physics of molecules and solids*" (Shokabo, 1996).

[2.29] K. Kusakabe and H. Aoki, "*Ferromagnetism*" (University of Tokyo Press, 1998).

[2.30] A. Shen, H. Ohno, F. Matsukura, Y. Sugawara, N. Akiba, T. Kuroiwa, A. Oiwa, A. Endo, S. Katsumoto, Y. Iye, J. Cryst. Growth **175/176** (1997) 1069.

[2.31] T. Hayashi, M. Tanaka, T. Nishinaga and H. Shimada, J. Appl. Phys. **81** (1997) 4865.

[2.32] L. Berger and G. Bergmann, in "*The Hall Effect and Its Applications*", edited by C. L. Chien and C. R. Westgate (Plenum, New York, 1980), p. 55.

[2.33] H. Ohno, F. Matsukura, Y. Ohno, S. Wang, N. Akiba, S. Kishimoto, R. Terauchi, T. Adachi, T. Omiya, E. Abe, and K. Nakata, proceeding of the PRESTO project of JDC, Grant-in-Aids for Scientific Research from the Ministry of Education, Science, Sports and Culture, Japan (1999) 1.

[2.34] T. Omiya, F. Matsukura, T. Dietl, Y. Ohno, T. Sakon, M. Motokawa, and H. Ohno, proceeding of the 5th symposium on "the Physics and Application of Spin-Related Phenomena in Semiconductors", in Sendai, Japan, Dec. 16-17 (1999) p.178.

[2.35] R. A. Chapman, W. G. Hutchinson, Phys. Rev. Lett. 18 (1967) 443; ibid. 18 (1967) 822.

[2.36] L. J. Vieland, J. Appl. Phys. 33, (1962) 2007.

[2.37] S. M. Sze and J. C. Irvin, Solid State Electron, 11, (1968) 599.

[2.38] N. F. Mott, "Metal-Insulator Transitions, 2nd Ed., (Tayler & Francis, London, 1990).

"The Metal Non-metal Transition in disordered Systems", ed. by L. R. Friedman and D. P. Tunstall (Edinburgh: SUSSP Publication, 1978, p.193).

[2.39] N. F. Mott, Proc. Phys. Soc. (London) 62 (1949) 416; Phil. Mag. 6 (1961) 287; Adv. Phys. 16 (1967) 49.

[2.40] P. P. Edwards and M. J. Sienko, Phys. Rev. B17 (1978) 2575.

[2.41] N. F. Mott and W. D. Twose, Adv. Phys. 10 (1961) 107.

[2.42] P. W. Anderson, Phys. Rev. 109 (1958) 1492.

[2.43] H. Aoki and H. Kamimura, J. Phys. Soc. Japan 40 (1976) 6.

[2.44] J. Hubbard, Proc. Roy. Soc. A 276 (1963) 238; ibid. 277 (1964) 237; ibid. 281 (1964) 401.

[2.45] D. A. Woodbury and J. S. Blackemore, Phys. Rev. B8 (1973) 3803.

[2.46] Y. Nagaoka, Phys. Rev. 147 (1966) 392.

[2.47] S. Katsumoto, A. Oiwa, Y. Iye, H. Ohno, F. Matsukura, A. Shen, Y. Sugawara, Phys. Stat. Sol. B 205 (1998) 115.

[2.48] K. Ando, T. Hayashi, M. Tanaka and A. Twardowski, J. Appl. Phys. 83 (1998) 6548.

[2.49] "*Handbook of magnetic materials*", edited by S. Chikazumi (Asakurashobo 1993).

[2.50] K. Ando, K. Takahashi, T. Okuda and M. Umehara, Phys. Rev. B46 (1992) 12289.

[2.51] G. Rebmann, C. Rigaux, G. Basterd, M. Menant, R. Triboulet, and W. Giriat, Physica B+C 117&118B (1983) 452.

[2.52] J. P. Lascaray, D. Coquillat, J. Deportes, and A. K. Bhattacharjee, Phys. Rev. B38 (1988) 7602.

[2.53] J. A. Gaj, J. Ginter, R. R. Galazka, Phys. Status Solidi B89 (1978)655.

[2.54] M. L. Cohen and J. R. Chelikowsky, "*Electronic Structure and Optical Properties of Semiconductors*" (Springer-Verlag, 1988).

[2.55] P. Y. Yu and M. Cardona, "*Fundamentals of Semiconductors*" (Springer-Verlag, 1996).

[2.56] K. Ando and A. Twardowski, in *Proceedings of the 23 rd International*

Conference on the Physics of Semiconductors, Berlin 1996, edited by M. Scheffler and R. Zimmermann (World Scientific, Singapore, 1996), p. 285.

[2.57] S-H. Wei and A. Zunger, Phys. Rev. B35 (1987) 2340.

[2.58] J. Okabayashi, A. Kimura, O. Rader, T. Mizokawa, A. Fujimori, T. Hayashi, and M. Tanaka, Phys. Rev. B58 (1998) R4211.

[2.59] B. Beschoten, P. A. Crowell, I. Malajovich, D. D. Awschalom, F. Matuskura, A. Shen, and H. Ohno, Phys. Rev. Lett. 83 (1999) 3073.

[2.60] J. Szczytko, W. Mac, A. Twardowski, F. Matsukura, and H. Ohno, Phys. Rev. B59 (1999) 12935.

[2.61] T. Kuroiwa, T. Yasuda, F. Matsukura, A. Shen, Y. Ohno, Y. Segawa, and H. Ohno, Electron. Lett. 34 (1998) 190.

[2.62] K. Hirakawa, S. Katsumoto, T. Hayashi, A. Oiwa, and Y. Iye, proceeding of the PRESTO project of JDC, Grant-in-Aids for Scientific Research from the Ministry of Education, Science, Sports and Culture, Japan (1999), p105.

[2.63] S. Jin, T. H. tiefel, M. McCormack, R. Fastnacht, R. Ramesh, and L. H. Chen, Science 264 (1994) 2331.

[2.64] D. D. Sarma, N. Shanthi, S. R. Krishnakumar, T. Saitoh, T. Mizokawa, A. Sekiyama, K. Kobayashi, A. Fujimori, E. Weschke, R. Meier, G. Kaindl, Y. Takeda, and M. Takano, Phys. Rev. B53 (1996) 6874.

3. *GaMnAs / AlAs superlattices*

In the previous chapter, the fundamental properties of GaMnAs single layers were described from the various view points. GaMnAs is a ferromagnetic semiconductor, having good compatibility with the existing III-V semiconductors in term of crystal structure and bandstructure. Semiconductor heterostructures are expitaxial layers of two or more different semiconductors. Heterostructures offer a new degree of freedom in the design of semiconductor devices, because both the impurity doping and the conduction and valence band offsets at the junction can be controlled. For example, semiconductor lasers employ the double heterostructures like a GaAs layer embedded in AlGaAs layers. Ferromagnetic semiconductors will add a new degree of spin freedom to the band engineering of conventional nonmagnetic semiconductors.

The concept of band gap and/or wavefunction engineering has been well established [3.1] and a number of works have been done in the field of semiconductor quantum heterostructures and superlattices (SLs). This concept was applied to II-VI based diluted magnetic semiconductors (DMSs), and many interesting spin-related phenomena were reported on the SLs having II-VI DMS layers [3.2]. On the other hand, since the knowledge of III-V based DMSs are limited so far, only a few papers on the ultarathin heterostructure containing III-V based DMSs [3.3,4] were published. However, those papers did not report on the bandstructure control, such as the shift of transition energy and the formation of subbands in the ultrathin layers of III-V based magnetic semiconductors.

In general, two possible band edge profiles exist for semiconductor heterostructures with respect to the valence and conduction edges. In type I configuration, one material is a barrier for both holes in the valence band and electrons in the conduction band. Another situation is also found where one material acts as a well for electrons in conduction band but as a barrier for holes in the valence band (type II configuration). Here magnetic semiconductor heterostructures are divided into two classes, respectively, depending on the role of magnetic semiconductor layers in the heterostructures. Type-A represents the heterostructures with magnetic ions in the well and type-B with magnetic ions in

the barrier, as depicted in Fig. 3.1. As discussed before, the mechanism of ferromagnetism of GaMnAs is on the basis of the interaction between itinerating holes and Mn local moments. In type-A configuration, conducting holes are confined in the well where a large amount of magnetic ions are located. In contrast, Mn ions in barrier layers are coupled with the penetration of wavefunction of holes in type-B configuration. In other words, conducting holes and magnetic moments are spatially divided.

It might be possible to adjust the exchange interaction strength of GaMnAs by controlling the well thickness, because quantum confinement effect transforms the shape of energy dispersion of the host GaAs, which might allow us to control the ferromagnetism of GaMnAs. In this case, the electronic states of Mn ions in the quantum well will not be affected so much, because the crystal field around Mn ions does not change even in 2-dimensional system. Confinement energies of a quantum well are generally sensitive to an electric field and a magnetic field. Resonant tunneling effect between quantum levels in an asymmetric double quantum well system might be expected to be induced by a magnetic field by utilizing large magneto-optic effect of ferromagnetic semiconductors.

In a modulation-doped GaMnAs / AlAs heterostructure, conducting holes which induce the ferromagnetic interaction of GaMnAs will increase in population due to charge transfer effects. A lot of carriers can be supplied into the GaMnAs layer by doping Be, which is a shallow impurity, in the AlAs layer. It might be possible to increase the concentration without increasing a number of Mn ions which is limited because of low Mn solubility in GaAs.

Based on the previously described fundamental properties in term of crystal structure and bandstructure, we are now able to design and fabricate a new class of magnetic quantum heterostructures.

3.1. Growth of GaMnAs / AlAs superlattices [3.5]

We have successfully grown magnetic (GaMnAs) / nonmagnetic (AlAs) semiconductor superlattices on semi-insulating GaAs (001) substrates by using LT-MBE. Fig. 3.2 shows the growth procedure of the superlattices. After growing a GaAs buffer layer at 580°C, the substrate temperature was cooled to 250°C while the As flux was kept on. During the cooling process, RHEED patterns changed from (2 x 4) to c(4 x 4). An AlAs layer was first grown on this c(4x4) GaAs surface. And then GaMnAs layer was grown. This cycle was repeated 30 times. The

growth was interrupted for 10 ~ 20 s at each interface. RHEED patterns with the azimuth of [-110] taken from AlAs and GaMnAs during the growth were fairly streaky despite low-temperature growth, as shown in Fig. 3.3. Clear two-fold streaks are observed on the GaMnAs surface whereas almost no reconstruction was seen on the AlAs surface. The (1 x 2) reconstructed GaMnAs surface and (1 x 1) unreconstructed AlAs surface were repeatedly observed during the growth of the GaMnAs /AlAs SLs.

3.2. *Structural characterization of GaMnAs / AlAs superlattices*

To characterize the structure of the GaMnAs / AlAs SLs, X-ray diffraction measurements were done on all the samples. Fig. 3.4 shows an X-ray diffraction spectrum of the GaMnAs (50Å, x = 0.047) / AlAs (30Å) superlattice with 31 periods [3.5]. In this graph, at least four satellite peaks can be seen on both sides of the GaAs (002) peak. Similar results were obtained for all other SL samples. Fig. 3.5 shows a cross-sectional transmission electron microscopy (TEM) image of the same SL [3.6]. In this picture, dark and bright regions are the GaMnAs and the AlAs layers, respectively. Clear contrast between the GaMnAs and the AlAs was observed, indicating the compositional SL structure was formed as intended. These TEM and X-ray results indicate that the superlattice has excellent crystal quality with abrupt interfaces between GaMnAs and AlAs. The periodic thickness D of this superlattice calculated from the satellite peak positions was about 81Å, which is in good agreement with the designed thickness of 80Å. It indicates the excellent controllability of the growth.

3.3. *Magnetic properties of GaMnAs / AlAs superlattices* [3.5]

In order to investigate the magnetic properties of the SLs, we performed magnetization measurements of all the samples using a SQUID. Fig. 3.6 show *M-H* (magnetization versus applied magnetic field) curves of a SL of GaMnAs (120Å) / AlAs (68Å) with a Mn concentration of x = 0.060 measured at 2.0 K, when the magnetic field was applied (a) in plane and (b) perpendicular to the plane, respectively. Clear hysteresis was observed, indicating that the SL is ferromagnetic at low temperatures. The coercive field H_c was 388 Oe at 2.0 K, larger than that (~50 Oe) of the 1.4μm-thick GaMnAs single layer. When the magnetic field was applied perpendicular to the plane, a distorted little hysteresis

was observed as shown in Fig. 3.6(b). Similar results were observed for other SL [GaMnAs (70Å) / AlAs (30Å)]. This indicates that the easy axis of magnetization lies in plane, as in the case of the GaMnAs single films grown on GaAs (001). In contrast, for the SL samples with the GaMnAs thickness of 50Å or less, no ferromagnetic order was found at the temperature range (2.0 ~ 300 K) measured in this experiments. Shimizu et al. reported later that the SL samples with the GaMnAs thickness of 50Å which was grown on the optimized condition showed ferromagnetic ordering [3.8]. Table 3.1 shows the comparison of magnetic properties between GaMnAs single layers and a GaMnAs / AlAs SL.

3.4. Magnetotransport properties of GaMnAs / AlAs superlattices [3.6,7]

In order to investigate the magnetotransport properties, we have done Hall and resistivity measurements at various temperatures in the same way described above. The SLs with narrow (≦50Å) GaMnAs layers were high resistive and transport measurements were difficult. This is probably because carriers are localized due to some structural fluctuations such as interface roughness, and/or because carriers are depleted due to strong quantum confinement. Hence, we measured the SLs with wider (≧70Å) GaMnAs which showed *p*-type conduction and ferromagnetic order at low temperature.

Fig. 3.7(a) shows the magnetic field dependence of R_{xy} of a [GaMnAs (70Å) / AlAs (30Å)] SL with x = 0.049 measured 10 K. The clear ferromagnetic behavior was observed at low temperature. Here only a little hysteresis loop appears under perpendicular magnetic field, because the easy axis of magnetization lies in-plane. The negative Hall resistance at high field is due to the contribution of resistivity ρ_{xx} through R_s (see Eq.(2.5)). Fig. 3.7(b) plots the resistance R_{xx} (= ρ_{xx}/d) versus magnetic field perpendicular to the film, which shows large negative magnetoresistance (MR). As described above, assuming that the magnetization at 10 K of this sample saturates at sufficiently low field and becomes constant at high filed, we can estimate R_0, thus the hole concentration from the R_{xy} and R_{xx} data at high field by excluding the negative MR contribution of R_{xx} (Fig. 3.7(b)) from the R_{xy} (Fig. 3.7(a)) data. The sheet hole concentration of this sample is estimated to be 7.0 x 10^{14} cm^{-2}, corresponding to 2.3 x 10^{13} cm^{-2} per GaMnAs layer. This value gives the critical hole concentration to produce ferromagnetic order in GaMnAs. The Arrott plots were made from the transport data, and the Curie temperature of the SL of [GaMnAs (120Å, x = 0.060) / AlAs (68Å)] SL and [GaMnAs (70Å, x = 0.049) /

AlAs (30Å)] SL were estimated to be 62.5 K and 45 K, respectively. The experimental fact that the SLs with wider (≧70Å) GaMnAs are ferromagnetic and conductive, whereas the SLs with narrow (≦50Å) GaMnAs are not ferromagnetic and high-resistive, strongly suggests that the ferromagnetic order in GaMnAs is induced by holes.

3.5. MCD of GaMnAs / AlAs superlattices [3.5]

In order to investigate the magneto-optic properties and the bandstructure of GaMnAs / AlAs superlattices, we performed MCD measurements under the same experimental set up described earlier (see Section 2.4). Fig. 3.8 shows MCD spectra of the superlattices at 5K under the magnetic field of 1T. The nominal thickness of GaMnAs well and AlAs barrier and the Mn contents x were (a) 120Å. 68Å, $x = 0.06$, (b) 70Å, 30Å, $x = 0.049$, and (c) 50Å, 30Å, $x = 0.047$. The spectrum of Fig. 3.8(c) is magnified by 5 times because the MCD of (c) is much weaker than that of (a) and (b). The reason is that the SLs of (a) and (b) are ferromagnetic, whereas the SL of (c) is paramagnetic at this temperature. It was found that these SLs have large MCD peaks at the critical energy points, which correspond to the transition energies between the electron subbands and hole subbands at the Γ point of GaMnAs. Large peaks were also seen at the Λ point at an energy of $E_1 \sim 3$ eV, as in the case of thick GaMnAs films. As the thickness of GaMnAs in the SLs decreases, the lowest transition energy, which is $1e - 1hh$ (the first electron subband to the first heavy-hole subband at Γ), is shifted to higher energy due to quantum confinement effect. Also, a higher transition peak, which is assigned to $2e - 2hh$, was observed in the SLs with wider GaMnAs layers. We have calculated the transition energies using Kronig-Penny model assuming that GaMnAs has the same band parameters as those of GaAs, and marked in Fig. 3.8 by arrows. Good agreement is seen between the observed transition energies and the calculated ones as shown in Table 3.2. This is a clear demonstration of the quantum confinement effect and 2-dimensional subband formation in III-V magnetic semiconductor system. As discussed in the previous chapter, the negative peaks of MCD spectra do not precisely correspond to the Γ points. Shimizu et al. found that transmission MCD spectra of GaMnAs / AlAs SLs had a step structure corresponding to the transition energies calculated from the Kronig-Penny model, and confirmed the formation of subband structures [3.9]. We believe the quantum confinement effect and subband formation in III-V magnetic semiconductor heterostructure system will open up the

unique possibility of coupling the spin-related phenomena with well-established band engineering in III-V semiconductors.

Shimizu et al. also performed transmission measurements on a GaMnAs (70Å, x = 0.043) / AlAs (30Å) SL near the fundamental edge at 5 K [3.9]. Fig. 3.9 shows the absorption spectra at a magnetic field B = 1 T measured for σ- and σ+ polarized light. Clear steps were observed in both the spectra. In contrast, no step was seen in transmission spectra of GaMnAs single layers, as shown in Fig. 2.27 [2.25]. Therefore the observed step structures are characteristic of the 2-dimensional system. However turnings of those spectra do not clearly correspond to the calculated transition energies (1.62 eV for $1e - 1hh$, 1.67 eV for $1e - 1lh$, and 1.99 eV for $2e - 2hh$).

Here it is emphasized that those spectra split in the vertical (intensity) direction, not in the horizontal (energy) direction. It definitely indicates that the absorption edge splitting does not come from only Zeeman splitting of the valence band. It is more suitable to say that the splitting is attributed to the increase of the density-of-states at E_F in the majority spin band, as discussed in the previous chapter.

On the other hand, there are some possibilities that observed peaks come from the optical interference effect within the epitaxial films [3.10].

3.6 Summary

- GaMnAs / AlAs superlattices with abrupt interfaces are grown by using low temperature molecular beam epitaxy.
- GaMnAs / AlAs superlattices with wider (≧70Å) GaMnAs are ferromagnetic and conductive, whereas the superlattice with narrow (≦50Å) GaMnAs are not ferromagnetic and high-resistive.
- The formation of subbands in GaMnAs / AlAs superlattices were confirmed by the MCD measurements.

References

[3.1] L. Esaki and R. Tsu, IBM J. Res. Dev. 14 (1970) 61; H. Sakaki, *Proceedings in Symposium Foundations of Quantum Mechanics* (Physical Society of Japan, Tokyo, 1984), p. 94.

[3.2] *Semiconductors and Semimetals*, edited by J. K. Furdyna and J. Kossut, Diluted Magnetic Semiconductors (Academic, Boston, 1986), vol. 25.

[3.3] H. Munekata, A. Zaslavsky, P. Fumaglli, and R. J. Gambino, Appl. Phys. Lett. 63 (1993) 2929; P. Fumagalli and H. Munekata, Phys. Rev. B53 (1996) 15045.

[3.4] A. Shen, H. Ohno, F. Munekata, Y. Sugawara, Y. Ohno, N. Akiba, and T. Kuroiwa, Jpn. J. Appl. Phys. Part 2 36 (1997) L73.

[3.5] T. Hayashi, M. Tanaka, K. Seto, T. Nishinaga, and K. Ando, Appl. Phys. Lett. 71 (1997) 1825.

[3.6] T. Hayashi, M. Tanaka, K. Seto, T. Nishinaga, H. Shimada, T. Hayashi, and K. Niihara, Physica E 2 (1998) 404.

[3.7] T. Hayashi, M. Tanaka, K. Seto, T. Nishinaga, H. Shimada, and K. Ando, J. Appl. Phys. 83 (1998) 6551.

[3.8] H. Shimizu, in private communication.

[3.9] H. Shimizu, T. Hayashi, T. Nishinaga, and M. Tanaka, MRS 1999 Spring Meeting, paper K4.2, San Francisco USA, April 1999.

[3.10] A. Twardowski, in private communication.

4. Spin-polarized electron tunneling

Although electron naturally has the freedom of spin as well as electronic charge, only charge current has been focused in present electronic devices. On the contrary, spin effects have been almost completely ignored because spin relaxation time is very short in non-magnetic semiconductors such as GaAs and its related heterostrucutres [4.1]. Apparently, spin dependent transport will give more degree of freedom to semiconductor electronic devices.

Spin dependent transport in ferromagnetic materials is attributed to the difference of electronic states between up-spin electrons and down-spin electrons. Electric current of up-spin electrons and down-spin electron can be considered separately under a good approximation (two-current model) [4.2,3]. The asymmetry of the density-of-states at Fermi energy is one of crucial factors in such transport. Spin-polarized electron tunneling, which has used special properties of the superconducting state, is a powerful experimental technique to probe spin-dependent features of the electron density-of-states of superconductors, magnetic metals, and magnetic semiconductors. The tunneling technique in superconductors was introduced by Giaever [4.4] and has been developed by R. Meservey and P. M. Tedrow [4.5,6]. In this chapter, in order to study the electronic structure of GaMnAs around the Fermi energy, we will discuss about spin-dependent tunneling spectroscopy of GaMnAs.

4.1. Theory of tunneling spectroscopy [4.6]

First, we introduce a theoretical model of tunneling spectroscopy. Detailed theoretical treatment of it is provided by the references [4.7-10]. Electron tunneling is a quantum phenomenon in which electric current can pass from one electrode through a thin insulating barrier layer into a second electrode. This three-layer system – electrode, barrier, and counterelectrode – is referred to as a tunnel junction. If the barrier is sufficiently thin (less than 10 or 20Å), there is a significant probability that an electron which impinges on the barrier will pass from one metal to the other. The quantity usually measured in a tunneling experiment

is the current or its derivative as a function of applied voltage. With no voltage applied, the Fermi levels of the two electrodes must be equal. An applied voltage manifests itself as a difference in energy between the two Fermi levels to preserve the balance of the chemical potential of both electrodes. The tunneling current is derived from the Fermi's golden rule; that is, the number of electrons tunneling is given by the product of the density of filled states at a given energy in one electrode and the density of empty states in the other electrode at the same energy multiplied by the square of a matrix element M describing the probability of tunneling. In our energy range (+/- 10 meV), this matrix element M is taken to be independent of energy. Tunneling current of electrons at energy E flowing from electrode 1 to electrode 2 is expressed as following,

$$I_+(V,E) \approx D_1(E-eV)D_2(E)|M|^2 f(E-eV)[1-f(E)] \tag{4.1}$$

Here V is the voltage on the first electrode with respect to the second, N_1 and N_2 are the densities-of-states of the first and second electrodes, and f is the Fermi function, and the energy E is measured from the Fermi energy. Similarly, the tunnel current from electrode 2 to electrode 1 is given by

$$I_-(V,E) \approx D_1(E-eV)D_2(E)|M|^2[1-f(E-eV)]f(E). \tag{4.2}$$

Assuming that $|M|^2$ is independent of energy in the region of interest, the total current then is given by $I_+ - I_-$ integrated over all energies which reduces to

$$I(V) \approx |M|^2 \int_{-\infty}^{\infty} D_1(E-eV)D_2(E)[f(E-eV)-f(E)]dE. \tag{4.3}$$

There are three cases to be considered: (i) both electrodes normal metals or normal semiconductors, (ii) one electrode normal and one superconducting, and (iii) both superconducting (Josepfson effect). Remembering that the effect of the applied voltage is to slide the density-of-states of one electrode relative to that of the other and that the total energy of electrons is kept in constant during the tunneling process from a full state on one side of the barrier to an empty state on the other, one can predict the voltage dependence of the tunneling current.

When both electrodes are normal (Fig. 4.1), Eq. (4.3) becomes

$$I \approx D_{n1}D_{n2} \int_{-\infty}^{\infty} f(E-eV)f(E)dE. \tag{4.4}$$

For $T = 0$, one can easily deduce graphically that Eq. (4.4) gives $I \propto V$, that is,

ohmic behavior. Eq. (4.4) can also be evaluated analytically for $T = 0$ if V is not too large, and the current is proportional to the applied voltage, as formulated by Simmons [4.11]. Using the diagrams in Fig. 4.1, one can see that increasing the bias voltage simply increases the number of full states facing empty states across the insulator, giving a linear increase in current with voltage.

When one electrode is normal metal such as Au which has a simple density-of-states and the other is GaMnAs which is expected to have a density-of-states around Fermi level, the importance of this experimental configuration can be appreciated by taking the derivative of I with respect to V in Eq. (4.4). The result can be written in the form

$$\frac{dI}{dV}(V) \sim D_n \int_{-\infty}^{\infty} D_{GaMnAs}(E) K(E - eV) dE. \tag{4.5}$$

Thus, dI/dV is the convolution of the GaMnAs density-of-states $D_{GaMnAs}(E)$ and $K(E\text{-}eV)$, the derivative the Fermi function $f(E\text{-}eV)$ with respect to V,

$$K = \frac{\beta \exp\left[\beta(E - eV)\right]}{\left\{1 + \exp\left(\beta(E - eV)\right)\right\}^2}. \tag{4.6}$$

Here $\beta = 1/kT$. The function K peaks at $E = eV$ and approaches a δ-function as the temperature $T \rightarrow 0$. Thus, in the limit of low temperature, the conductance approaches $D_{GaMnAs}(E)$ and a measurement of tunneling conductance closely reflects the density-of-states of the GaMnAs near the Fermi energy.

$$\frac{dI}{dV}(V) \sim D_{GaMnAs}(E). \tag{4.7}$$

4.2. Tunneling spectroscopy of GaMnAs [4.12]

In order to study the electronic structure of GaMnAs, we have performed tunneling spectroscopy of GaMnAs with normal metal (Au) counterelectrode. The sample structure is Au (1000 Å) / Al_2O_3 (80 Å) / $Ga_{1-x}Mn_xAs$ (2000 Å), with Mn concentration $x = 0.031$. Notice that this GaMnAs thin film in this sample is not in metallic region. The bottom electrode (GaMnAs) was grown by MBE on p-GaAs (001) substrate. By using an electrode beam evaporator, the Al_2O_3 barrier and the top Au electrode were successively deposited on the GaMnAs surface, monitoring the thickness in situ during the deposition.

Good quality of the tunnel junction was confirmed by current-voltage and

conductance (dI/dV) measurements at 77K. At low bias, the current was proportional to the applied voltage, as formulated Simmons [4.11]. Vertical transport (current perpendicular to the plane, CPP) and its magnetic field dependence were made using a standard Lock-in technique at 43.2Hz with the excitation voltage 10μV employing a current amplifier. On the other hand, the tunneling spectroscopy was carried out by monitoring the net electric current through the junction area with respective to the applied DC bias voltage. All the measurements are done in an electromagnetically shielded room and several eletromagnetically compatible filters were used in the signal. Fig. 4.2 shows dI/dV curves of this sample at 4.2K and 0.2K. There is a dip at zero-bias, and it becomes sharp at lower temperature. This indicates that the electrode material, GaMnAs, has a small energy gap around the Fermi energy, like the doped semiconductors [4.13.14].

4.3. Impurity band model in doped semiconductors

Efros and Shklovskii (E-S) introduced a simple and well-known model of the long-range Hartree interaction between single-particle excitations in a localized insulator (variable-range hopping: VRH) [4.15]. Here we will review the E-S model. At low impurity concentrations we can ignore the quantum effects and allow only for the electrostatic interaction between the charged centers. We can minimize the total energy at Fermi energy with respect to an addition of one electron to the system or an extraction of one. The number of electrons n_i at site i is expressed as

$$\begin{aligned} n_i &= 1 \ \text{if} \ E_i < \mu \\ &= 0 \ \text{if} \ E_i > \mu \end{aligned}, \tag{4.8}$$

where E_i and μ stand for the energy at site i and the chemical potential of the system, respectively. Eq. (4.8) means that the Fermi level exists separating occupied and empty states. Now we consider the other conditions which restrict the single-particle density-of-states $D(E)$. Suppose that in the ground state site i is occupied by an electron while site j is empty (see Fig. 4.3). The change of total energy upon moving the electron from site i to site j is

$$\Omega_i^j = E_j - E_i - \frac{e^2}{\varepsilon r_{ij}}, \tag{4.9}$$

wher ε and r_{ij} stand for the dielectric constant and the distance between site i and site j. The last term is due to electron-electron interaction. It can be easily

understood by dividing the process into two steps. At the first step the electron moves from site i to infinity. The change of the total energy is equal to $-E_i$. At the second step the electron moves from infinity to site j. The energy E_j is necessary provided that the system is in the ground state and site i is occupied. However it is empty, and the extra-attraction acts on the electron from the site i which leads to the last term in Eq. (4.9).

From the ground state of the system all the changes of the energy should be positive. So the inequality

$$E_j - E_i - \frac{e^2}{\varepsilon r_{ij}} \geq 0 \tag{4.10}$$

has to be valid for all occupied sites i and all empty sites j in the system. Efros and Shklovskii have shown that it leads to the essential depletion of the single-particle density-of-states in the vicinity of the Fermi level which they called "Coulomb gap" [4.16].

Let us consider the energy interval of the width E near the Fermi level (Fig. 4.3). In other words, consider all sites such that

$$E_j - E_i < E. \tag{4.11}$$

It follows from Eq. (4.11) that the distance between any two sites one occupied and the other empty cannot be smaller than $e^2/\varepsilon E$. Then the concentration $N(E)$ of the sites within the interval ε cannot exceed $\varepsilon^3 E^3/e^6$ while the density-of-states $D(E) = dN/dE$ cannot exceed $\varepsilon^3 E^2/3e^6$. It should be clear that a stronger depletion than E^2 is not self-consistent so that in three-dimensional case one has

$$D(E) = \frac{\alpha_3 (E-\mu)^2 \varepsilon^3}{e^6}, \tag{4.12}$$

where E is now a single-particle energy.

The same consideration shows that in two-dimensional case

$$D(E) = \frac{\alpha_2 |E-\mu| \varepsilon^2}{e^4}. \tag{4.13}$$

Here α_3 and α_2 are dimensionless constants. Eq. (4.12) and Eq. (4.13) describe the behavior of the density-of-states within the Coulomb gap region.

The Coulomb gap is due to the long-range interaction. Eq. (4.12) and Eq. (4.13) are valid only if $D(E) << D_0$, where D_0 is the density-of-states without interaction. So the Coulomb gap width Δ can be estimated from the relation $D(\Delta) = D_0$. It gives

$$\Delta = \frac{e^3 D_0^{\frac{1}{2}}}{\varepsilon^{\frac{3}{2}}} \quad for \ d=3 \qquad (4.14)$$
$$= \frac{e^4 D_0}{\varepsilon^2} \quad for \ d=2$$

where d is dimensionality of space and $D_0 = (1/2)Al^d$. Here the constant of A represents the distribution width of the energies ϕ_i at site i.

The Coulomb gap plays an important role in the low temperature DC conductivity. For the three-dimensional case the energy interval of width $E_M = T^{3/4}a^{3/4}D_0^{1/4}$ is responsible for the hopping conductivity, which obeys the Mott law (here a is the localization length). The influence of the gap can be neglected if $E_M >> \Delta$ i.e. $T >> T_c = e^4 a D_0/\varepsilon^2$, at such temperatures the Mott law is valid. If $T << T_c$ the states within the Coulomb gap are particularly important. Using Eq. (4.12) and by analogy with the Mott law derivation we obtain

$$\sigma(T) \propto \exp\left[-\left(\frac{T_0}{T}\right)^{\frac{1}{2}}\right] \qquad (4.15)$$

where $T_0 = e^2/\varepsilon a$. The same result is valid for the two-dimensional case [4.16].

Katsumoto et al. investigated temperature dependence of the DC conductance of $Ga_{1-x}Mn_xAs$ ($x = 0.07$) at low temperature and showed it followed the E-S theory [4.17]. These results are consistent with our finding of a small energy gap at the Fermi energy in GaMnAs by tunneling spectroscopy measurements (Fig. 4.2).

For three-dimensional (3D) systems at finite temperature and with energy disorder, analytical and numerical results yield a power law $D(E = E_F, T) \sim T^\alpha$, where the exponent α is 2 [4.18,19], 2.7 +/- 0.1 [4,20,21], and 1 [4.22], assuming structural disorder. Fig. 4.4 shows temperature dependence of the tunnel conductance of dI/dV ($\propto D(E = E_F, T)$) follows the power the law of $\alpha = 0.5$. This value is close to $\alpha = 0.7$ recently reported in n-type Ge systems [4.14].

We have considered the origin of the energy gap of GaMnAs in the insulating region. We showed tunneling spectroscopy was powerful tool to investigate the density-of-states of GaMnAs around Fermi energy and the transport properties at low temperature. These properties are strongly related to the ferromagnetism of GaMnAs. Therefore further experiments must be done. Unfortunately, the quality of Al_2O_3 barrier and Au electrode is not so good because it is not deposited under ultra high vacuum. In addition, both spin bands in GaMnAs are counted together in the tunneling conductance. In next section, more powerful technique of

spin-polarized tunneling spectroscopy with Al superconductor will be discussed.

4.4 Spin-polarized tunneling spectroscopy of conventional ferromagnets with Al superconductor [4.6]

As described above, when both metals are normal conductors, the current-voltage relation of the sandwich or tunneling junction is ohmic at low voltages, with the current directly proportional to the applied voltage. Giaever [4.4] discovered that if one of the metals in a tunnel junction becomes superconducting the current-voltage characteristic changes from the straight line to the curve. According to the BCS theory, two electrons with $k\uparrow$ and $-k\downarrow$ in a superconductor form a pair (Cooper pair) with an attractive interaction [4.23]. It can lead to a ground state in which the density-of-states has a energy gap in the excitation spectrum of Δ on each side of the Fermi level and characteristic singularities in $D_s(E)$ for $E = +/-\Delta$. The BCS- density-of-states for the superconductor has the form

$$\begin{aligned} D_s(E) &= \frac{D_n(E)E}{\sqrt{E^2-\Delta^2}} \quad |E| \geq \Delta \\ &= 0 \qquad\qquad |E| \leq \Delta \end{aligned}, \tag{4.16}$$

where D_n is the density-of-states of the metal in the normal state. For simplicity, the density-of-states of the normal state is assumed to be independent of energy and can be removed from the integral in Eq. (4.3). In this case, Eq. (4.3) becomes

$$I \sim D_n \int_{-\infty}^{\infty} D_s[f(E+eV)-f(E)]dE. \tag{4.17}$$

The gap $E_g = 2\Delta$ corresponds to the break-up energy of a pair of electrons in the superconducting state, with the formation of two electrons, or an electron and a hole, in the normal state. Little current flow when $|eV| < \Delta$ because there are only a few thermally filled states in one electrode facing a similar number of empty states in the other (Fig. 4.5). When eV exceeds the gap energy, the current rapidly increases. At higher voltage, the current again approaches a linear dependence on V. Differential tunneling conductance is also important here (see Eq. (4.5)).

$$\frac{dI}{dV}(V) \sim \int_{-\infty}^{\infty} D_s(E)K(E+eV)dE. \tag{4.18}$$

At low temperature, the conductance approaches $D_s(E)$ and a measurement of

tunneling conductance closely reflects the density-of-states of the superconductor.

After the discovery of spin splitting of the quasiparticle states in superconducting Al, it was apparent that using Al with a ferromagnetic counterelectrode should lead to interesting results [4.6]. Cooper pair has opposite momentum and opposite spin ($k\uparrow$, $-k\downarrow$). Therefore cooper pair in a magnetic field is expected to have interesting properties. Yoshida showed that the spin susceptibility χ_s of superconducting electrons should approach zero exponentially as T approaches zero [4.24], which means that the Knight shift should vanish well below T_c. However, Reif showed the Knight shift for mercury did not go to zero as T approached zero [4.25]. Ferrell [4.26] and Anderson [4.27] suggested that the spin-orbit interaction mixed the spin states and that the pairing was between time-reversed states of a more general kind. This theory was further developed by Abrikosov and Gorkov [4.28]. The combined effect of a magnetic field on electron orbital motion and electron spins in the present of spin-orbit scattering was worked out by Maki [4.29]. Considering all described above, Al is one of the best candidates for elucidating the spin properties of high-field superconductors because spin-orbit scattering which destroys cooper pair ($k\uparrow$, $-k\downarrow$) is small in it. Indeed Hammond and Kelly [4.30] and later Fined et al. [4.31] observed in Al a substantial fraction of the Knight shift change predicted by Yoshida [4.24].

A superconductor prevents the penetration of a magnetic field into the body, producing a permanent eddy current screen. It is called the Meissner effect. The applied magnetic field increases the free energy of the superconductor. Therefore a sufficiently strong magnetic field will destroy Cooper pairs. The critical field H_c and the thermal properties are deduced from the BCS theory in a natural way. Al is one of type I superconductors. The values of H_c are always too low for type I superconductors to have any useful technical application in coils for superconductor magnets. The transition temperature T_c and critical field H_c of bulk Al are only 1.18 K and about 100 gauss, respectively. However, the confluence of several material properties makes Al unique in its suitability for this high-field study. An applied magnetic field will penetrate a thin film fairly uniformly if the thickness is much less than the penetration length λ. Thus in a thin film the Meissner effect is not complete. In a thin film the induced field is much less than the applied magnetic field and there is little effect of the field on the energy density of the superconducting state. It follows that the critical field H_c of thin films in parallel magnetic fields will be very high. Al films can be made as thin as 4nm with little difficulty, and the transition temperature of such thin films T_c becomes higher (2.5

K) [4.32,33]. For such thin films the critical field H_c increases by orders of magnitude to allow measurements in substantial magnetic fields, as shown in Fig. 4.6 [4.32,34]. In addition, the electrons in Al have long spin lifetimes [4.35], allowing the full range of spin effects to be studied.

Generally, in a tunneling conductance in a magnetic field, the orbital depairing parameter dominates and the measured conductance simply reflects a broadening of the density-of-states with increasing a magnetic field. In the case of a thin Al film with the magnetic field parallel to the film plane, the orbital response is largely suppressed. The effect of the spin interaction with the field, that is, Zeeman splitting of the density-of-states can then be observed. Meservey et al. first observed the energy splitting of the quaiparticle density-of-states [4.36,37]. Fig. 4.7 shows how the two peaked structure develops from the spin density-of-states [4.38]. The explanation of the results is that the paired quasiparticles must be in time-reversed states. Thus, when the field is applied, they keep their $k\uparrow$, $-k\downarrow$ pairing, but now the spin-up and spin-down members of the pair have difference energy, one being raised in energy by μH, and the other lowered by μH. The excited states remain separated from the paired state by Δ, so that in a tunneling measurement the peaks of the BCS- density-of-states appear at different voltage for quasiparticles of different spin. This Zeeman splitting of the spin states provided the basis for spin-polarized tunneling, since at an energy of $\Delta - \mu H$ the electrons in the tunnel current will be almost entirely of one spin direction and at $-\Delta + \mu H$ almost entirely of the opposite spin direction. To observe this splitting, it is required that the orbital depairing parameter α should be small in the direction of the applied field and that the spin lifetime of the quasiparticles should not be too short.

The main limitation of spin lifetime in systems not containing magnetic impurities is spin-orbit scattering. In the absence of spin-orbit scattering and orbital depairing, the measured conductance is the sum of that for each spin in the form of Eq. (4.18).

$$\frac{dI}{dV}(V) \propto \int_{-\infty}^{\infty} D_s(E+\mu H)K(E+eV)dE + \int_{-\infty}^{\infty} D_s(E-\mu H)K(E+eV)dE. \qquad (4.19)$$

Spin-polarized tunneling spectroscopy of ferromagnetic metals are analyzed by using essentially the same form as with a spin-split density-of-states as in Eq. (4.19) but in which the conductance is the sum of contributions by spin-up and spin-down electrons:

$$\frac{dI}{dV} = \sigma(V) \approx \int_{-\infty}^{\infty} aD_s(E+\mu H)\frac{\beta \exp[\beta(E+eV)]}{\{1+\exp[\beta(E+eV)]\}^2}dE + \int_{-\infty}^{\infty}(1-a)D_s(E-\mu H)\frac{\beta \exp[\beta(E+eV)]}{\{1+\exp[\beta(E+eV)]\}^2}dE. \quad (4.20)$$

Here $\beta = 1/kT$ and a is the fraction of the electrons whose magnetic moment is in the direction of the applied magnetic field. The spin polarization P is then defined as

$$P \equiv \frac{n\uparrow - n\downarrow}{n\uparrow + n\downarrow} = 2a - 1 \quad (4.21)$$

Here $n\uparrow$ and $n\downarrow$ are the number of electrons whose magnetic moments are parallel and antiparallel to the field, respectively. This analysis is based on two assumptions: (1) The density-of-states of the superconductor for each spin direction in a given magnetic field has the same functional form and is merely displaced in energy by +/- μH. This assumption neglects the effects of spin-orbit or spin-flip scattering in the superconductor, which is a good first approximation for pure Al films. (2) There are no spin-flip tunneling processes, which was shown to be true for Al films with Al_2O_3 barriers [4.37]. Fig. 4.8 depicts superconductor / ferromagnetic-metal tunneling [4.38].

4.5 Spin-polarized tunneling spectroscopy of GaMnAs with Al superconductor

Spin-polarized tunneling spectroscopy with Al superconductor counterelectrodes allows us to investigate the fine structure of density-of-states of GaMnAs around the Fermi energy and estimate the value of spin polarization P as well as its polarity. Here P means the spin polarization of electrons at Fermi energy which contribute to electron tunneling, not the total spin polarization of the ferromagnet. It would be an easy assumption that p-holes in the valence band of GaMnAs mainly contribute to tunneling conductance in GaMnAs based tunnel junctions. Therefore it would be possible to deduce the polarity of the p-d interaction of GaMnAs according to the polarity of spin polarization P. And this value is also important with respect to tunneling magnetoresistance (TMR) of GaMnAs based heterostructures, as described later.

To realize the tunneling spectroscopy measurements of GaMnAs, it is important to fabricate high quality Al / AlAs / GaMnAs tunnel junctions in ultra-high vacuum systems. Yao et. al. have successfully grown AlAs / Al / AlAs

epitaxial heterostructures grown on GaAs (001) substrates by using LT-MBE [4.39]. Similarly, it would be possible to produce an Al / AlAs / GaMnAs epitaxial tunnel junctions on *p*-type GaAs (001) substrates in ultra-high vacuum.

After the As back-ground pressure in the MBE chamber was completely cut off (< 1.0×10^{-9} torr), an Al thin film was deposited in-situ at room temperature on AlAs / GaMnAs heterostructures grown on *p*-type GaAs (001) by LT-MBE. Fig. 4.9 shows a RHEED pattern of a single crystal Al layer. The Al / AlAs heterostructures had the epitaxial relationship of (001)[100]Al (F.C.C.) // (001)[110]AlAs (Zincblende). Yao et al already pointed out in their paper that the interfaces were relatively smooth on an atomic scale and that the intrusion of As from AlAs layers to Al layers was not observed [4.39]. To confirm that the obtained Al film has the superconductor phase at low temperature, we measured temperature dependence of the in-plane resistance of the Al film. The sample structure of #B1253 is Al (338Å) / AlAs (30Å) / GaMnAs (2000Å) on a semi-insulating GaAs (001) substrate. Au electrode pads were deposited on the Al surface by using an evaporator without any chemical process. Fig. 4.10(a) shows resistance in ohms of the Al thin film versus temperature. At high temperature the resistance decreased with decreasing temperature. And then it almost saturated below 30K due to impurity scattering. Finally, it abruptly dropped down to zero ohm at 1.26 K, indicating that superconductivity occurred. The transition temperature T_c (=1.26 K) and critical field H_c (~1000 Oe) of the Al thin film (338Å) is slightly larger than those of bulk Al (T_c = 1.14 K and H_c ~ 105 Oe), as pointed out by Mersevey and Tedrow [4.32]. Chemical etching process does not give fatal damage to the sample although the process deteriorates the Al film quality to some extent.

There is still one more problem to implement the tunnel junctions. Al is extremely reactive and easily oxidized in the atmosphere. Because oxidation of Al thin film surface is really fatal at the two-terminal tunneling conductance measurements in our case, a cap layer which is hardly oxidized has to be deposited over the Al surface in a ultra-high vacuum chamber. Although Au is one of barely oxidized materials, a Au thin film is not suitable for this purpose because Cooper pairs are destroyed at the interface between Al layer and Au layer due to strong spin-orbit interaction in Au. We have looked for the most appropriate metallic materials which can be deposited in our MBE system. Vanadium (V) is one of the best candidates in this sense. Since the vapor pressure of V is quite low, a high temperature Knudsen cell is required for this purpose. We have already tried to grow Al / AlAs / GaMnAs heterostructures covered with a Vanadium cap layer.

A Vanadium cap layer was deposited on Al superconductor layers at room temperature in order to prevent oxidation of Al film surface. The cell temperature of V was 1700 °C, which approximately corresponds to the growth rate of 6 Å/min. The RHEED pattern gradually changed as a Vanadium layer was deposited and finally it looked like rings. This means that the obtained Vanadium films were amorphous. The sample structure of #B1252 is V (180Å) / Al (100Å) / AlAs (30Å) / GaMnAs (2000Å) on a semi-insulating GaAs (001) substrate. We measured temperature dependence of the in-plane resistance of #B1252 with Au electrode pads deposited without any chemical process. Fig. 4.11(a) shows resistance in ohms of the Al thin film covered with V cap layer versus absolute temperature and Fig. 4.11(b) shows field dependence of the resistance at 0.5 K. The resistance abruptly drops to zero ohm at the transition temperature and the Al films turns to be the superconducting state at low temperature. On the other hand, we could not find any evidence of the superconducting state of the V film, although V is also one of superconducting elements. The thinner Al films, the higher the transition temperature and the critical field are, as pointed out by Mersevey and Tedrow [4.32]. As shown in Fig. 4.10, the transition temperature and critical field of this Al thin film (100Å) are T_c (=1.42 K) and H_c (~1.1 T) of the Al thin film, respectively. Those properties of the Al superconductor are enough to perform spin-polarized tunneling spectroscopy of GaMnAs. Furthermore we can easily make a thinner Al superconducting film, which is expected to have the higher T_c and higher H_c and make it easy to carry out the experiments.

We had some attempts to process the V / Al / AlAs / GaMnAs heterostructure and do the spin-polarized tunneling spectroscopy measurements in CPP configuration. Unfortunately we could not obtain any results due to the high resistivity of the tunnel junction. Further investigations are underway.

4.5 Summary

- We have studied tunneling spectroscopy of GaMnAs with Au / Al_2O_3 / GaMnAs tunnel junction.
- GaMnAs was found to have a small energy gap around the Fermi energy, which is attributed to the soft Coulomb gap.
- A superconductor al thin films were deposited on Al / GaMnAs heterostructures in a ultra-high vacuum chamber.

Reference

[4.1] A. Tackeuchi, S. Muto, T. Inata, and T. Fujii, Appl. Phys. Lett. **56** (1990) 2213.

[4.2] T. Valet and A. Fert, Phys. Rev. **B48** (1993) 7099.

[4.3] S. Zhang, P. M. Levy, J. Appl. Phys. **69** (1991) 4786.

[4.4] I. Giaever, Phys. Rev. Lett. 5 (1960) 464.
L. Solymar, "*Superconducting Tunneling and Applications*" (Wiley, New York, 1972).

[4.5] R. Meservey, P. M. Tedrow, R. C. Bruno, Phys. Rev. **B11** (1975) 4224.

[4.6] R. Meservey and P. M. Tedrow, Phys. Rep. **238** (1994) 173.

[4.7] P. Fulde, Adv. Phys. **22** (1973) 667.

[4.8] E. L. Wolf, "*Principle of Tunneling Spectroscopy*" (Clarendon Press, Oxford, 1985).

[4.9] E. Burstein and S. Lundqvist (eds.), "*Tunneling Phenomena in Solids*" (Plenum Press, New York, 1969).

[4.10] C. B. Duke, "*Tunneling in Solids*", Solid State Physics (Suppl.) 10 (Academic Press, New York, 1969).

[4.11] J. G. Simmons, J. Appl. Phys. **34** (1963) 1793.

[4.12] T. Hayashi, H. Shimada, H. Shimizu, and M. Tanaka, J. Cryst. Growth **201/202** (1999) 689.

[4.13] M. Lee, J. G. Massey, Phys. Stat. Sol. B **205** (1998) 25.

[4.14] B. Sandow, K. Gloos, Yu. Naidyuk, R. Rentzsch, A. N. Ionov, Phys. Stat. Sol. B **205** (1998) 281.

[4.15] B. I. Shklovski, A. L. Efros, "*Electronic Properties of Doped Semiconductors*" (Springer, Berlin, 1984).

[4.16] A. L. Efros and B. I. Shklovski, J. Phys. C: Solid State Phys. **8** (1975) L49.

[4.17] S. Katsumoto, A. Oiwa, Y. Iye, H. Ohno, F. Matsukura, A. Shen, Y. Sugawara, Phys. Stat. Sol. B **205** (1998) 115.

[4.18] C. J. Muller, J. M. van Ruitenbeek, L. J. de Jongh, Physica C **191** (1992) 485.

[4.19] E. I. Levin, V. L. Nguen, B. I. Shklovskii, A. L. Efros, Sov. Phys. –J. Exper. Theor. Phys. **65** (1987) 842.

[4.20] T. Vojta, W. John, M. Schreiber, J. Phys.: Condensed Matter **5** (1993) 4989.

[4.21] M. Sarvestani, M. Schreiber, T. Vojta, Phys. Rev. **B52** (1995) R3820.

[4.22] E. R. Grannan, C. C. Yu, Phys. Rev. Lett. **71** (1993) 3335.

[4.23] J. Bardeen, L. N. Cooper and J. R. Schrieffer, Phys. Rev. **108** (1957) 1175.

[4.24] K. Yoshida, Phys. Rev. **110** (1958) 769.

[4.25] F. Reif, Phys. Rev. **106** (1957) 208.

[4.26] R. A. Ferrel, Phys. Rev. Lett. 3 (1959) 262.

[4.27] P. W. Anderson, Phys. Rev. Lett. 3 (1959) 325.

[4.28] A. A. Abrikosov and L. P. Gorkov, Zh. Eskp. Teor. Fiz. 42 (1962) 1088, Sov. Phys. JETP 15 (1962) 752.

[4.29] K. Maki, Progr. Theor. Phys. 32 (1964) 29.

[4.30] R. Hammond and G. M. Kelly, Phys. Rev. Lett. 18 (1967) 156.

[4.31] H. L. Fine, M. Lipsicas, and M. Strongin, Phys. Lett. A 29 (1969) 366.

[4.32] R. Meservey and P. M. Tedrow, J. Appl. Phys. 42 (1971) 51; P. M. Tedrow and R. Meservey, Phys. Re. B8 (1973) 5098.

[4.33] A. F. Mayada and M. Shatzkes, Phys. Rev. B1 (1970) 1382; O. A. E. Cherney and J. Shewchun, Can. J. Phys. 47 (1969) 1101.

[4.34] M. Strongin and O. F. Kammerer, Phys. Rev. Lett. 16 (1966) 456.

[4.35] R. Meservey and P. M. Tedrow, Phys. Rev. Lett. 41 (1978) 805.

[4.36] R. Meservey, P. M. Tedrow, and P. Fulde, Phys. Rev. Lett. 25 (1970) 1270.

[4.37] R. Meservey, P. M. Tedrow, and R. C. Bruno, Phys. Rev. B11 (1975) 4224.

[4.38] R. Meservey and P. M. Tedrow, Phys. Rev. B7 (1973) 318.

[4.39] T. Yao, H. Nakahara, H. Matuhata, and Y. Okada, J. Cryst. Growth 111 (1991) 221.

5. *Tunneling magnetoresistance (TMR) of GaMnAs based heterostructures*

One of the most interesting extended studies of the tunneling phenomena is the tunneling between two ferromagnetic metals separated by a thin insulating tunnel barrier [5.1]. A simple model proposed by Julliere assumes that the spin is conserved in the tunneling process and that the conductance of each spin direction is proportional to the densities of states of that spin in each electrode [5.2], as shown in Fig. 5.1. In this model one expects that the tunnel current will be larger when the magnetizations of the two metals are parallel than when they are antiparallel. Analyzing the results in much the same ways as with tunneling between a ferromagnet and a superconductor, the conductances in the parallel and antiparallel arrangements G_P and G_{AP} are then

$$G_P = a_1 a_2 + (1-a_1)(1-a_2), \tag{5.1}$$

$$G_{AP} = a_1(1-a_2) + (1-a_1)a_2, \tag{5.2}$$

where a_1 and a_2 are the fractions of majority spin electrons in the density of states of the two ferromagnets at Fermi energy. The fractional difference in conductivity was defined by Maekawa and Gafvert to be

$$\frac{\Delta G}{G} = 2P_1P_2, \tag{5.3}$$

where the polarizations of the two metals are $P_1 = 2a_1 - 1$ and $P_2 = 2a_2 - 1$. In general, the conductance of the magnetic tunnel junctions (MTJ) varies as the cosine of the angle between the magnetic moments of two ferromagnet layers. The relative orientation of the magnetic moments in the most basic MTJ structures is varied by utilizing ferromagnet layers with different magnetic coercivities. After the report of giant magnetoresistance in metallic multilayers, the MR ratio is usually expressed using the magnetoresistance at both parallel (R_p) and antiparallel (R_a) magnetization states. Further, the definition in most cases is that the relative change of resistance (ΔR) is divided by the resistance at the parallel state of magnetization. By taking into account these and discussions made by Julliere [5.2] and Maekawa and Gafvert [5.3], we can express the tunneling magnetoresistance

(TMR) ratio as following,

$$TMR = \frac{\Delta R}{R_p} = \frac{R_a - R_p}{R_p} = \frac{2P_1P_2}{1-P_1P_2}. \quad (5.4)$$

Spin-dependent tunneling magnetoresistance in ferromagnet / oxide / ferromagnet structures attracts much interest from the viewpoint of device application as well as fundamental physics [5.4-7]. However, the reliability of the oxide insulator and its interface quality are problematic. The insulating oxide material is mostly Al_2O_3 made by natural or plasma oxidization of a deposited Al thin film, in conventional MTJs. On the other hand, the feasibility of preparing GaAs based magnetic semiconductor heterostructure with abrupt interfaces will offer unique opportunities for studying the spin-dependent transport and interlayer exchange coupling (IEC) [5.4,8] in well controlled III-V systems. In this chapter, in order to investigate spin dependent transport in III-V based magnetic semiconductor heterostructures, we will discuss TMR effects in (GaMn)As / AlAs / (GaMn)As tunnel junctions grown by LT-MBE.

5.1. *TMR of GaMnAs / AlAs / GaMnAs tunnel junctions* [5.9]

Recently we have grown GaMnAs / AlAs / GaMnAs trilayer structures on *p*-Ga (001) substrates and semi-insulating GaAs (001) substrates by LT-MBE at the same time. Tunnel junctions of pillar shapes with 200μm diameter were processed by conventional lithography technique. The sample structure is depicted in Fig. 5.2(a). Fig. 5.2(b) shows a valence band profile along the direction perpendicular to the material interfaces. By current-voltage and conductance (dI/dV) measurements in CPP configuration at 77K, it was confirmed that the tunnel junction of GaMnAs (2000Å) / AlAs (30Å) / GaMnAs (2000Å) with Mn concentration x = 0.039 showed a ohimic behavior at low bias, which indicates the junction of good quality. On the other hand, small dip at zero bias in the $dI/dV - V$ characteristics appeared at low temperature (4.2K and 1.6K), as shown in Fig. 5.3. It can be attributed to the Coulomb gap in the GaMnAs electrodes, as described in section 4.2 and 4.3.

We performed tunneling magnetoresistance (TMR) measurements on the sample under a magnetic field parallel to the plane. Fig. 5.4 shows field dependence of the tunnel resistance at 4.2K. Large negative magnetoresistance was observed with small hysteresis at low field. The TMR ratio ($= \left(R_{ap} - R_p\right)/R_p$)

was estimated to be 44.4%. In the *M-H* curve, there is no evidence that the GaMnAs layers has different coercive forces or interlayer exchange coupling, which lead to the anti-parallel configuration of magnetization of them. The resistivity of these GaMnAs thin films is 2.4 x 10^{-2} Ωcm at 4.2K. Since the GaMnAs layers are so thin the resistance of GaMnAs adds up to 3.0 x 10^{-3} Ω, which is much smaller than the total tunneling resistance. Therefore the observed TMR comes from the epitaxial tunnel junction because their magnetoresistance effect hardly contributes to the total tunneling resistance. TMR is generally very sensitive to the interface magnetization of a tunnel junction. In our case, the interface coercive force of the top and bottom GaMnAs layers should be slightly different because the interface quality is different due to the growth sequence. Therefore this large TMR ratio is probably due to the magnetic valve effect. There is another possible reason. Anderson localization was broken by applying a magnetic filed because time inverse symmetry is broken. GaMnAs is a heavily doped semiconductor with local moments at impurity sites. As an external field aligns the local moments, the electric potential energy reduces and tunneling resistance of GaMnAs / AlAs /GaMnAs tunnel junction decreases.

5.2. *TMR of GaMnAs / AlAs double barrier resonant tunneling diodes* [5.10]

Now we will extend our study to tunneling phenomena through multiple potential barriers. Semiconductor band engineering has led us to various intriguing transport properties since one-dimensional superlattices, having a period shorter than the electron mean free path, were proposed by L. Esaki and R. Tsu [5.11,12]. Especially, the phenomenon of resonant tunneling of electrons through double potential barriers manifested itself as negative differential resistance (NDR) [5.13]. Phase coherence of the tunneling carrier is maintained in resonant tunneling, while the phenomenon that phase coherence is lost through the multitude of scattering processes, is known as sequential tunneling. Resonant tunneling is analogue of Fabry-Perot interference encountered in optics. The first observation of resonant tunneling was done by Chang, Esaki, and Tsu, in 1974, on heterostructures grown by molecular beam epitaxy [5.13]. Their *I-V* characteristics showed peaks at voltages near the quasibound states of the potential well, although the current did not decrease to values near zero. It has provided one of the first evidence of the formation of QW states in ultrathin semiconductor films. Since then, the quality of epitaxial layers made by MBE (and more recently also by

metalorganic chemical vapor deposition) has improved dramatically. It is the intrinsic negative differential resistance (NDR) associated with resonant tunneling that has drawn interest for this kind of heterostructures as possible high-frequency devices.

In general, the TMR ratio strongly depends on the spin polarization of the magnetic electrodes at Fermi energy. Therefore, introducing a magnetic quantum well (QW) is predicted to enhance the TMR effect because each wave number normal to the interface is quantized separately depending on the spin direction of electrons (Fig. 5.5). In this section, we introduce a spin-dependent band engineering approach and propose a new type of MTJs using a magnetic QW.

As a first step towards new type of TMR using QW states, we consider a double barrier magnetic resonant tunneling diode (RTD) structures. For the device application of the TMR effect, the high resistivity of the conventional MTJ is unattractive in terms of response time and noise, which gives the limitation of the downsizing of the device. Although the higher bias voltage allows us to obtain the larger signals, the TMR ratio of the conventional MTJ shows a significant decrease with increasing the bias voltage. On the other hand, in a magnetic RTD, the best driving voltage can be designed by choosing the adequate thickness of the magnetic QW because a large TMR effect is expected at the resonant bias voltage. Hence, by properly designing the magnetic RTD device, a large TMR effect and the large signals will be realized at the same time.

We have calculated transmission probability of a double barrier RTD structure with transfer matrix method: GaMnAs (300Å) / AlAs (14Å) / GaMnAs (50Å) / AlAs (14Å) / GaMnAs (300Å). A valence band profile along the direction perpendicular to the material interfaces is depicted in Fig. 5.6.

In the calculation, several assumptions of GaMnAs are introduced as following way.

Assumptions

- the band parameters of GaMnAs are same as those of GaAs because MCD measurements [5.14] and angle-resolved photoemision measurements [5.15] have revealed that the band structure of GaMnAs is of zincblende semiconductor type and is very similar to that of GaAs.
- the Fermi energy of GaMnAs is 0.1 eV which corresponds to the hole density of about 3×10^{19} cm^{-3}.
- split energy is $\Delta E = 44$ meV estimated by Ohno et al. [5.16] from tunneling

spectroscopy measurements.

- the magnetization directions of both electrodes (GaMnAs 300Å) are parallel to one other, and only the magnetization direction of the magnetic QW (GaMnAs 50Å) is changeable relative to the magnetization directions of the electrodes. In fact, one can easily realize the anti-parallel configuration because the coercive force of thin GaMnAs films is larger than that of thick GaMnAs films.

In addition, the abrupt change in quantization axis at $z = z_1$ and z_3 requires the spinor transformation

$$\begin{aligned}\psi_{i\uparrow} &= \psi'_{i+1\uparrow}\cos\left(\frac{\theta}{2}\right) + \psi'_{i+1\downarrow}\sin\left(\frac{\theta}{2}\right)\\ \psi_{i\downarrow} &= -\psi'_{i+1\uparrow}\sin\left(\frac{\theta}{2}\right) + \psi'_{i+1\downarrow}\cos\left(\frac{\theta}{2}\right)\end{aligned}, \tag{5.5}$$

and similarly for the derivatives.

Fig. 5.7(a) and (b) shows the energy dependence of transmission probability ($TT^*(E_z)$) from one majority spin band to the other majority spin band in such magnetic resonant tunneling structures. Fig. 5.7(a) and (b) correspond to heavy holes ($m_{hh} = 0.45m_0$) and light holes ($m_{lh} = 0.08m_0$), respectively. The peak energies shift in both cases, depending on the magnetization direction of the magnetic QW. This fact indicates that a magnetic QW works as a very sharp spin filter as well as an energy filter, leading to the enhancement and unique bias dependence of TMR.

We also calculated *J-V* characteristics of the RTD by following Esaki's formula,

$$\begin{aligned}J_{\pm} &= \left(J_{L\to R} - J_{R\to L}\right)\\ &= \int_{\mp\frac{\Delta}{2}}^{\infty} dE_z TT^*(E_z)S(E_z)\end{aligned} \tag{5.6}$$

where $S(E_z)$ is called as supply function. Fig. 5.8 shows the calculated *J-V* characteristics for the magnetic RTD structure, where only heavy holes are taken into account for simplicity. Some intriguing features are predicted. One is that large negative magnetoresistance effects are expected around zero bias and 0.25eV. It is much larger than the MR ratio estimated from the Julliere's model. Positive magnetoresistance effects are also expected around 0.2eV and 0.5eV. Although this is a very simple calculation, it suggest that the RTD structure of GaMnAs / AlAs heterostructure systems gives new degree of freedom in designing TMR devices. Next, we show our experimental results on two samples of RTD based on GaMnAs / AlAs heterostructures

(i) B1011: GaMnAs (300Å, Mn concentration $x = 0.04$) / AlAs (14Å) / GaMnAs (50Å, $x = 0.04$) / AlAs (14Å) / GaMnAs (300Å, $x = 0.04$)

We grew the same magnetic RTD structure as described in the theoretical model, on *p*-type GaAs (001) and on semi-insulating GaAs (001) substrates by using LT-MBE: GaMnAs (300Å, Mn concentration $x = 0.04$) / AlAs (14Å) / GaMnAs (50Å, $x = 0.04$) / AlAs (14Å) / GaMnAs (300Å, $x = 0.04$) magnetic RTD sample. Two-terminal RTD devices, with active areas of 20μm diameter circles, were fabricated on the *p*-type substrate, and Hall bars on the semi-insulating substrate using photolithographic techniques. Their *I-V* and *dI/dV* characteristics and TMR were measured at 4.2K in CPP (current perpendicular to the plane) configuration, applying an in-plane magnetic field generated by a superconducting magnet. At the same time, we also performed magnetotransport measurements on the Hall bar of the same sample in CIP (current in-plane) configuration, applying an in-plane magnetic field.

Fig. 5.9(a) shows field dependence of magnetization of this sample at 2.0K. The magnetization reverses with two steps at low magnetic field. Fig. 5.9(b) shows magnetic field dependence of tunneling resistance measured at nearly zero bias at 4.2K by using the conventional lock-in technique. The modulation amplitude is 1mV (42Hz). As shown in Fig.5.9(b), the tunneling resistance increases at about 180 Oe and decreases at about 800 Oe on the negative magnetoresistance background. This is probably because that the magnetization of both GaMnAs electrodes sharply reverses at about 180 Oe and then the magnetization of GaMnAs quantum well gradually reverses. This fact indicates that the coercive force of a GaMnAs film is controllable depending on the thickness.

(ii) B1114: GaMnAs (2000 Å, Mn concentration $x = 0.045$) / AlAs (28 Å) / GaMnAs (80 Å, $x = 0.035$) / AlAs (28 Å) / GaMnAs (2000 Å, $x = 0.045$)

We grew another magnetic RTD structure as described in the theoretical model, on p-type GaAs (001) and on semi-insulating GaAs (001) substrates by using LT-MBE: GaMnAs (2000 Å, Mn concentration $x = 0.045$) / AlAs (28 Å) / GaMnAs (80 Å, $x = 0.035$) / AlAs (28 Å) / GaMnAs (2000 Å, $x = 0.045$).

The magnetization curve has a unique structure (Fig. 5.10). There are clear steps in the hysteresis loop at low field. In general, step structures in a hysteresis

loop of a magnetic multilayer indicate two possibilities. One is that those magnetic layers have different coercive force from one another. The other possibility is that those magnetic layers are magnetically connected with neighbor layers. This is called as interlayer exchange coupling (IEC). One can distinguish between the two by measuring the minor loop of magnetization curve. Fig. 5.10 also shows the minor loops of this sample at 4.2K. Clear two minor loops were observed without shifting in the horizontal direction, indicating that the magnetic layers of this sample has no magnetic coupling. In other words, the coercive force of upper GaMnAs electrode layer (Layer I) is different from that of bottom GaMnAs electrode layer (Layer III). Here, the magnetization of middle GaMnAs quantum well layer (Layer II) is negligible compared with two other layers because Layer II (80 Å) is much thinner than the others (2000 Å). Layer I and III show different coercive forces due to the growth sequence, although they were grown under a same condition.

Fig. 5.11 shows magnetic field dependence of tunneling resistance measured at nearly zero bias at 4.2K by using conventional lock-in technique. The modulation amplitude is 1mV (42Hz). Very large negative tunneling magnetoresistance (TMR) was observed up to high field. The TMR ratio, defined by $(R_{max} - R_{min}) / R_{min}$, is about 170%, which is much higher than the CIP-MR ratio (about 10%) of the same sample (see Fig. 5.12), where R_{min} is the resistance at 11.1kOe. Note here that the resistance of GaMnAs electrodes is much smaller than the total tunneling resistance, therefore, the magnetoresistance effect of the GaMnAs electrodes hardly contributes to the observed TMR effect. A clear hysteresis behavior appeared at low field, as shown in the inset of Fig. 5.11, which is caused by the different magnetization configuration of the ferromagnetic GaMnAs, that is, the spin valve (magnetic valve) effect.

Although the magnetization of these three GaMnAs layers is almost saturated at 500 ~ 1000 Oe, negative TMR continued to be observed up to higher field. The TMR effect at high field is much larger than that at low field. This situation is similar to the CIP-MR of GaMnAs single layers and the TMR of simple GaMnAs / AlAs / GaMnAs single barrier (SB) tunnel junctions. However, as shown in Fig. 5.13, it is worth while noting that magnetic field dependence of tunneling conductance of the present RTD sample behaves in a slightly different way from that of its CIP-conductance, also from that of tunneling conductance of the SB tunnel junctions. It is rather similar to the CIP-conductance of GaMnAs / AlAs SLs. Tunneling conductance at nearly zero bias in the present double barrier system is

almost perfectly proportional to the applied magnetic field in the range of 0.5 ~ 11 kOe. The proportional coefficient is 0.33 μS/T. On the other hand, its CIP-conductance and the tunneling conductance of the SB tunnel junctions have non-linearity and show a saturation behavior with increasing the applied magnetic field.

The present TMR behavior observed in the GaMnAs based heterostructures can be explained in the following way. The ferromagnetic ordering between Mn spins in GaMnAs is induced by itinerate holes through *p-d* exchange interaction. That is to say, itinerate holes drag magnetic clouds of Mn spins along with them. Therefore, with a magnetic field larger, in case of tunneling process, the penetrating length of hole wavefunctions into the tunnel barriers becomes larger due to the restoration of the kinetic energy of conducting holes. In other words, transmission probability becomes exponentially larger with increasing the magnetic field, leading to the giant negative TMR up to high field (Fig. 5.14).

Fig. 5.15 (a) and (b) show the *I-V* and *dI/dV-V* characteristics at 4.2K. Negative differential conductance was not observed in the *I-V* characteristic although the shape of the derivative *dI/dV-V* looked like wavy. In order to make the wavy character clear, its d^2I/d^2V-*V* curves at 4.2K at two different magnetic fields (22 kOe and 122 Oe) are presented in Fig. 5.15(c). At high field (22 kOe), where the magnetization directions of all three GaMnAs layers are aligned parallel to the applied magnetic field direction, a large peak appeared at about 0.5V and a few tiny shoulders at smaller bias voltages (25mV and 250mV). On the other hand, at low field (122Oe), which corresponds to the magnetic field for the peak tunneling resistance, a new peak appeared at around 1.35V while the whole spectrum shifted toward higher voltage and became a little smaller. Apparently, this spectrum shift accounts for the observed very large TMR effect.

The resonant tunneling of holes in high quality non-magnetic AlAs-GaAs-AlAs heterostructures was reported by Mendez et al [5.17]. Although one should expect to see peaks associated with GaAs heavy and light hole virtual bound states, the experimentally observed peaks in the current-voltage characteristics did not fit these predictions, reflecting the complicated valence-band states. For the same reason, the quantitative discrepancy between the calculation and the experiment in our system is probably very large. In addition, some irreducible depletion layers, which prohibit net bias voltage from being applied over the AlAs double barriers, can exist in this two-terminal device, making the resonant tunneling voltage higher. Considering all described above, the new additional peak at ~1.35V measured at 122

Oe in Fig. 5.15(c) probably indicates a sign of spin-dependent resonant tunneling of holes through the subbbands in the magnetic quantum well.

Clear negative differential resistance (NDR) would enhance the TMR effect much more. Some experimental factors may make it difficult to obtain NDR in our sample. One reason is phase and spin decoherence of the tunneling hole due to impurity scattering (especially, Mn magnetic impurities in the AlAs barriers) and interface roughness because the present double barrier heterostructure contains GaMnAs which is a very heavily doped semiconductor and needs to be grown at low temperature. Another possible reason is that the Fermi energy of GaMnAs is extremely high (E_F= ~100meV or more when the hole concentration of GaMnAs is 10^{19} ~ 10^{20}cm^{-3}) and therefore tunneling process through several quantum energy levels occurs at the same time. Despite these detrimental factors, in such epitaxial magnetic heterostructures, one can design a suitable structure by some structural parameters such as barrier thickness, well width and Mn concentration of GaMnAs layers. Introducing of a double quantum well system is probably one of the possible solutions.

5.3. TMR of GaMnAs / AlAs double well resonant tunneling diodes

In a double quantum well (DQW) system, tunneling current flows perpendicularly between two parallel 2D electron system separated by a barrier. In the ideal case (i.e., there is no disorder, no electron-electron interactions, etc.) where the in-plane momentum of electrons are conserved in the tunneling process, electrons can tunnel only if the quantized energy levels in the two wells precisely correspond to one another. This implies that the current-voltage characteristics of an ideal 2D-2D tunnel junction are singular; the tunneling conductance should be zero everywhere except at those discrete voltages which produce alignment of the proper energy levels. In a magnetic double quantum well structure, tunneling from one magnetic quantum well to the other should strongly depend on the alignment of magnetization direction in the magnetic wells (Fig. 5.16). In case of the parallel configuration, electrons are able to transport through a barrier at zero bias because these wells have the corresponding energy levels each other. When spin flip does not occur during the tunneling process, electrons can transmit through a barrier in case of parallel configuration, although electron cannot flow in case of antiparallel configuration. Fig. 5.17 shows spin-dependent energy dispersion in two-dimensional system, where the solid curve and dotted curve denote up-spin and

down-spin dispersions, respectively. The right/ left corns of the dispersion of electrons with the same spin direction do not have any crossing points. Therefore when the phase coherence of tunneling carriers is maintained without any scattering, no electron can transmit at zero bias in case of antiparallel configuration. We predict that it is possible to obtain large tunneling magnetoresistance effects with magnetic double quantum well structures.

We grew a magnetic double quantum well sample whose structure is GaMnAs (2000 Å, Mn concentration $x = 0.043$) / AlAs (28 Å) / GaMnAs (80 Å, $x = 0.043$) / AlAs (28 Å) / GaMnAs (80 Å, $x = 0.043$) / AlAs (28 Å) / GaMnAs (2000 Å, $x = 0.043$) on *p*-type GaAs (001) and on semi-insulating GaAs (001) substrates by using LT-MBE. The sample structure is depicted in Fig. 5.18. We performed CIP-MR measurements of it at 4.2K. Fig. 5.19 (a) and (b) show the total view and up-close of the CIP-MR. Some distinctive fine structures which have not been observed in the CIP-MR of GaMnAs single layers were seen at low magnetic field. Corresponding to them, some structures were observed in magnetic field dependence of tunneling magnetoresistance measured at nearly zero bias at 4.2K, as shown in Fig. 5.20 (a) and (b). They probably indicate the Barkhausen effect [5.18,19] corresponding to sudden propagation of domain walls, the idea of which has been applied to InMnAs [5.20] by Oiwa recently. However it remains unclear in detail.

5.4. Future works

5.4.1 spin valve transistor

In the previous sections, spin dependent tunneling of GaMnAs-based conventional MTJs and magnetic RTDs has been described. In those cases, electrons with around Fermi energy mainly contribute to the electron tunneling so that the transmission probability at low bias voltage definitely reflects the density-of-states in both magnetic electrodes. On the other hands, Monsma et al. demonstrated the perpendicular hot electron effects in the spin valve transistor structure which constitutes of three regions: a pin-valve base, a hot electron injector such as a Schottly barrier or a tunneling barrier and a collector barrier which discriminates between scattered and ballistic electrons [5.21]. They observed a very large MR effect (215% at 77K) in collector current under application of a magnetic field of 500 Oe. This large MR effect principally comes from the difference of the mean free paths (or the spin dependent scattering process) between

spin-up and spin-down hot electrons. The mean free paths of spin-up and spin-down electrons exponentially affect their transmission probabilities through each layer and interface which is proportional to the collector current when the leakage current is neglected. In addition, because the spin valve transistor is three-terminal device, semiconductor MOS transistors to diminish the active cell are not needed for the magnetic random access memory (MRAM) application. Unfortunately, the collector current is very small compared to the base current. The common-base current gain α_0 (= J_C/J_E: J_C and J_E stand for the collector current and the emitter current, respectively) is 10^6 at the coercive force. That is, most of the injected hot electrons are drained in the base. This is because the electrons with the energy less than the collector barrier height are also injected and can not transmit to the collector over the collector barrier.

An energy filter implemented in the barrier between the emitter and the base will improve the current gain. Yokoyama et al. proposed resonant tunneling hot electron transistor (RHET) which a quantum well structure in the emitter-base junction and demonstrated a high gain of 5.1 with the transistor [5.22]. However it is difficult to apply this technique for the metallic spin valve transistor.

It is possible to grow GaMnAs-based heterostructures with abrupt interfaces, as discussed in the previous chapters. Here we propose a GaMnAs-based spin valve transistor. The sample structure is [GaMnAs: emitter] / [AlAs / GaAs / AlAs: quantum well] / [InGaMnAs: base] / [AlGaAs: collector barrier] / [GaMnAs (or p-GaAs): collector]. The MCD spectra of GaMnAs (Fig. 2.10) show the difference between the absorption coefficients for σ^+ and σ^- polarized lights is maximum around 1.85 eV. The hot electrons are expected to be strongly suffered from spin dependent scatterings during the traveling in the base region and cause large MR effects.

5.4.2 magnetic field induced superlattice subbands

As described in the previous sections, itinerate holes drag magnetic clouds of Mn spins along with them and a magnetic field breaks down Mott-Hubbard localization in GaMnAs. At the same time, a magnetic field hinders the quantum interference of wavefunctions which causes Anderson localization. Therefore, with a magnetic field larger, in case of tunneling process, the penetrating length of hole wavefunctions into the tunnel barriers becomes larger due to the restoration of the kinetic energy of conducting holes in GaMnAs layers. This viewpoint gives a new

interpretation on GaMnAs / AlAs superlattices. In GaMnAs / AlAs multilayer systems, it is possible to transform from multi quantum wells which are not coupled each other with adequate barrier thickness to superlattices with subbands by applying a magnetic field.

5.5 Summary

- Large TMR was observed in a GaMnAs / AlAs / GaMnAs tunnel junction.
- The usefulness of magnetic quantum wells in terms of TMR effect was proposed.
- Transmission probability of a magnetic resonant tunneling diode structure was calculated, indicating spin-filter together with energy filter functions.
- Very large TMR effect was observed in a GaMnAs / AlAs double barrier system grown by LT-MBE, mainly due to the enhanced penetration of the hole wavefunctions into the barriers at high magnetic field.
- Some features in the magnetic field induced change in the d^2I/d^2V-V characteristic were attributed to the spin-dependent resonant tunneling.
- TMR effect was observed in a GaMnAs / AlAs double quantum well structure.

References

[5.1] R. Meservey and P. M. Tedrow, Phys. Rep. 238 (1994) 173.

[5.2] M. Julliere, Phys. Lett. 54A (1975) 225.

[5.3] S. Maekawa and U. Gafvert, IEEE Trans. Magn. 18 (1982) 707.

[5.4] J. C. Slonczewski, Phys. Rev. B39 (1989) 6995.

[5.5] T. Miyazaki and N. Tezuka, J. Magn. Magn. Mater. 139 (1995) L231.

[5.6] J. S. Moodera, L. R. Kinder, T. M. Wong, and R. Meservery, Phys. Rev. Lett. 74 (1995) 3273.

[5.7] S. S. P. Parkin, R. E. Fontana, and A. C. Marley, J. Appl. Phys. 81 (1997) 5521.

[5.8] P. Bruno, Phys. Rev. B52 (1995) 411.

[5.9] T. Hayashi, H. Shimada, H. Shimizu, and M. Tanaka, J. Cryst. Growth 201/202 (1999) 689.

[5.10] T. Hayashi, M. Tanaka, and A. Asamitsu, to be published in JAP.

[5.11] L. Esaki and R. Tsu, IBM J. Res. Dev. 14 (1970) 61.

[5.12] R. Tsu and L. Esaki, Appl. Phys. Lett. 22 (1973) 562.

[5.13] L. L. Chang, L. Esaki, and R. Tsu, Appl. Phys. Lett. 24 (1974) 593.

[5.14] K. Ando, T. Hayashi, M. Tanaka, and A. Twardowski, J. Appl. Phys. 83 (1998) 6548.

[5.15] J. Okabayashi, A. Kimura, O. Rader, T. Mizokawa, T. Nambu, A. Fujimori, T. Hayashi, and M. Tanaka, proceeding of the 5th Symposium on the Physics and Application of Spin-Related Phenomena in Semiconductors, Grant-in-Aids for Scientific Research from the Ministry of Education , Science, Sports and Culture, Japan, Dec. 16-17, 1999, p.158.

[5.16] H. Ohno, N. Akiba, F. matsukura, A. Shen, K. Ohtani, and Y. Ohno, Appl. Phys. Lett. 73 (1998) 363.

[5.17] E. E. Mendez, W. I. Wang, B. Ricco, and L. Esaki, Appl. Phys. Lett. 47 (1985) 415.

[5.18] H. Barkhausen, Z. Phys. 20 (1919) 401.

[5.19] S. Zapperi, P. Cizeau, G. Durin, and H. E. Stanley, Phys. Rev. B58 (1998) 6353.

[5.20] A. Oiwa, Y. Hashimoto, S. Katsumoto, Y. Iye, and H. Munekata, in Proceedings of the 6th International Symposium on the Foundation of Quantum Mechanics in the Light of New Technology (1998), to be published.

[5.21] D. J. Monsma, J. C. Lodder, Th. J. A. Popma, and B. Dieny, Phys. Rev. Lett. 74 (1995) 5260.

[5.22] N. Yokoyama, K. Imamura, S. Muto, S. Hiyamizu, and H. Nishi, Jpn. J. Appl. Phys. 24 (1985) L853: T. Mori, H. Ohnishi, K. Imamura, S. Muto, and N. Yokoyama, Appl. Phys. Lett. 49 (1986) 1779.

6. *Concluding remarks*

This thesis is constituted of two main parts. The former one (chapter 2) is devoted to the properties of GaMnAs single layers. The latter one (chapter 3 ~ 5) is described about GaMnAs based magnetic semiconductor heterostructures. They are strongly correlated with each other in the following way.

Diluted magnetic semiconductors (DMSs) are one of the best candidates to combine electronics and magnetism as discussed in chapter 1. Especially III-V based DMSs have been studied energetically because one can see the magnetic properties through magnetotransport measurements. The studies of GaMnAs have attracted much interest as a new class of III-V based DMSs with respect to device applications as well as solid state physics, because GaMnAs is based on the most widely used III-V compound semiconductor GaAs and the fundamental properties of GaMnAs show good compatibility with the existing III-V semiconductor devices.

In terms of the design of device applications of GaMnAs, it is needed to elaborate a proper model which represents the basic properties of GaMnAs. The studies of the fundamental properties of GaMnAs are placed in the interdisciplinary field between semiconductor physics and magnetism. The interpretations of experimental results on this new material should be described from the viewpoints of both of the subjects. In chapter 2 we aimed at the general understanding of the fundamental properties of GaMnAs. Especially the relationship of the ferromagnetism with the metal-insulator (nonmetal) transition was described.

Two prospective mechanisms to explain the ferromagnetism of GaMnAs have been proposed so far. One is on the basis of the RKKY interaction. The other is founded upon the double exchange interaction. The ideas of both interactions are very similar but the device concepts resulting from each interpretation will be definitely different. Therefore we have to pick up the one which elucidates the characteristics of GaMnAs and discard the other.

The picture of the composite system with local magnetic moments in a semiconductor which deduced from the model based on the RKKY interaction is very simple and easy to understand. Carriers transport through the host epitaxial semiconductor although they are under the influence of the magnetism by way of

the Coulomb interaction with local magnetic moments by doping a large amount of Mn ions. According to the above consideration, many effects of magnetism are naturally introduced to semiconductor technologies.

However the author is not on the side of the model of GaMnAs based on the RKKY interaction. The author believes that the formalism of GaMnAs led by the double exchange interaction can better explain the experimental results of magnetic measurements, transport measurements, and magneto-optical measurements of GaMnAs. Carriers diffuse through a heavily doped semiconductor and are affected by the electron-electron interaction. Mn impurities promote the carrier movement in the random system by arranging their own 3*d*-magnetic moments to reduce the total energy by the kinetic energy of carriers. This carrier transport mechanism is completely different from that of conventional nonmagnetic semiconductors. It will be taken into account on the occasion of the device design of GaMnAs. Anderson localization still remain even if all local magnetic moments align in one direction, which might limit the strength of the ferromagnetic coupling between the local magnetic moments.

These days the expectation for the device applications of spin dependent transport phenomena in magnetic multilayers has been surging in storage technology. For this purpose, high quality multilayers with abrupt interfaces are required. The implementation of producing all metallic multilayers already met this requirements for some applications. For that reason GMR heads with magnetic multilayers have been installed into hard disks. On the other hand, the preparation of magnetic tunnel junctions with high crystal quality is still a troublesome problem because it is difficult to obtain a very smooth oxide tunnel barrier inserted between two metallic electrodes. All epitaxial magnetic semiconductor (GaMnAs / AlAs) superlattices with abrupt interfaces was discussed in chapter 3. In addition, we have found the formation of quantum well states in the GaMnAs / AlAs SLs. The feasibility of preparing such magnetic semiconductor heterostrucutres with abrupt interfaces allows us to investigate spin-dependent transport in better controlled magnetic heterostructure systems.

Tunneling spectroscopy measurements of GaMnAs have been done as the application of such magnetic semiconductor heterostructures, as discussed in chapter 4. It was confirmed that the effect of carrier localization plays an essential role in the transport in GaMnAs. Further studies are required in this subject. The author believes that spin-dependent tunneling spectroscopy with a superconductor counterelectrode will clarify the nature of carriers in GaMnAs.

As an attempt for device application of GaMnAs, we have studied tunneling magnetoresistance (TMR) effects of GaMnAs based magnetic tunnel junctions (MTJs), as described in chapter 5. TMR effects take place due to spin-dependent tunneling in MTJs. Recently magnetic RAM (MRAM) which is a nonvolatile random access memory by utilizing TMR effects of metallic MTJs (ferromagnetic metal electrode / oxide barrier / ferromagnetic metal electrode) has drawn much attention in storage technology. There are two main problems of TMR effects which should be solved for the MRAM application. One is how to produce a smooth insulator barrier with high crystal quality in a MTJ. The other is how to prevent the drop of TMR effects at high bias voltage. A GaMnAs based MTJ is an all-epitaxial tunnel junction with abrupt interfaces and has a very smooth AlAs barrier in it, which gives an opportunity to study the mechanism of TMR effects. In addition, TMR effect of GaMnAs based magnetic resonant tunneling diode is considered to provide unique bias voltage dependence. Future works are needed to realize large TMR effects enhanced by resonant tunneling.

The possibility of the implementation of unique device applications based on GaMnAs and its heterostructure is very high. It is necessary to design the devices based on the fundamental properties of GaMnAs.

Appendix ~ spin dependent transport and its applications ~

1. Spin dependent transport [A.1]

A ferromagnetic metal has the exchange splitting between the up and down spin states to lower the total energy of the system. Here there is imbalance of spin population between up-spin electrons and down-spin electrons. The spin polarized carriers should produce the spin dependent transport. Fortunately electrons can travel without losing "memory" of their spin orientation, within the "spin depth" length of the material considered. The resistance change of a ferromagnetic metal itself by applying a magnetic field could be expected. However the anisotropic magnetoresistance effect (AMR) of a ferromagnetic metal is not so large for device application.

Spin dependent transport has attracted great interest since giant magnetoresistance (GMR) effect was reported [A.2]. GMR effect is based on spin dependent transport between ferromagnetic layers separated by a nonmagnetic layer. It depends on the relative orientation of magnetization of the ferromagnetic layers. GMR effect has realized magnetic field sensors with much higher sensitivity than the old ones such as AMR sensors and semiconductor Hall devices. For example, the recent progress of the recording capacity of hard disk drives is quite remarkable in storage technology. The capacity of the world highest drive is 73 gigabytes, as IBM reported [A.3]. This progress is mainly owing to the great development of GMR recording head.

On the other hand, tunneling magnetoresistance (TMR) effect of magnetic tunnel junctions (MTJs) was proposed by Julliere in 1975 [A.4]. Although TMR effect has equal or more potential for device applications than GMR effect, the study was not beyond basic physics until Miyazaki et al. [A.5] and Moodera et al. [A.6] reported large TMR effects at room temperature in 1995. Since then, the mechanism of TMR effects has been investigated energetically and the device performance of MTJs has been greatly improved. Very recently large MR ratio exceeding 40 % at room temperature was reported by IBM [A.7].

2. *Application for memory*

Devices based on spin dependent transport are considered to have high availability for a variety of practical applications. In particular, the expectation of non-volatile magnetic random access memory (MRAM) has been surging in storage industry.

Contemporary computer main memory is constituted of dynamic random access memory (DRAM). Semiconductor technology has implemented DRAM which has great advantages of large capacity and low cost per bit. DRAM is the most widely employed memory. However DRAM is volatile and requires a refresh of the storage capacitor every few milliseconds. Therefore there is great interest in the possibility of fabricating a nonvolatile random access memory integrated with Si substrates, which retains its memory even after removing power from the device.

Nonvolatile DRAM could have important commercial applications if the non-volatility were accomplished without degrading other properties of the memory, notably density, read and write speed, and lifetime. For example, portable PC and cellular phones are in urgent need of a memory with large capacity and high speed to deal with a large amount of information. Non-volatile DRAM will be a key device in such fields.

DRAM has been continuously improved to reduce the feature size, increase the memory density, and raise the driving speed to date. The rapid progress enables one to introduce of a new generation of memory every three years or less. Driving bias voltage are also moving from 5 V to as low as 0.9 V in order to reduce the power consumption of high density memories. Therefore hopeful nonvolatile RAM must meet the criteria of high speed, high density, low driving bias voltage, low cost per bit and low energy consumption. MRAM is one of the candidates to fulfill those requirements.

The recent advances in GMR effects and TMR effects have significantly increased the MR ratio while lowering the switching field. Use of these effects as a memory element has made it possible for the signal difference between the two memory states (0 / 1) to be increased by more than an order of magnitude, thus making high density, high speed, and low power MRAM viable [A.7,8]. The MRAM will be coming up as the next generation memory of DRAM.

References

[A.1] G. A. Prinz, Physics Today, 48 April (1995) 58.

[A.2] M. N. Baibich, J. M. Broto, A. Fert, F. Nguyen van Dau, F. Petroff, P. Etienne, G. Creuzet, A. Friedrich, J. Chazeles, Phys. Rev. Lett. 61 (1988) 2472.

[A.3] http://www.storage.ibm.com/press/hdd/991015.htm

[A.4] M. Julliere, Phys. Lett. 54A (1975) 225.

[A.5] T. Miyazaki and N. Tezuka, J. Magn. Magn. Mater. 139 (1995) L231.

[A.6] J. S. Moodera, L. R. Kinder, T. M. Wong, and R. Meservey, Phys. Rev. Lett. 74 (1995) 3273.

[A.7] S. S. Parkin, K. P. Roche, M. G. Samant, P. M. Rice, R. B. Beyers, R. E. Scheuerlein, E. J. O'Sullivan, S. L. Brown, J. Bucchigano, D. W. Abraham, Yu Lu, M. Rooks, P. L. Trouilloud, R. A. Wanner, and W. J. Gallagher, J. Appl. Phys. 85 (1999) 5828.

[A.8] S. Tehrani, E. Chen, M. Durlam, M. DeHerrera, J. M. Slaughter, J. Shi, and G. Kerszykowski, J. Appl. Phys. 85 (1999) 5822.

Publication list

(first author)

- T. Hayashi, M. Tanaka, T. Nishinaga and H. Shimada, "GaMnAs: New III-V Based Diluted Magnetic Semiconductors Grown by Molecular Beam Epitaxy", J. Crystal Growth **175/176**, pp. 1063 – 1068 (1997).
- T. Hayashi, M. Tanaka, T. Nishinaga and H. Shimada, "Magnetic and Magnetotransport Properties of a New III-V Diluted Magnetic Semiconductor: GaMnAs", J. Appl. Phys. **81**, pp. 4865 – 4867 (1997).
- T. Hayashi, M. Tanaka, K. Seto, T. Nishinaga and K. Ando, "New III-V Based Magnetic (GaMnAs) / Nonmagnetic (AlAs) Semiconductor Superlattices", Appl. Phys. Lett. **71**, pp. 1825 – 1827 (1997).
- T. Hayashi, M. Tanaka, K. Seto, T. Nishinaga, H. Shimada and K. Ando, "Hall Effect and Magnetic Properties of III-V Based $(Ga_{1-x}Mn_x)As$ / AlAs Magnetic Semiconductor Superlattices", J. Appl. Phys. **83**, pp. 6551 – 6553 (1998).
- T. Hayashi, M. Tanaka, K. Seto, T. Nishinaga and H. Shimada, "Magnetotransport Properties of New III-V Based Magnetic (GaMnAs) / Nonmagnetic (AlAs) Semiconductor Superlattices", Physica E **2**, pp. 404 – 407 (1998).
- T. Hayashi, H. Shimada, H. Shimizu and M. Tanaka, "Tunneling Sepectroscopy and Magnetoresistance in (GaMn)As / AlAs / (GaMn)As Ultrathin Magnetic Semiconductor Heterostructures", J. Crystal Growth **201/202**, pp. 689 – 692 (1999).
- T. Hayashi, M. Tanaka, A. Asamitsu, "Tunneling magnetoresistance of a GaMnAs based double barrier ferromagnetic tunnel junction", J. Appl. Phys., to be published.

(coauthor)

- K. Ando, T. Hayashi, M. Tanaka and A. Twardowski, "Magnetooptic Effect of Ferromagnetic Diluted Magnetic Semiconductor $Ga_{1-x}Mn_xAs$", J. Appl. Phys. **83**, pp. 6548 – 6550 (1998).
- R. Shioda, K. Ando, T. Hayashi and M. Tanaka, "Local Structures of III-V Diluted Magnetic Semiconductor GaMnAs Studied by Extended X-ray Absorption Fine Structure", Phys. Rev. **B58**, pp. 1100 – 1102 (1998).
- H. Shimizu, T. Hayashi, T. Nishinaga and M. Tanaka, "Magnetic and Transport Properties of III-V Based Magnetic Semiconductor (GaMn)As: Growth

Condition Dependence", Appl. Phys. Lett. 74, pp. 398 – 400 (1999).

- H. Shimizu, T. Hayashi, T. Nishinaga and M. Tanaka, "Properties of III-V Based Ferromagnetic Semiconductor ($Ga_{1-x}Mn_x$)As: As Pressure Dependence", J. Magn. Soc. Jpn. 23, pp. 96 – 98 (1999).
- J. Okabayashi, A. Kimura, O. Rader, T. Mizokawa, A. Fujimri, T. Hayashi and M. Tanaka, "Core-level photoemission study of $Ga_{1-x}Mn_xAs$", Phys. Rev. B58, pp. R4211 – R4214 (1998).
- J. Okabayashi, A. Kimura, T. Mizokawa, A. Fujimri, T. Hayashi and M. Tanaka, "Mn 3d Partial Density of States in (GaMn)As Studied by Resonance Photoemission Spectroscopy", Phys. Rev. B59, pp. R2486 – R2489 (1999).

International conference

(first author)

- T. Hayashi, M. Tanaka and H. Shimada,
  "GaMnAs: New III-V Based Diluted Magnetic Semiconductors Grown by Molecular Beam Epitaxy"
  9th Int. Conference on Molecular Beam Epitaxy,
  Mailbu, U.S.A., August 1996.
- T. Hayashi, K. Ando, T. Nishinaga and M. Tanaka,
  "A New III-V Magnetic Semiconductor (GaMn)As and (GaMn)As / AlAs superlattices: Magnetic and Magneto-Optic Properties"
  8th Int. Conf. on Modulated Semiconductor Structures,
  Santa Barbara, U.S.A., July 1997.
- T. Hayashi, K. Takahashi, H. Shimizu, T. Nishinaga and M. Tanaka,
  "Tunneling Magnetoresistance of (GaMn)As / AlAs Heterostructures"
  Int. Symp. On the Physics of Magnetic Materials,
  Sendai, August 1998.
- T. Hayashi, H. Shimada, H. Shimizu and M. Tanaka,
  "Magneti Coupling in (GaMn)As / AlAs / (GaMn)As Magnetic Semiconductor Trilayers"
  10th Int. Conf. on Molecular Beam Epitaxy,
  Cannes, France, September 1998.
- T. Hayashi, H. Shimada, and M. Tanaka,
  "Tunneling Magnetoresistance in (GaMn)As / AlAs / (GaMn)As Ferromagnetic Semiconductor Trilayers"

43rd Annual Conference on Magnetism & Magnetic Materials,
Miami, November 1998.

- T. Hayashi, H. Shimada, H. Shimizu and M. Tanaka,
"Tunneling Magnetoresistance in (GaMn)As / AlAs / (GaMn)As Ferromagnetic Semiconductor Heterostructures"
Materials Research Society 1999 Spring Meeting,
San Francisco, April 1999.
- T. Hayashi, H. Shimada, H. Shimizu, and M. Tanaka,
"Tunneling Magnetoresistance in GaMnAs-based Ferromagnetic Semiconductor Heterostructures"
9th Int. Conf. on Modulated Semiconductor Structures,
Fukuoka, Japan, July 1999.
- T. Hayashi, M. Tanaka, and H. Shimada,
"Tunneling Magnetoresistance of GaMnAs-based Ferromagnetic Semiconductor Heterostructures"
44th Annual Conference on Magnetism & Magnetic Materials,
San Jose, U.S.A. November 1999.

(coauthor)

- M. Tanaka, T. Hayashi, T. Nishinaga and H. Shimada,
"Epitaxial Growth and Properties of a New III-V Diluted Magnetic Semiconductor: GaMnAs"
41th Annual Conf. on Magnetism & Magnetic Materials,
Atlanta, U.S.A., November 1996.
- K. Ando, M. Tanaka, T. Hayashi and A. Twardowski,
"Magneto-optic Effects of New III-V Diluted Magnetic Semiconductors: GaMnAs"
American Physicall Soceity 1997 March Meeting,
Kansas City, U.S.A., March 1997.
- M. Tanaka, T. Hayashi, T. Nishinaga, H. Shimada and K. Ando,
"Properties of III-V Based (GaMn)As / AlAs Magnetic Semiconductor Superlattices"
7th Joint MMM-Intermag Conference,
San Francisco, Januray 1998.
- K. Ando, T. Hayashi, M. Tanaka and A. Twardowski,
"Magnetooptic Effect of Ferromagnetic Diluted Magnetic Semiconductor

$Ga_{1-x}Mn_xAs$"

7th Joint MMM-Intermag Conference,

San Francisco, Januray 1998.

- H. Shimizu, T. Hayashi, T. Nishinaga and M. Tanaka,

"Control of Magnetic Properties of III-V Based Ferromagnetic Semiconductor (GaMn)As"

Int. Symp. On the Physics of Magnetic Materials,

Sendai, August 1998.

- H. Shimizu, T. Hayashi, T. Nishinaga, and M. Tanaka,

"Control of Electric Properties of III-V Based Magnetic Semiconductor (GaMn)As"

43rd Annual Conference on Magnetism & Magnetic Materials,

Miami, November 1998.

- H. Shimizu, T. Hayashi, T. Nishinaga, M. Tanaka, and K. Ando,

"Magneto-optic Properties of (GaMn)As Thin Films and Its Heterostructures"

Materials Research Society 1999 Spring Meeting,

San Francisco, April 1999.

Figures

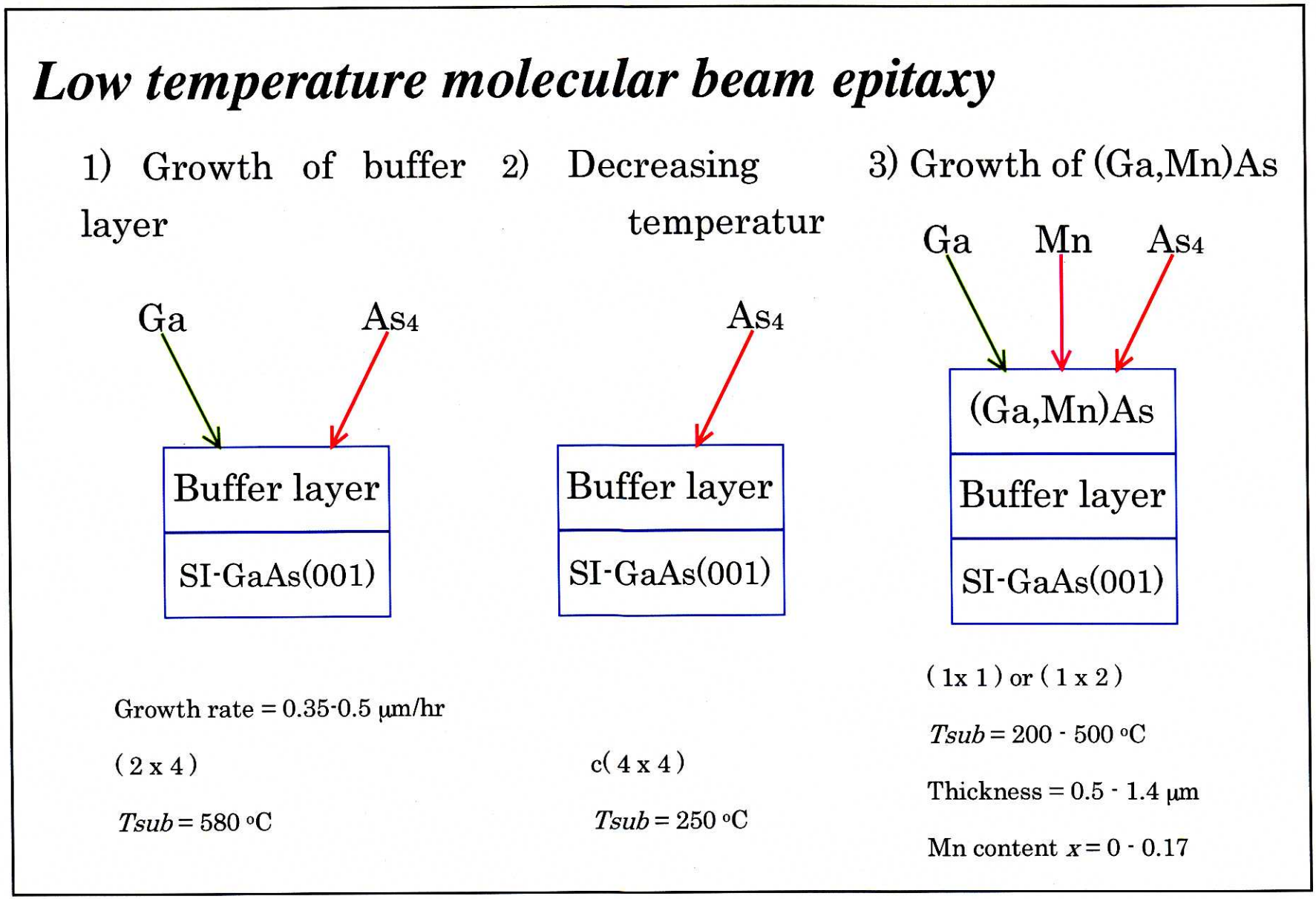

Fig. 2.1 Growth process of GaMnAs by low-temperature molecular beam epitaxy

(a) Homogeneous GaMnAs

x = 0.05 grown at 250°C

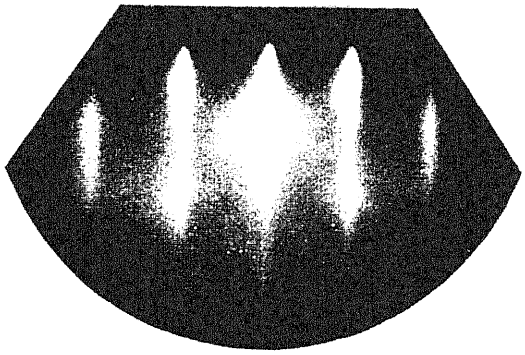

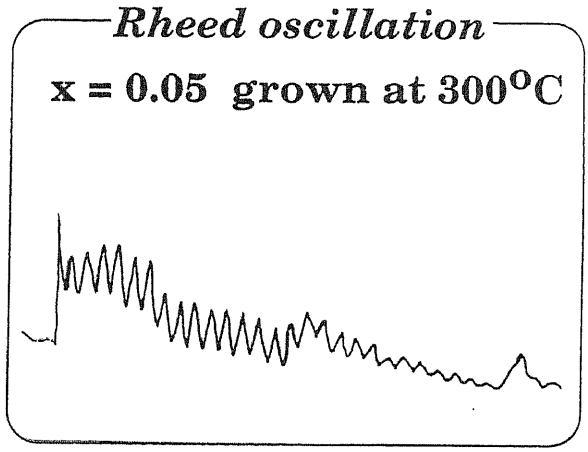

(b) Inhomogeneous MnAs + GaAs (GaMnAs)

x = 0.10 grown at 300°C

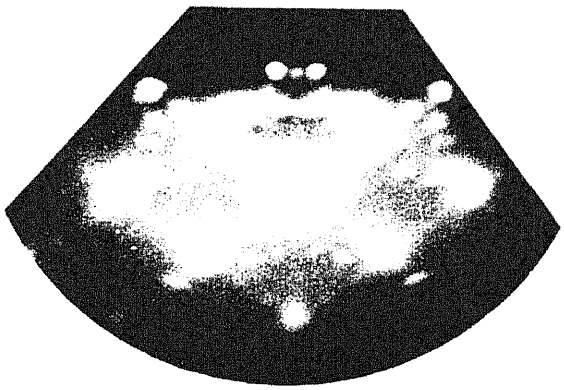

Fig. 2.2 RHEED patterns during the growth of GaMnAs with the azimuth of [110]: (a) the Mn content x = 0.05 grown at 250 °C, (b) x = 0.10 grown at 300 °C.

	Ts[℃]	Mn content [%]	lattice constant[Å]	thickness [μm]	growth rate [μm/hr]	RHEED patterns
B594	300	17	–	0.5		poly
B595	300	0.462	5.654883	1		1x2
B599	300	10	–	0.5		poly
B600	300	0.448	5.655327	1		1x2
B613	250	0.746	5.656858	0.5		1x2
B614	200	2.49	5.660002	0.5	0.5	1x1
B616	300	0.227	5.65482	0.5		1x1
B617	300	8	–	0.5		poly
B626	200	3.272	5.661796	0.5		1x1
B627	400	2	–	0.5		2x3
B628	500	2	–	0.5		2x3
B672	250	7.42	5.670937	1.4		1x1
B678	250	3.71	5.663111	1.4		1x1
B679	250	3.71	5.663374	1.4	0.35	1x1
B680	250	3.71	5.664109	1.4		1x1
B681	250	6.37	5.668888	0.44		1x1
B726	250	5.5	5.666806	0.87		1x
B727	250	7.8	5.671409	1.08	0.5	1x2
B733	250	6	5.669226	0.98		1x

Table 2.1 Growth conditions and the corresponding RHEED patterns

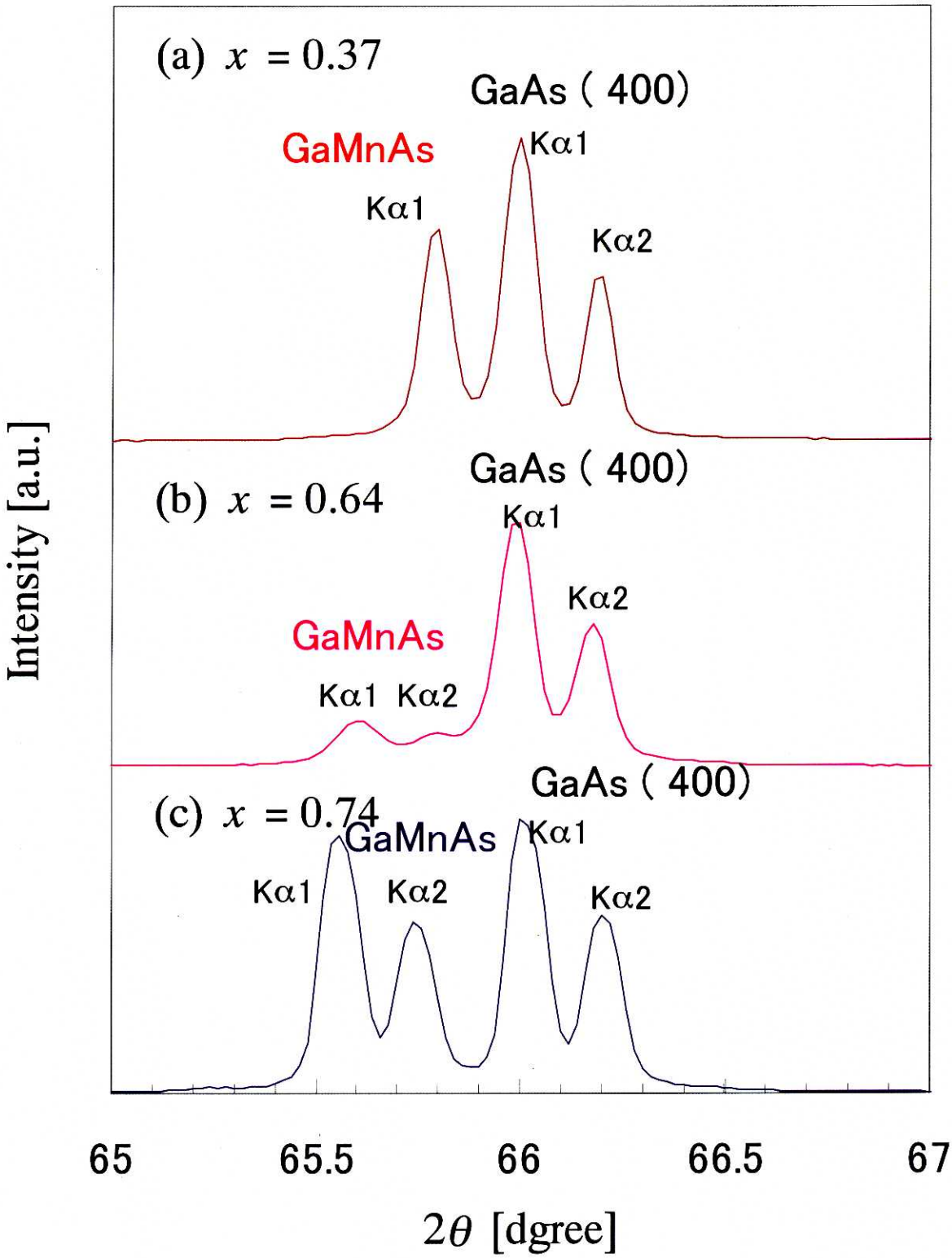

Fig 2.3 X-ray diffraction (θ-2θ) spectra of various homogeneous GaMnAs films grown on GaAs (001) at 250°C: (a) x = 0.037, (b) x = 0.064, (c) x = 0.074.

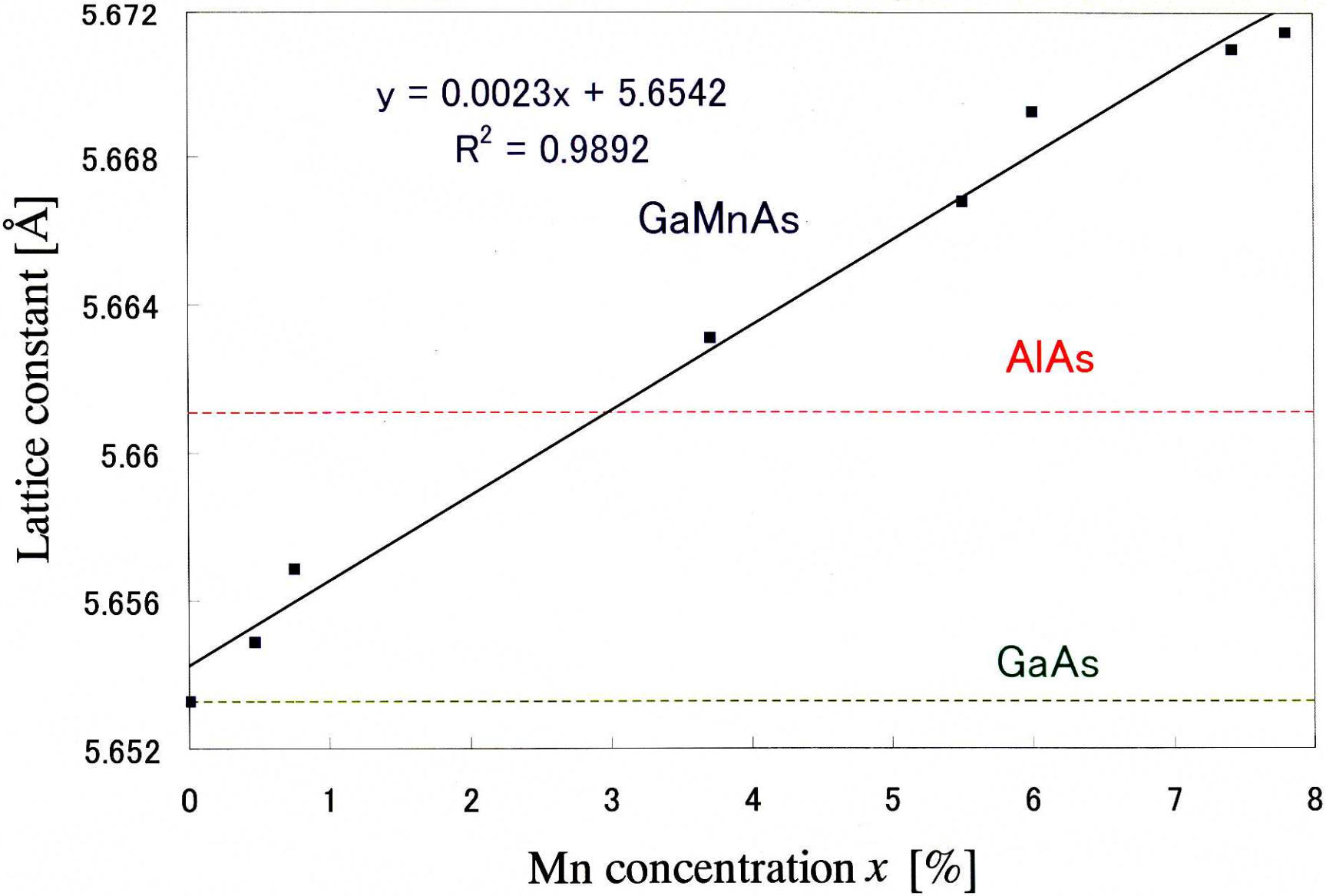

Fig. 2.4 The lattice constant of GaMnAs at various Mn concentration x, investigated with double crystal X-ray diffraction measurements. The values of x were estimated by EPMA.

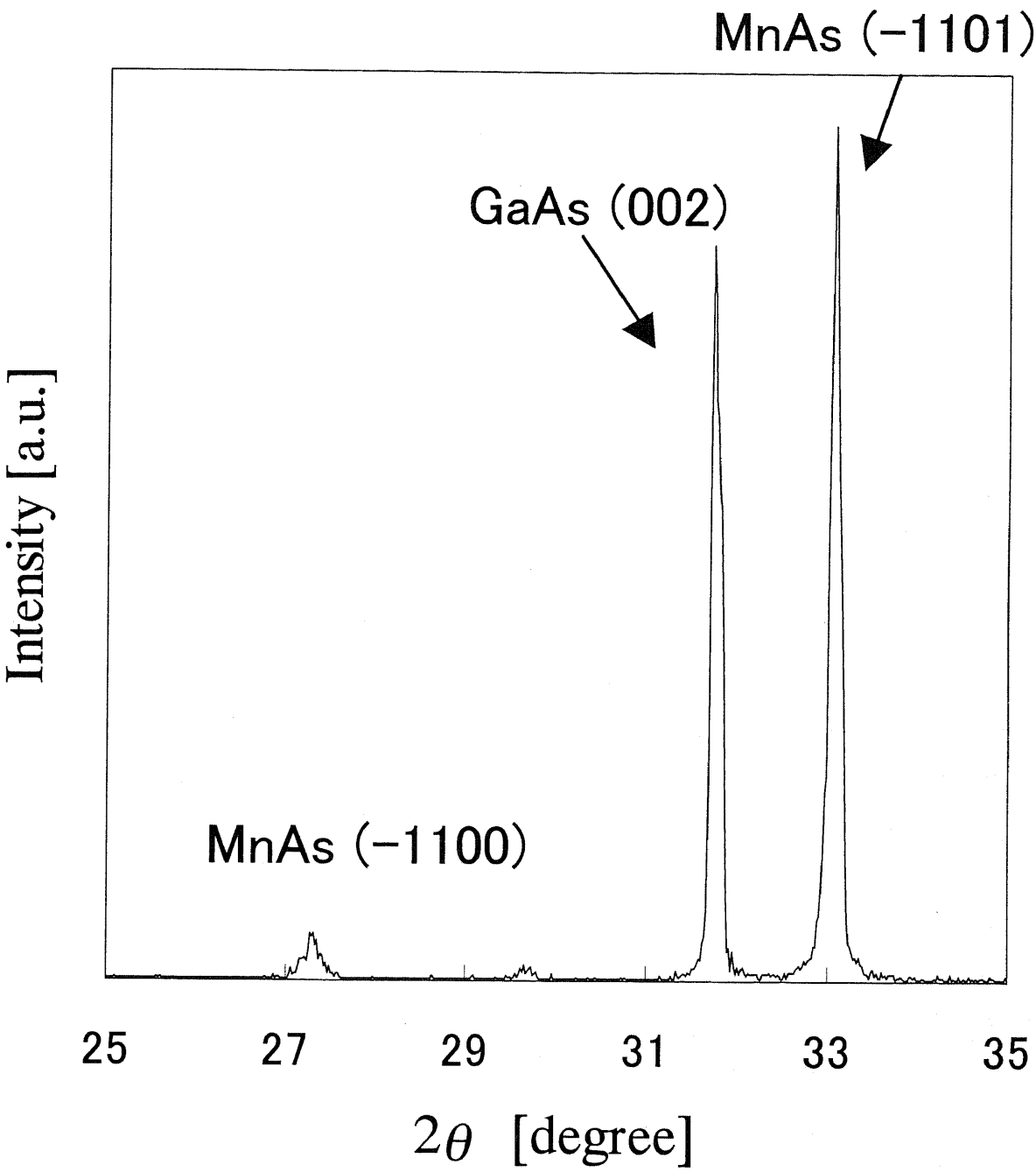

Fig. 2.5 X-ray spectrum of an inhomogeneous film of GaAs (or GaMnAs) + MnAs with the nominal value of x = 0.08 grown at 300°C.

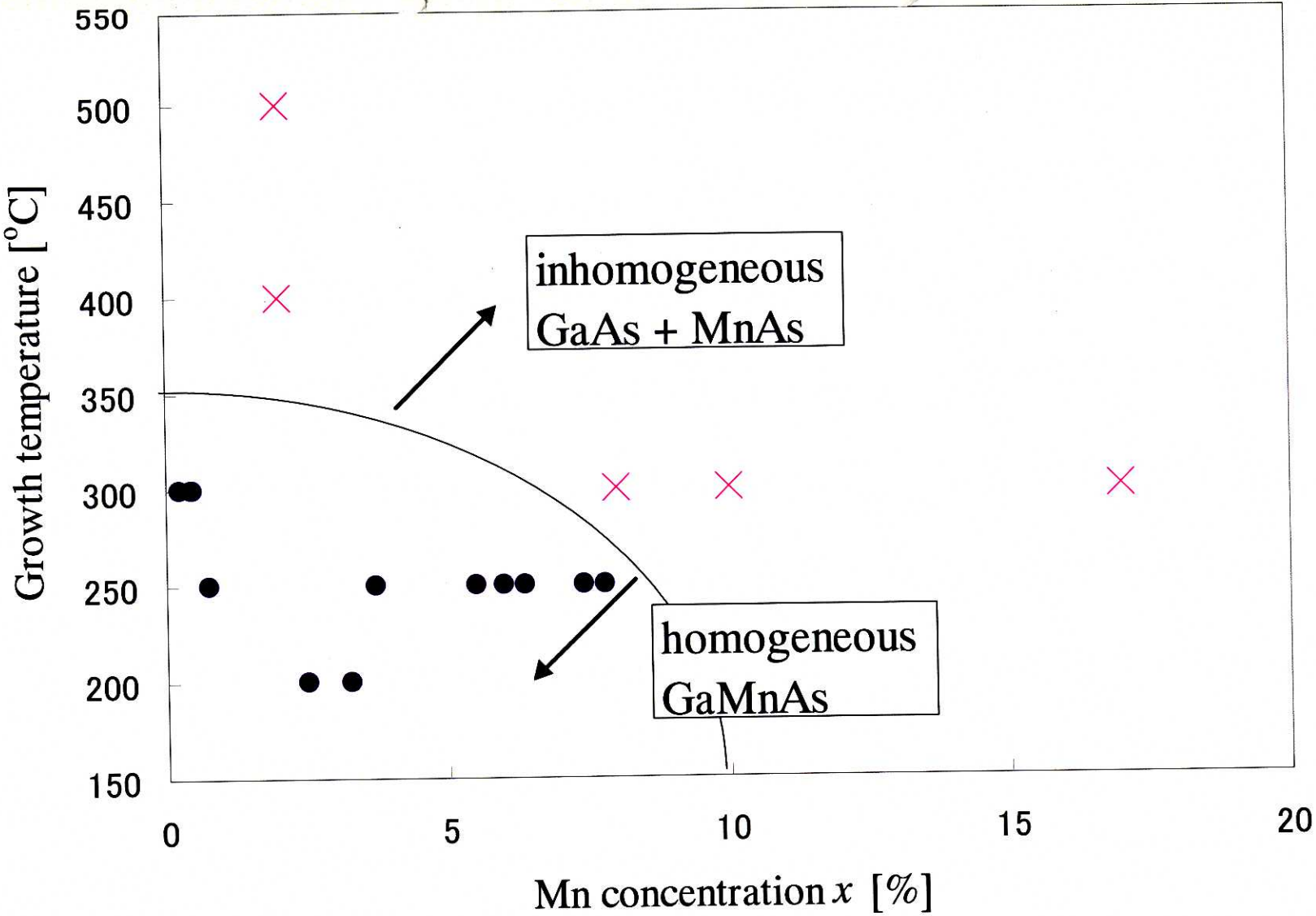

Fig. 2.6 Diagram of the GaMnAs film properties in relation to the two growth parameters (Mn concentration x and growth temperature). Solid circles and crosses denote homogeneous and inhomogeneous structures, respectively.

(a) H: in-plane

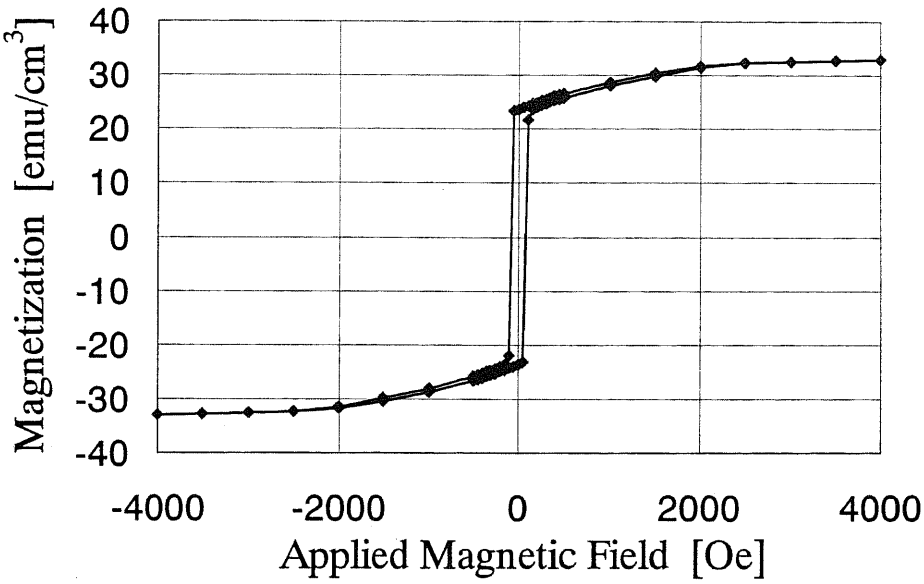

(b) H: perpendicular

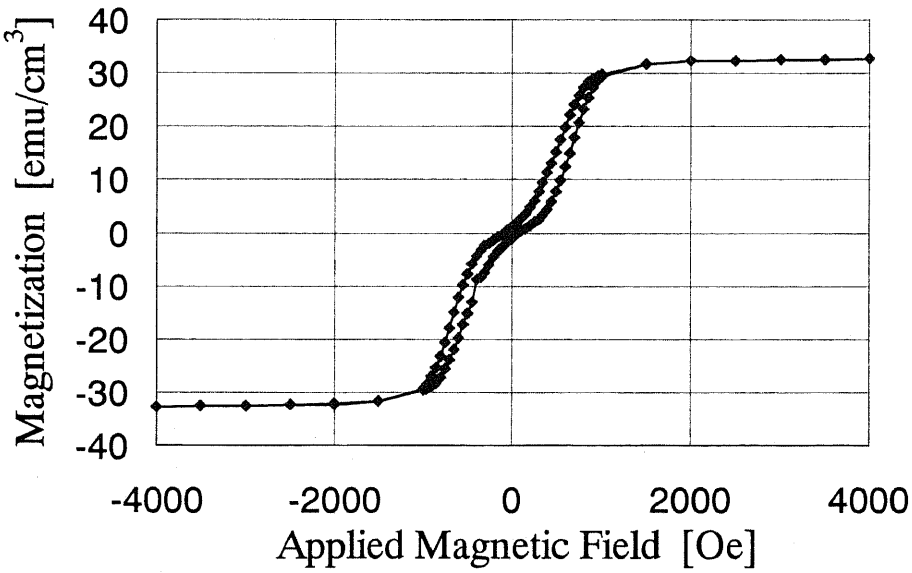

Fig. 2.7 Magnetization (M-H) curve of a 1.4 μm-thick GaMnAs (x =0.074, grown at 250°C) measured by SQUID at 1.9K, when the magnetic field was applied (a) in plane and (b) perpendicular to the plane, respectively.

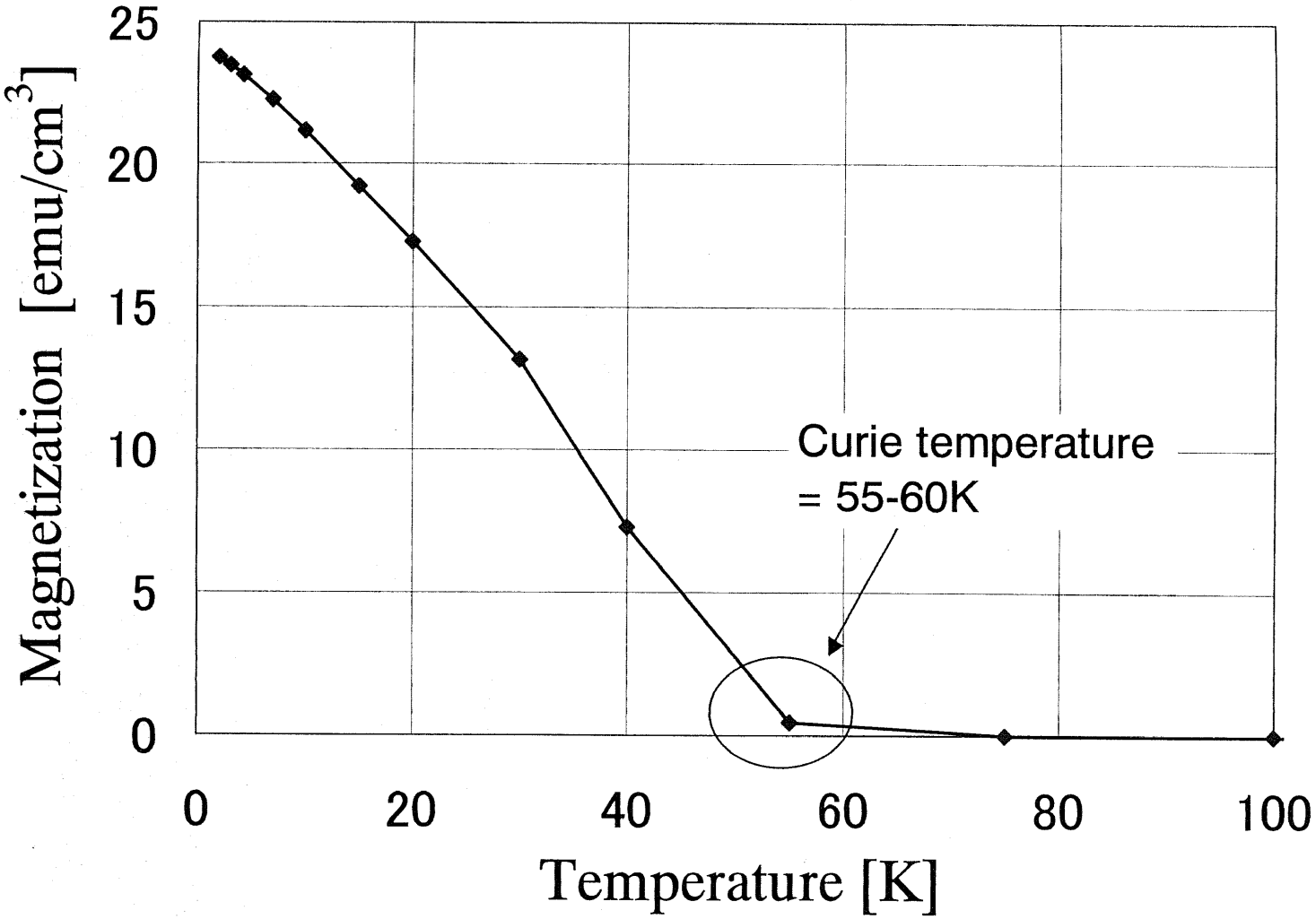

Fig. 2.8 Temperature dependence of the residual magnetization of a 1.4 mm-thick GaMnAs (x = 0.074, grown at 250°C), indicating the Curie temperature of this sample is 55 - 60K.

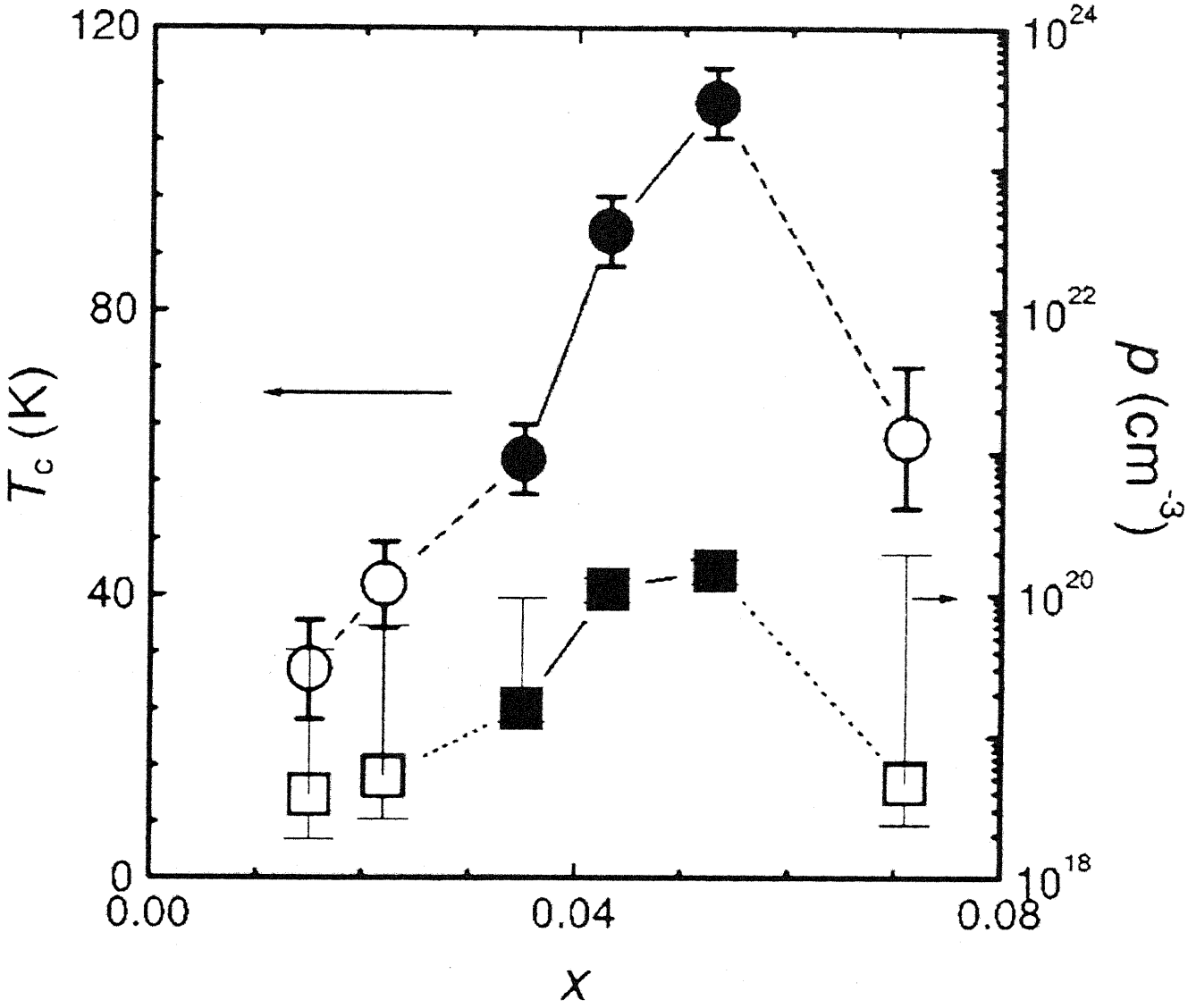

Fig. 2.9 Mn composition dependence of ferromagnetic transition temperature T_c and hole concentration p. Samples on the metal side of the metal insulator transition are shown by the closed symbols. After Matsukura et al. (Ref. [2.16])

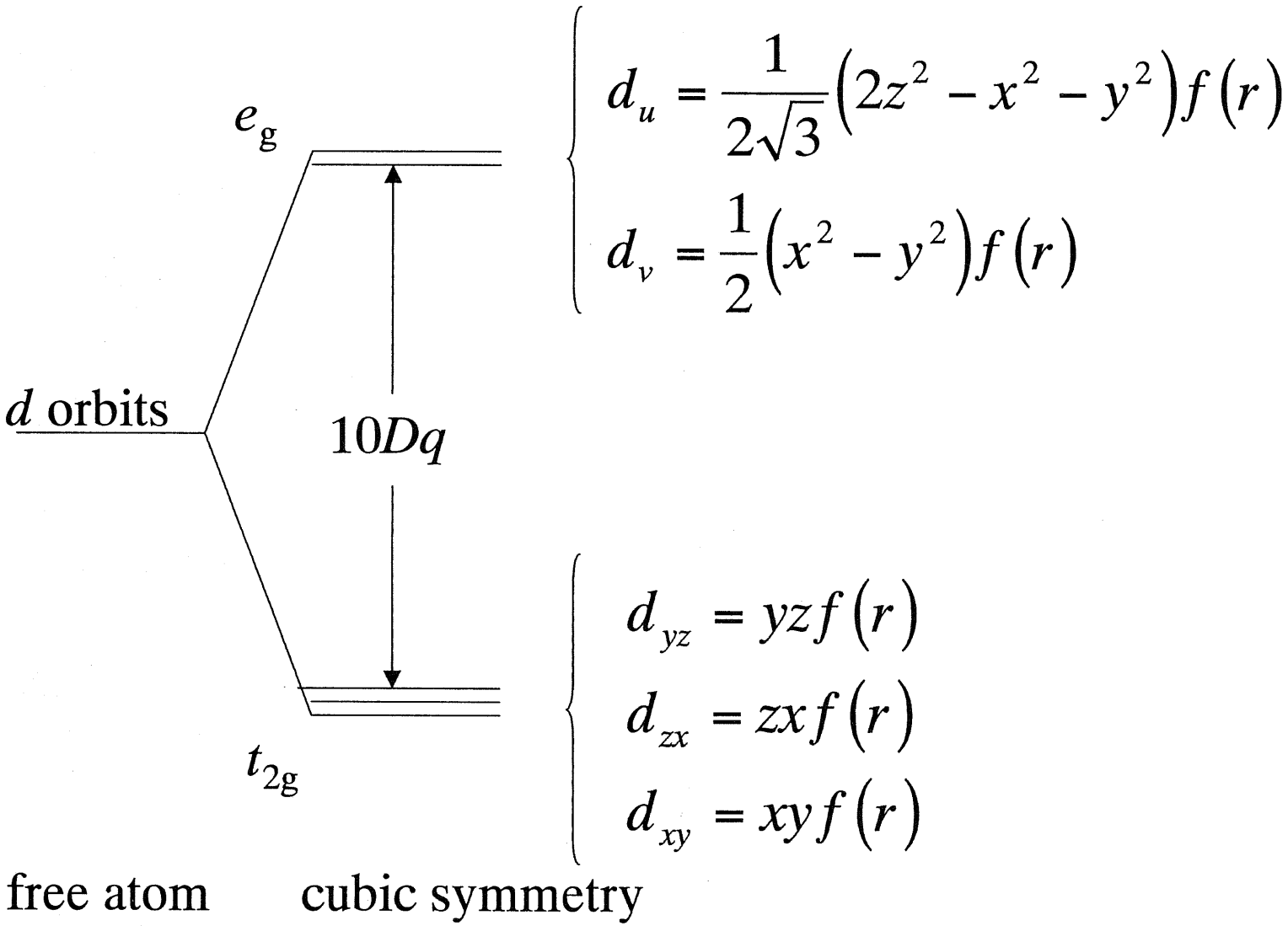

Fig. 2.10 The energy splitting of 3*d* orbits in a crystal field with cubic symmetry.

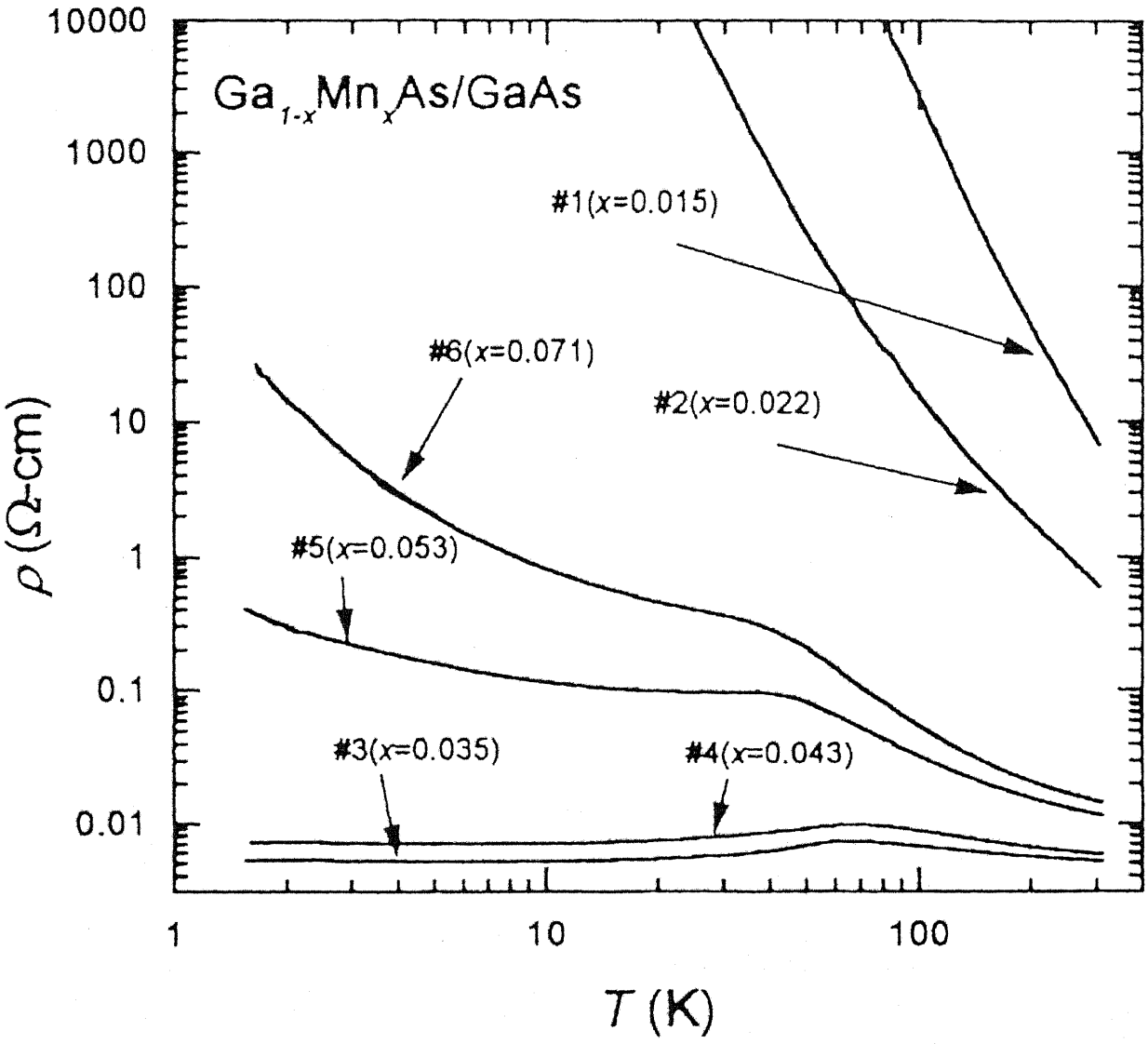

Fig. 2.19 Temperature dependence of resistivity for six samples of $Ga_{1-x}Mn_xAs/GaAs$ with x ranging from 0.015 to 0.071. After Oiwa et al. (Ref.[2.18])

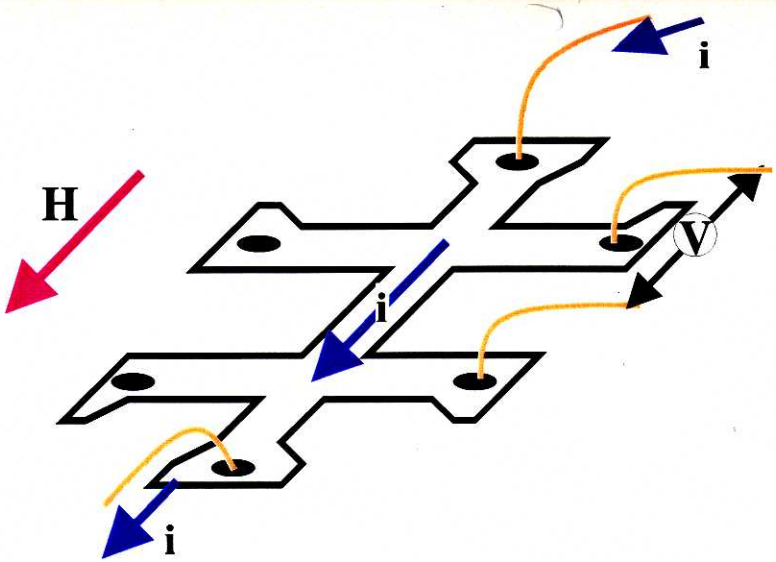

longitudinal effect

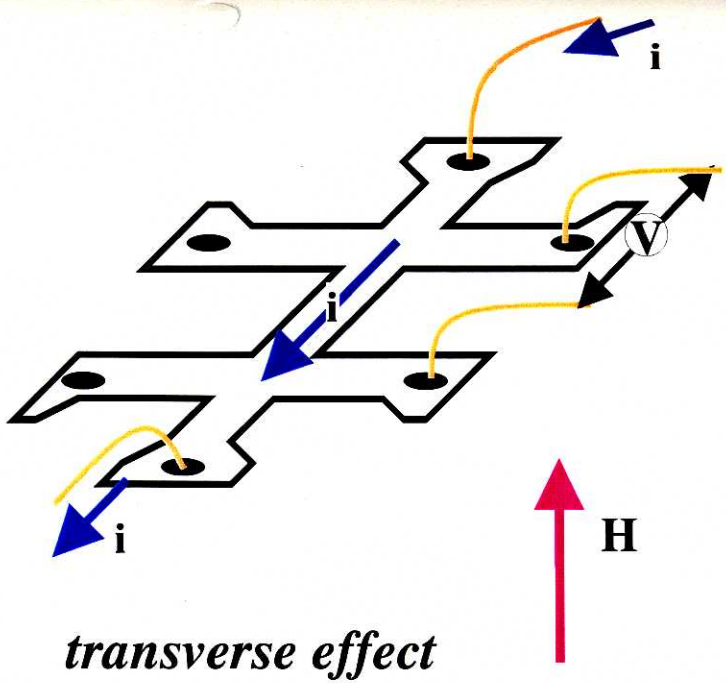

transverse effect

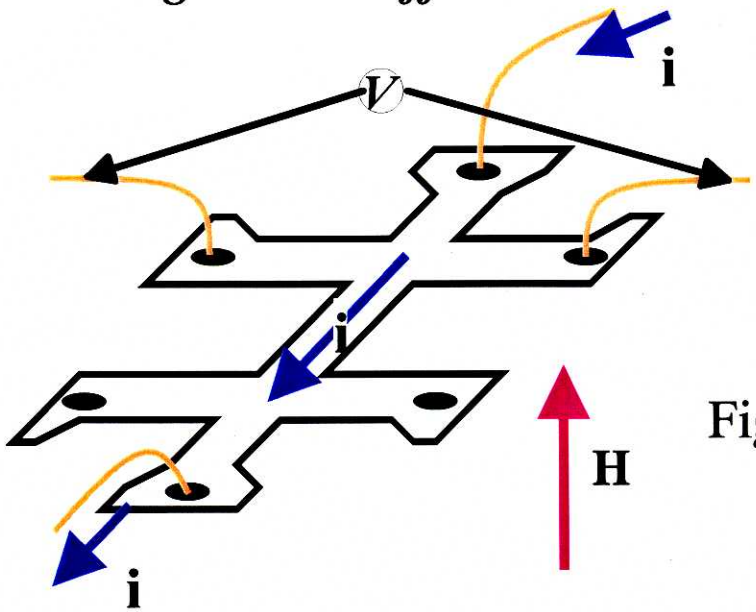

Hall effect

Fig. 2.11 The geometry of MR measurements .

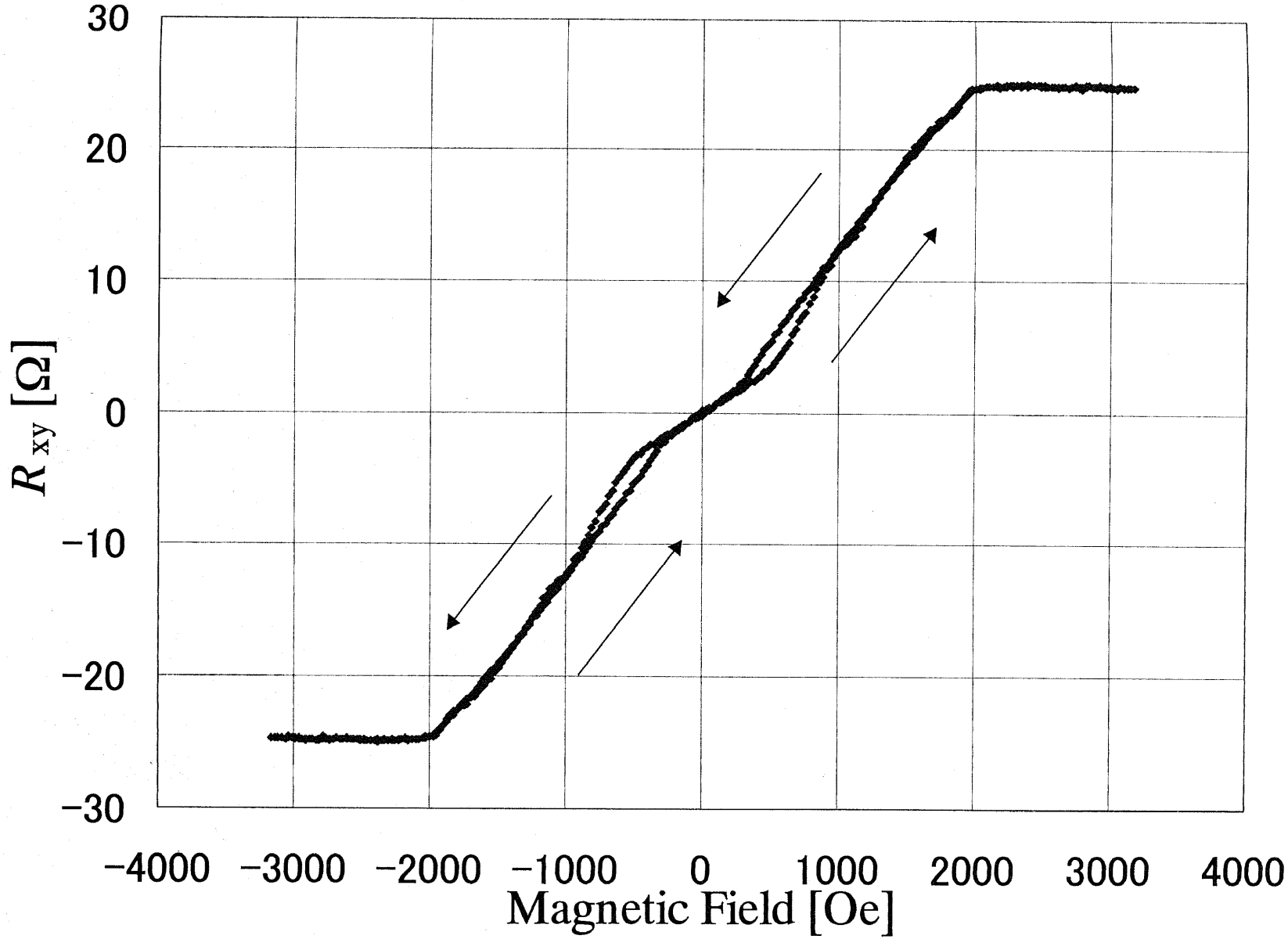

Fig. 2.12 Extraordinary Hall effect of GaMnAs (x = 0.074) at 1.6K.

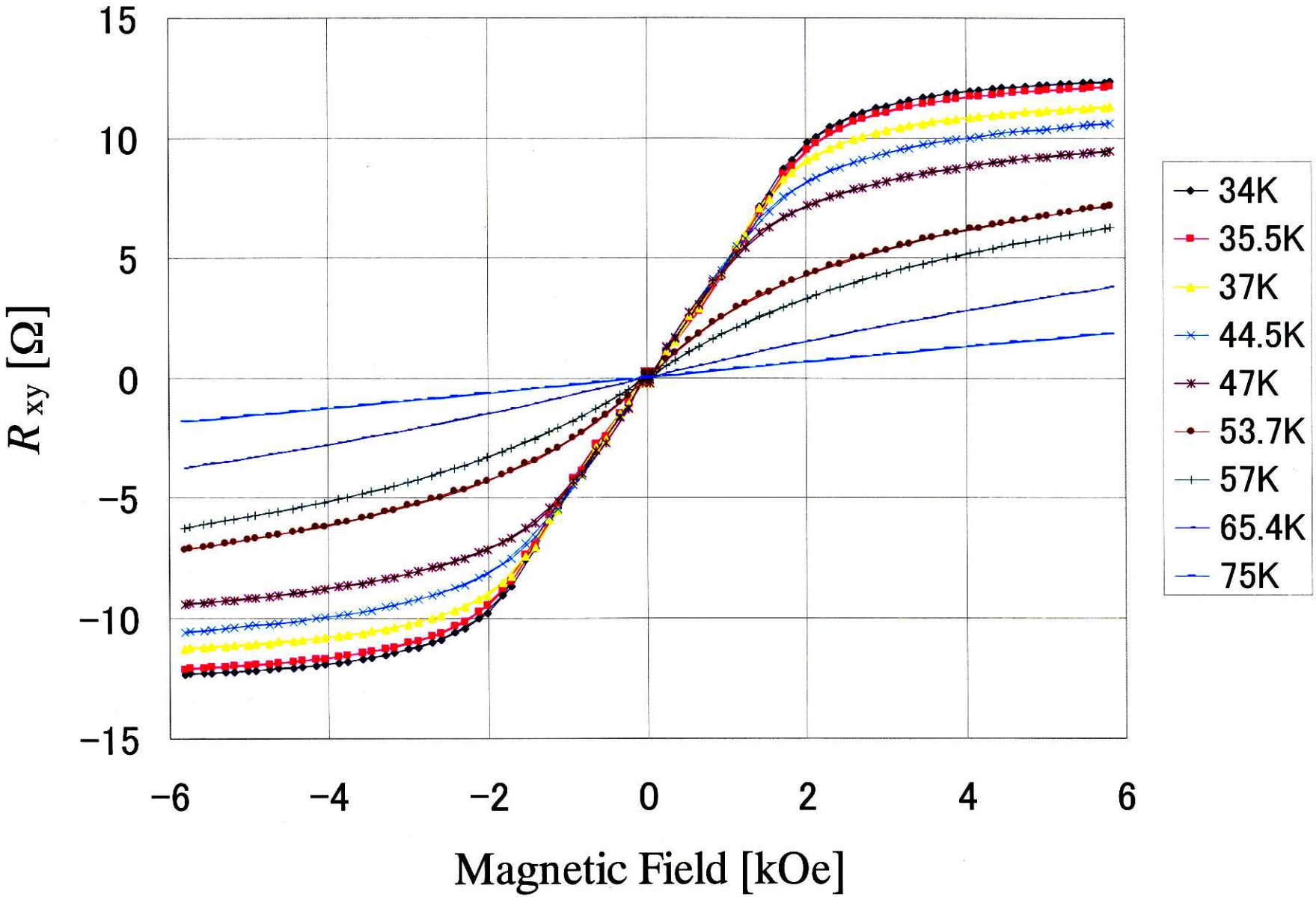

Fig. 2.13 Temperature dependence of EHE of GaMnAs (x = 0.037)

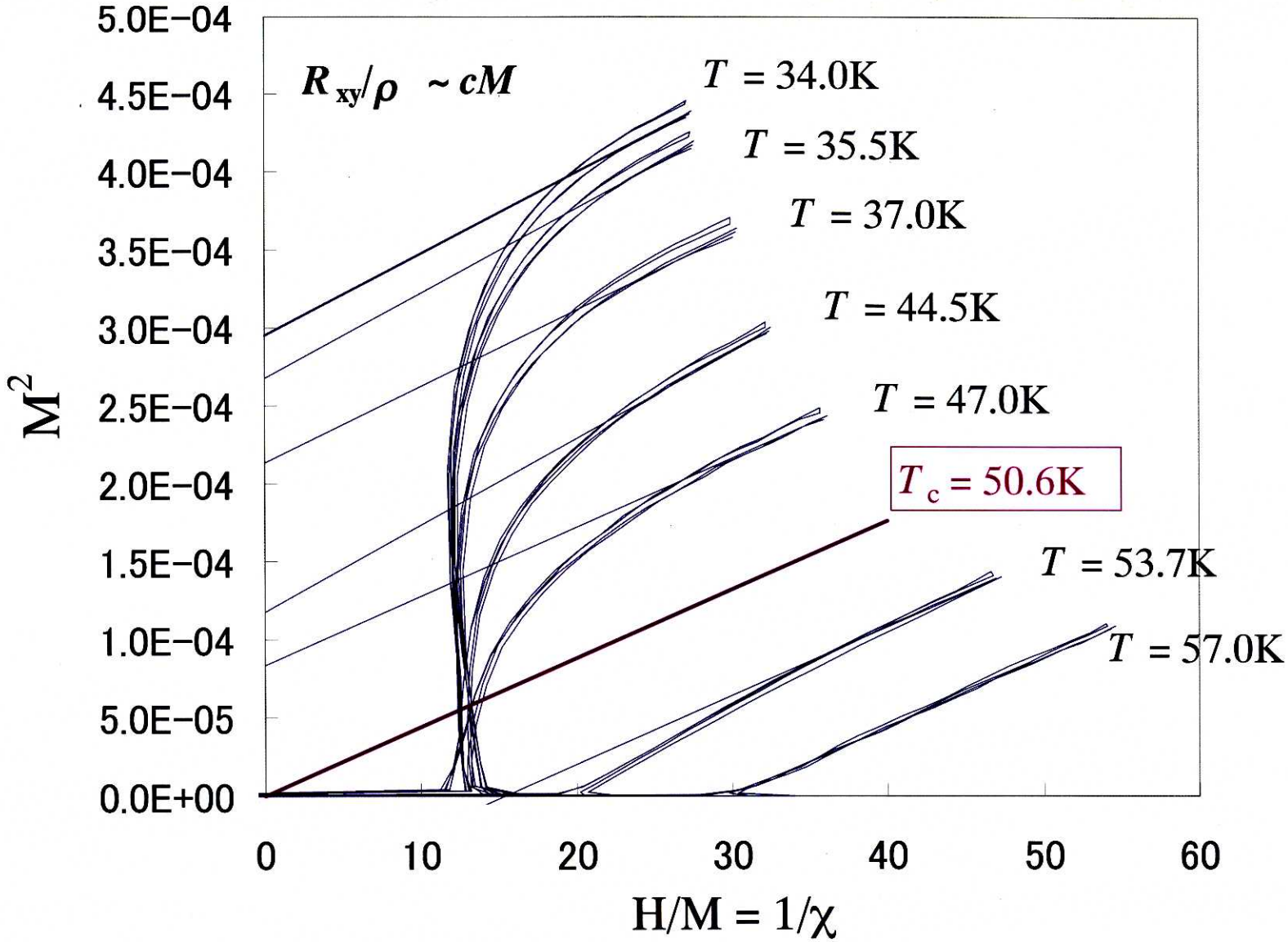

Fig. 2.14 Arrott plot of GaMnAs (x = 0.037) calculated from EHE measurements.

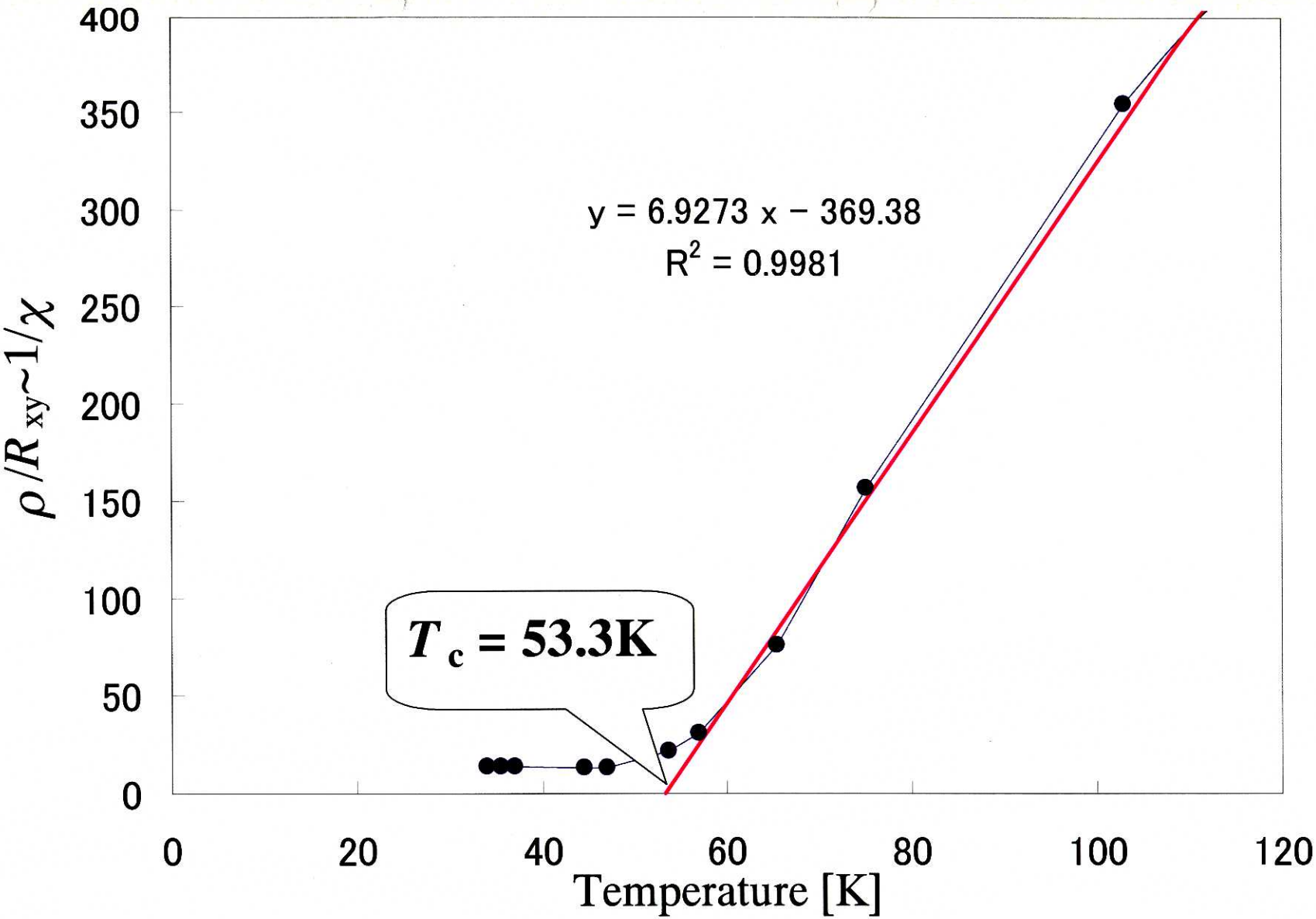

Fig. 2.15 Reciprocal susceptibility ($\rho/R_{xy} \sim 1/\chi$) in the neighborhood of the Curie temperature of GaMnAs (x = 0.037).

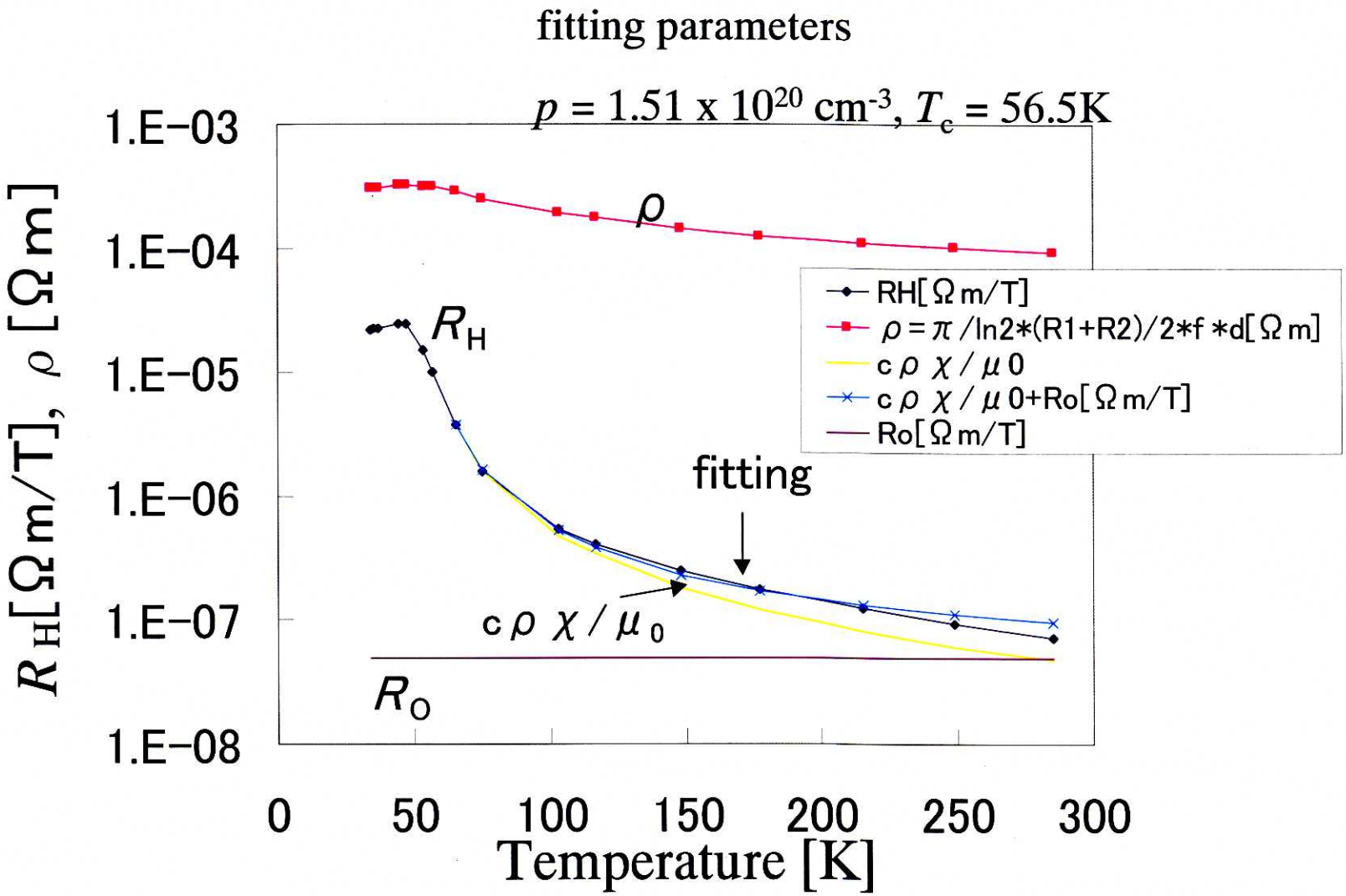

Fig. 2.16 Fitting curve of GaMnAs (x = 0.037) according to Eq. (2.6)

c: fitting parameter

sample	thickness (Å)	Mn x (%)	arrott (K)	1/χ (K)	fitting (K)	p(RH)[1/cm3]	p(fit)[1/cm2]	c
B801	5000	3.7	50.6	53.3	56.5	1.06E+20	3.01E+24	1.56E+00
B803	5000	3.5	51.3	54.5	55.1	6.23E+19	2.32E+24	1.31E+00
B807	5000	3.9	43.2	44	48.5	6.49E+18	3.04E+22	6.92E−01
B808	2000	3.9	61.2	65.9	70.7	3.00E+18	3.65E+22	3.08E+00
B809	500	3.9	73.9	78.2	79.1	2.65E+19	6.32E+24	3.68E+00
B810	15000	4.8	–	–	–	7.56E+18	0.00E+00	–
B812	2000	5.93	56.2	64.8	64.6	5.24E+19	2.27E+25	2.23E+00
B833	5000	6.06	40.6	40.4	42.8	3.47E+19	1.91E+24	2.20E+00
B834	5000	6.92	44.5	44.3	46	2.02E+19	3.96E+23	1.24E+00
B843	100	4.16	48.4	47.3	53.1	9.16E+18	3.82E+24	9.11E−01
B862	50	4.16	47	47.8	49.8	6.67E+19	5.91E+25	1.35E+00
B873	5000	5.27	–	–	–	1.28E+17	0.00E+00	–
B874	5000	5.5	–	–	–	7.93E+17	0.00E+00	–

Table 2.2 The summary of the Curie temperature and hole concentration.

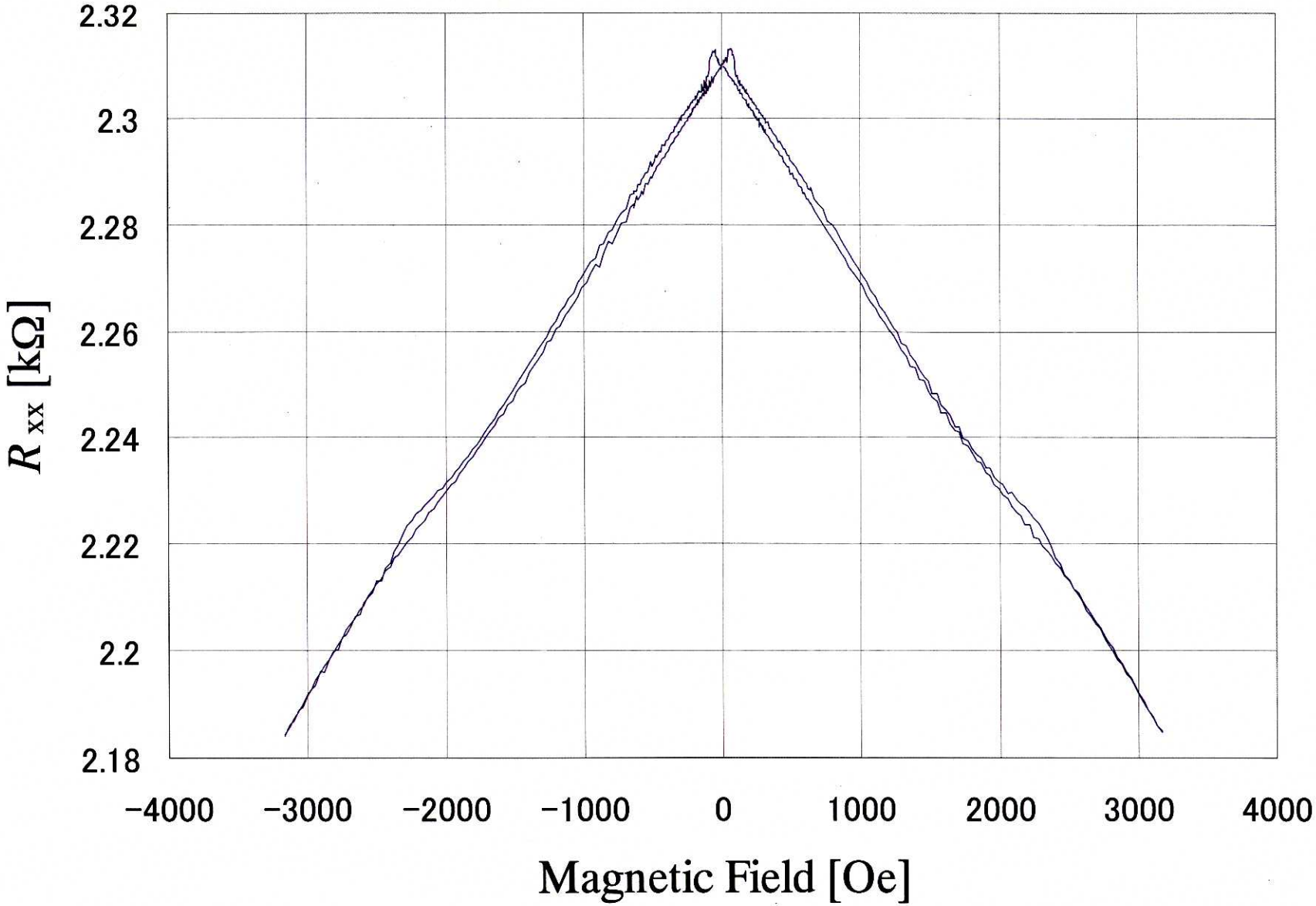

Fig. 2.17 Magnetoresistance of GaMnAs (x = 0.074) at 1.6K, where the magnetic field is applied in-plane parallel to the current.

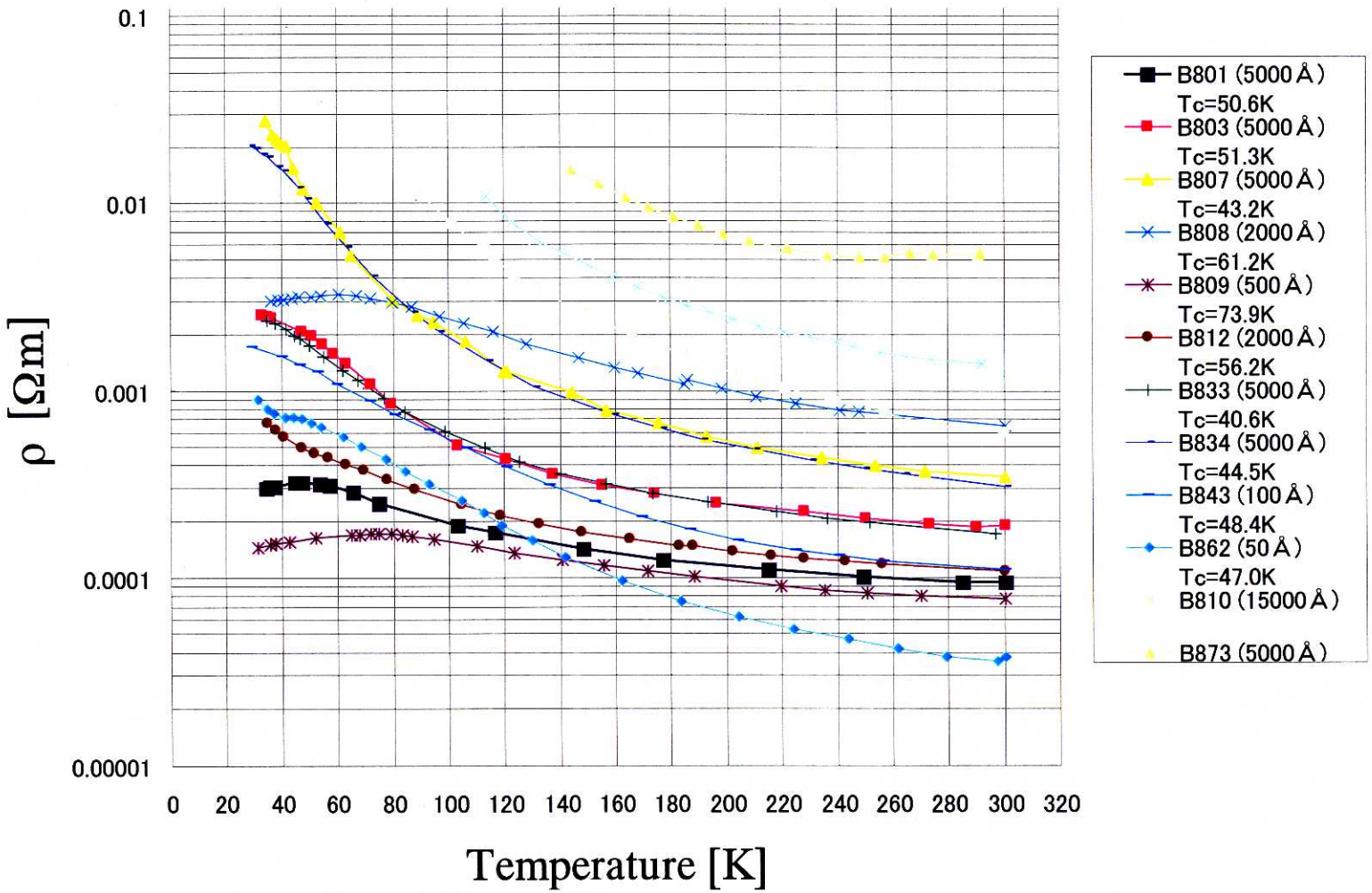

Fig. 2.18 Temperature dependence of the resistivity of GaMnAs films.

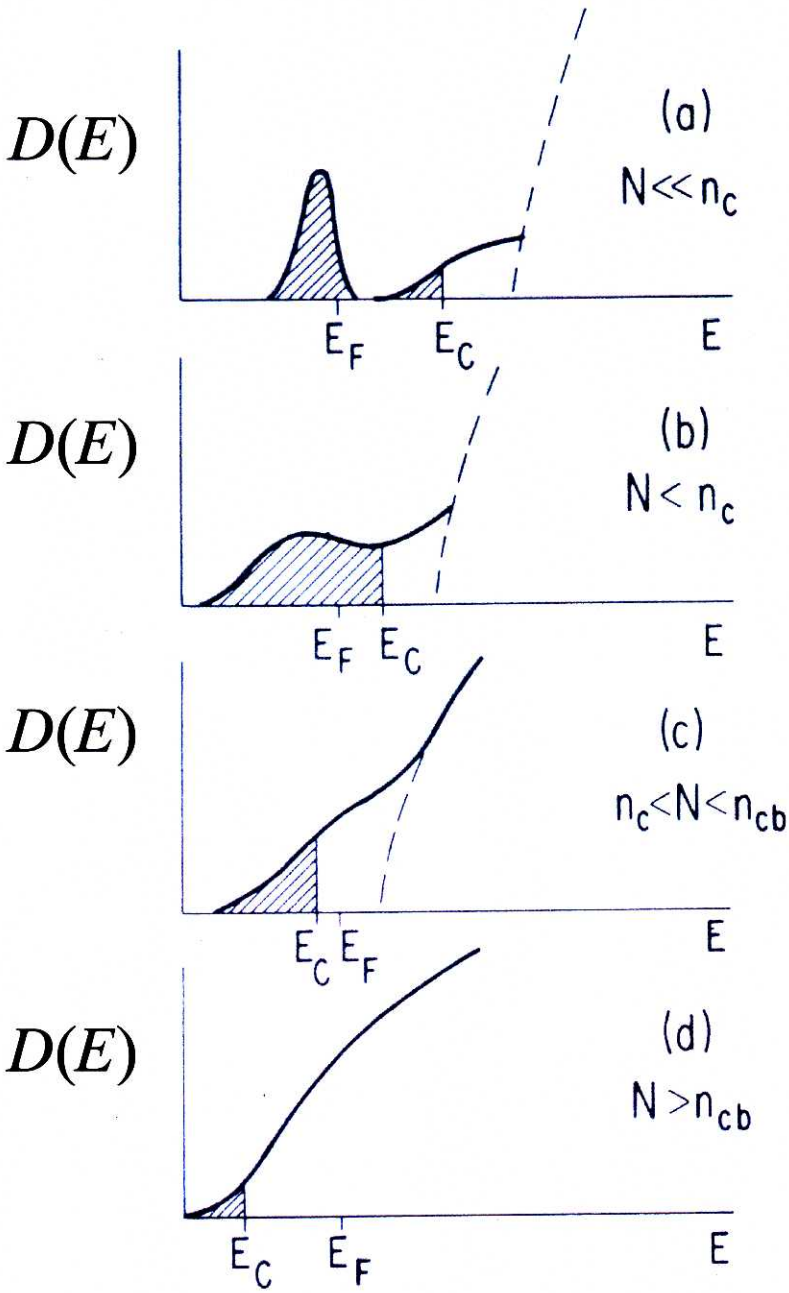

Fig. 2.20 Sketch of density-of-states $D(E)$ of a doped semiconductor corresponding to different concentration regimes. Shaded regions are localized states. N and E_c stand for an impurity concentration and the mobility edge. n_c and n_{cb} are the critical concentrations to divide impurity conduction ($E_F < E_C$), metallic impurity conduction ($E_F > E_C$) and true-metallic conduction. Ref. [2.38].

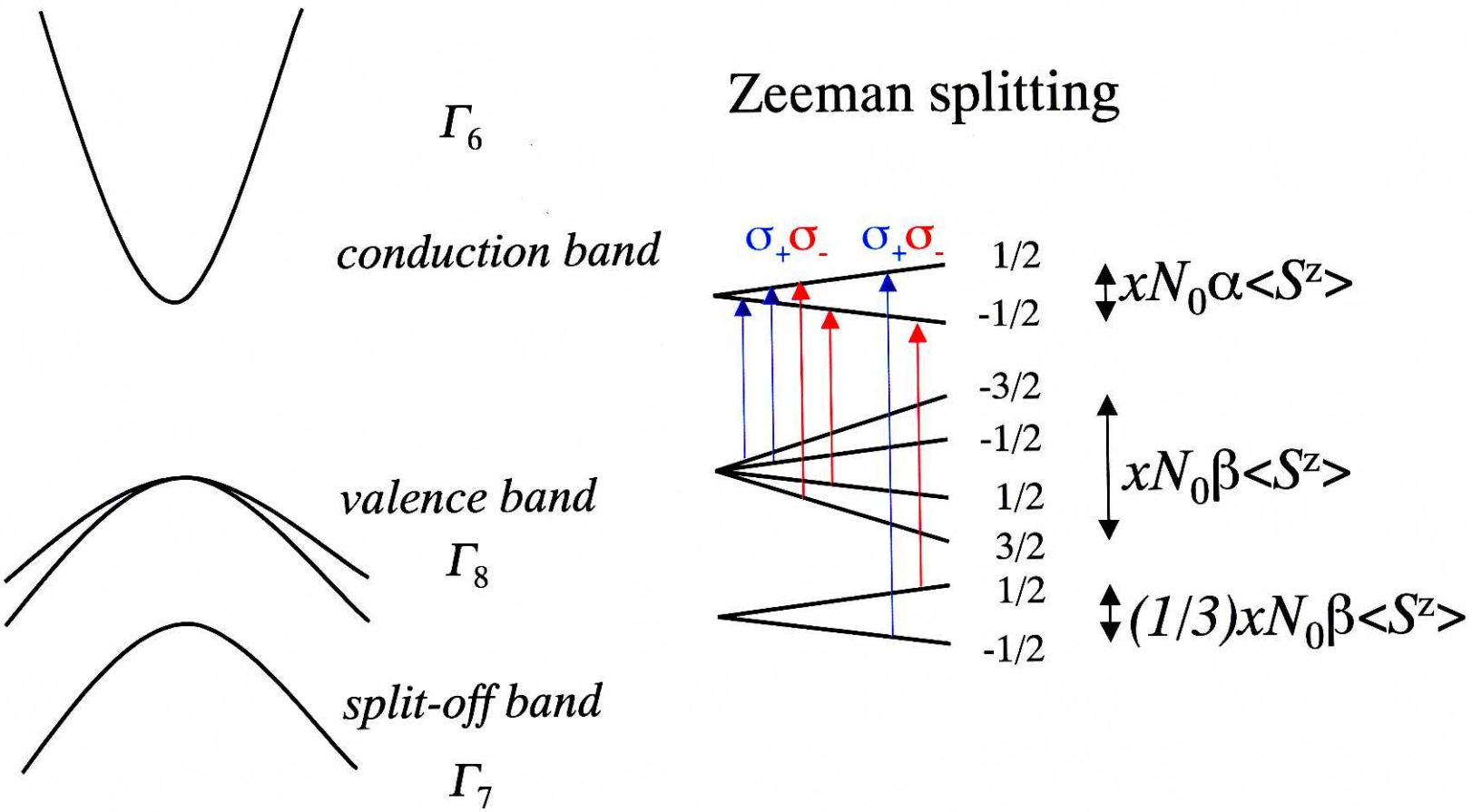

Fig. 2.21 Sketch of band diagram of zincblende type semiconductors and Zeeman splitting.

(a) *The band structure of GaAs*

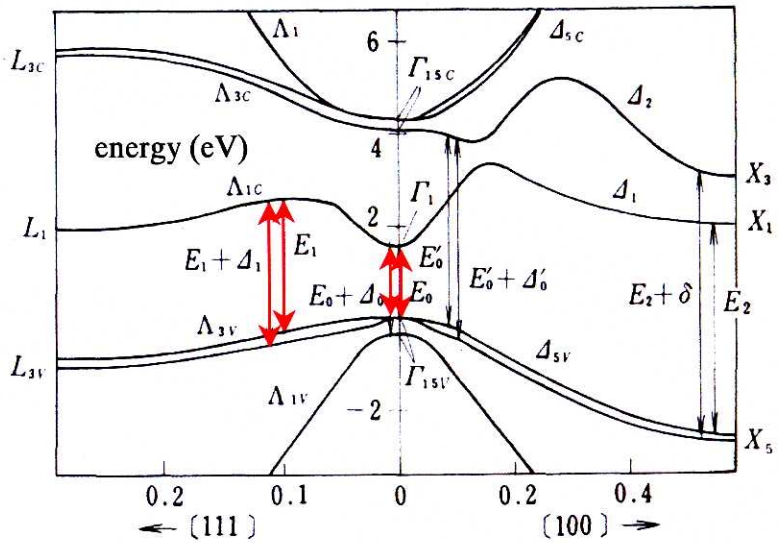

(b) *The MCD Spectrum of GaAs*

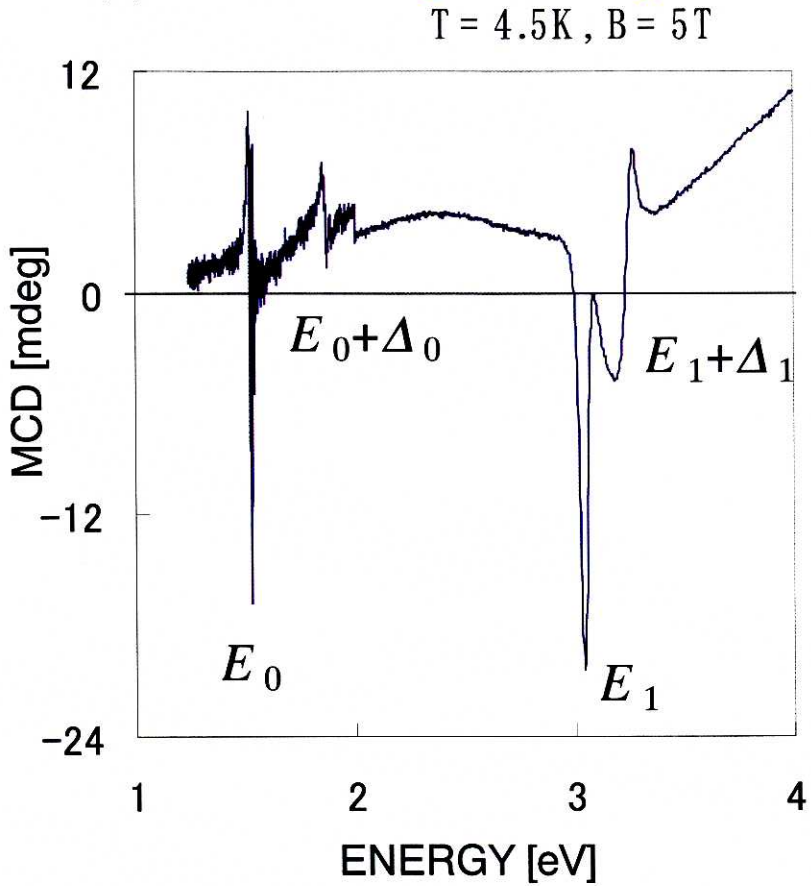

Fig. 2.22 The band structure and MCD spectrum of GaAs

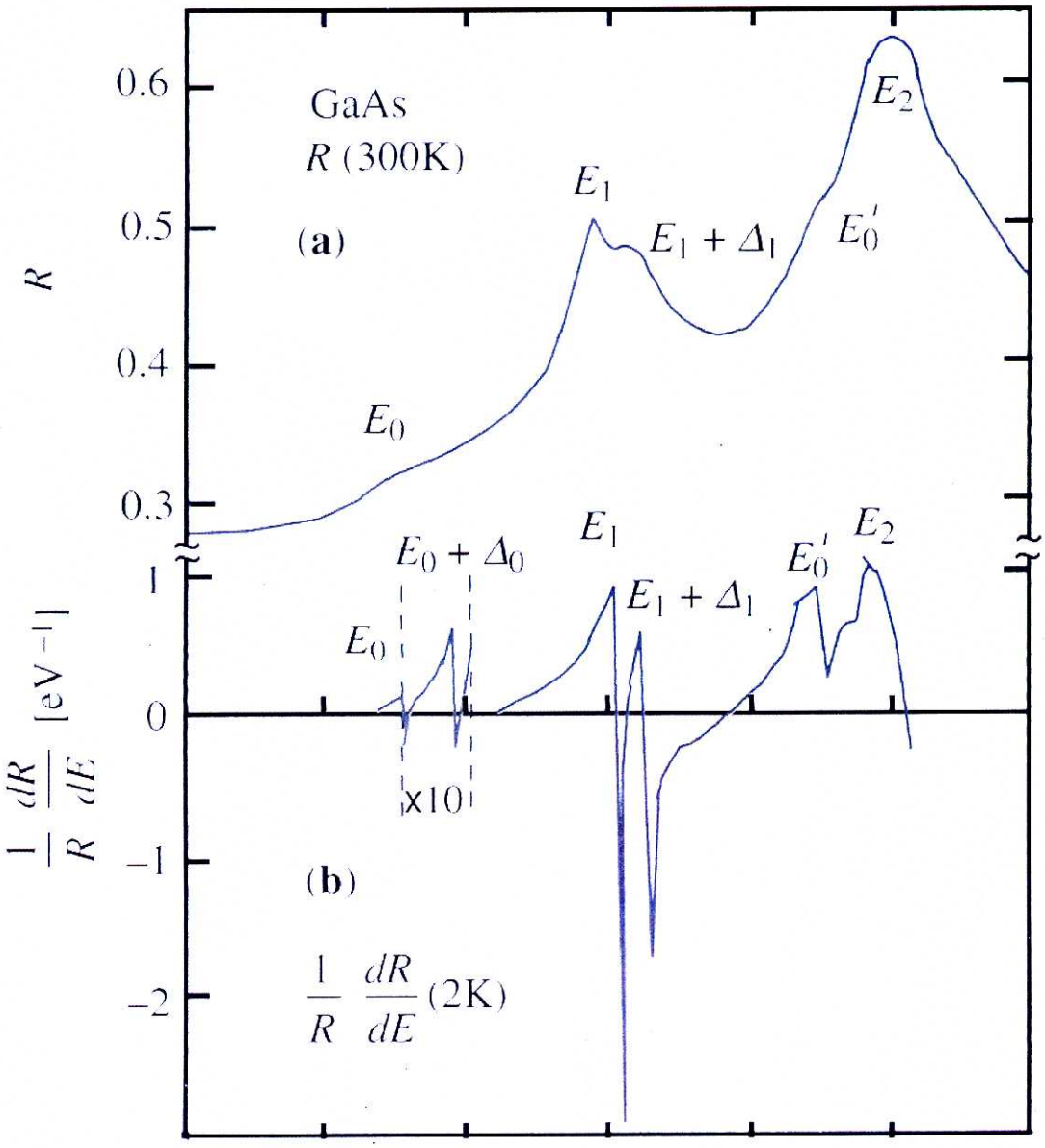

Fig. 2.23 Reflectance and frequency modulated reflectance spectra of GaAs (Ref.[2.50]).

Transition	Theory				Experiment	
	Critical Point	Non-local EPM	Local EPM	OPW	Reflectivity Structure	MCD Spectrum
E_0	1.52	1.51	1.52	1.34	1.52	1.53
$E_{0+}\Delta_0$	1.86	1.86	1.87	1.66	1.86	1.87
E_1	3.04	3.03	2.82	2.62	3.02	3.04
$E_{1+}\Delta_1$	3.25	3.25	3.05	2.82	3.25	3.27

Table 2.3 Comparison of theoretical and experimental critical point energies (in eV) for GaAs (Ref. [2.54]). The critical point energies estimated from the MCD spectrum in this work are also written in the table.

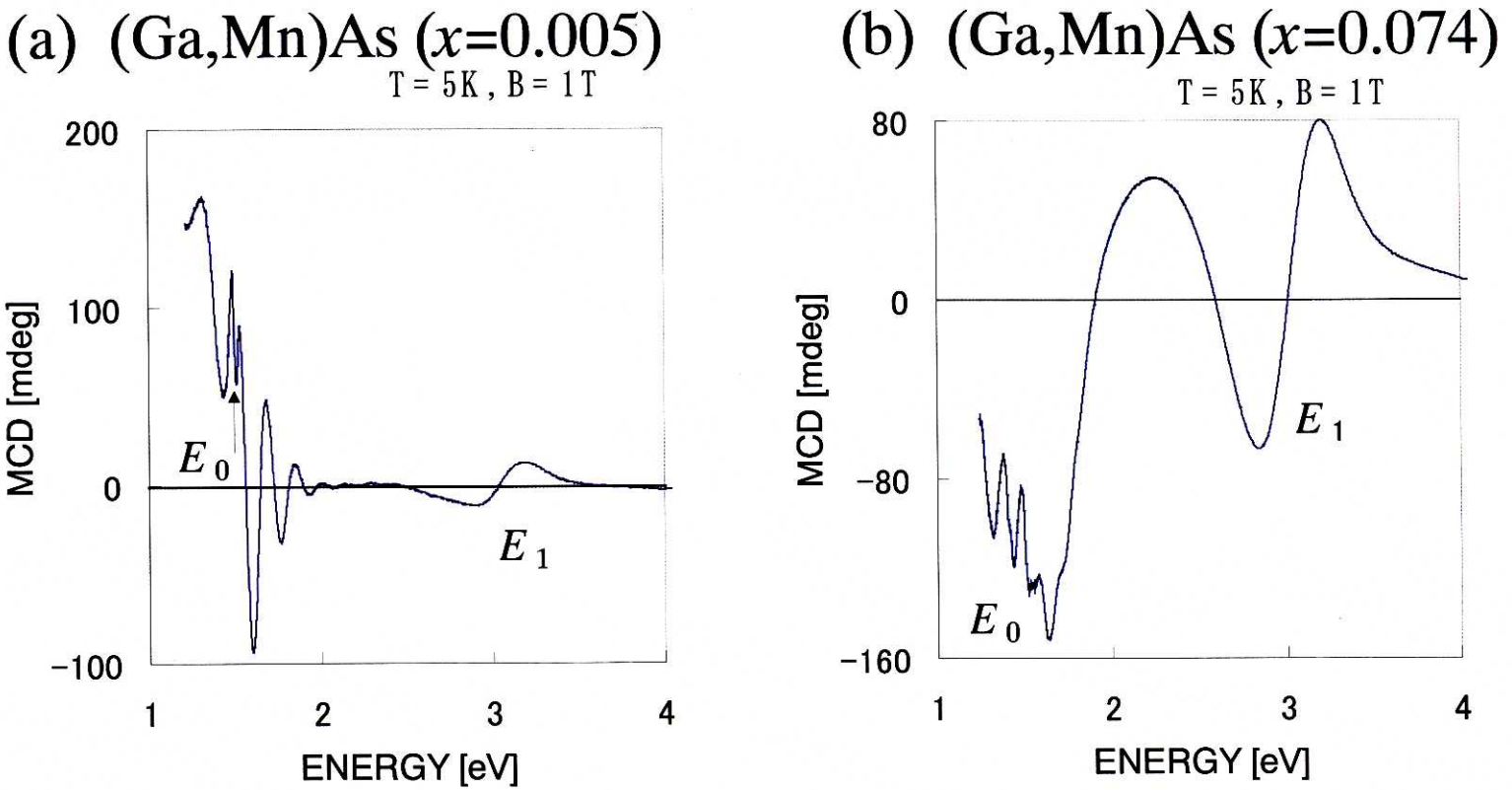

Fig. 2.24 MCD spectra of two GaMnAs films; (a) for B595 (x = 0.005) and (b) for B672 (x = 0.074).

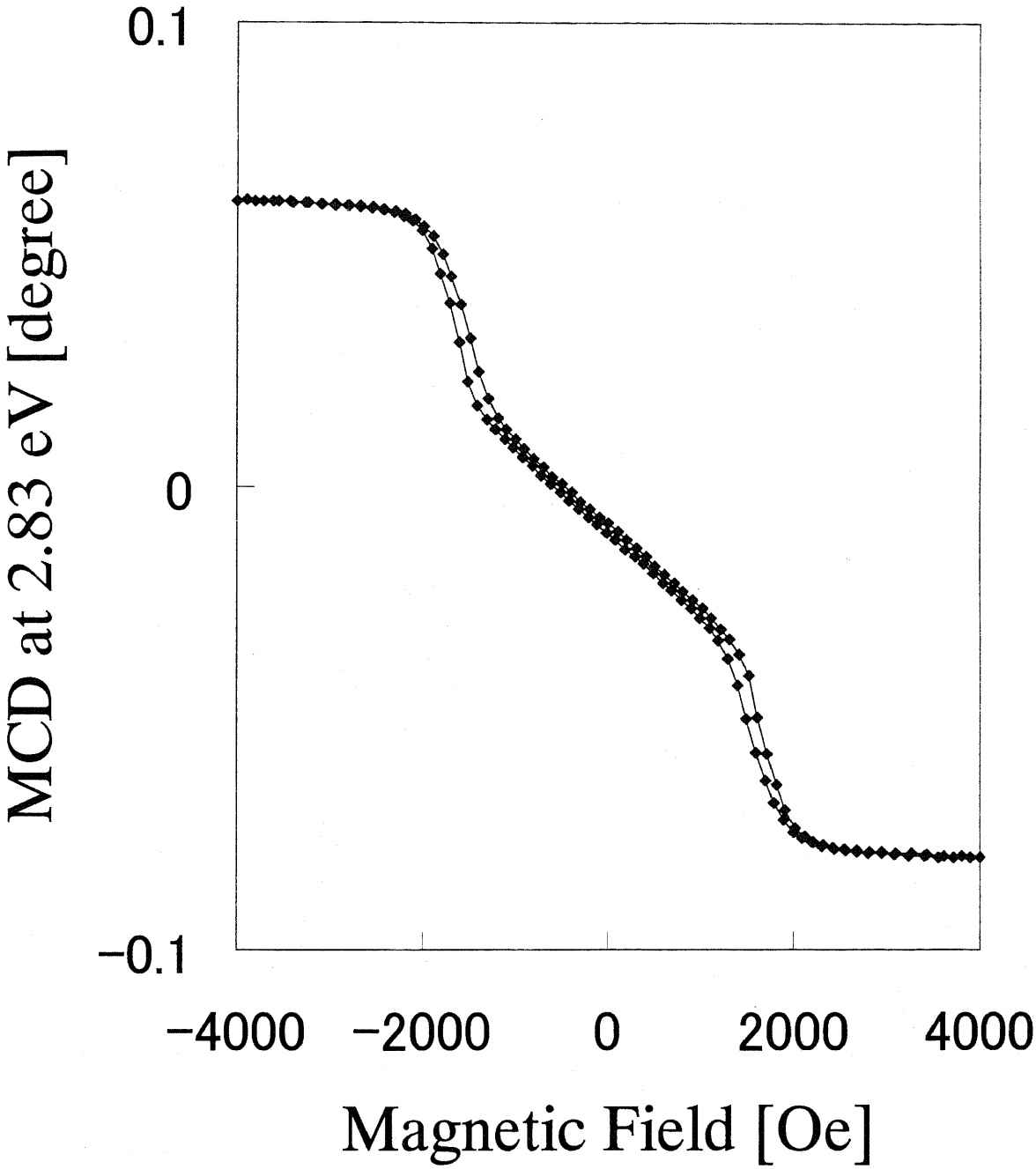

Fig. 2.25 Magnetic field dependence of E_1 MCD at 2.83 eV of GaMnAs (x =0.074) at T = 5 K.

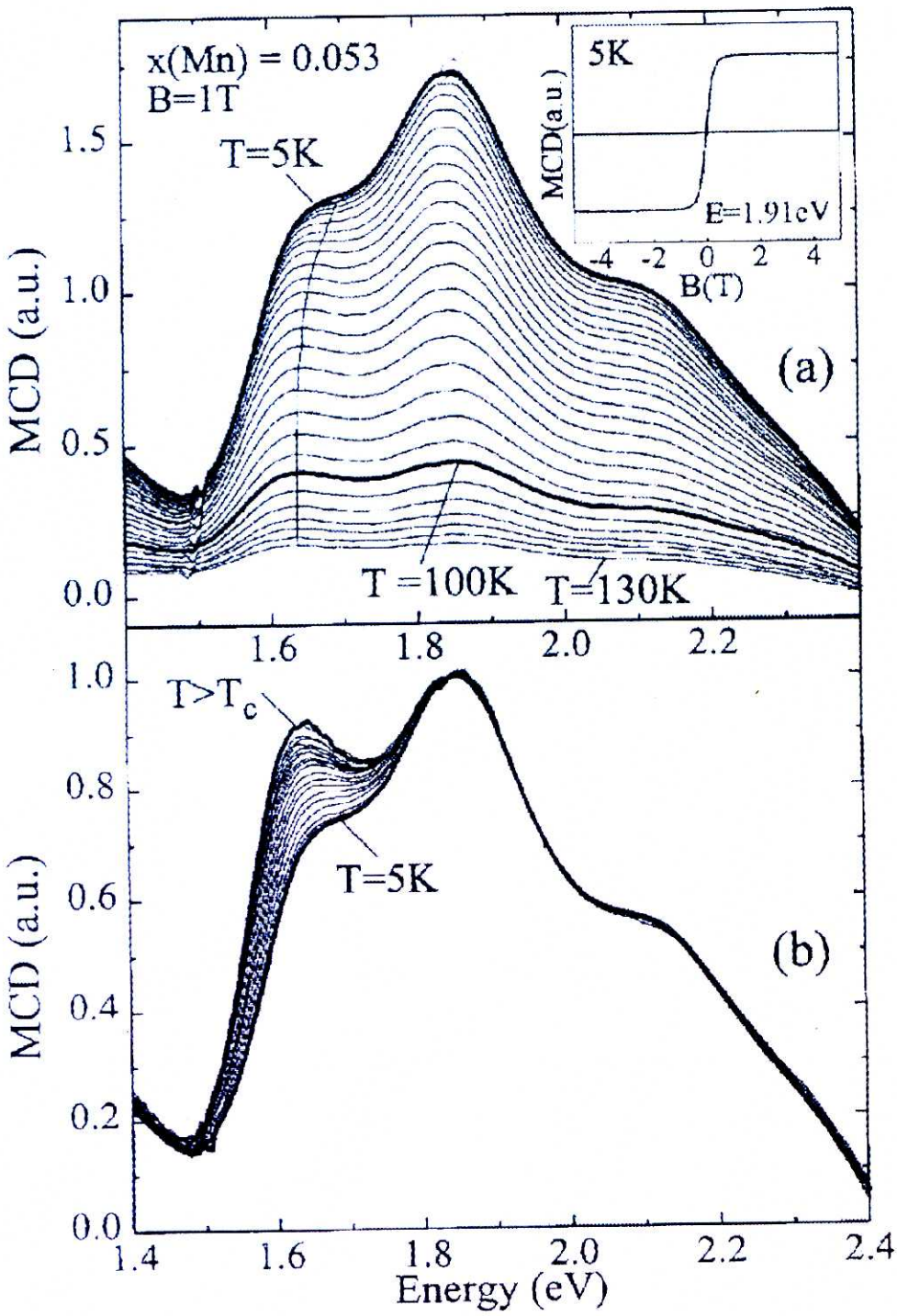

Fig. 2.26 Energy-dependnet MCD of GaMnAs as x = 0.053. (a) The MCD signal at B = 1 T at different temperatures ranging from 5 K (top curve) to 130 K (bottom curve) in steps of 5 K. A field sweep at T = 5 K and E =1.91 eV is shown in the inset. (b) MCD spectra taken from (a) normalized at 1.85 eV. After Beschoten et al. (Ref. [2.54]).

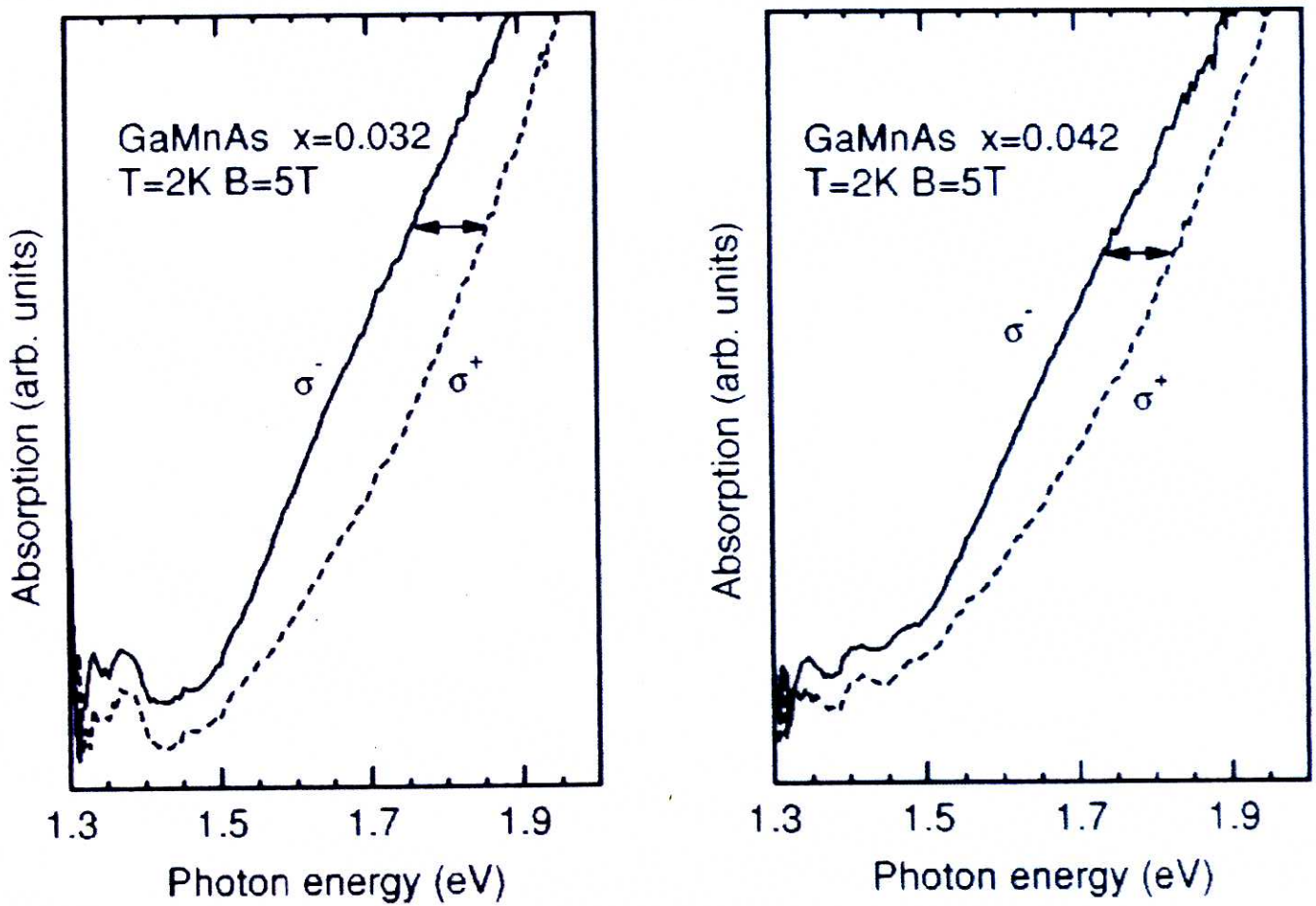

Fig. 2.27 Absorption edge of GaMnAs, x = 0.032 (left plot) and 0.042 (right plot) at T =2 K and magnetic field B = 5 T measured for σ^- and σ^+ polarized light. The double head arrow shows the splitting of the edge. After J. Szczytko et al. (Ref. [2.55]).

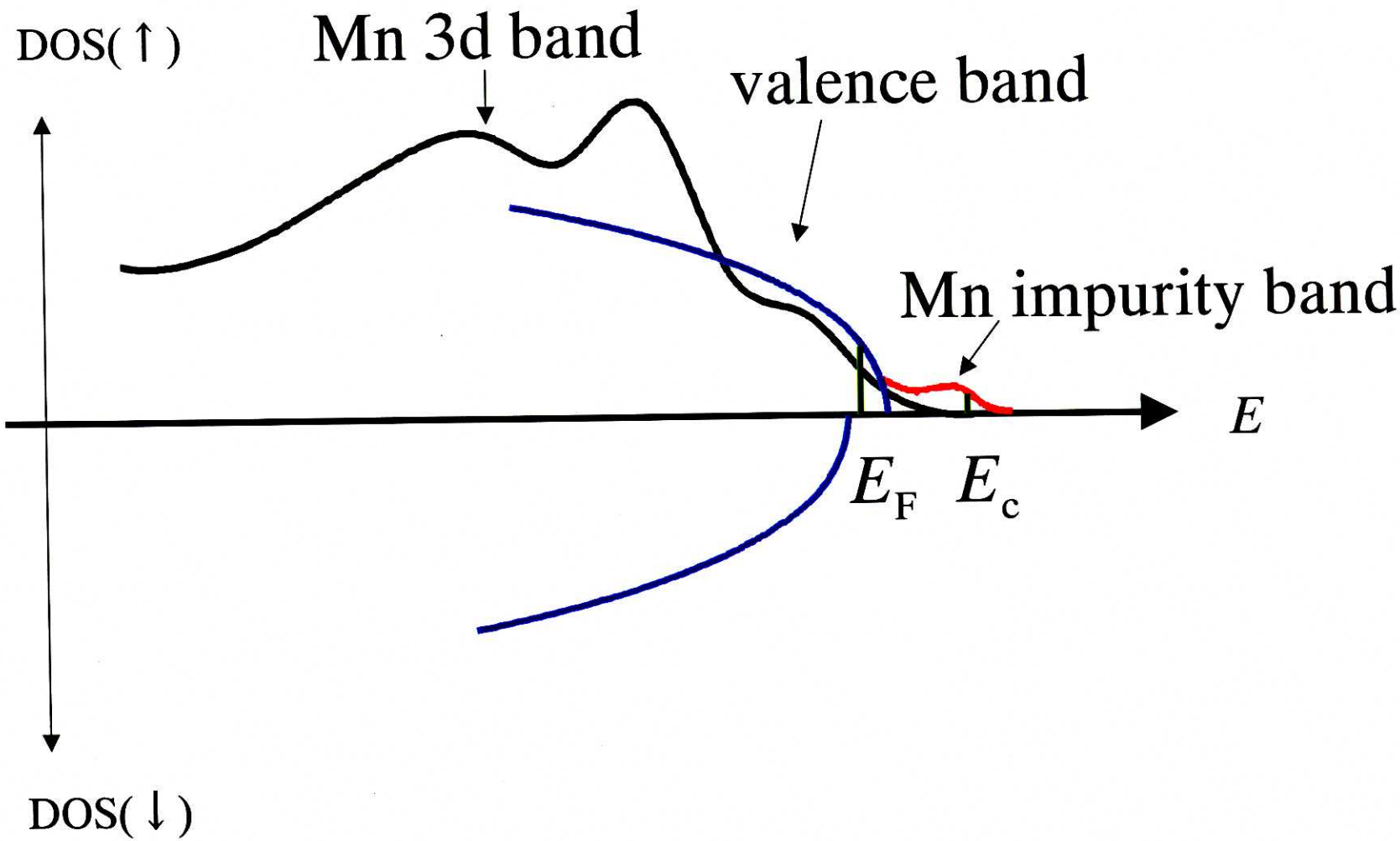

Fig. 2.28 Hypothetical density-of-states of GaMnAs. Mobility edge E_c is defined for holes.

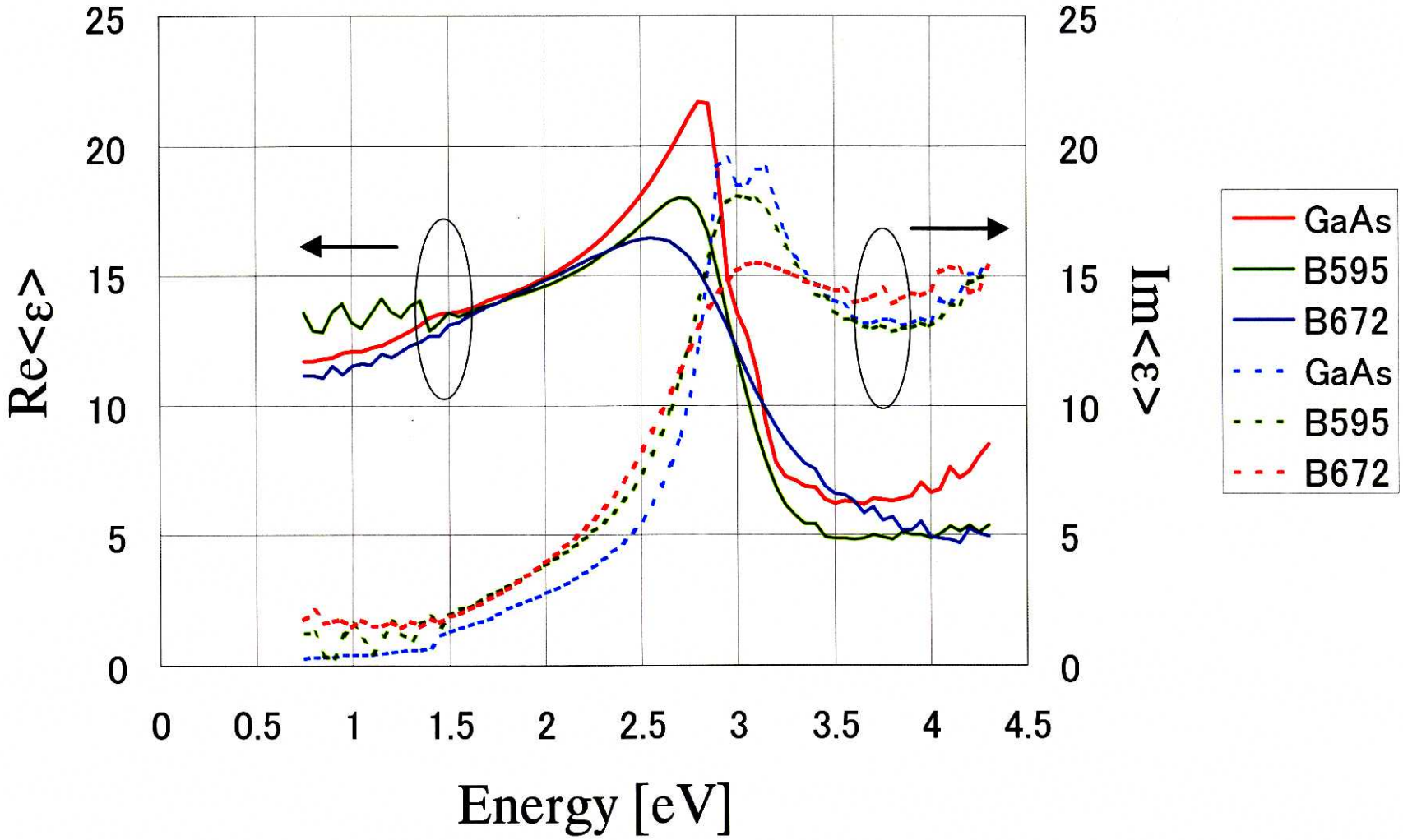

Fig. 2.29 Real and imaginary part of dielectric function of GaAs and GaMnAs measured by ellipsometry.

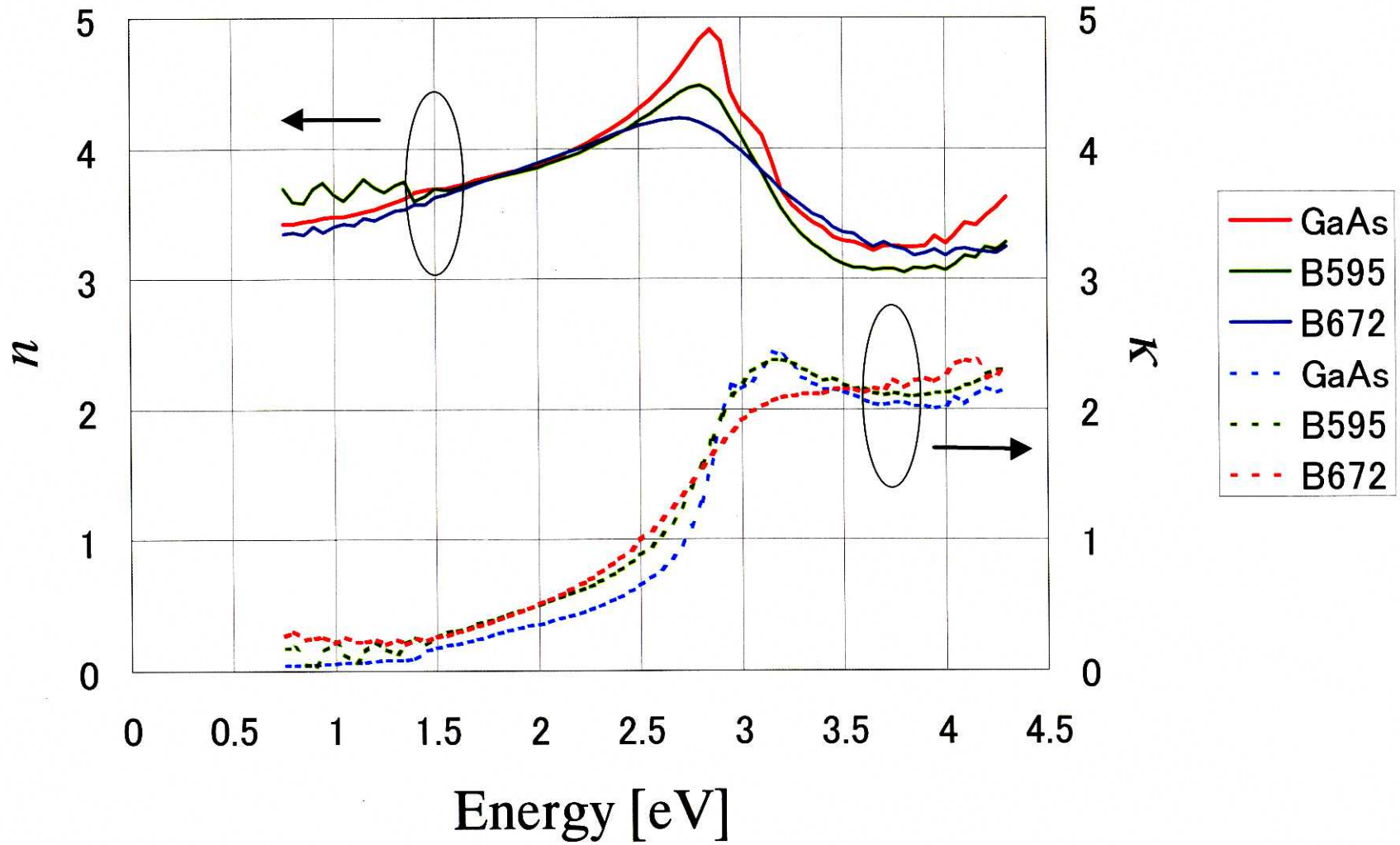

Fig. 2.30 Complex index of reflection of GaAs and GaMnAs measured by ellipsometry.

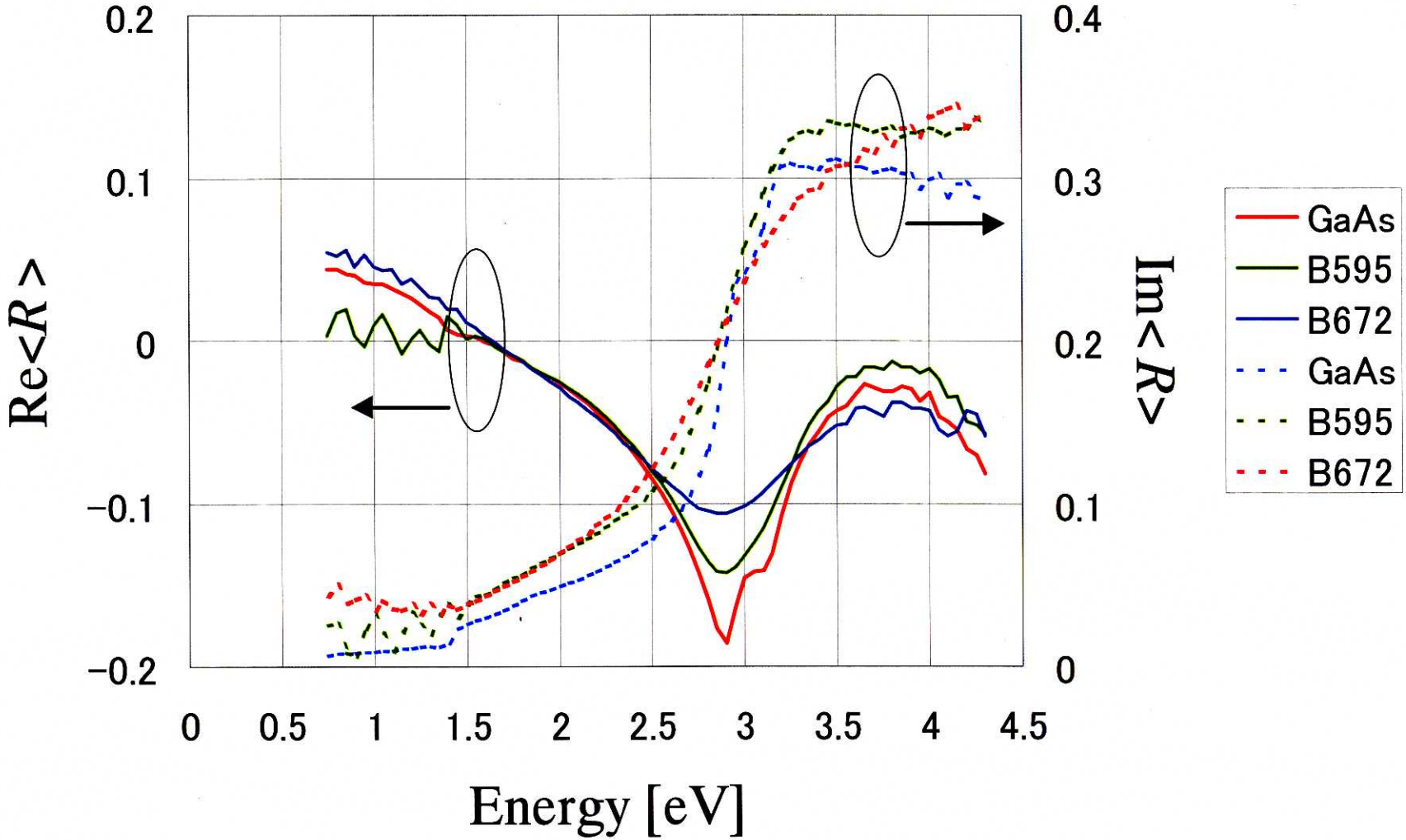

Fig. 2.31 Real and imaginary part of reflectivity of GaAs and GaMnAs measured by ellipsometry.

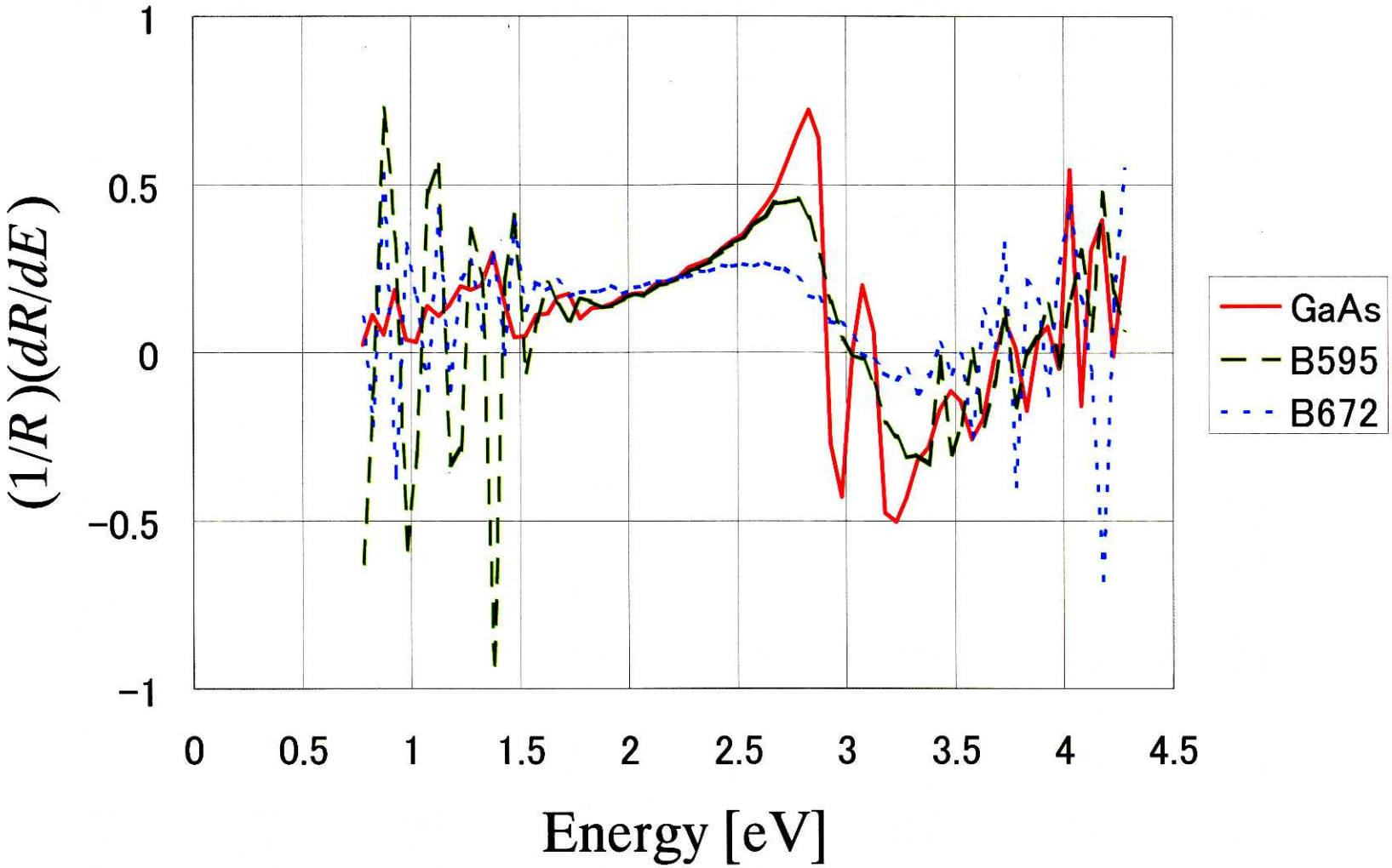

Fig. 2.32 Differential reflectivity of GaAs and GaMnAs calculated from the experimental complex dielectric function.

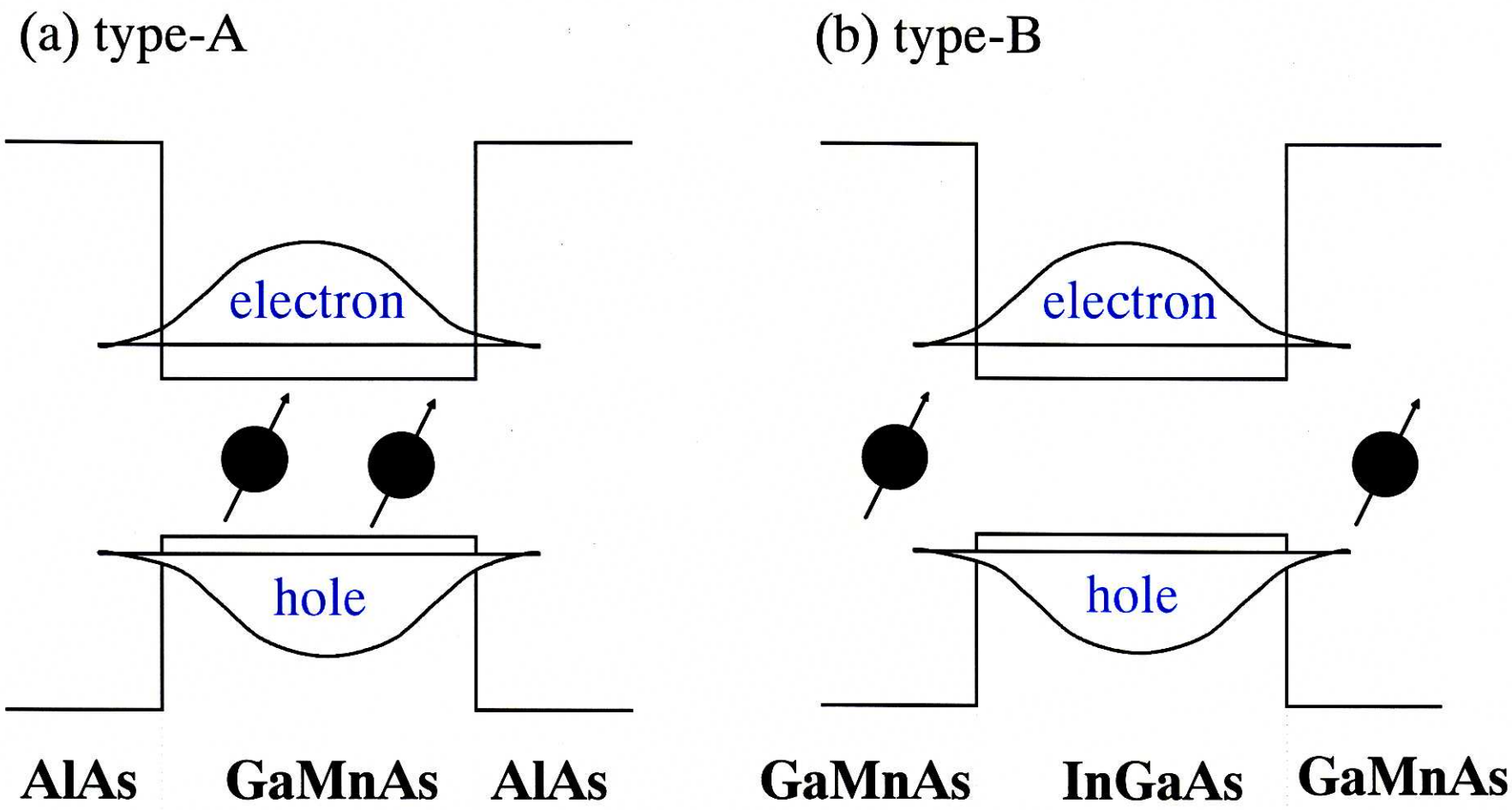

Fig. 3.1 Magnetic semiconductor heterostructures; (a) type-A and (b) type-B

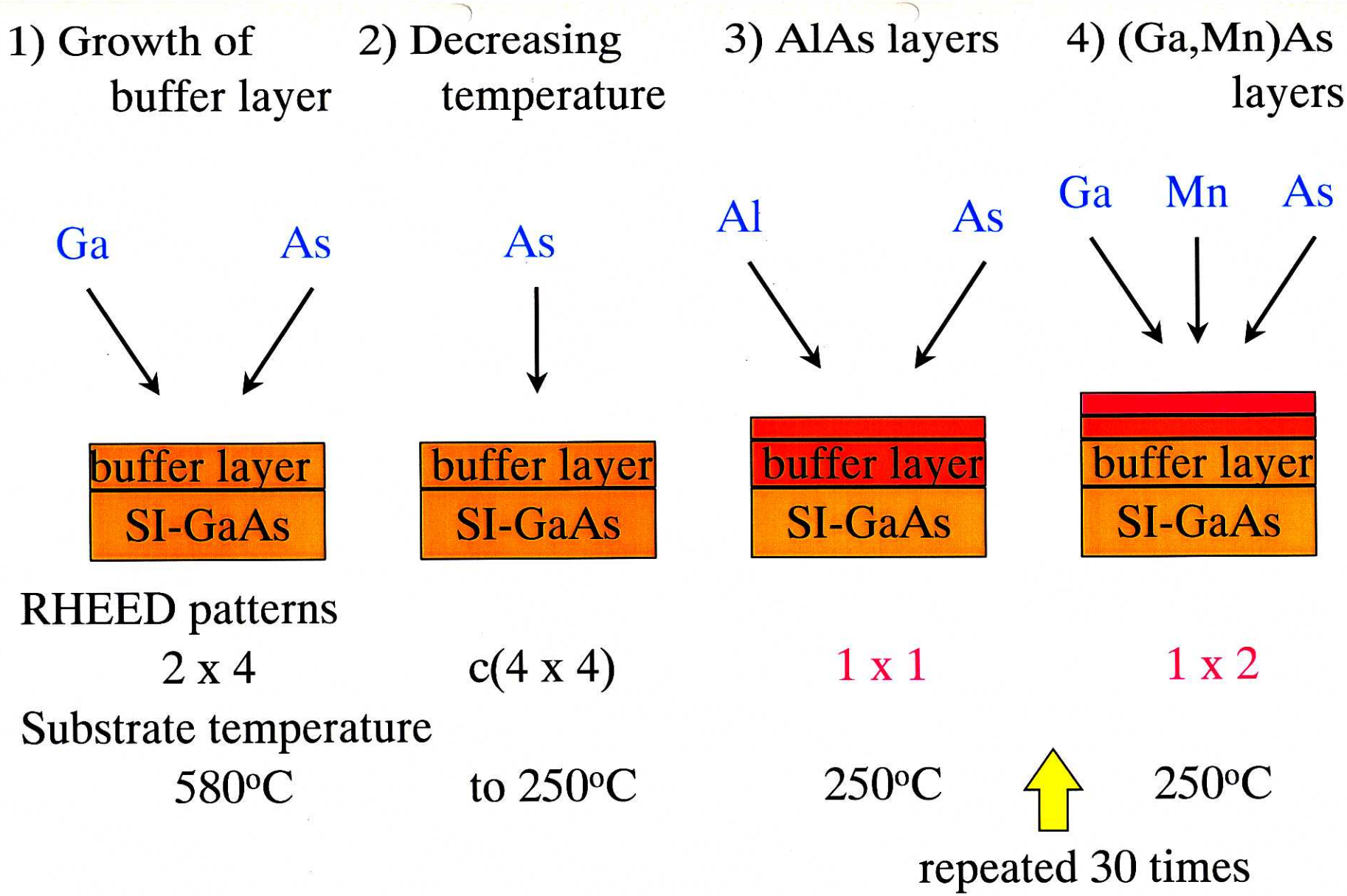

Fig. 3.2 Growth procedure of GaMnAs / AlAs superlattices by using LT-MBE.

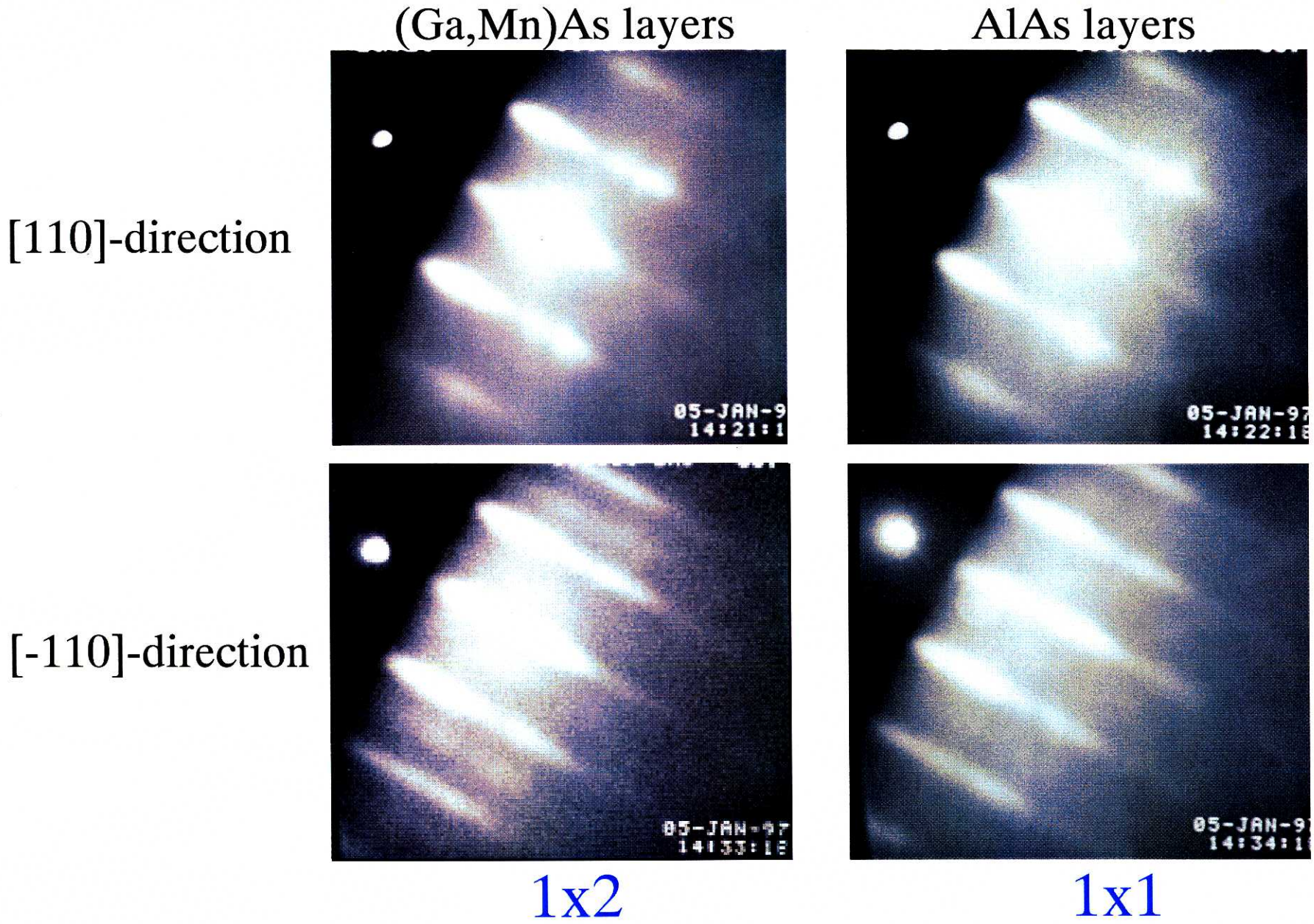

Fig 3.3 RHEED patterns of GaMnAs / AlAs superlattices during the growth

Periodic thickness

D=81.05Å

Calculated from satellite peaks positions

indicating the excellent controllability of the growth

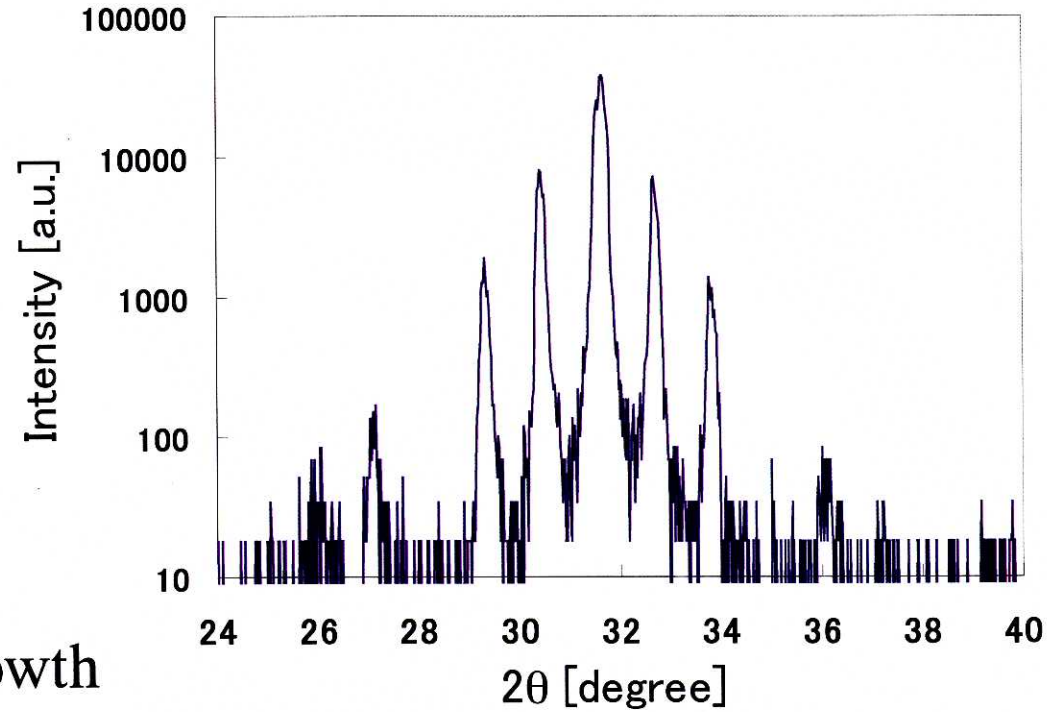

Fig. 3.4 X-ray diffraction (θ - 2θ) of a superlattice [GaMnAs (50Å, x = 0.047) / AlAs (30Å)] with 31 periods.

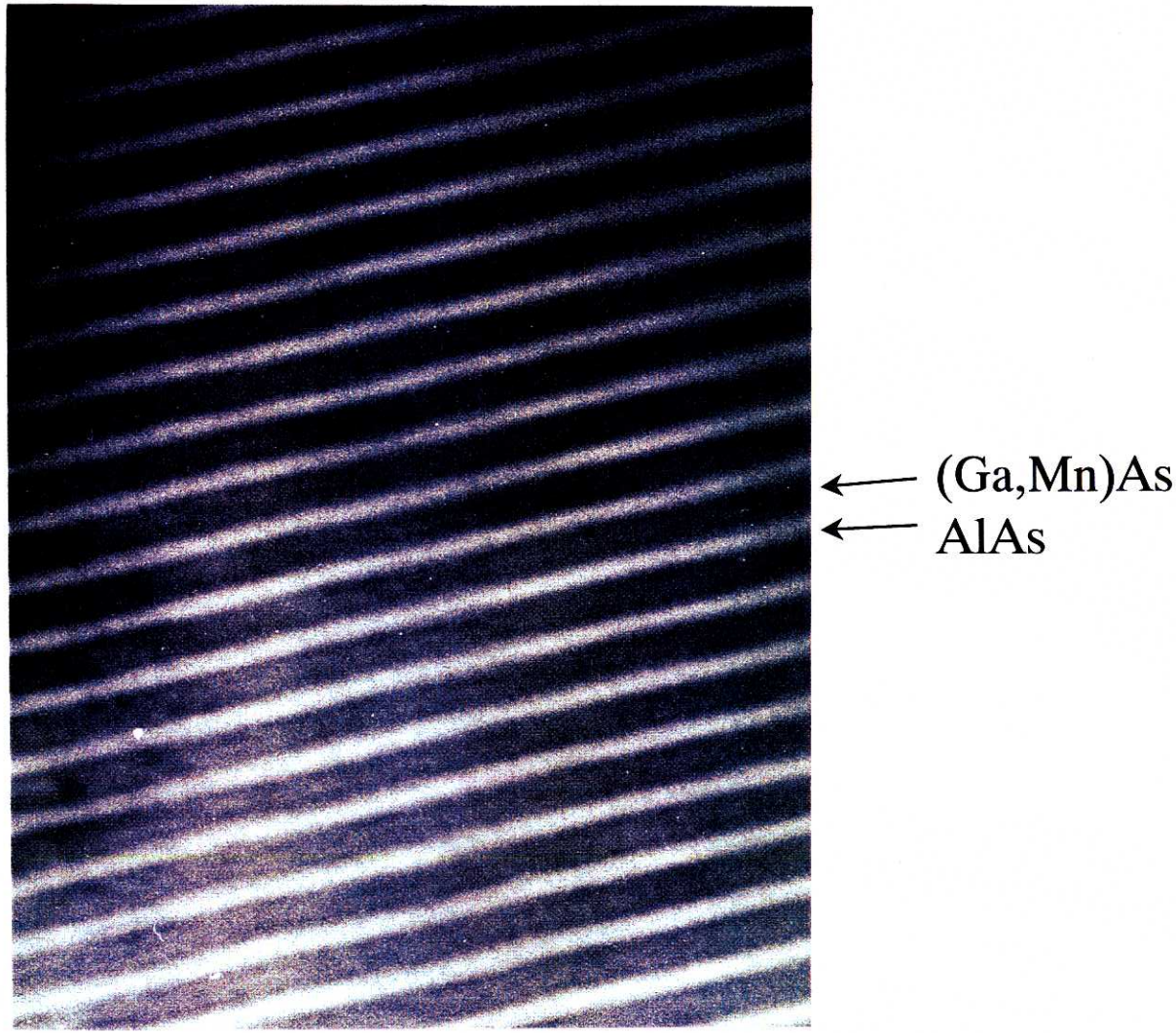

Fig. 3.5 Cross-sectional TEM image of a GaMnAs (50Å) / AlAs (30Å) sueprlattice.

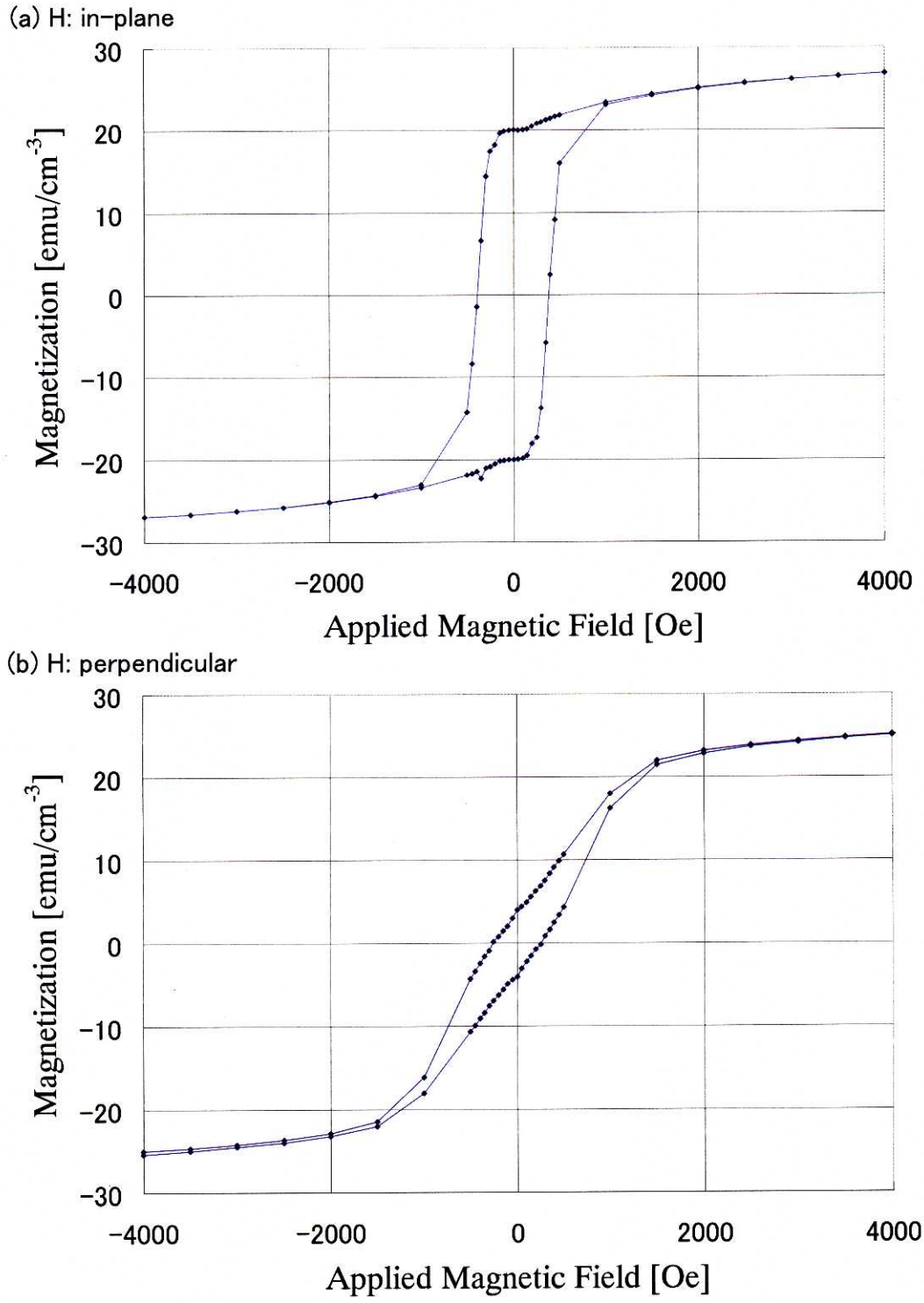

Fig. 3.6 Magnetization (*M-H*) curves of a superlattice [GaMnAs (120Å, x = 0.060) / AlAs (68Å)] with 31 periods measured by a SQUID at 2.0 K, when the magnetic field was applied (a) in plane and (b) perpendicular to the plane, respectively.

	x	H_c	M_r	M_s	effective I	T_c
B672 (single)	0.074	56 Oe	23.7 emu/cm^{-3}	34.9 emu/cm^{-3}	2.30μB	60.0K
B734 (SL)	0.060	380 Oe	20.8 emu/cm^{-3}	33.2 emu/cm^{-3}	2.70 μB	62.5K

Table 3.1 Comparison of magnetic properties of a 1.4μm-thick GaMnAs single layer (Fig. 2.7) and a GaMnAs (120Å) / AlAs (68Å) SL (Fig. 3.6).

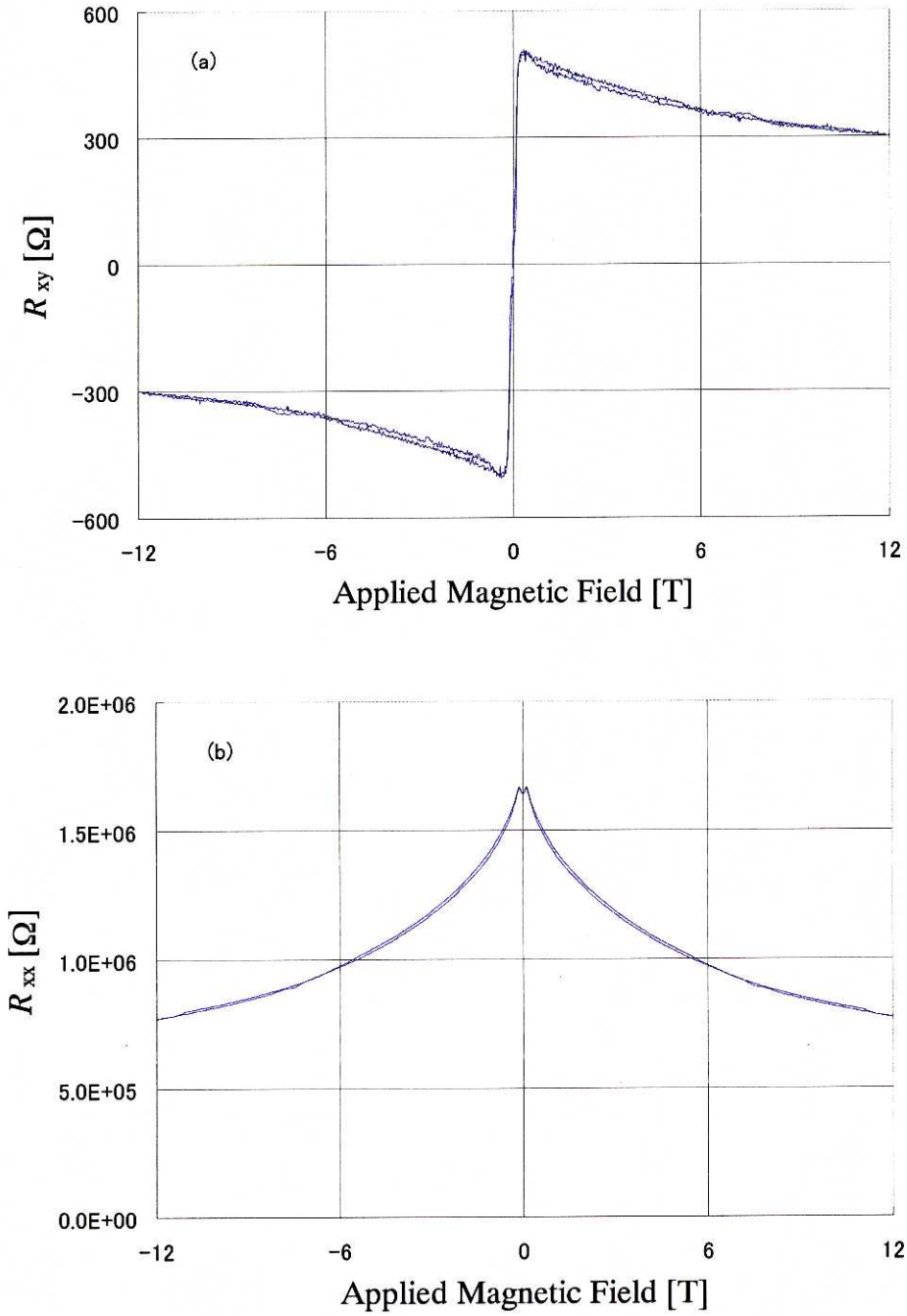

Fig. 3.7 Magnetic field dependence of (a) Hall resistance R_{xy} and (b) the resistance R_{xx} at zero field of a GaMnAs (70Å, x = 0.049) / AlAs (30Å) SL sample. The field was applied perpendicular to the film plane.

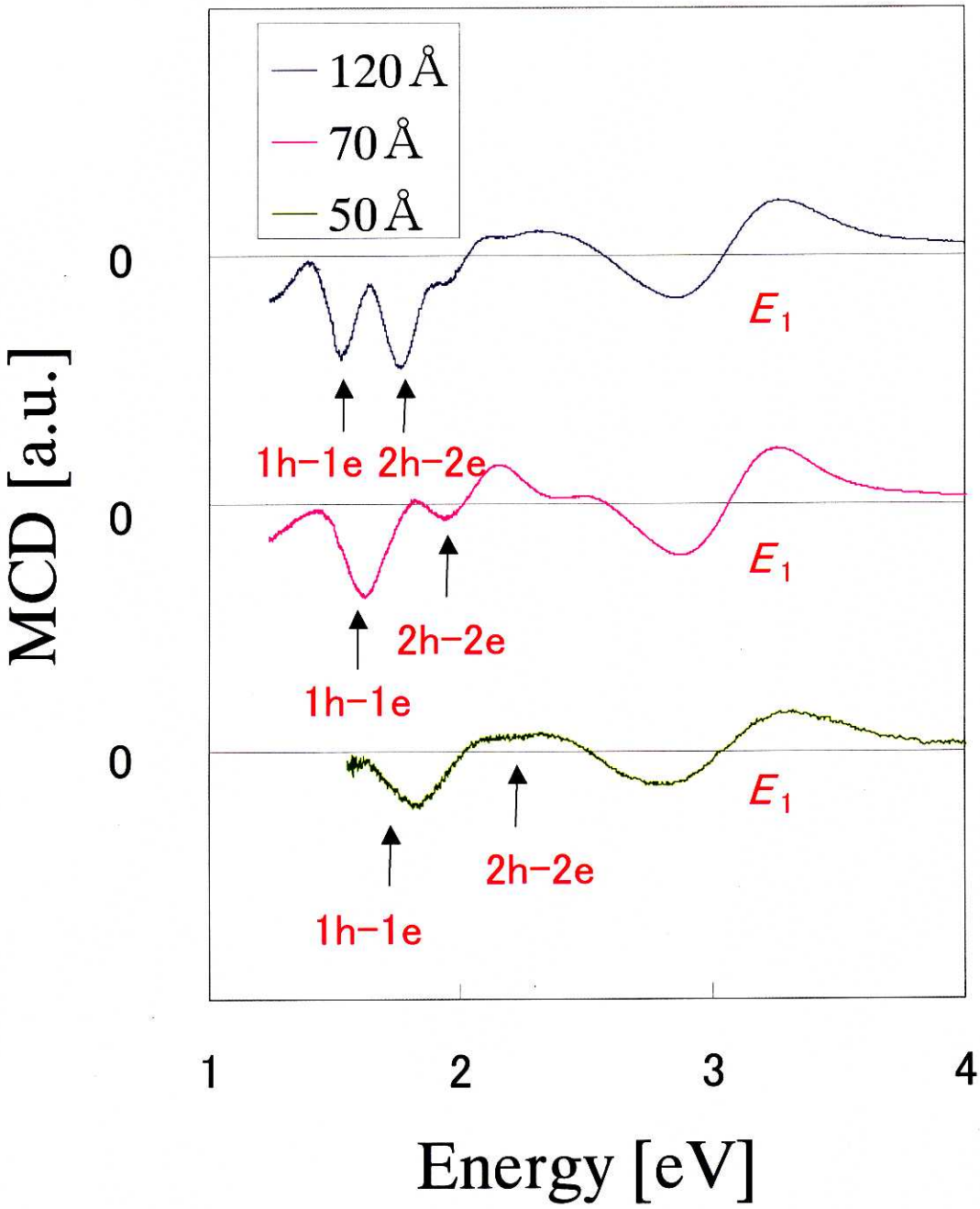

Fig. 3.8 MCD spectra of GaMnAs / AlAs SLs with 31 periods measured at 5 K under a magnetic field of 1 T perpendicular to the plane. The nominal thickness of GaMnAs and AlAs and the Mn concentration x in the SLs were (a) 120 Å, 68 Å, x = 0.06, (b) 70 Å, 30 Å, x = 0.049, (c) 50 Å, 30 Å, x = 0.047, respectively. The spectrum of (c) is magnified by 5 times.

Sample name	B734	B739	B740
Well width [Å]	120	70	50
Barrier width [Å]	68	30	30
Mn concentration *x*	0.06	0.049	0.047
1e-1h (Kronig-Penny;5K)	1.56	1.62	1.7
1e-1h (MCD;5K)	1.52	1.62	1.81
2e-2h (Kronig-Penny;5K)	1.70	1.99	2.21
2e-2h (MCD;5K)	1.76	1.93	-

Table 3.2 Comparison between the transition energies calculated from the Kronig-Penny model and the MCD peak energies

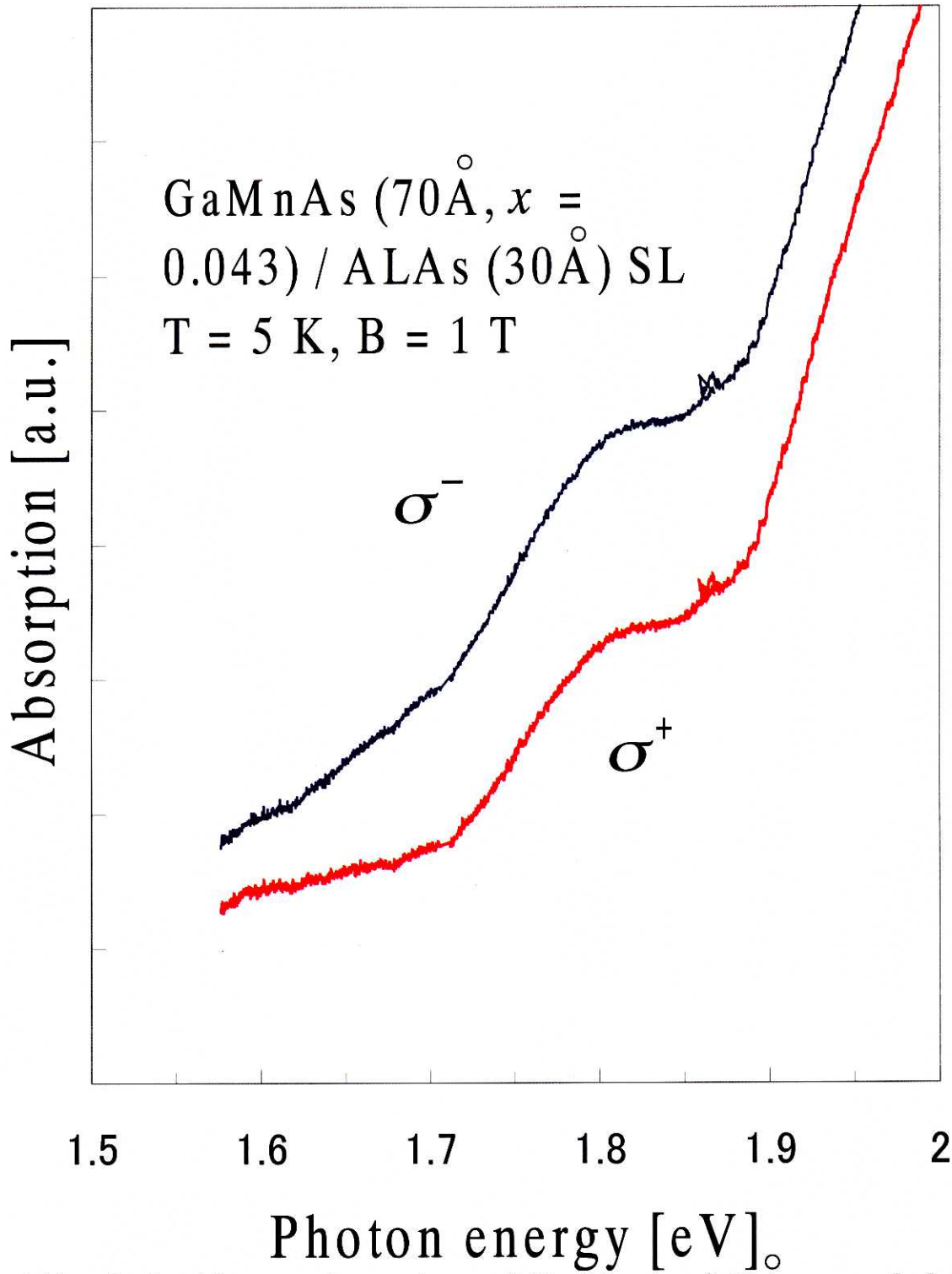

Fig. 3.9 Absoprtion edge of GaMnAs (70Å, x = 0.043) / AlAs (30Å) at T = 5K and magnetic field B = 1T measured for σ- and σ+ polarized light. After H. Shimizu et al. (Ref.[3.9]).

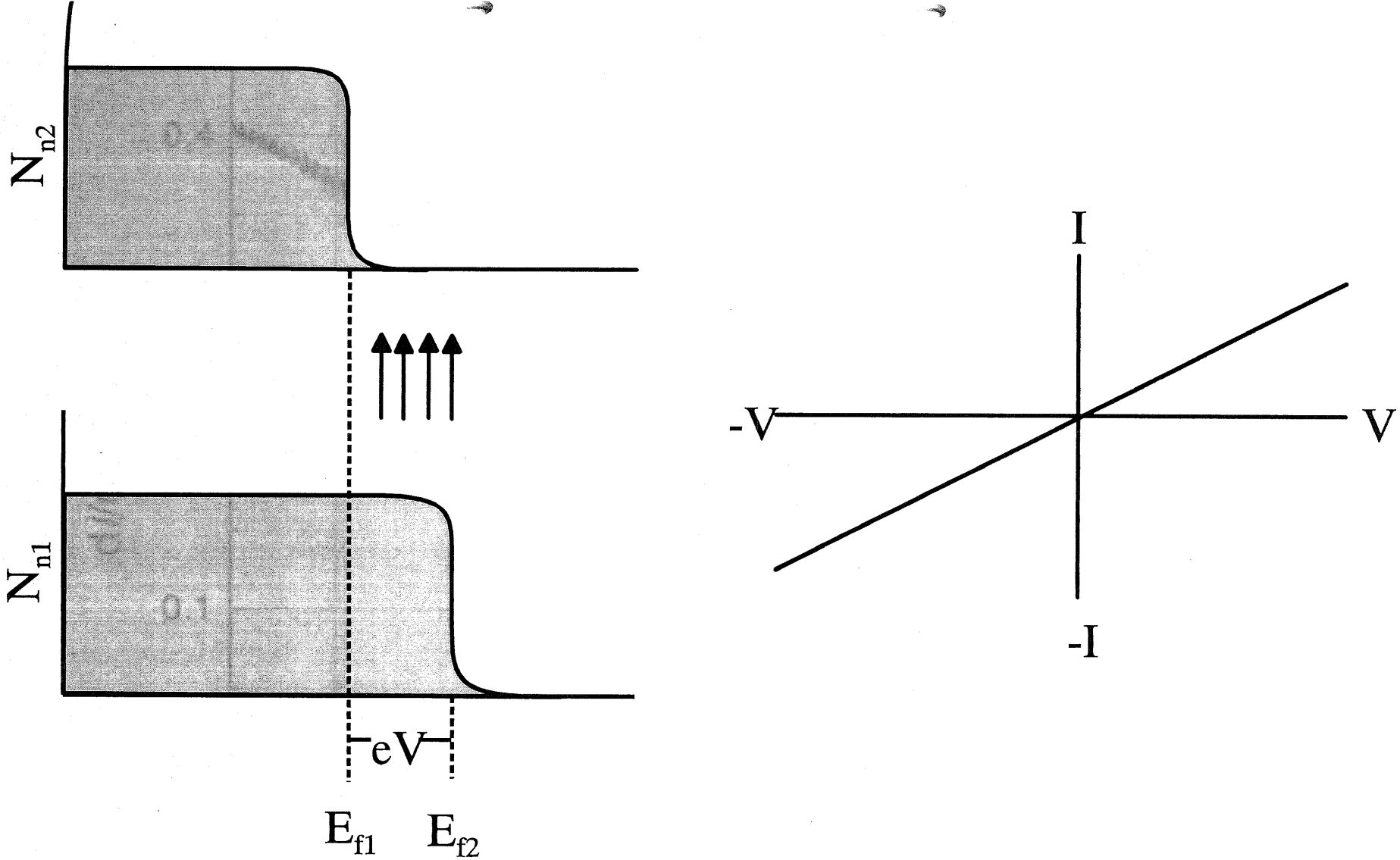

Fig. 4.1 Linear (Ohmic) *I-V* tunneling characteristic. Ref. [4.6]

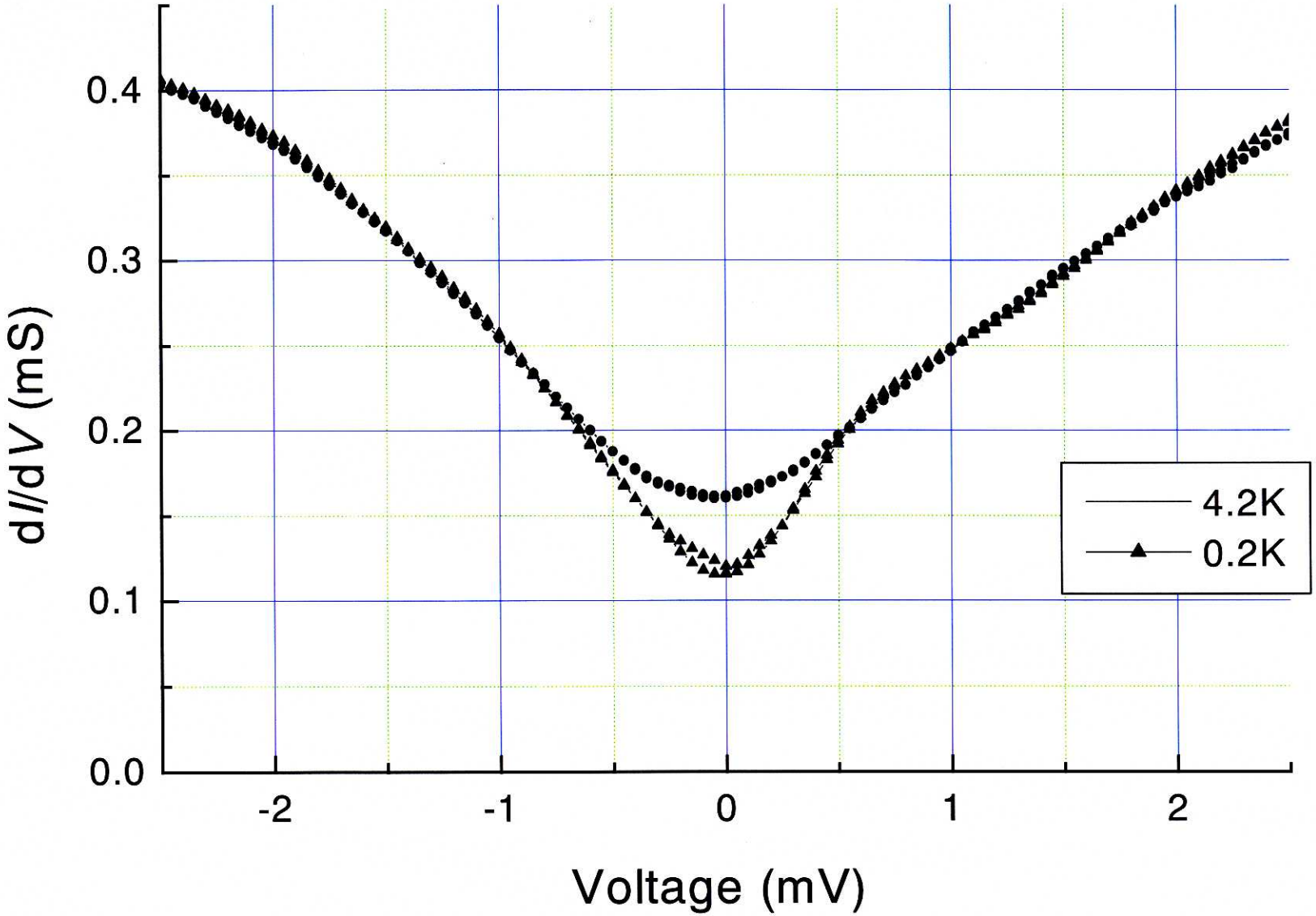

Fig. 4.2 *dI/dV-V* characteristic of Au / Al_2O_3 / GaMnAs tunnel junction at 4.2K and 0.2K.

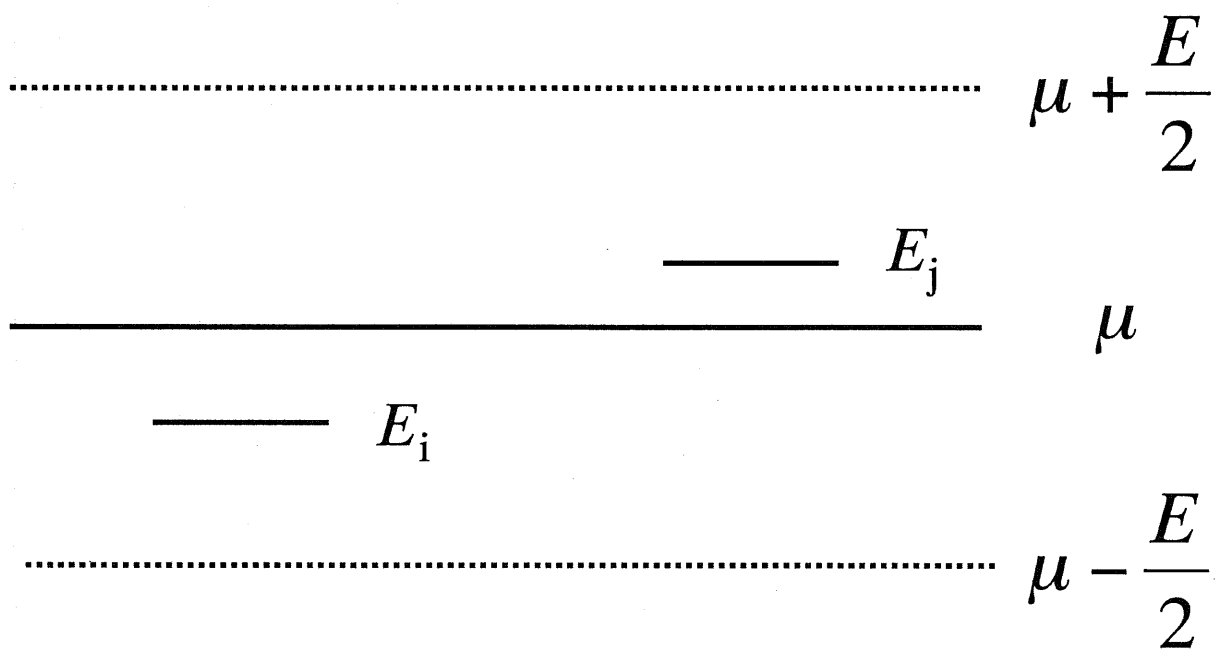

Fig. 4.3 Energy diagram near the Fermi level. Ref. [4.13]

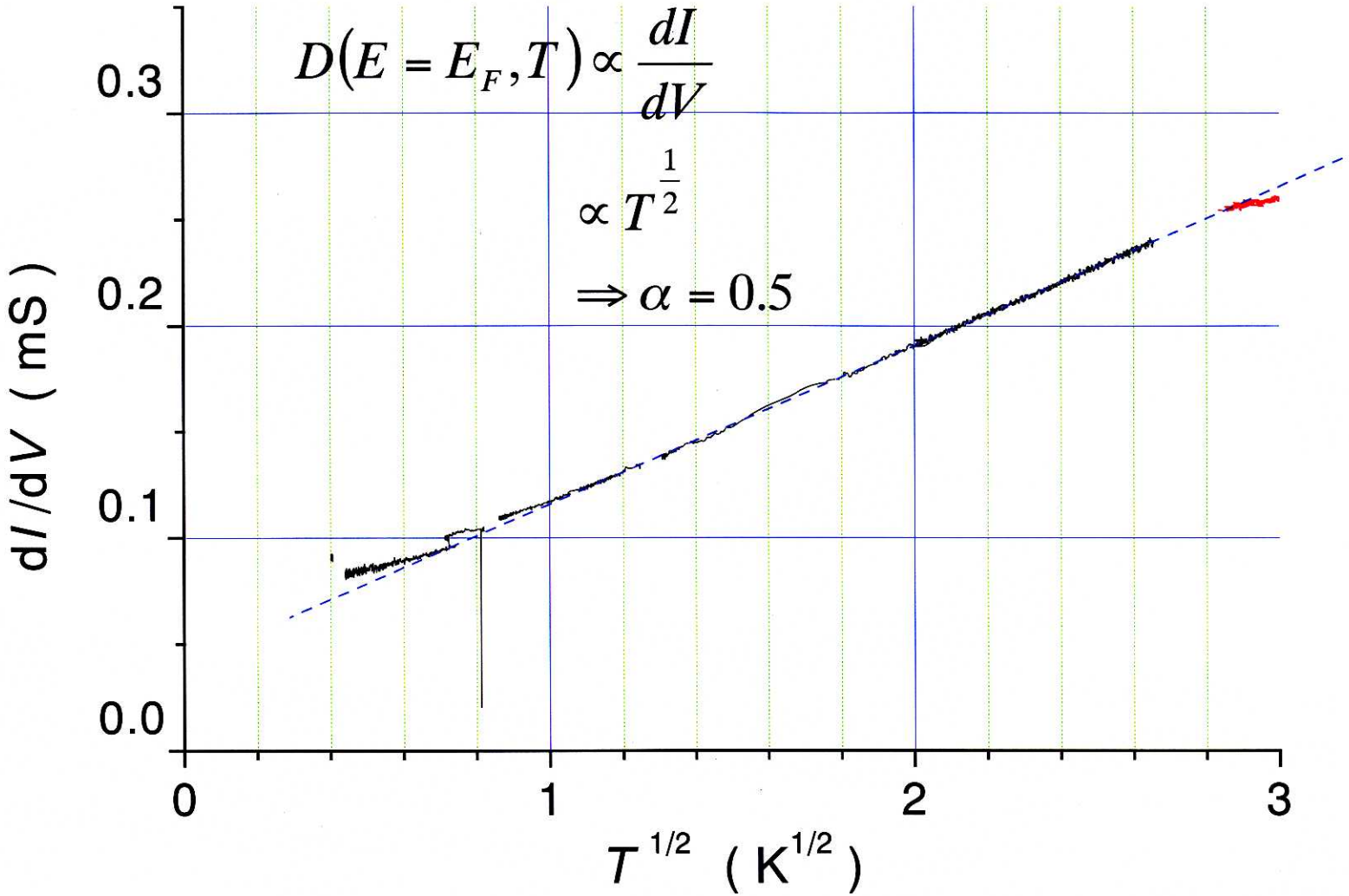

Fig. 4.4 Temperature dependence of the conductance *dI*/*dV* of a Au / Al_2O_3 / GaMnAs tunnel junction.

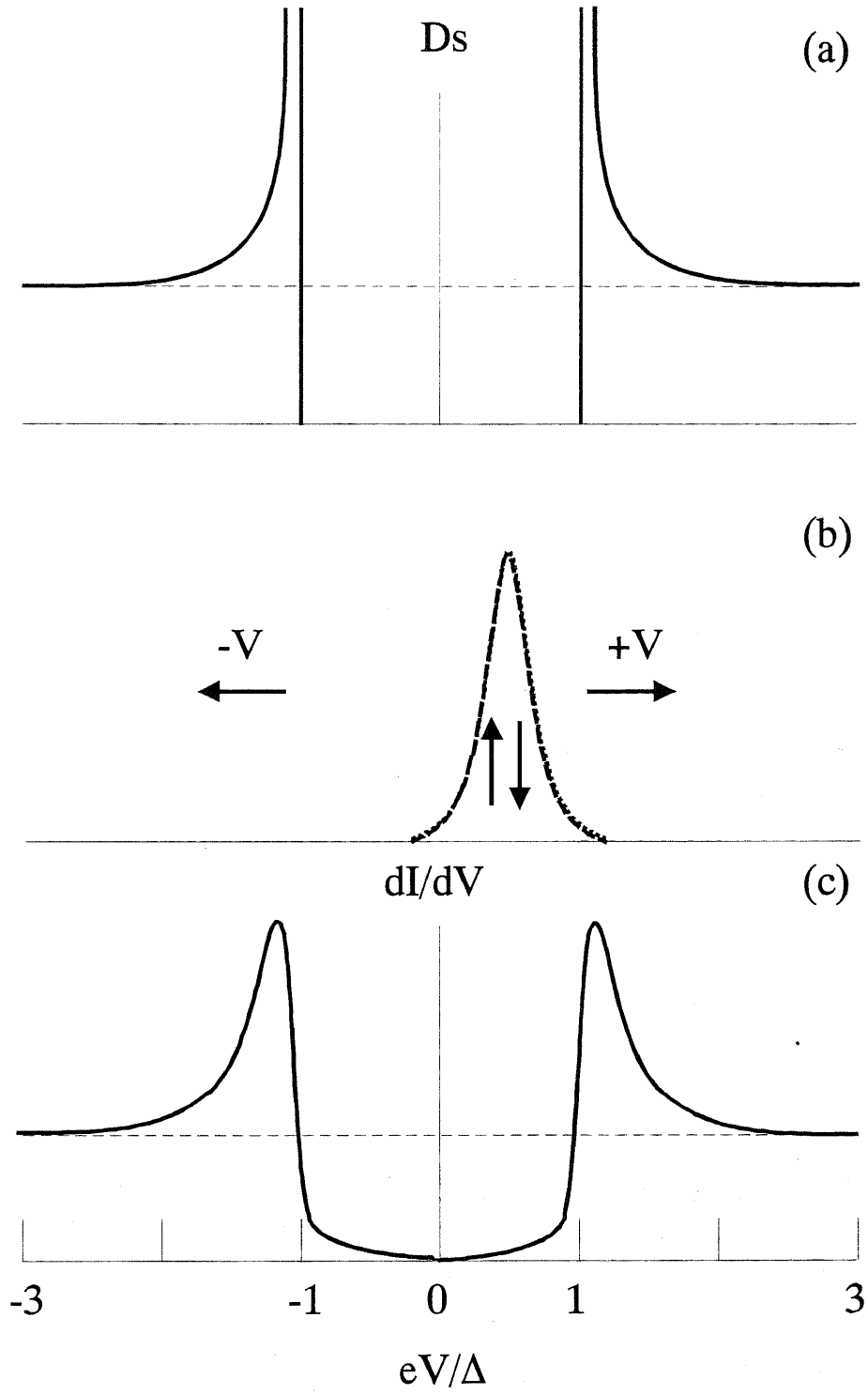

Fig. 4.5 Superconductor-normal metal tunneling. (a) BCS density-of-states of a superconductor as a function of voltage. (b) the product of density-of-states of a normal metal with the derivative of the Fermi function. (c) Theoretical normalized conductance d*I*/d*V*. Ref. [4.6]

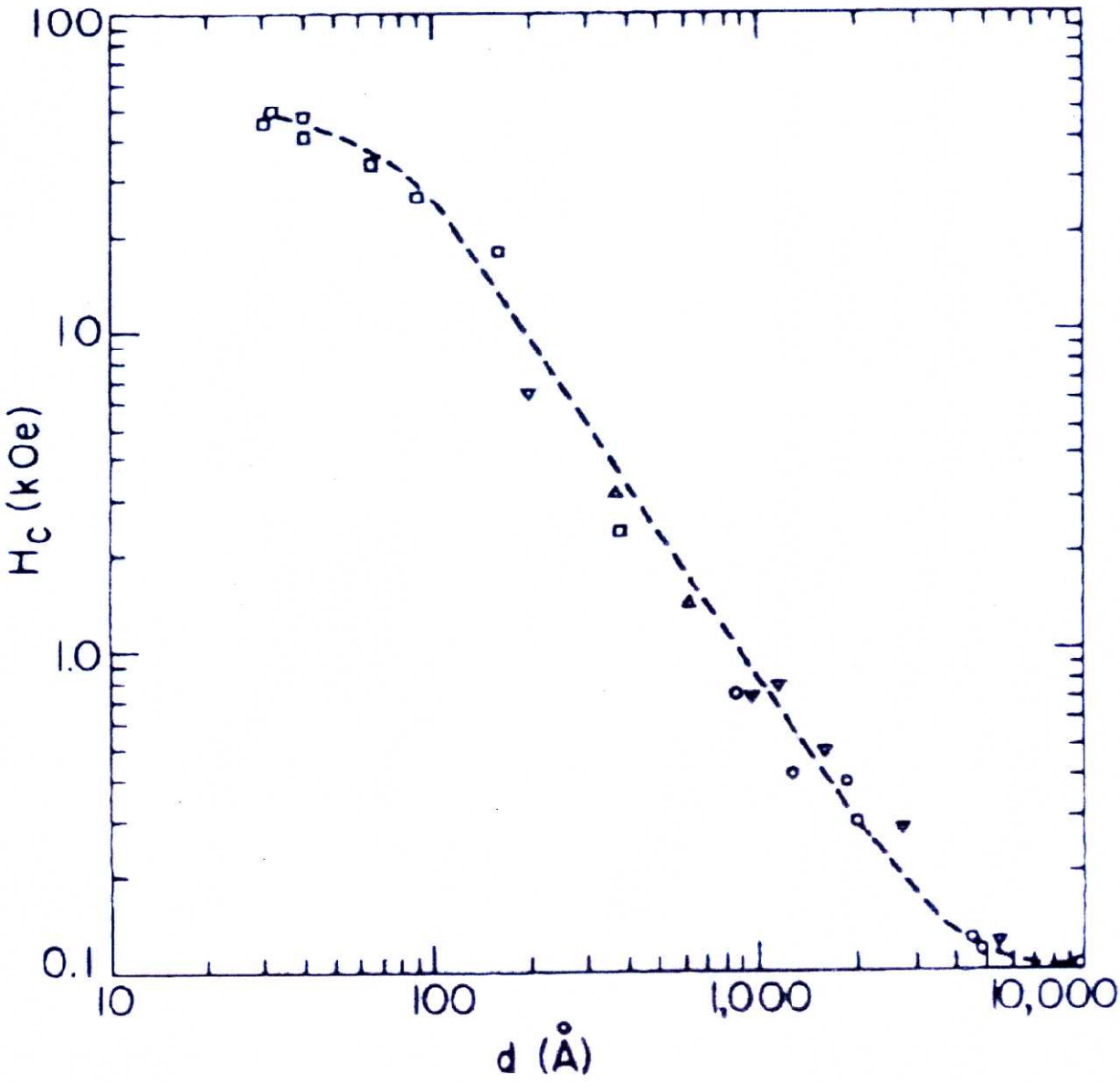

Fig. 4.6 Critical magnetic field H_c as a function of thickness d of Al thin films. The dashed line has a sloe of -3 / 2 in the region from 2000 to 200Å. □, △, ▽, and ○ are all experimental data. Ref. [4.32]

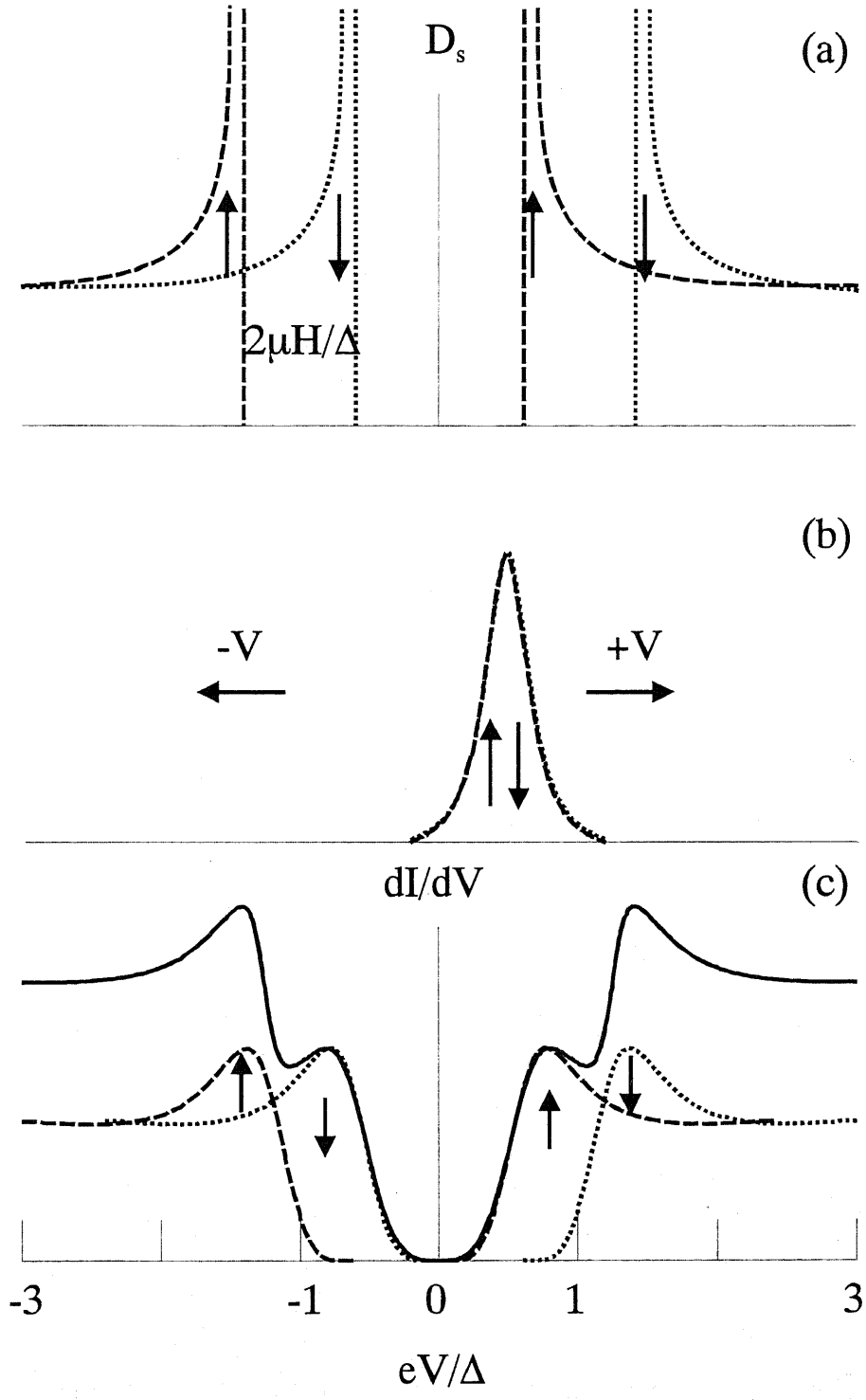

Fig. 4.7 (a) Magnetic field splitting of the quasiparticle states into spin-up (dashed) and spin-down (dotted) densities. (b) the product of density-of-states of a normal metal with the derivative of the Fermi function. (c) Spin-up (dashed) conductance, spin-down (dotted) conductance, and total conductance. Ref. [4.6]

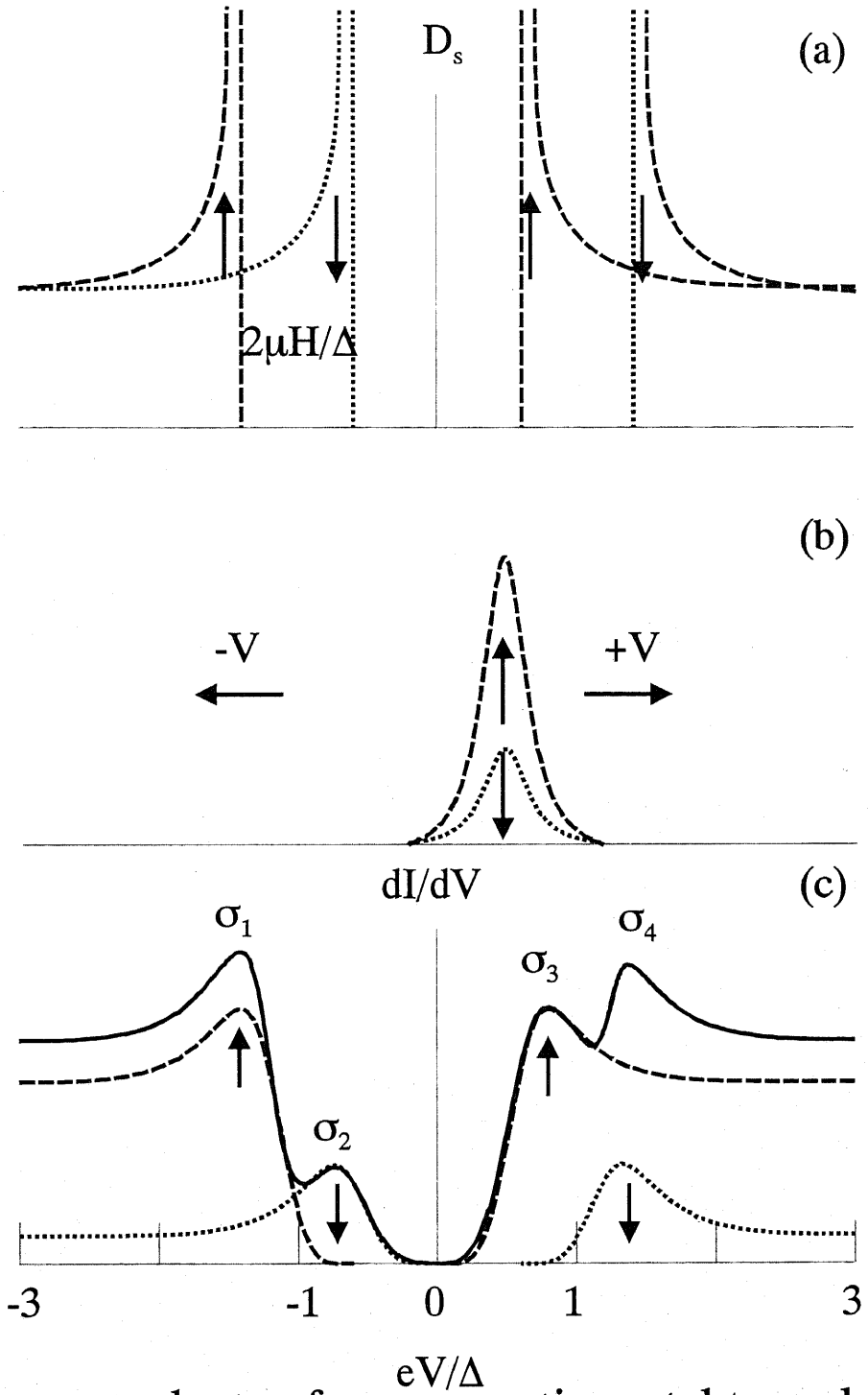

Fig. 4.8 Superconductor-ferromagnetic metal tunnel junction. (a) BCS density -of-states of a superconductor as a function of voltage in a magnetic field. (b) the spin-dependent product of the density-of-states of a ferromagnetic metal with the derivative of the Fermi function. (c) Spin-up (dashed) conductance, spin-down (dotted) conductance, and total conductance. Ref. [4.6]

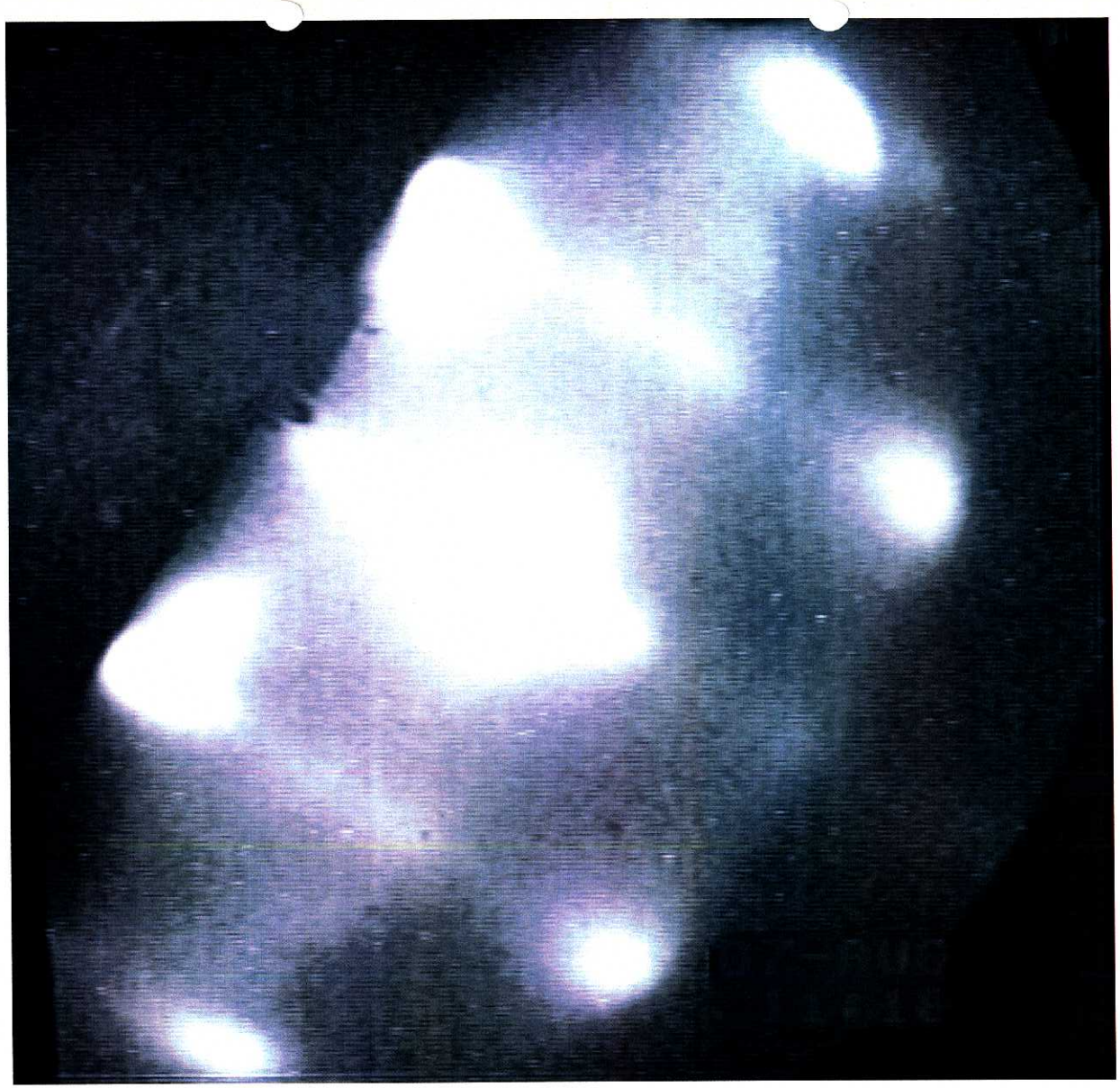

Fig. 4.9 RHEED pattern of epitaxial Al film grown on AlAs by using MBE.

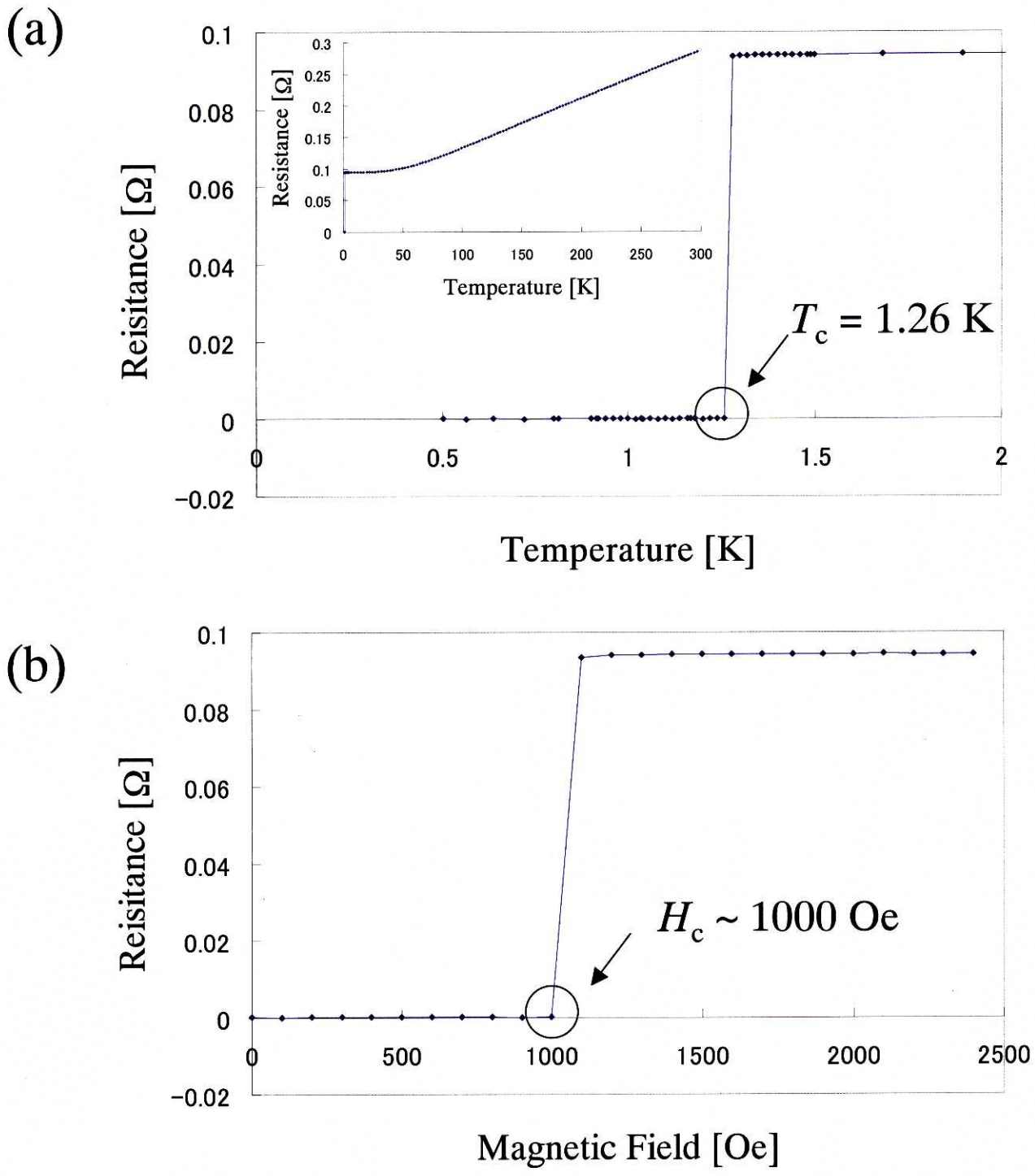

Fig. 4.10 Superconductivity of the Al thin film (338Å) grown on AlAs (30Å) / GaMnAs (2000Å) heterostructures. (a) the temperature dependence of the resistance at low temperature. The inset shows the whole view of the temperature dependence. (b) the field dependence of the resistance.

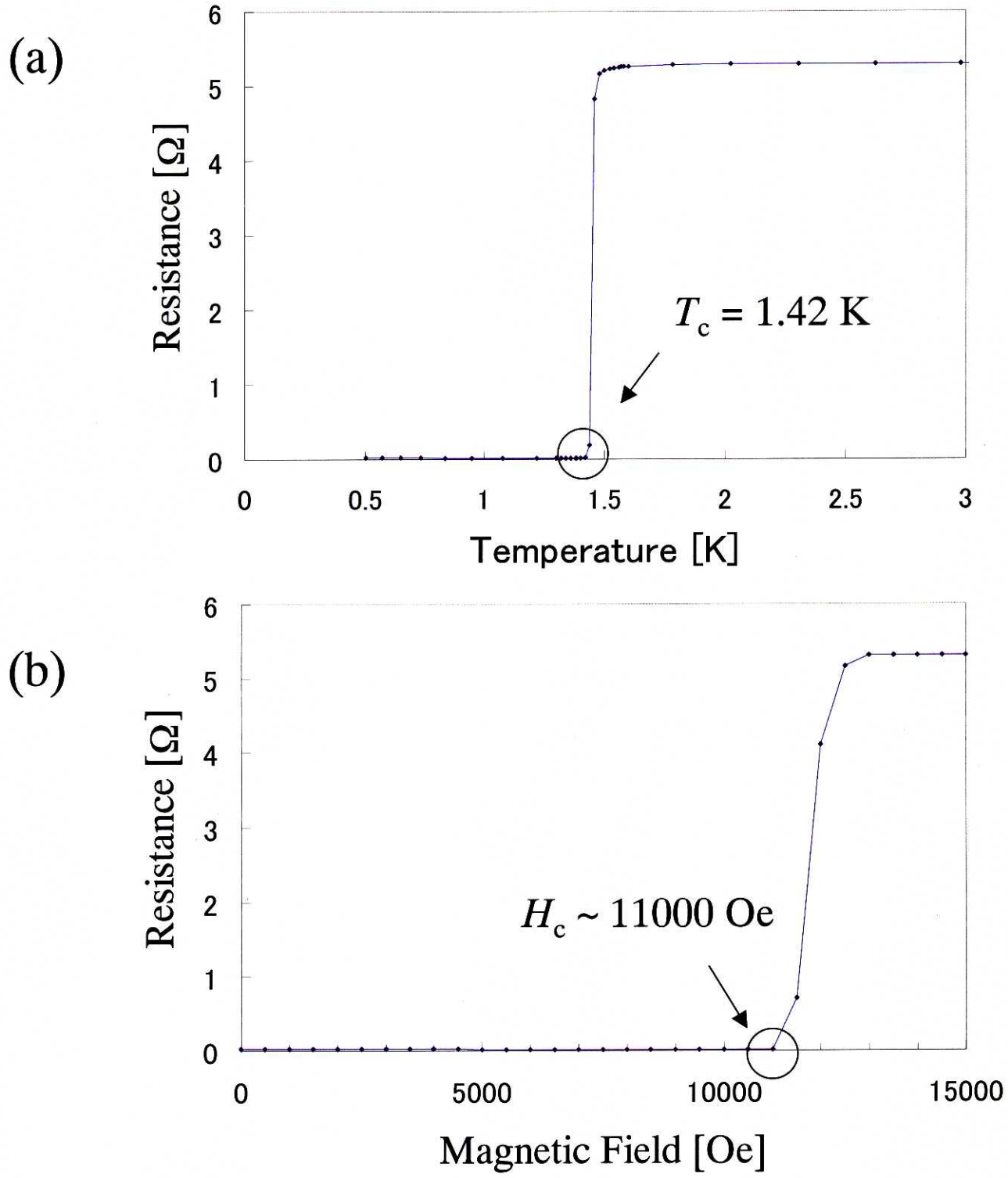

Fig. 4.11 Superconductivity of V (180Å) / Al (100Å) / AlAs (30Å) / GaMnAs (2000Å) heterostructures. (a) the temperature dependence of the resistance at low temperature. The inset shows the whole view of the temperature dependence. (b) the field dependence of the resistance.

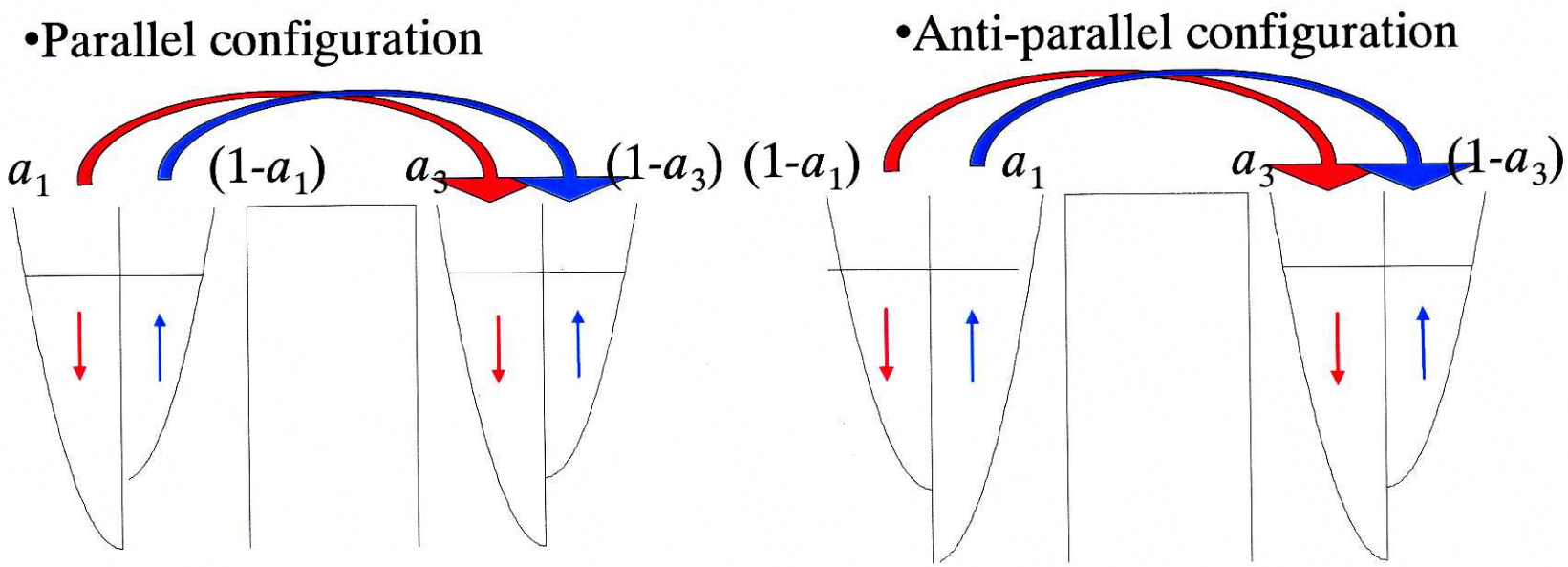

$$G_p \propto a_1 a_3 + (1-a_1)(1-a_3) \qquad G_{ap} \propto a_1 (1-a_3) + (1-a_1) a_3$$

$$TMR\,ratio = \frac{R_{ap} - R_p}{R_p} = \frac{2P_1P_3}{1 - P_1P_3}, \quad P = \frac{n_\uparrow - n_\downarrow}{n_\uparrow + n_\downarrow}$$

Assuming that there is no spin-flipping during the tunneling

Fig. 5.1 The concept of tunneling magnetoresistance (TMR) effect.

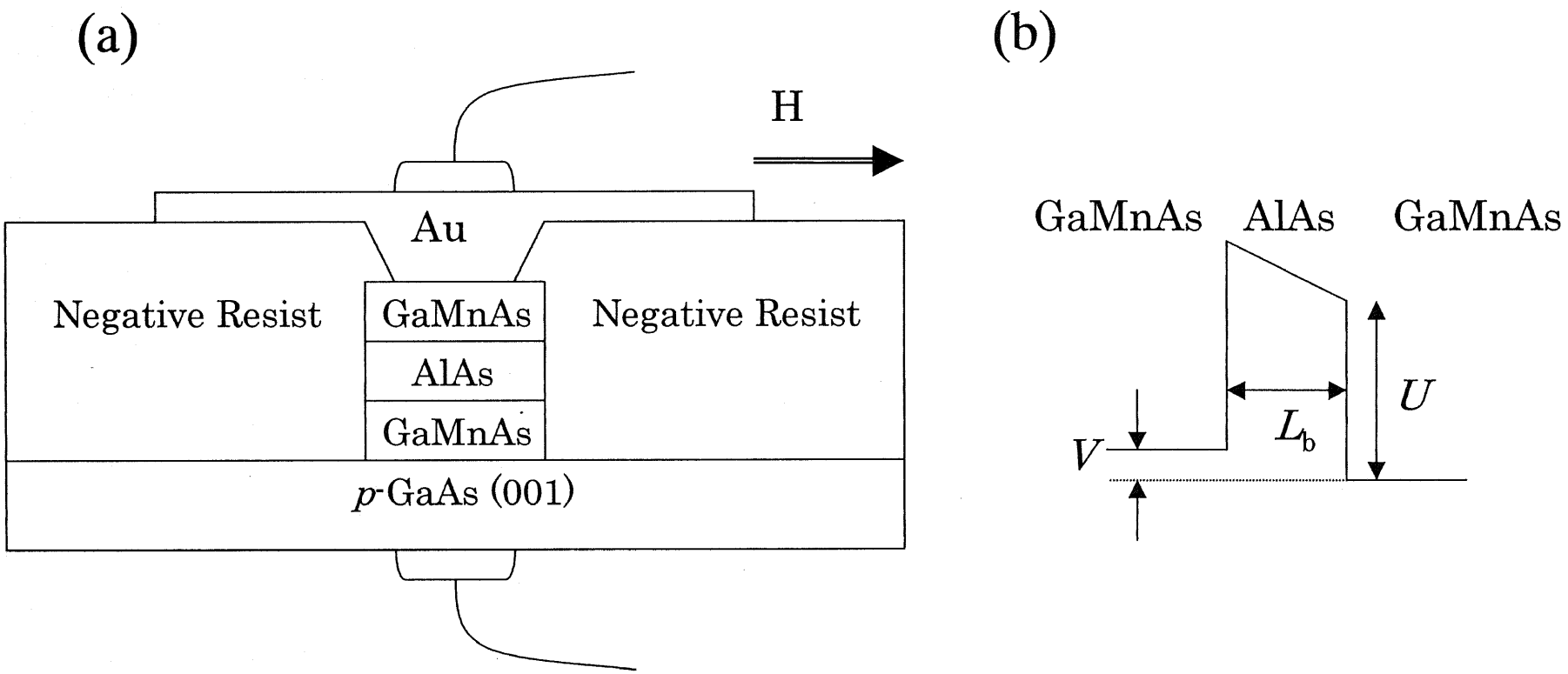

Fig. 5.2 (a) Magnetic tunneling junction structure and (b) valence band profile.

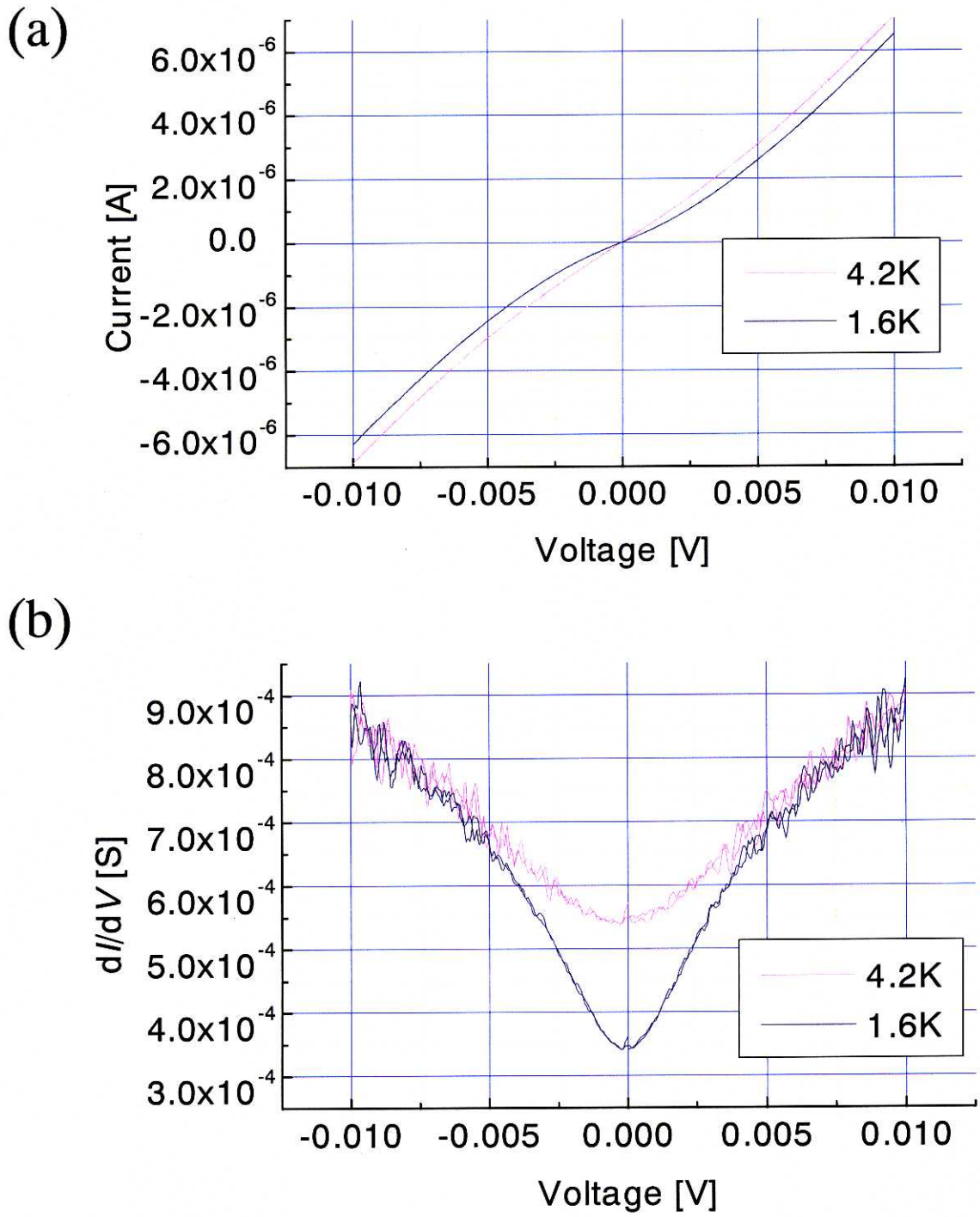

Fig. 5.3 *I-V* and *dI/dV-V* curves of GaMnAs (2000Å) / AlAs (30Å) / GaMnAs (2000Å) with Mn concentration $x = 0.039$.

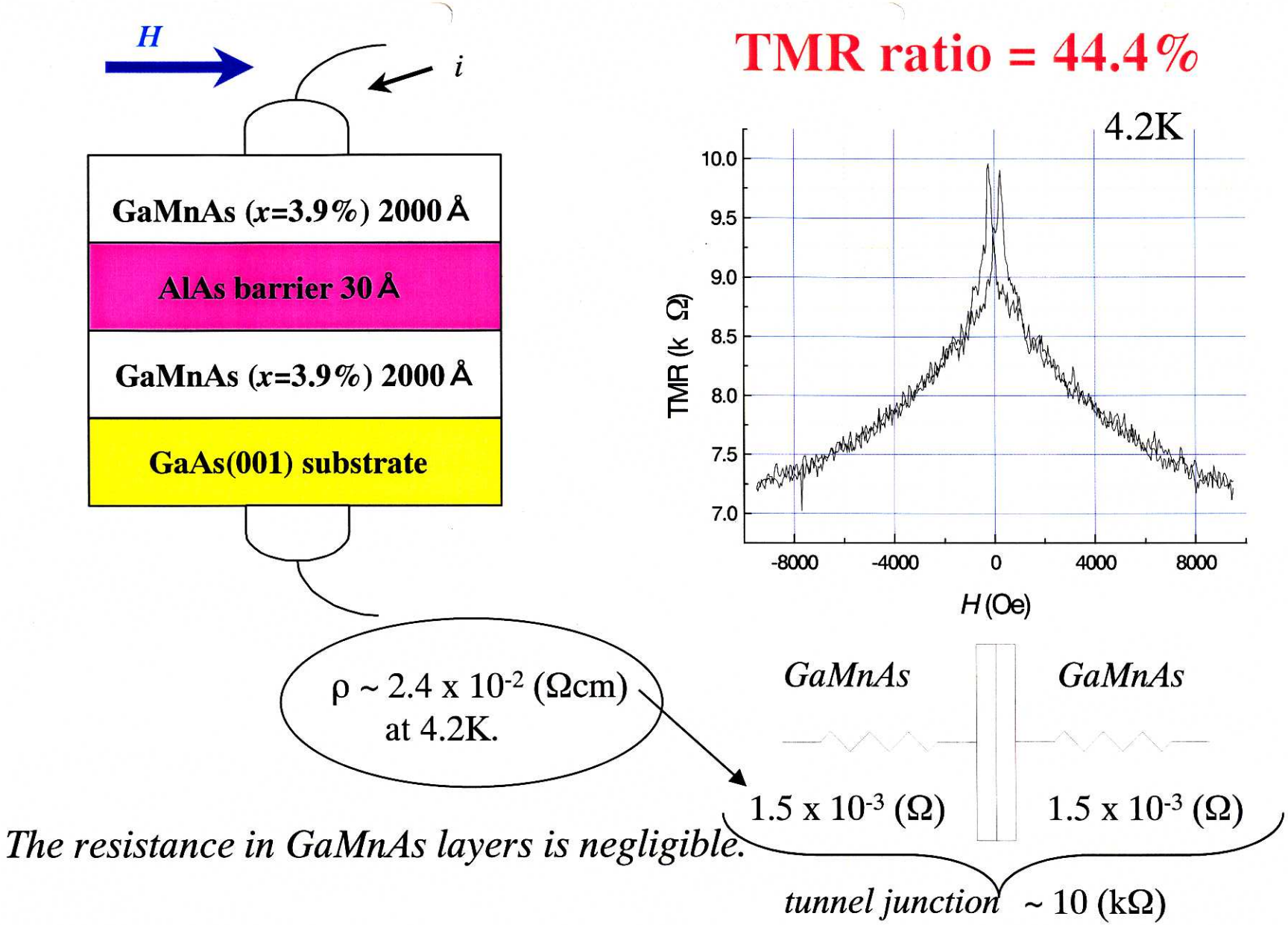

The resistance in GaMnAs layers is negligible.

Fig. 5.4 Tunneling magnetoresistance of a GaMnAs (2000Å) / AlAs (30Å) / GaMnAs (2000Å) tunnel junction measured at nearly zero bias at 4.2K.

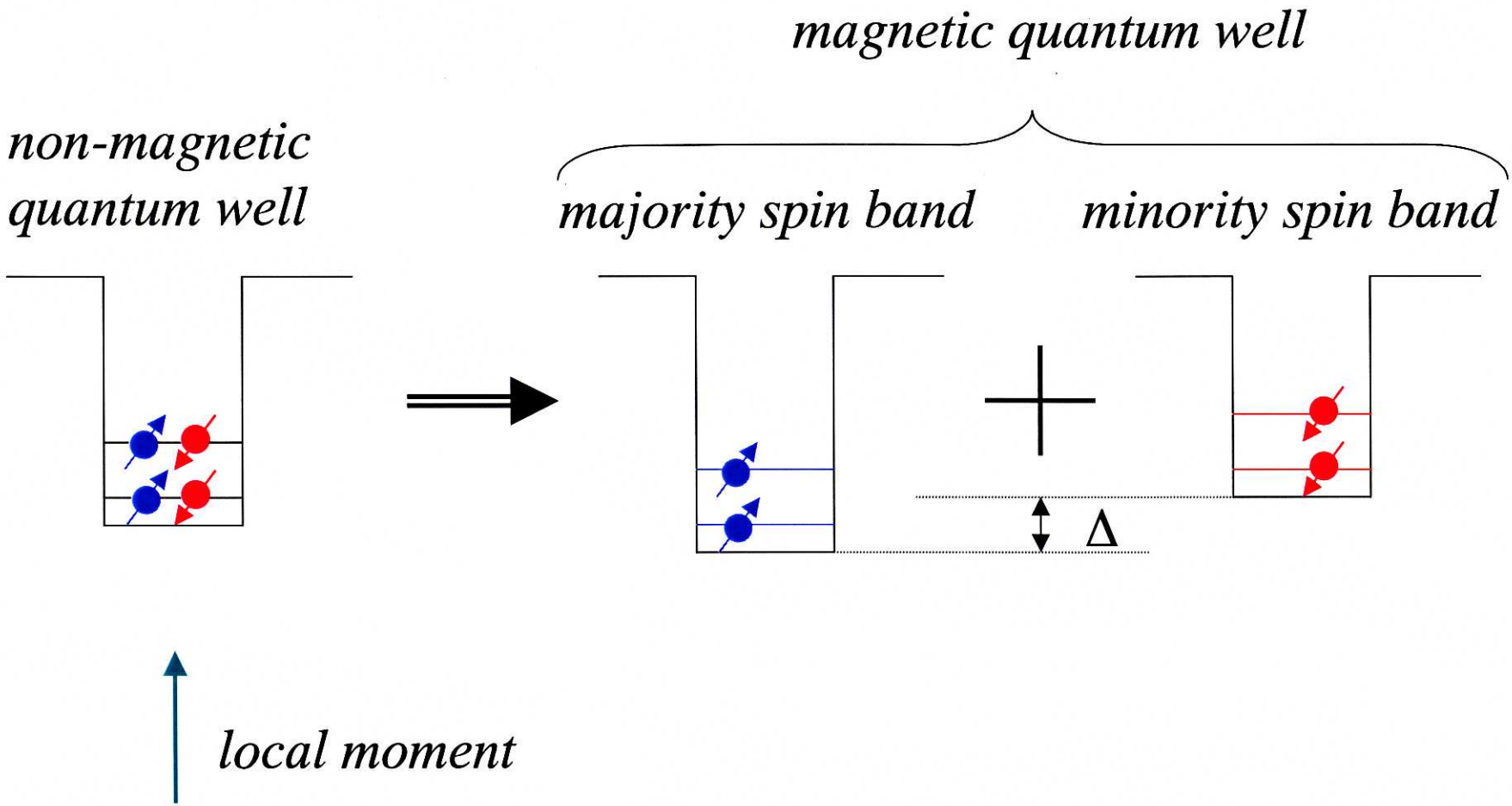

Fig. 5.5 Quantum energy levels in a magnetic quantum well.

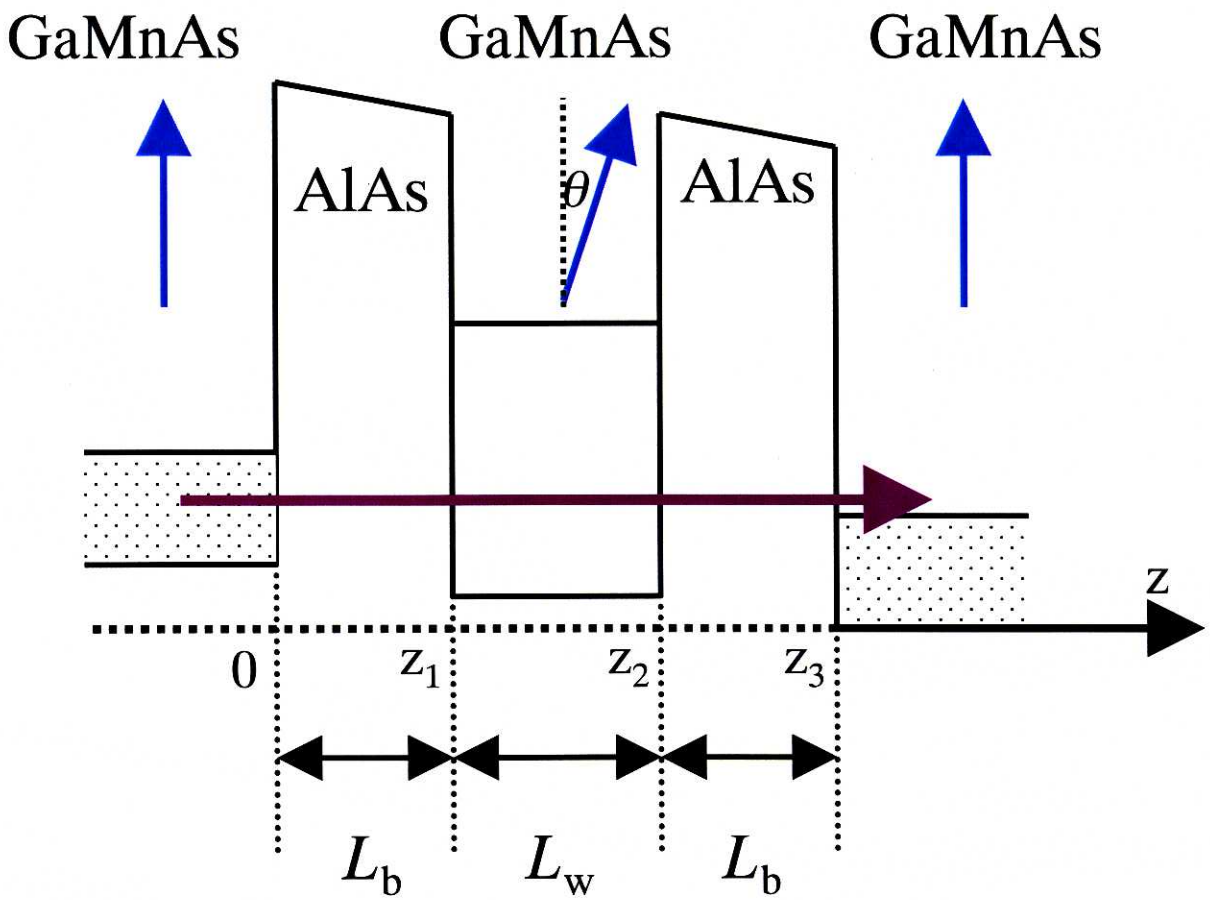

Fig. 5.6 Valence band profile of GaMnAs-based double barrier RTD.

(a) heavy hole

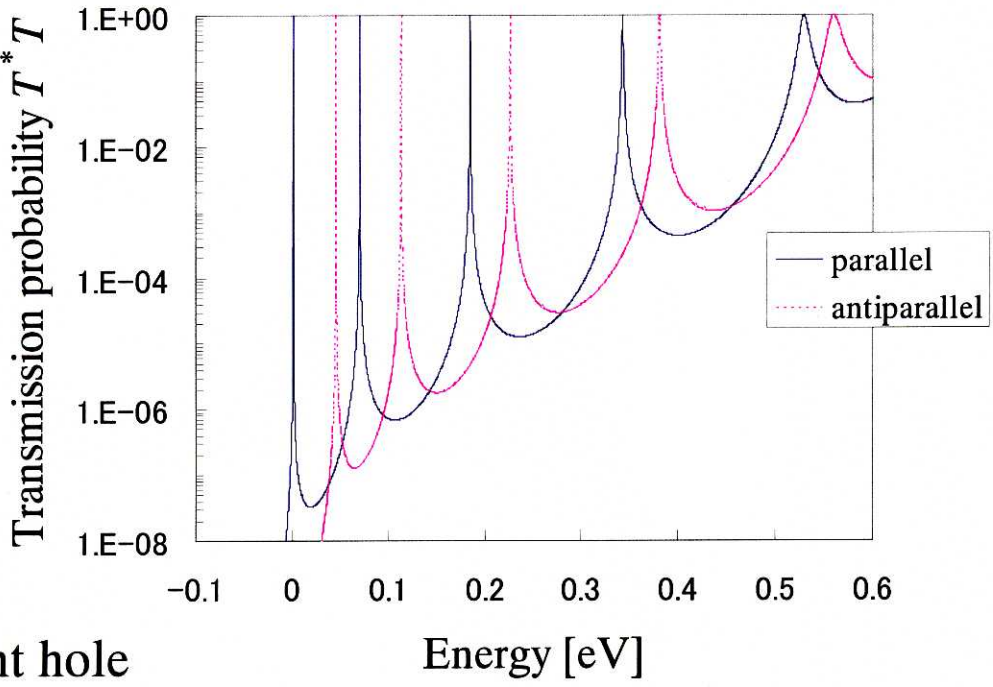

(a) light hole

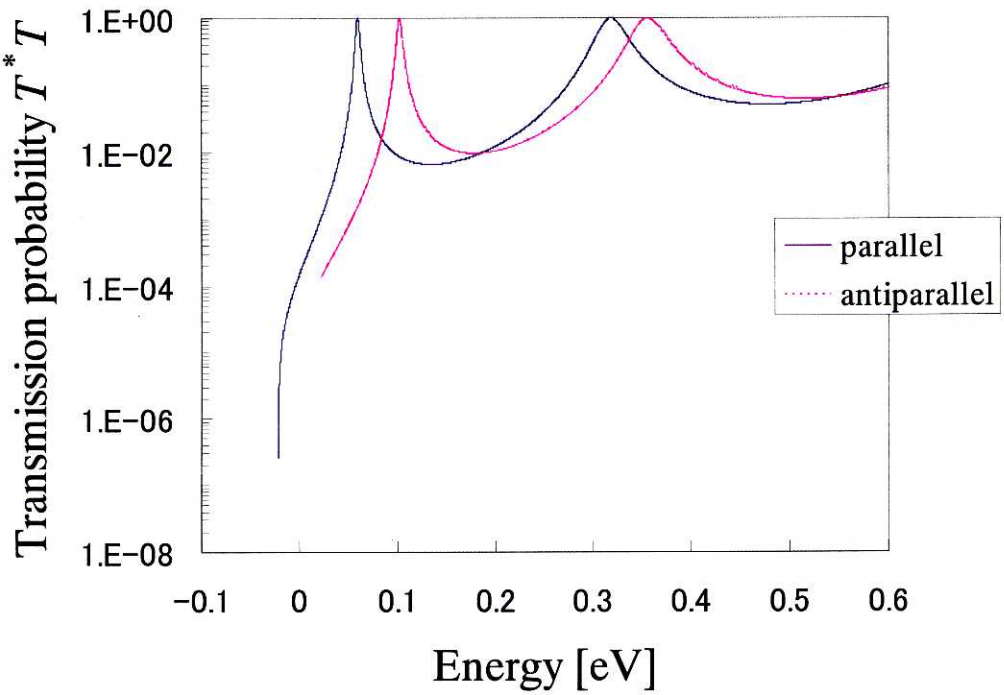

Fig. 5.7 Transmission probability of the GaMnAs / AlAs (14Å) / GaMnAs (50Å) / AlAs (14Å) / GaMnAs RTD.

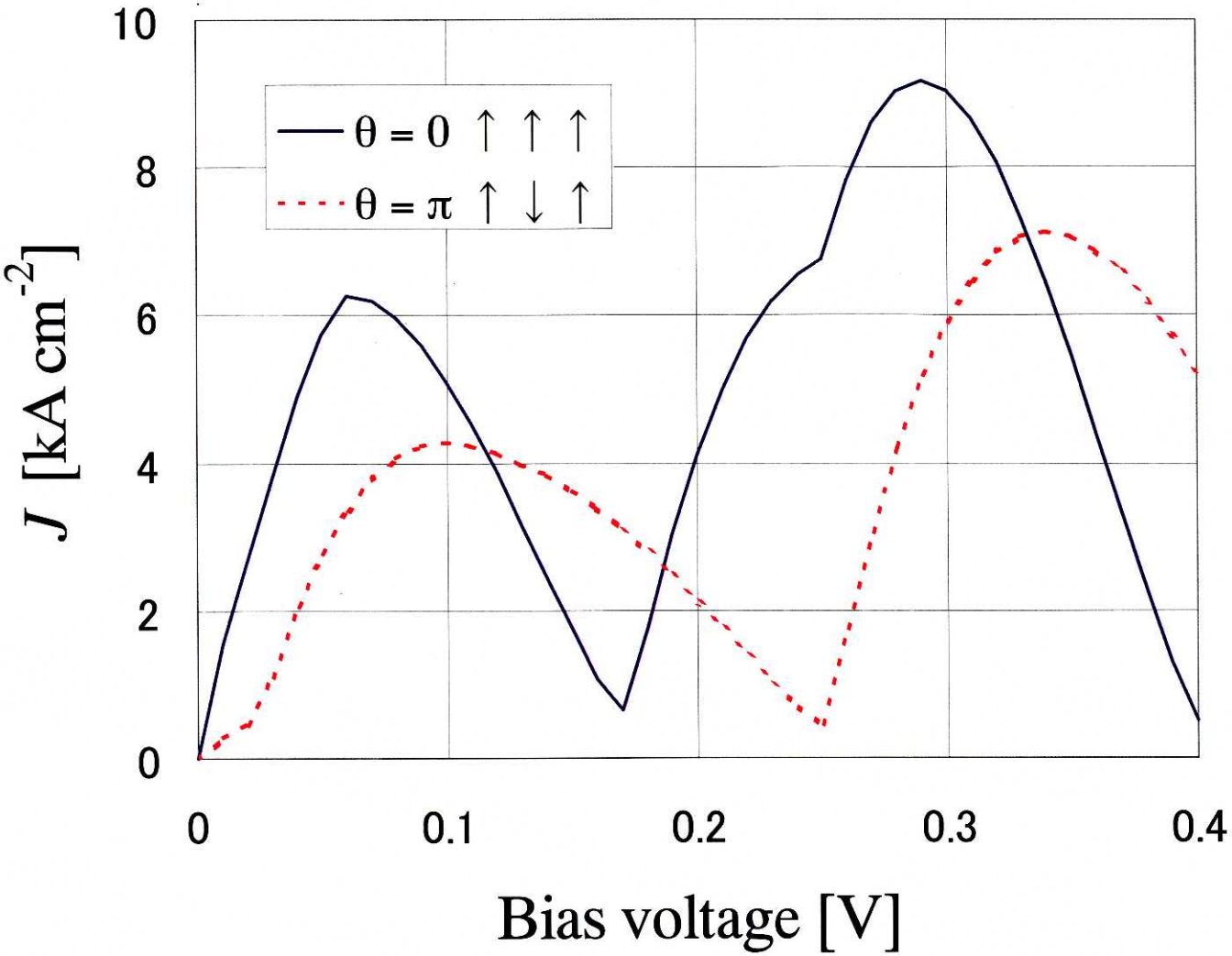

Fig. 5.8 Calculated *J-V* characteristics for the magnetic GaMnAs / AlAs (14Å) / GaMnAs (50Å) / AlAs (14Å) / GaMnAs RTD structures.

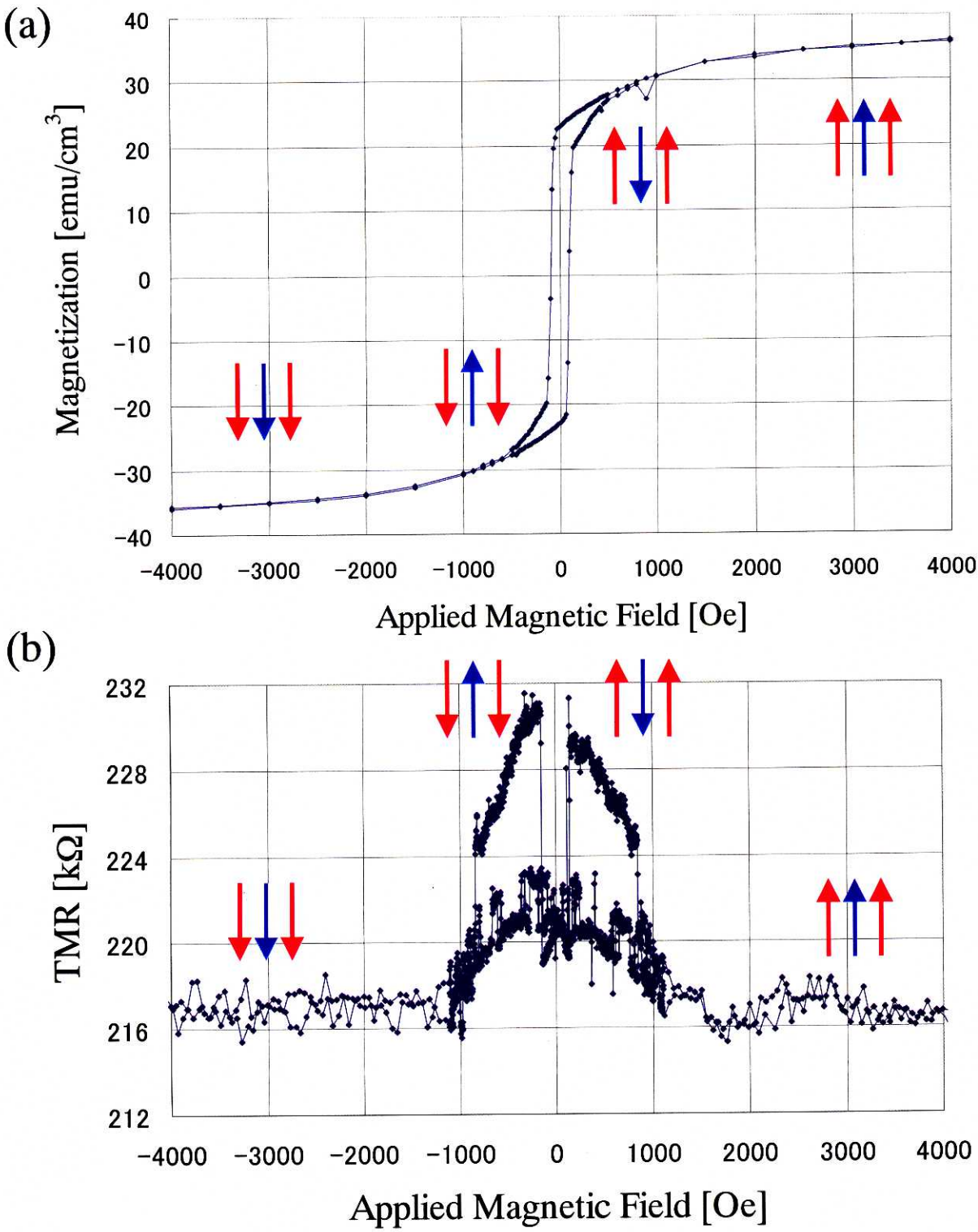

Fig. 5.9 (a) Magnetic field dependence of magnetization and (b) TMR of the GaMnAs (300Å, Mn concentration x = 0.04) / AlAs (14Å) / GaMnAs (50Å, x = 0.04) / AlAs (14Å) / GaMnAs (300Å, x = 0.04) RTD.

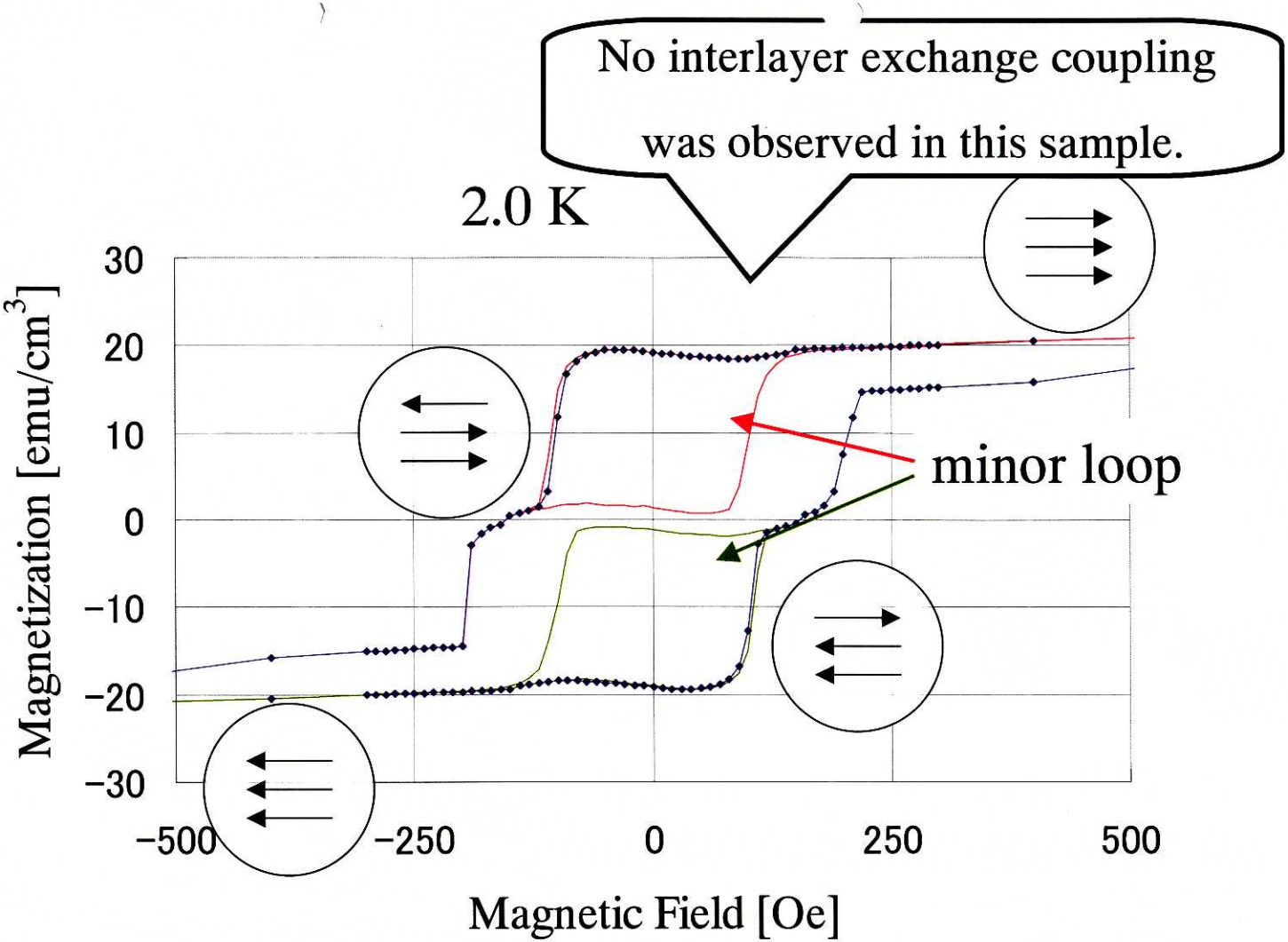

Fig. 5.10 Magnetization (*M-H*) curve of the GaMnAs (2000Å, Mn concentration x = 0.045) / AlAs (28Å) / GaMnAs (80Å, x = 0.035) / AlAs (28Å) / GaMnAs (2000Å, x = 0.045) RTD at 2.0K.

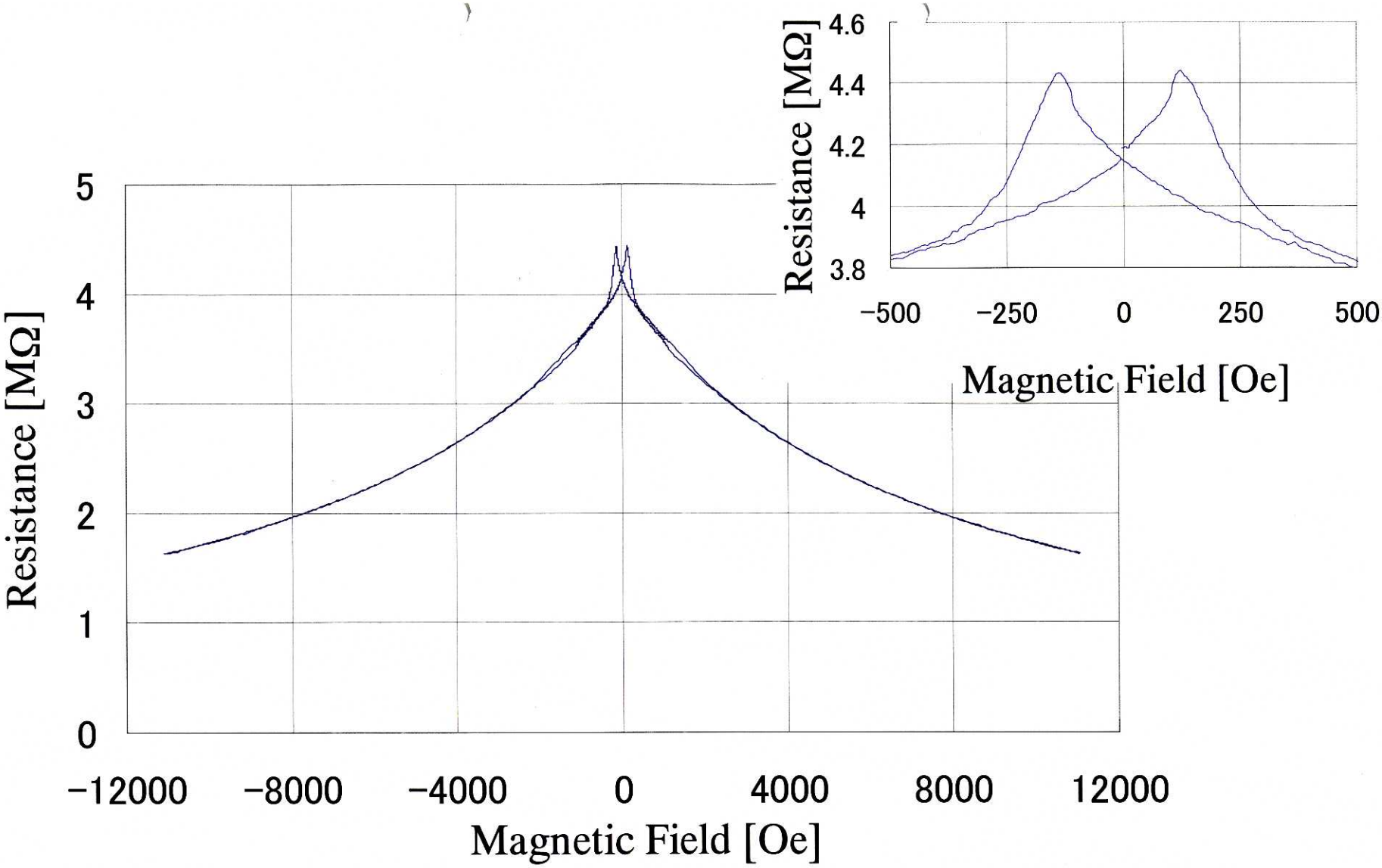

Fig. 5.11 Tunneling magnetoresistance of the GaMnAs (2000Å, Mn concentration x = 0.45) / AlAs (28Å) / GaMnAs (80Å, x = 0.035) / AlAs (28Å) / GaMnAs (2000Å, x = 0.45) RTD measured at nearly zero bias at 4.2K .

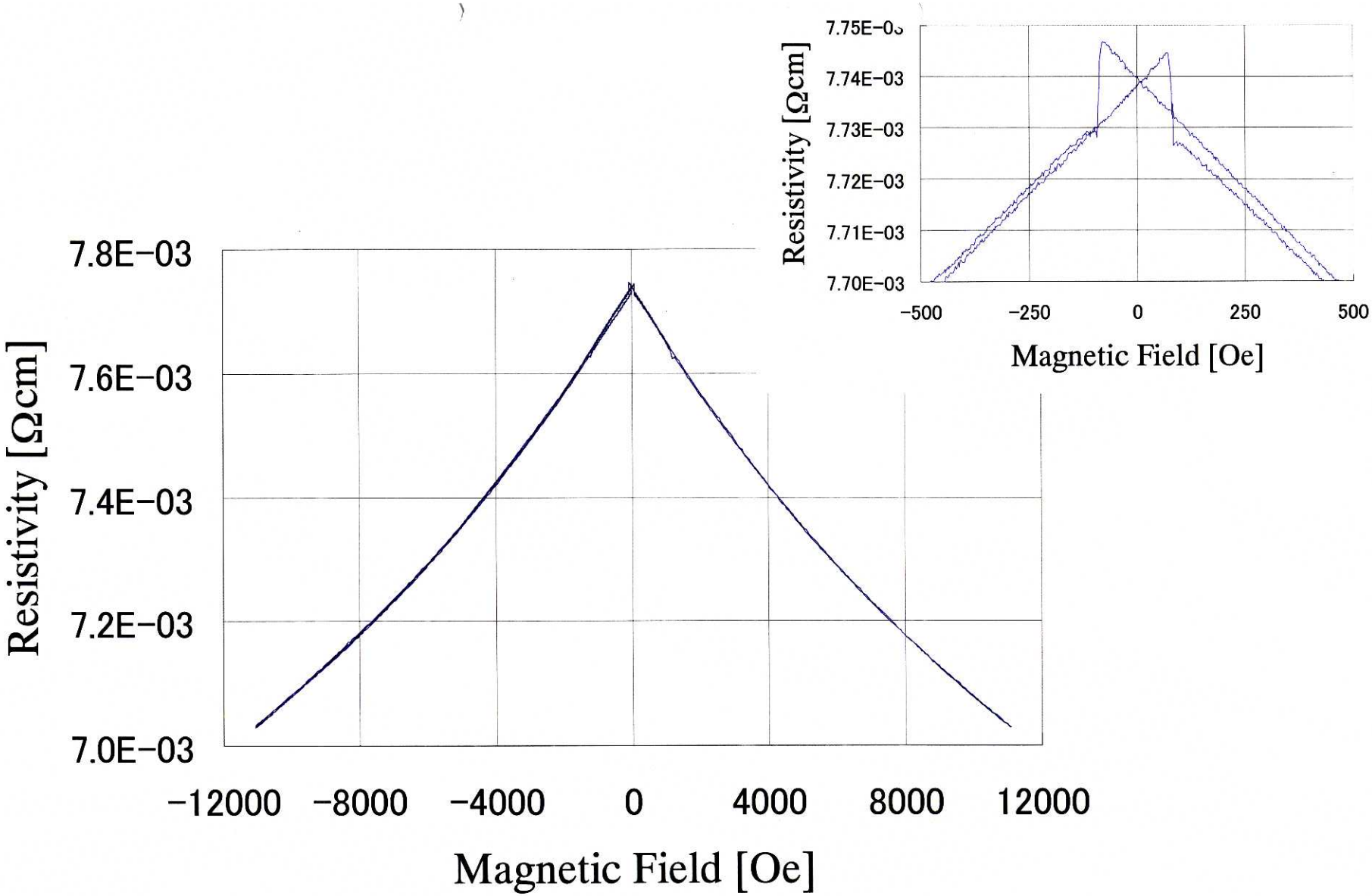

Fig. 5.12 CIP-MR of the GaMnAs (2000Å, Mn concentration x = 0.45) / AlAs (28Å) / GaMnAs (80Å, x = 0.45) / AlAs (28Å) / GaMnAs (2000Å, x = 0.45) RTD measured at nearly zero bias at 4.2K .

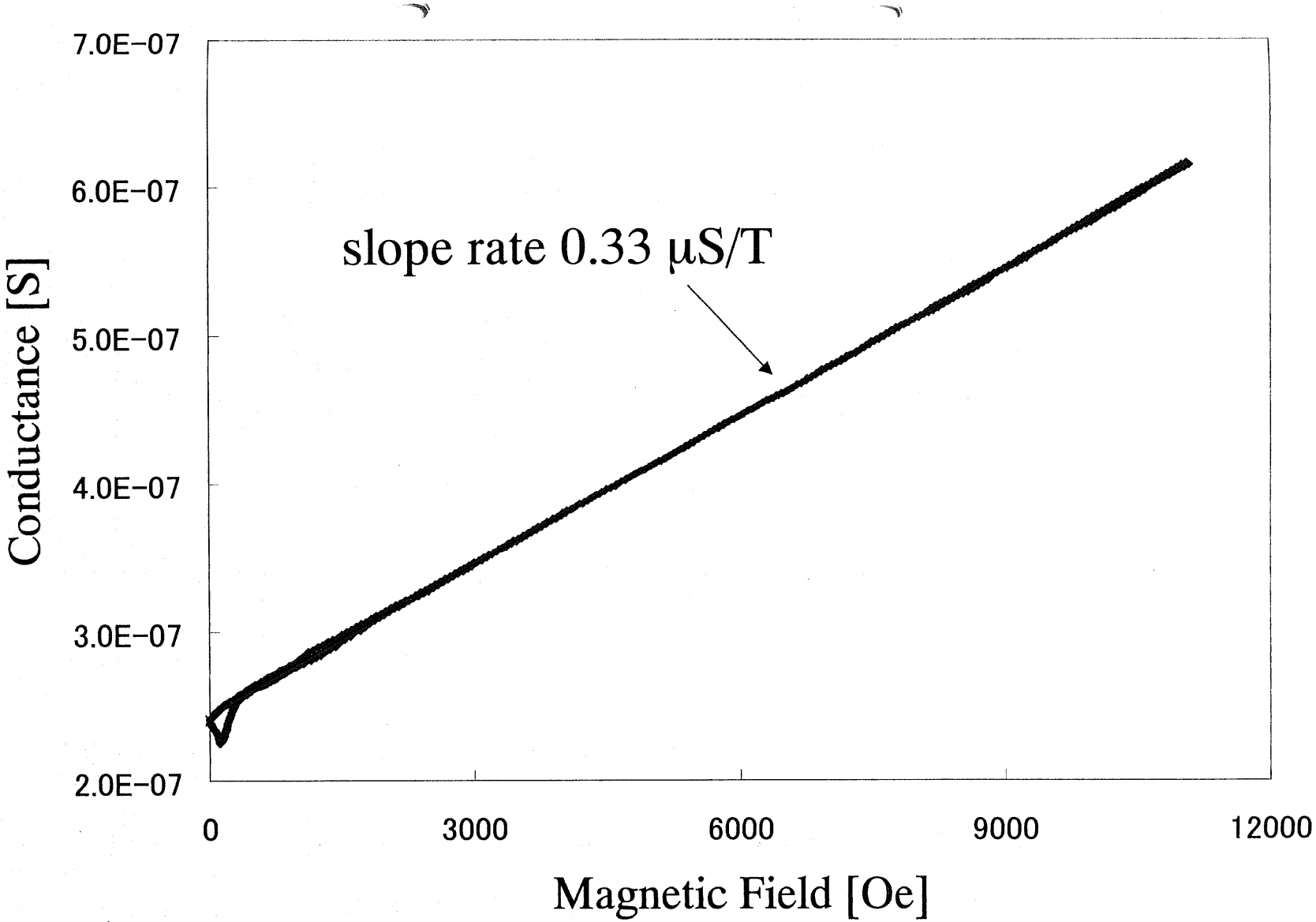

Fig. 5.13 Magnetic field dependence of tunneling conductance of the GaMnAs (2000Å, Mn concentration x = 0.045) / AlAs (28Å) / GaMnAs (80Å, x = 0.035) / AlAs (28Å) / GaMnAs (2000Å, x = 0.045) RTD at 4.2K.

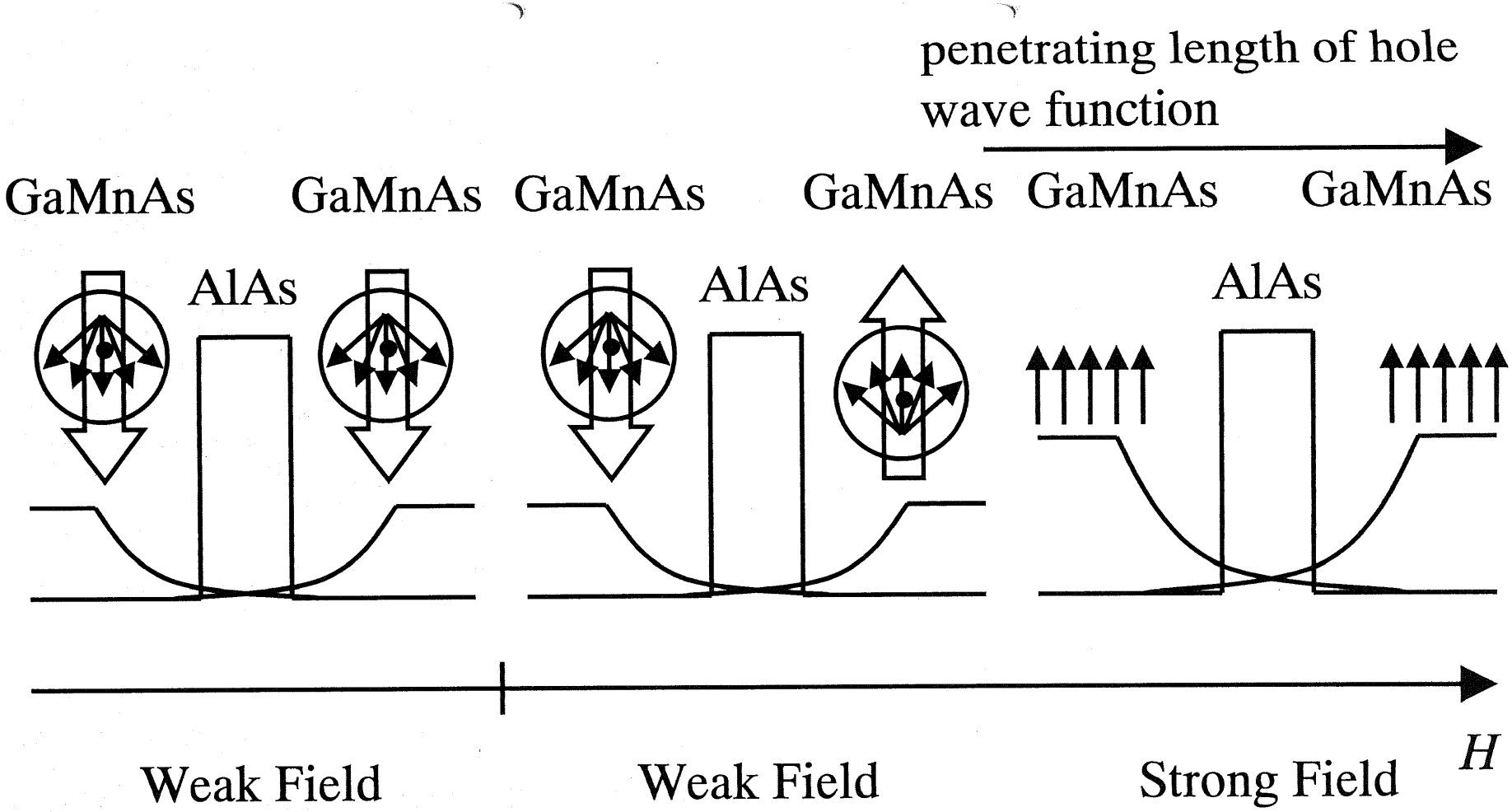

Fig. 5.14 Schematic explanation of magnetic field dependence of the tunneling magnetoresistance effect of GaMnAs-based tunnel junctions.

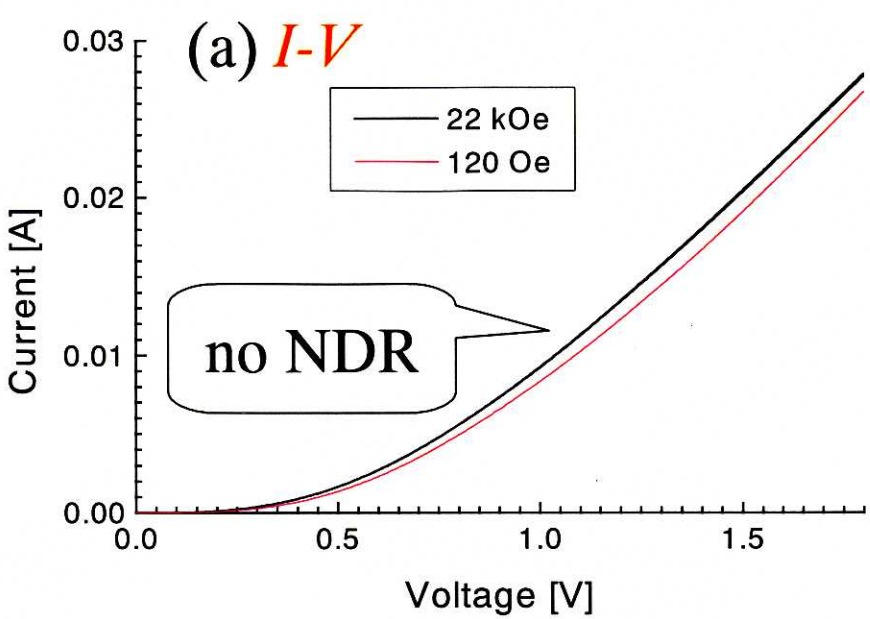

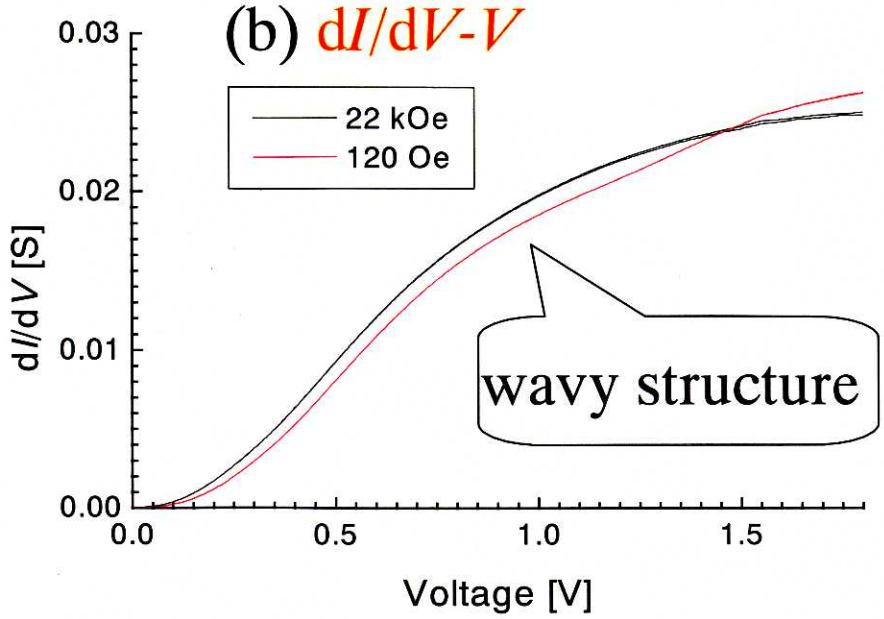

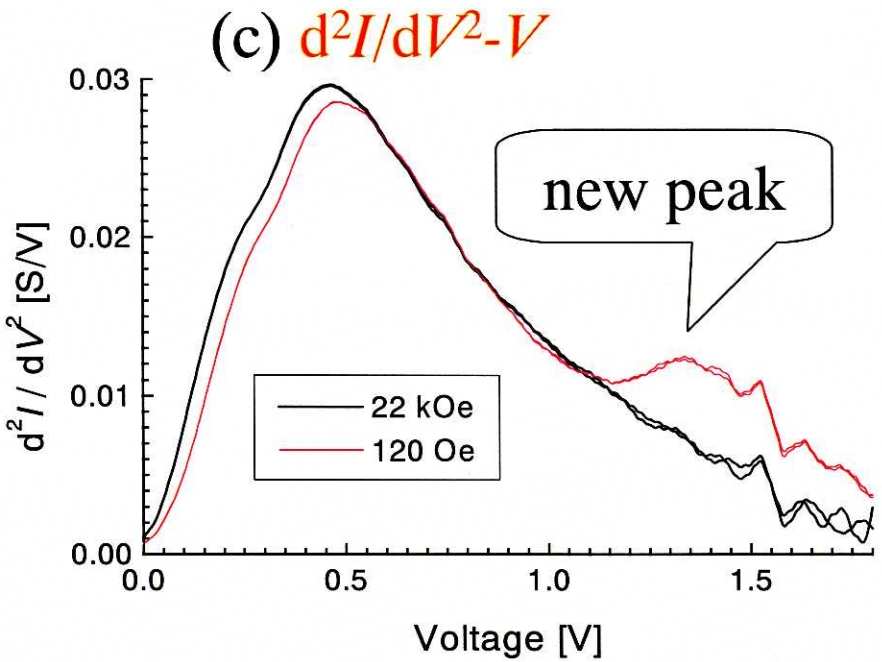

Fig. 5.15 The (a) *I-V*, (b) *dI/dV-V*, and (c) d^2I/dV^2-*V* characteristics of the GaMnAs (2000Å, Mn concentration x =0.045) / AlAs (28Å) / GaMnAs (80Å, x =0.035) / AlAs (28Å) / GaMnAs (2000Å, x =0.045) RTD at 4.2K.

•Parallel configuration: $\theta = 0$

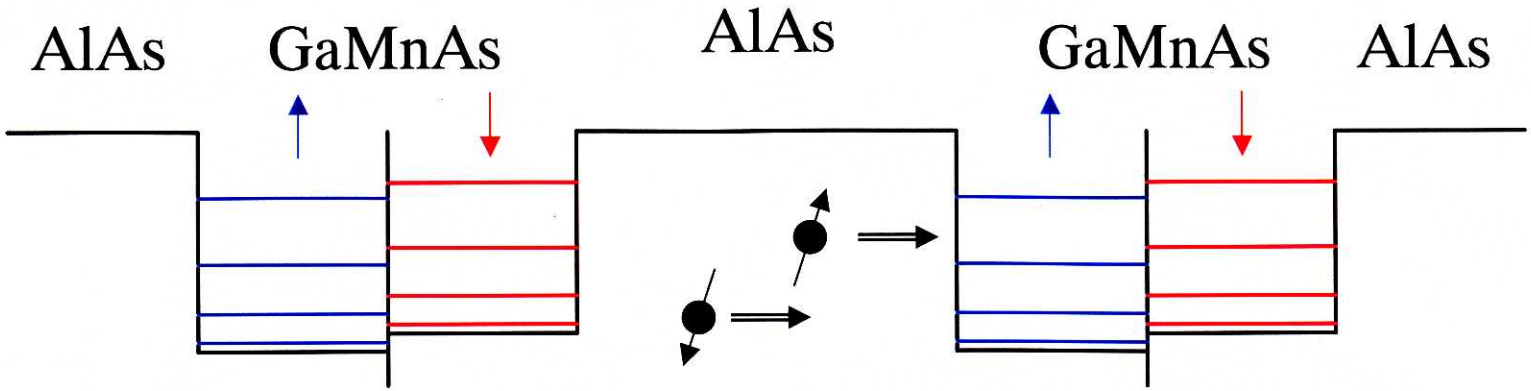

•Anti-parallel configuration: $\theta = \pi$

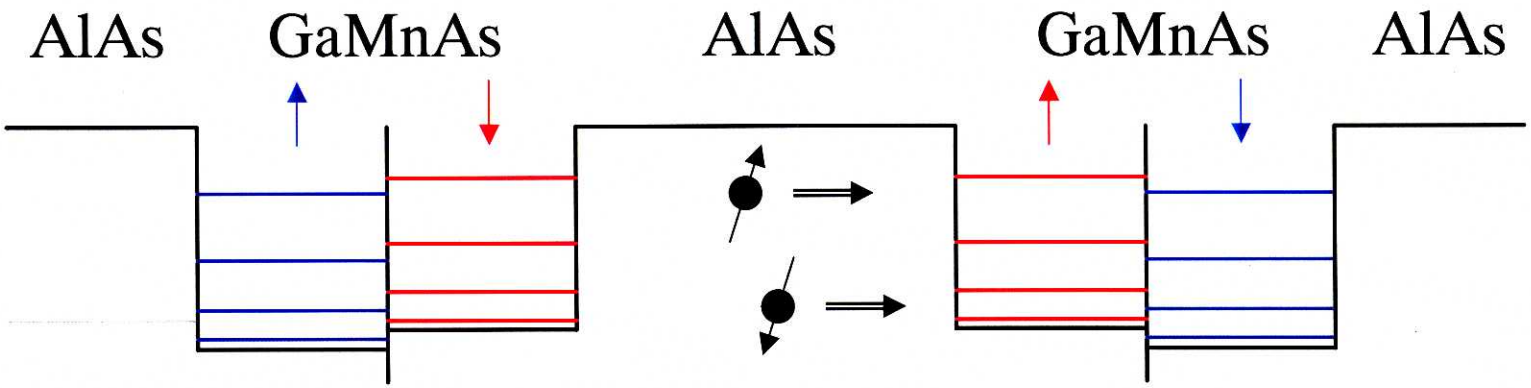

Assuming that there is no spin-flipping during the tunneling

Fig. 5.16 Schematic explanation of tunneling magnetoresistance of a magnetic magnetic quantum well structure

In case of anti-parallel configuration

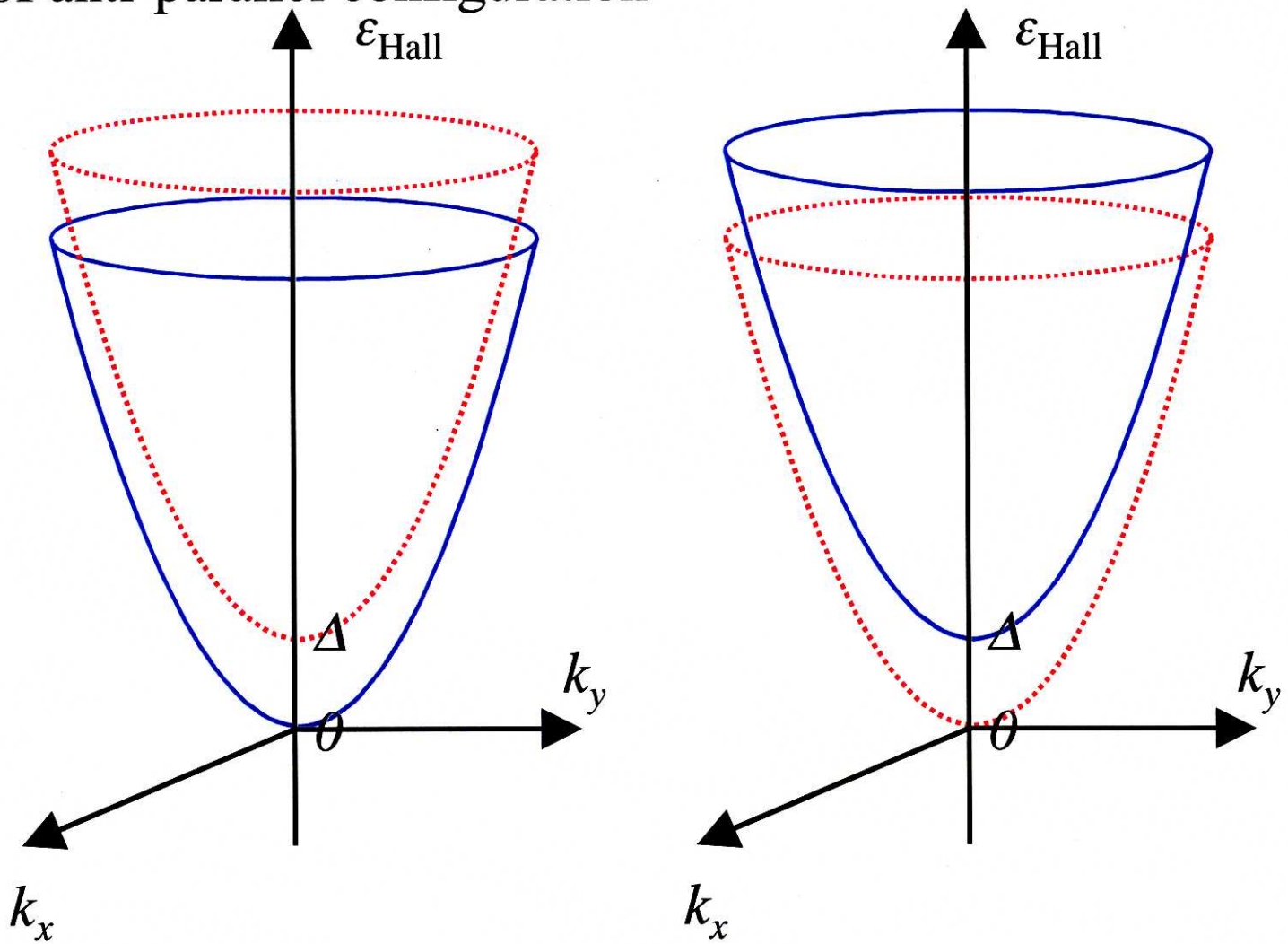

Fig. 5.17 Schematic explanation of tunneling magnetoresistance of magnetic double magnetic quantum wells in the antiparallel configuration of their magnetization direction . We assume that electron coherency is kept during the tunneling process

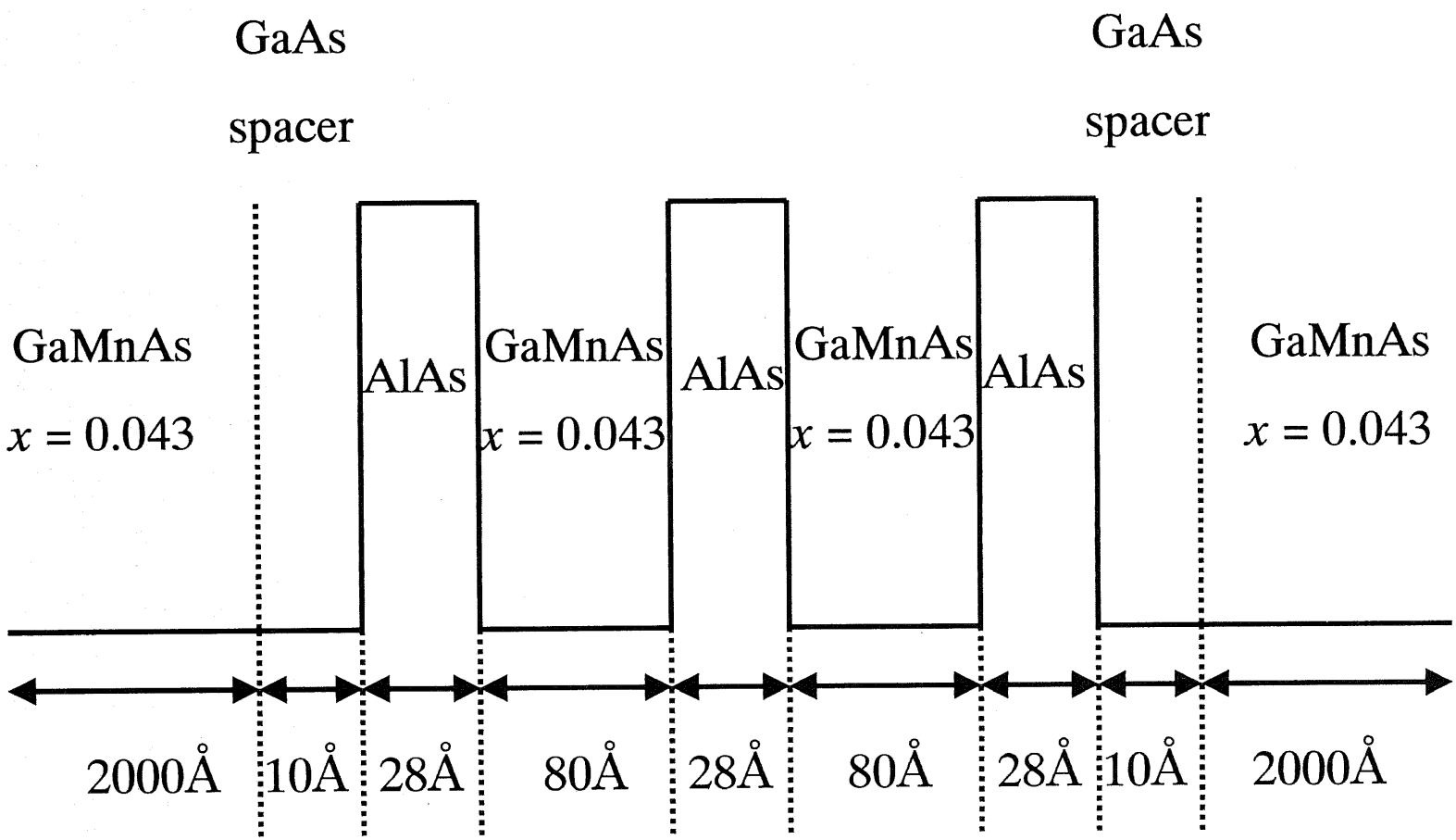

Fig. 5.18 Sample structure of a magnetic double quantum well diode.

(a) total view

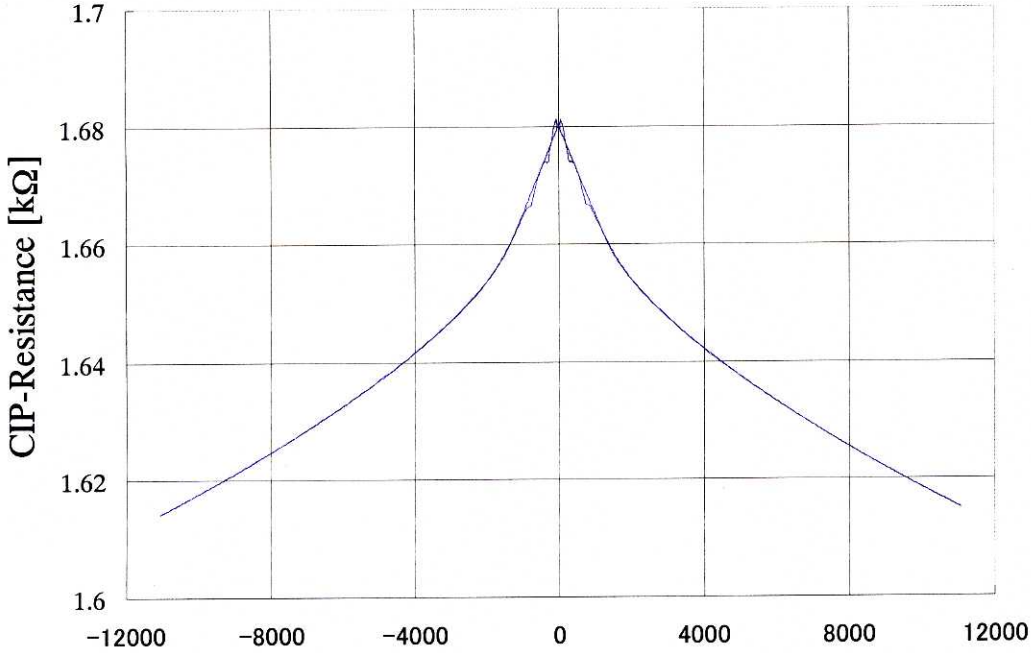

(b) close-up

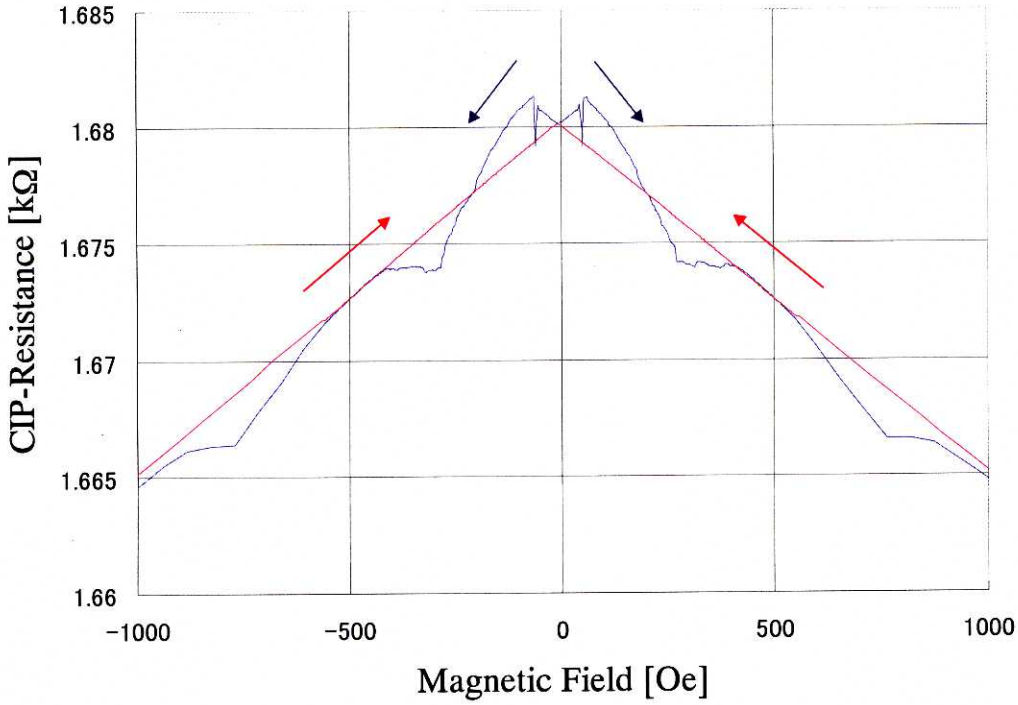

Fig. 5.19 CIP-magnetoresistance of a magnetic double quantum well diode GaMnAs (2000 Å, x = 0.043) / AlAs (28 Å) / GaMnAs (80 Å, x = 0.043) / AlAs (28 Å) / GaMnAs (80 Å, x = 0.043) / AlAs (28 Å) / GaMnAs (2000 Å, x = 0.043) at 4.2K.

(a) total view

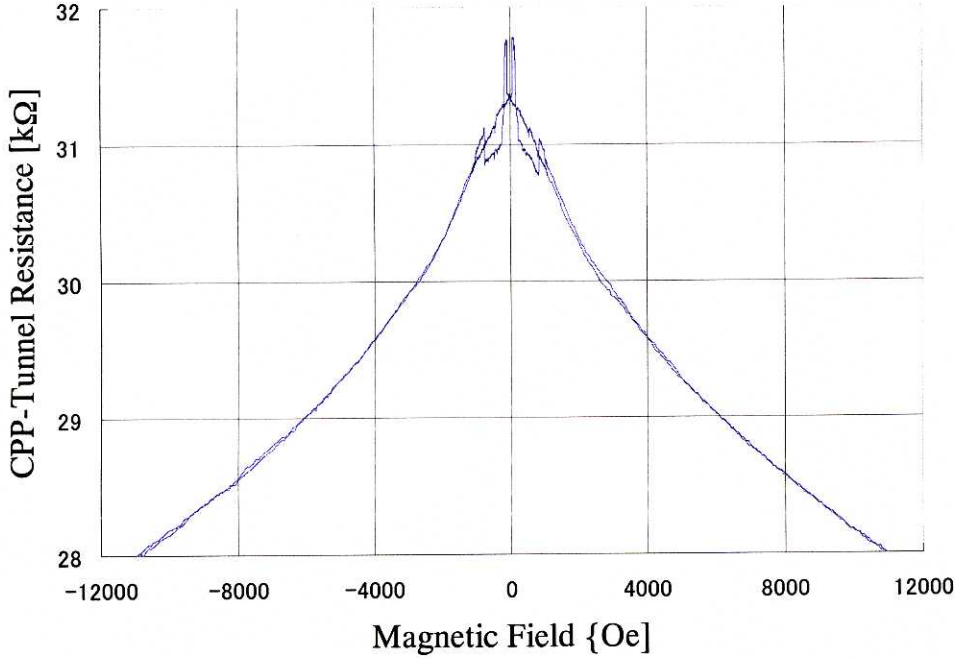

(b) close-up

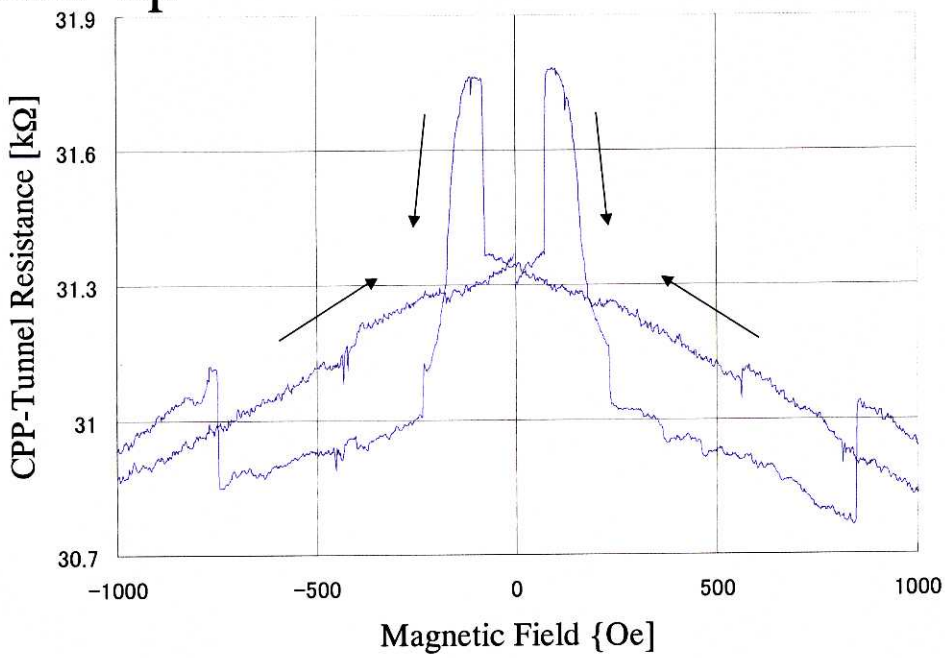

Fig. 5.20 Tunneling magnetoresistance of a magnetic double quantum well diode GaMnAs (2000 Å, x = 0.043) / AlAs (28 Å) / GaMnAs (80 Å, x = 0.043) / AlAs (28 Å) / GaMnAs (80 Å, x = 0.043) / AlAs (28 Å) / GaMnAs (2000 Å, x = 0.043) at 4.2K.